MOLECULAR IMAGING AGENTS FOR RHEUMATOID ARTHRITIS AND CANCER

SYNTHESIS OF NOVEL PET AND FLUORESCENT PROBES FOR THE MOLECULAR IMAGING OF RHEUMATOID ARTHRITIS AND CANCER

By SALMA A. AL-KARMI, BSc., MSc.

A Thesis Submitted to the School of Graduate Studies in Partial Fulfilment

of the Requirements for the Degree of Doctor of Philosophy

McMaster University DOCTOR OF PHILOSOPHY (2016) Hamilton,

Ontario (Chemical Biology)

TITLE: Synthesis of Novel PET and Fluorescent Probes for the Molecular Imaging of Rheumatoid Arthritis and Cancer

AUTHOR: Salma A. Al-Karmi, B.Sc., MSc. (Ryerson University),

SUPERVISORS: Professor John F. Valliant and Professor Alfredo Capretta

NUMBER

OF PAGES: xxx, 199

Abstract

This thesis describes novel molecular imaging strategies that can ultimately be used for imaging rheumatoid arthritis (RA) and cancer. In the first approach, a convenient method for the preparation of a “turn on” near-infrared (NIR) optical reactive oxygen species (ROS) probe and its ^{18}F analogue is described. The probe and its radiolabeling precursor are prepared in high yield (82 and 98% respectively) *via* a Suzuki coupling in two steps. Chemical induction studies revealed the probe selectively responds to hydroxyl and superoxide radicals. The PET probe was accessed *via* a late-stage fluorination approach from a nitropyridine precursor in a 62% decay-corrected radiochemical yield. As a proof of concept, the PET probe was assessed *in vivo* in C57BL/6 mice using a doxorubicin induced model of cardiac ROS which revealed a statistically significant retention in the heart as compared to untreated mice ($p < 0.05$). The probe additionally demonstrated high-blood retention *in vivo*, which is likely due to albumin binding. Less hydrophobic derivatives of this probe were synthesized in a similar approach with the ultimate goal of improving *in vivo* clearance.

Building on this work, the synthesis of a *meso* fluorinated cyanine dye derived from copper-catalyzed halogen exchange of IR780 iodide is discussed. Optimized reaction conditions led to a 68% yield in the presence of a phosphaadamantane ligand and a copper (II) catalyst. The fluorinated probe exhibited enhanced fluorescence in comparison to IR780 in solution. The corresponding ROS probes (hydrocyanines) were assessed in a PC-3 cell assay where the fluorinated probe exhibited 2-3 fold fluorescence enhancement. Radiolabeling to produce the ^{18}F analogue was attempted, but this was found to be irreproducible. This fluorinated dye along with IR780 and other synthesized fluorescent probes were encapsulated in F-127 micelles which resulted in the preparation of monodispersed micelles (PDI ≤ 0.2). Improved solubility and fluorescence were observed as compared with unencapsulated dyes. An MTT assay performed on the encapsulated ROS probe revealed it was considerably less cytotoxic than the parent probe.

Alternatively, a targeted approach *via* the development of molecular probes based on two classes of high affinity TACE enzyme inhibitors is described. Three compounds were synthesized and assessed in a fluorogenic assay in which one compound demonstrated binding in the micromolar range (IC_{50} = 1770 nM) while the remaining compounds demonstrated low nanomolar affinity (IC_{50} = 5-10 nM). Intermediates that could serve as precursors in ^{18}F labeling *via* a prosthetic group labeling strategy were prepared.

Acknowledgements

While pursuing my graduate studies, I have come across many bright, motivated and skilled individuals who have not only influenced me to become a better scientist, but also, inspired me on a personal level. Firstly, I would like to thank my supervisors Dr. John Valliant and Dr. Fred Capretta who over the years, have provided unlimited guidance and support. Along the way, they supported my keen curiosity for science and encouraged me to pursue project ideas further. At the same time, they kept me grounded and focused (which for me, is a very difficult task). Under their supervision, I was exposed to many great opportunities such as attending (inter)national conferences where I spoke to leading scientists, participating at workshops and having the ability to visit and be trained at the University of Alberta. I am grateful for these opportunities. Thank you for listening to me and supporting me throughout the years.

I would also like to thank my committee member, Dr. Paul Harrison, for his insightful comments and suggestions regarding my project. I really do appreciate the effort and input you have given throughout the years.

I would like to thank the Valliant and Capretta group members I have had the honour of meeting throughout the years who quickly became my second family. I would like to extend thanks to Dr. Silvia Albu and Dr. Patricia Edem for entertaining great scientific (in addition to non-scientific) discussions and listening to a good earful of my blabbing. I would like to thank Dr. Ramesh Patel for providing valuable scientific insight, but also for being one of the most generous people I have ever met. I am thankful for Alyssa Vito and Stephanie Rathmann who are both always on my speed dial, share common pet-peeves and always tell the best jokes. I would like to thank Reza Yazdani and Omid Beiraghi for all their support and once again, for listening to my blabbing. I would also like to thank Dr. Lisa Walter for her upbeat attitude and contagious optimism. I feel blessed to have gained such great friends.

Last but not least, I would like to thank my family. My husband, Jonathon, who has supported and encouraged me immensely throughout the years. In fear of sounding Cliché, it must be said, undoubtedly, that the completion of this degree would not have been possible without him. Also, without the late night shawarmas I don't think I would have had the energy to keep on rolling. Thank you for everything. I would also like to thank my lovely siblings Sarah and Ahmad who also provided unlimited support. Lastly, I would like to thank my parents, who have sacrificed so much to make me into the person I am today. I owe my work ethic, determination and perseverance to the values they have instilled in me at a very young age. All accomplishments that I have achieved thus far and in the future is as a result of my upbringing. Thank you all.

Table of Contents

List of Figures

List of Schemes

List of Tables

List of Equations

List of Abbreviations and Symbols

[^{18}F]FAZA	^{18}F-fluoroazomycin arabinoside
[^{18}F]DOPA	^{18}F fluorodihydroxyphenylalanine
[^{18}F]FDG	2-deoxy-2-[^{18}F]-fluoro-D-glucose
[^{18}F]FLT	^{18}F-fluorothymidine
β-APP	beta amyloid plaque
ATP	adenosine triphosphate
Ala	alanine
Boc	*tert*-butyloxycarbonyl
BSA	bovine serum albumin
CCD	charge coupled device
CT	computed tomography
DAPI	4',6-diamidino-2-phenylindole
DCFH	2,7-dichlorodihydrofluorescein
DCM	dichloromethane
DCY	decay-corrected yield
DHE	dihydroethidium
DHR 123	dihydrorhodamine 123
DIPEA	*N*,*N*-diisopropylethylamine
DL	drug loading
DLS	dynamic light scattering
DMARD	disease-modifying anti-rheumatic drugs
DMF	dimethylformamide
DMSO	dimethylsulfoxide
DNA	deoxyribonucleic acid
Dox	doxorubicin
EDC	1-ethyl-3-(3-dimethylaminopropyl)carbodiimide
EE	entrapment efficiency
EGF	epidermal growth factor
ELISA	enzyme-linked immunosorbent assay
eNOS	endothelial nitric oxide synthase
EPR	enhanced permeability and retention
ETC	electron transport chain
EtOAc	ethyl acetate
FAD	flavin adenine dinucleotide
FDA	Food and Drug Administration
GSH	glutathione
HALEX	halogen exchange

HEPES	4-(2-hydroxyethyl)-1-piperazineethanesulfonic acid
HIV	human immunodeficiency virus
HOBT	hydroxybenzotriazole
HPLC	high performance liquid chromatography
HRMS	high resolution mass spectrometry
HRP	horseradish peroxidase
HAS	human serum albumin
IC_{50}	half maximal inhibitory concentration
ICG	indocyanine green
IV	intravenous
LDA	lithium diidopropylamide
MeOH	methanol
MMP	matrix metalloprotease
MRI	magnetic resonance imaging
MsCl	methanesulfonyl chloride
MTBE	methyl *tert*-butyl ether
MTT	3-(4,5-dimethylthiazol-2-yl)-2,5-diphenyltetrazolium bromide
NAC	N- acetylcysteine
NAD	nicotinamide adenine dinucleotide
NADP	nicotinamide adenine dinucleotide phosphate
NHC	N-heterocylic carbene
NIR	near infrared
NMR	nuclear magnetic resonance
OI	optical imaging
PA	phosphaadamantane
PAI	photoacoustic imaging
PBS	phosphate buffered saline
PD	Pharmacodynamics
PDI	polydispersity index
PDT	photodynamic therapy
PET	positron emission tomography
PK	pharmacokinetics
PTT	photothermal therapy
PYBOP	(benzotriazol-1-yl-oxytripyrrolidinophosphonium hexafluorophosphate
R_f	retention factor
RA	rheumatoid arthritis
RBC	red blood cells
RCY	radiochemical yield

ROS	reactive oxygen species
R.T.	room temperature
SET	single electron transfer
SOD	superoxide dismutases
SPECT	single photon emission computed tomography
SUV	standardized uptake value
TACE	tumour necrosis factor-alpha converting enzyme
TBAF	tetrabutylammonium fluoride
tBu	tert-butyl
TBDMS	*tert*-butyldimethylsilyl
TBHP	tetrabutyl hydrogen peroxide
t-BuxPhos	2-di-*tert*-butylphosphino-2′,4′,6′-triisopropylbiphenyl
TEM	transmission electron microscopy
TEMPOL	4-hydroxy-2,2,6,6-tetramethylpiperidin-1-oxyl
TFEF	trifluoroethylformate
THP	tetrahydropyranyl
THF	tetrahydrofuran
TLC	thin layer chromatography
TNF-α	tumour necrosis factor-alpha
US	ultrasound
UV	ultraviolet
Val	valine
Γ	gamma
$\Delta\Psi_m$	mitochondrial membrane potential
β^+	positron
N	neutrino

Declaration of Academic Achievement

As part of the NSERC CREATE molecular imaging probes program, I worked alongside scientists of various disciplines in an effort to develop molecular imaging probes for the detection and characterization of rheumatoid arthritis (RA). My PhD work describes new platforms that can be used to create tools for imaging this disease. Firstly, I developed the first known example of a radiolabeled (^{18}F) hydrocyanine dye, which are a unique class of probes that are capable of fluorescing in the near-infrared region in the presence of elevated ROS levels. In this way, the probe can be utilized as a dual modality probe for either optical imaging or PET imaging. This probe exhibits superior stability and can be accessed *via* a late-stage fluorination approach. While performing the biological studies, it was found that the probe exhibited exceptional blood-binding properties which preliminary studies suggest is due to albumin binding.

In terms of contribution, I initiated and developed the project. I synthesized the probes and radiolabeling precursors in addition to performing optical studies, stability studies and all experiments related to radiolabeling. I developed synthetic and radiosynthetic protocols and optimized all conditions for these probes. Characterization was performed by myself and Dr. Silvia Albu. Alyssa Vito and I designed and performed albumin binding studies. Shannon Czorny performed *in vivo* experiments in addition to the optical cell imaging studies and the toxicity study. Nancy Janzen performed *in vivo* studies and a PC-3 based fluorescence assay. Despite not directly handling the mice and cells, I was involved in experimental design and data acquisition including statistical analyses and quantification of optical fluorescence. Laura Banevicious performed preliminary excitation and emission spectra. Dr. Max Nanao and Dr. Jon Zubieta generated the X-ray crystallography data. Dr. John Valliant and Dr. Alfredo Capretta are the principle investigators and led the research efforts. The work described in Chapter 2 has been prepared as a manuscript for submission to *Chemistry- A European Journal*. As an extension of this work, I also synthesized less hydrophobic derivatives and performed optical studies and characterization. A precursor for one of the probes was synthesized and the compound was successfully ^{18}F-labeled.

Secondly, F-127 micelle-encapsulated fluorophores were prepared with synthesized fluorophores and commercially available IR780. Similarly, these agents are capable of accumulating in areas of hypervascularity which is applicable for the assessment of RA but can also be used in theranostic approaches. One of the fluorophores that were used in the encapsulation procedure was a *meso* fluorinated analogue of IR780, which was accessed *via* a one step halogen exchange reaction from IR780. This compound showed enhanced fluorescence in solution and the reduced derivative accessed by reduction of the iminium bond demonstrated greater fluorescence response in cells by comparison to the chlorinated dye. Currently, this is the first example of a *meso* fluorinated cyanine dye. For this compound, I performed all synthetic work, optimization, radiolabeling, characterization and optical studies. Nancy Janzen performed the PC-3 cell assay with the respective reduced probes. For the micelle project, I performed the encapsulation and purification of all fluorophores. I generated all calibration curves for the loading calculations and performed all optical studies described. Stuart McNelles performed dynamic light scattering (DLS) measurements and Dr. Carmen Andrei generated TEM images. Toxicity studies (MTT assay) were performed by Shannon Czorny.

Finally, the work also describes a targeted approach to imaging RA, which involves the synthesis of inhibitors for the metalloprotease enzyme TACE. Preliminary work described in this thesis includes the synthesis of hydroxamic and reverse hydroxamate inhibitors, *in vitro* assessment of the synthesized compounds and the synthesis of radiolabeling precursors. The scaffolds were synthesized using some procedures that varied from the reported literature protocols due to low yields and difficulty in accessing the compounds of interest. I performed the synthesis of all hydroxamic acid compounds and Dr. Ramesh Patel was involved in the scale-up synthesis of some intermediates. Blake Helka (in collaboration with Dr. John Brennan) was involved in preliminary assay optimization and Nancy Janzen performed the *in vitro* assay in addition to generating IC_{50} curves.

Peer-reviewed Publications

Al-Karmi, S, Albu, S., Vito, A., Janzen, N., Czorny, S., Banevicius, L., Nanao, M., Zubieta, J., Capretta, A., Valliant, J. "A Near-IR Turn-on Dye and its Isostructural 18F-Analogue for Imaging Reactive Oxygen Species (ROS) (in preparation, to submitted to *Chemistry- A European Journal*).

Chapter 1: Introduction

1.1 Molecular Imaging

"Molecular imaging" is defined as the noninvasive *in vivo* visualization of biological processes at the cellular and molecular levels.[1] This typically involves the construction of a 2 or 3 dimensional image capable of being quantified over time.[2] Diagnostic medicine relies on molecular imaging techniques to provide information on the location and extent of a given disease. Typically, highly specialized instruments used solely or in combination with "molecular probes" are used to assess underlying pathology or mechanisms of a disease. Consequently, molecular imaging has shown utility and impact in clinical research and drug discovery in addition to being used for diagnostics in monitoring therapeutic response.[3]

Generally, molecular imaging probes can be classified as being used for a "direct" imaging approach which involves the development of probes that bind or cross cell membranes and become trapped intracellularly.[4,5] Images constructed with the aid of such probes rely on signal intensity proportional to the local concentration of the probe.[8] Successful probe design relies on specific criteria such as accessibility to the target, pharmacokinetics/dynamics, target affinity/specificity, probe stability, and low non-specific binding .These probes span from low (*i.e.* small molecule ligands) to high molecular weight entities (*i.e.* antibodies, recombinant proteins).

A number of molecular imaging modalities are routinely used in a clinical setting. These include magnetic resonance imaging (MRI), ultrasound (US), optical imaging (OI) and nuclear imaging. Nuclear imaging, which is the focus of the research described in this thesis, is comprised of two modalities; single photon emission computed tomography (SPECT) or positron emission tomography (PET).

1.1.1 SPECT

SPECT is a nuclear tomographic imaging technique that employs gamma-emitting radiotracers. These radiotracers are injected intravenously into the patient and emitted gamma rays are detected by a rotating gamma camera that ultimately generates a 3D image. The gamma rays pass through a lead collimator which omit photons that are not within linear view of the detector,[6] and are ultimately converted into an electrical signal by a photodetector. Because of the need to use collimators, the sensitivity of the technique is compromised compared to PET. The most commonly used SPECT isotopes are ^{99m}Tc, ^{131}I, ^{111}In, and ^{67}Ga.[2] As SPECT isotopes commonly used in clinical nuclear medicine typically possess longer half-lives than PET isotopes, SPECT images can be acquired hours after administration of the agent.[7]

1.1.2 PET

PET is a nuclear imaging technique that relies on neutron deficient nuclides that emit positrons (β^+ decay). In β^+ decay, neutron deficient nuclei attempt to achieve stability through the simultaneous emission of a positron (β^+) and a neutrino (v); a process that converts a proton into a neutron. The emitted positrons interact with electrons resulting in an annihilation event which results in the generation of two 511 keV γ-rays traveling at opposite directions (approximately 180° apart, Figure 1.1) that are detected by the PET camera.[8] Signals from two photons originating from a single positron annihilation event are counted simultaneously by the detector (*i.e.* "a coincident event") thereby eliminating the need for collimation.[2] After image reconstruction, quantitative information such as the 3D tracer concentration localized within a specific organ can be obtained. Traditionally, PET isotopes are short-lived in comparison to SPECT isotopes. The most commonly used PET isotopes are ^{11}C and ^{18}F, exemplified by the most commonly employed radiotracer [^{18}F] FDG.[9] [^{18}F] FDG (a fluorinated glucose analogue) targets areas of high glucose metabolism, making it effective at detecting the high metabolic rate experienced in tumours, inflammation and infection. Other clinically relevant tracers include intracellular detection of hypoxia *via* nitroimidazoles [^{18}F] MISO and [^{18}F] FAZA, cellular profliferation *via* [^{18}F] FLT in addition to various others currently in development.[10]

While both PET and SPECT provide greater depth penetration and the capability of performing whole body imaging, PET is commonly regarded as the superior imaging modality in terms of sensitivity, resolution and quantitation when compared to SPECT. One key advantage is that PET exhibits an appreciatively higher sensitivity (by two to three orders of magnitude) due to a higher amount of detected emission events brought about by the absence of a collimator.[6] Enhanced sensitivity permits improved image quality, temporal resolution and the ability to acquire images in a shorter period of time.[6]

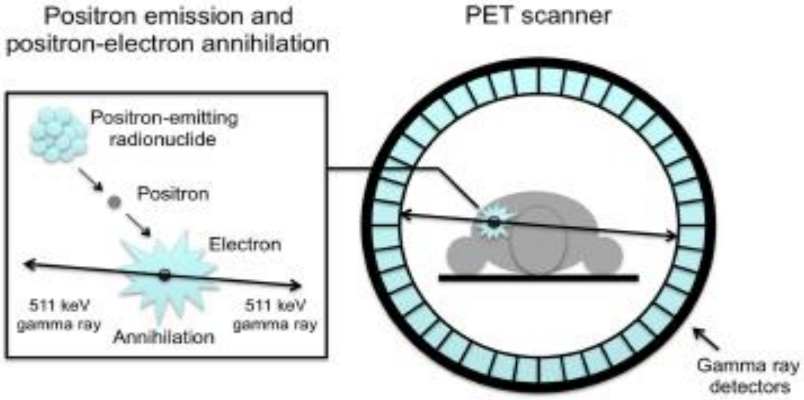

Figure 1.1 Schematic representation of positron-electron annihilation and coincident events identified by gamma detectors.[11]

1.1.3 Optical Imaging

Optical imaging (OI) utilizes nonionizing photons ranging from visible to near infrared (NIR) wavelengths (650-900 nm).[12] Several contrast mechanisms exist for OI techniques such as light absorption/scattering, bioluminescence and fluorescence.[13] Briefly, bioluminescence imaging involves cells that are transfected to express the enzyme luciferase, where the emitted light is detected by a charge-coupled device (CCD) camera.[14] The luciferase enzyme catalyzes conversion of the substrate D-luciferin to oxyluciferin, causing emission of green light at 562 nm.[15] This approach does not require an external excitation source which ultimately leads to a superior signal-to-noise ratio.[12] However, this imaging technique is limited to preclinical models as a result of the need to transfect cells.

Unlike bioluminescence, optical fluorescence imaging generally requires administration of a fluorescent agent. The applied external light source immediately causes photons (at longer wavelengths to the excitation wavelength) to be emitted by the localized fluorophore and subsequently detected by a CCD camera (Figure 1.2).[3]

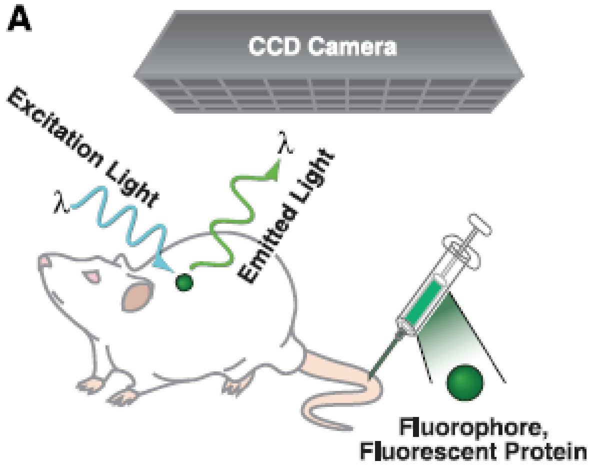

Figure 1.2 A schematic representation showing the general principles of fluorescence OI (reproduced with permission according to CC-BY 4.0 licence).[3]

Fluorescence imaging at greater depths (several centimeters) requires administration of a fluorescent agent that emits in the NIR region of the spectrum (650-900nm).[16] Since tissues do not autofluoresce at these wavelengths, signal-to-noise is significantly improved through the use of such agents.[17] One major advantage of fluorescence imaging is that it is a highly sensitive technique, capable of detecting sub-picomolar concentrations.[16] Despite this, optical techniques usually require higher concentrations of injectable probe by comparison with PET/SPECT which require nano- to picomolar concentrations of the agent.[3]

While a number of advantages such as ease of use and low costs exist for OI, optical techniques suffer from major drawbacks in comparison to other molecular imaging modalities particularly nuclear imaging. While the use of NIR imaging aids in the maximum achievable depth of signal penetration, this is still limited when compared with nuclear imaging techniques that demonstrate unlimited depth penetration. Furthermore, OI quantification is challenging due to light attenuation differences experienced in different organs.[3] These challenges impede the use of optical molecular imaging agents in patients.

Thus far, various NIR agents have been developed for use in the imaging of cancer cells, sentinel lymph nodes (SLN), cardiovascular, neurological and inflammatory diseases.[18] Due to limitations brought about by depth penetration and attenuation, the majority of fluorescent agents have been used for the purpose of intraoperative surgery, tumour margin assessment or as contrast agents for hypervascularity. Currently, there are two fluorophores approved by the FDA for clinical use; fluorescein and indocyanine green (ICG) (Figure 1.3).[19] Fluorescein has been successfully implemented for use in ophthalmology, while ICG has been used as a reagent for testing hepatic function.[19] More recently, ICG has been used as a contrast agent in the clinical evaluation of arthritic inflammation by assessing the angiogenesis characteristic of this disease.[20]

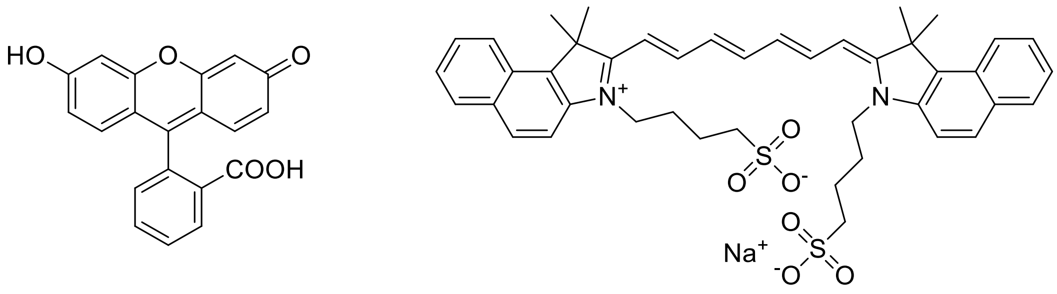

Fluorescein

Indocyanine green (ICG)

Figure 1.3 Chemical structures of FDA approved fluorophores for clinical use.

1.2 Current imaging techniques for the detection of rheumatoid arthritis

In Canada, the annual cost of rheumatism is estimated at 6 billion Canadian dollars [21] and as such, represents a substantial economic burden as one of the most financially draining diseases. This can largely be attributed to delayed diagnosis resulting in expensive corrective orthopedic procedures. Today, the “accepted” and most frequently prescribed modality used to image the disease remains conventional radiography.[22] Because this imaging technique is the basis of many widely accepted grading systems followed by physicians, diagnosis and monitoring of the disease is restricted to anatomical manifestations that arise in later stages such as bone erosion and joint destruction. This presents a health care predicament, since current medications used to treat RA are only effective at early stages of the disease, rendering prescribed disease-modifying anti-rheumatic drugs (DMARD) ineffective. The bone erosion and joint-space narrowing are well defined in radiography but signify irreversible damage.[23] As a result of the limitations of anatomical methods, there has been a recent interest in being able to image molecular processes associated with RA[24] (Table 1.1.). Various studies have shown that early therapeutic intervention resulting from early diagnosis promotes reversal of the molecular events of the disease.[25]

Entry	Class	Radioisotope	Target	Reference
1	nanocolloid	^{99m}Tc	macrophages	26
2	immunoglobulins	^{99m}Tc, ^{111}In	Fc receptor	27
3	monoclonal antibodies	^{111}In	E-selectin	28
4	monoclonal antibodies	^{99m}Tc	lymphocytes	29,30
5	monoclonal antibodies	^{99m}Tc	TNF-α	25
6	peptide (octreotide)	^{99m}Tc, ^{111}In	somatostatin receptor	31,32
7	glucose analog	^{18}F	metabolizing cells	25

Table 1.1 Radiolabeled agents used for the molecular imaging of RA.

Many of the strategies employed for nuclear imaging now have OI surrogates. This is because penetration depth affecting small joints of the hand which are typically involved in the disease are unaffected and can be easily visualized.[40] Examples include the tagging of monoclonal antibodies and vitamins with fluorophores.[33] A notable example includes the conjugation of folic acid to a NIR cyanine dye, permiting the targeting of the over-expressed folate receptor in activated macrophages.[34] Table 1.2 summarizes the various optical techniques used clinically for assessing rheumatic diseases.

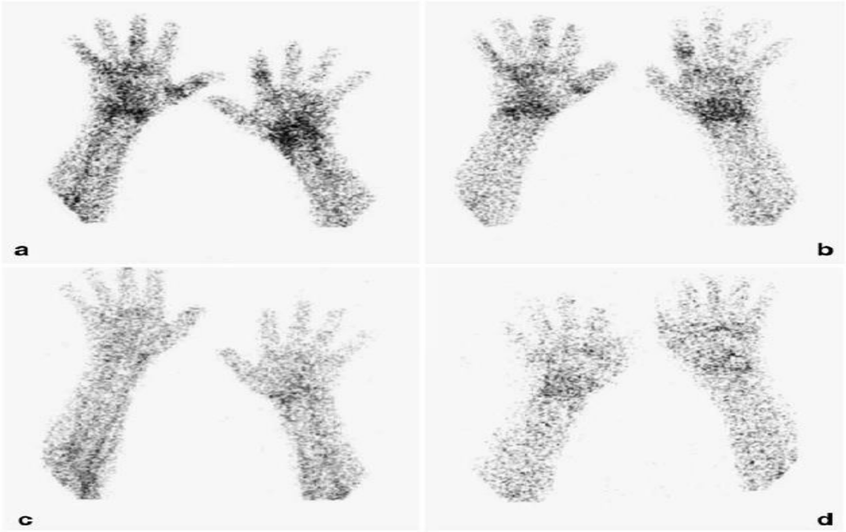

Figure 1.4 Scintigraphic images of wrists of a RA patient after injection with ^{99m}Tc labeled adalimumab a) before therapy, 6 hours after adminstration b) before therapy, 20 hours after adminstration c) after 3 months of therapy, 6 hours after administration d) after 3 months of therapy, 20 hours after administration.[25]

Technique	Assessment	Reference
Invasive microscopy	microhaemodynamic parameters	35,36
Non targeted	angiogenesis	25,32,37,40
Targeted	over-expression of targets	34,38
Activity-Based*	cathepsin B activity	41

*used in osteoarthritis mice model.

Table 1.2 Different clinical approaches using optical probes in rheumatology.

Non-targeted optical agents have become fast and easy methods to image hypervascularity in RA. In 2008, a non-targeted optical procedure known as “Rheumascan” was clinically approved in Europe to assess changes in microcirculation associated with RA.[32,42,43] Indocyanine green (ICG) is injected intravenously and optical images are obtained based on localization of the dye. This will differ dramatically in a RA patient as a result of the high microvascular density and increased capillary blood flow associated with the disease. In this way, the signal enhancement provided by the localization of the dye is directly proportional to the neoangiogenesis found in the synovial membrane of a RA patient.

1.3 Reactive Oxygen Species (ROS)

The term "reactive oxygen species" (ROS) is used to describe any reactive molecules and radicals derived from the partial reduction of molecular oxygen (Figure 1.5). These molecules are central to all aerobic organisms as they are pivotal players in various biological functions such as signal transduction, immune system control, gene expression, cellular signaling, and neurotransmission.[44] Redox regulation of ROS is necessary to prevent the over-production of ROS in the cell, which would otherwise trigger the destruction of cellular components such as DNA and cell membranes. This phenomenon, whereby the redox status of the cell is in the pro-oxidative state is often referred to as "oxidative stress" and is found in various disease states including inflammatory diseases[45], Alzheimers, Parkinson's disease[46] and cancer.[47] The role of ROS in pathogenesis is not limited to impairment at the macromolecular level. ROS has been heavily linked to gene activation leading to tumour metastasis and in this way, ROS has been associated with both initiation and progression of disease.[48]

Radicals

$^{\bullet}O_2^{-}$	$^{\bullet}O_2^{-2}$	$^{\bullet}OH$	$HO_2^{\bullet}$	$ROO^{\bullet}$
Superoxide	Peroxide	Hydroxide	Hydroperoxyl	Peroxyl

Non-Radicals

H_2O_2	OH^{-}	$^{1}O_2$
Hydrogen peroxide	Hydroxyl ion	Singlet oxygen

Figure 1.5 Common ROS produced intracellularly.

Under normal conditions, cells possess multiple defense mechanisms to impart a balance in the intracellular redox status, thus preventing the damaging effects of oxidative stress. Superoxide dismutases (SOD) are a class of enzymes that catalyze the conversion of superoxide to hydrogen peroxide and oxygen[49] (eq 1.1). The generated hydrogen peroxide is then converted to water and oxygen by catalase enzymes (eq 1.2). Numerous antioxidants are also found in the cell to promote protection against ROS, such as vitamin C, glutathione and vitamin E.[49]

$$\boxed{\begin{array}{ll} 2O_2^{\bullet -} + 2H^+ \xrightarrow{\text{SOD}} H_2O_2 + O_2 & \text{(eq 1.1)} \\ 2H_2O_2 \xrightarrow{\text{Catalase}} 2H_2O + O_2 & \text{(eq 1.2)} \end{array}}$$

Endogenous ROS are primarily produced in the mitochondria through the electron transport chain (ETC) or by oxidoreductase enzymes.[45] It has been reported that the ETC is responsible for 90% of cellular oxygen consumption of which 1-5% are converted to ROS under normal physiological conditions.[50] These species are formed as a direct consequence of oxidative phosphorylation, a vital cellular process that consumes oxygen to create adenosine triphosphate (ATP).[51] The ETC carries out oxidative phosphorylation through five proteins, simply known as complex I, II, III, IV and V (Figure 1.5). Electrons are passed through the ETC *via* electron donors NAD(P)H (taking place at complex I) and $FADH_2$ (taking place at complex II), which ultimately lead to the reduction of oxygen to water at complex IV.[51] This sequence of redox events simultaneously causes protons (H^+) to be pumped into the intermembrane space from the mitochondrial matrix, generating a mitochondrial membrane potential ($\Delta\Psi_m$). This generated electrochemical gradient is the main driving force for ATP synthesis in complex V.[51] Leakage of electrons at complex I and complex III can occasionally result in the reduction of molecular oxygen to superoxide ($O_2^{\cdot -}$).[52,53]

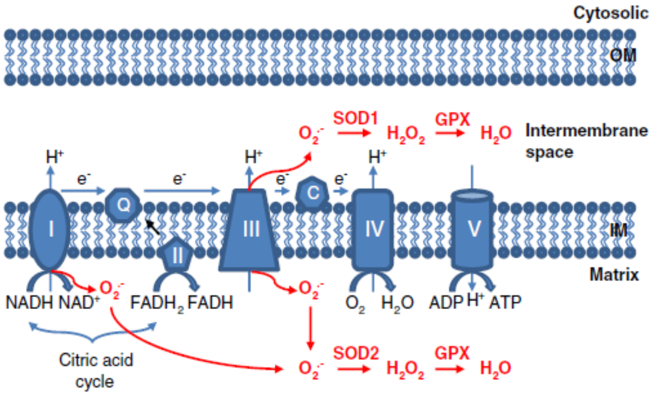

Figure 1.6 Schematic representation of the ETC and mitochondrial ROS production.[51]

Superoxide ($O_2^{\cdot -}$) and hydrogen peroxide (H_2O_2) generation within the mitochondria are widely known and have been studied extensively.[50] H_2O_2 is produced *via* conversion of $O_2^{\cdot -}$ through the enzyme SOD.[52,53] As a result of its electrophilic character and short half-life, $O_2^{\cdot -}$ is less likely to be found exterior to the mitochondrial membrane or be involved in cellular signaling.[51] Instead, this ROS may promote generation of other species (such as $ONOO^{\cdot -}$) which stimulate irreversible cellular destruction.[54] Comparatively, H_2O_2 is considerably more stable and accordingly intracellular concentrations of H_2O_2 are 100-fold higher than $O_2^{\cdot -}$, making it more likely to be involved in signaling.[55] Exceedingly reactive ROS such as the hydroxyl radical ($^{\cdot}OH$) are produced as secondary products to $O_2^{\cdot -}$ and H_2O_2 generation.[51] More specifically, $^{\cdot}OH$ is produced *via* Fenton chemistry catalyzed by iron and copper commonly present in the mitochondria. The *in vivo* half-life of $^{\cdot}OH$ is said to be 10^{-9} seconds and the short-lived nature of this radical makes it extremely destructive to cellular components and therefore, profoundly involved in pathogenesis.[56]

As previously mentioned, various redox enzymes independent of the mitochondria are also responsible for ROS production which themselves further increase ROS concentrations in the mitochondria. This phenomenon is known as "ROS-induced-ROS".[51] Such enzymes include NADPH oxidase, xanthine oxidase and (uncoupled) eNos.[51] The best known example of "ROS-induced-ROS" is the positive feedback mechanism whereby NADPH oxidase ROS activation results in angiotensin (ang II) promoted mitochondrial ROS which further promotes NADPH oxidase derived ROS.[57]

1.3.1. The role of ROS in RA

Activated macrophages play a critical role in RA pathogenesis. The oxidative stress brought about by a high concentration of ROS in arthritic joints has been linked to the localization and function of T-cells.[45] In response to oxidative stress, macrophages migrate and destroy the surrounding synovial joint.[45] RA patients exhibit an increase in ROS levels in the inflammatory site and a decreased ability to counteract the imbalance in the redox potential of a cell. Activated macrophages found in the synovial joint compartment display an over expression of the enzyme NADPH oxidase, which further promotes activation of these macrophages.[45] This redox imbalance provided by the over production of ROS also promotes the increased levels of biological markers, cytokines and the over-expression of various metalloprotease enzymes including the enzyme TNF-α converting enzyme (TACE).[58] Various experiments have confirmed that ROS levels govern the behavior of T-cells in the inflammatory site, suggesting that the redox status of the cell is a significant tool to utilize in detection and treatment of the disease.[59]

1.3.2 Existing probes used to assess elevated ROS levels: challenges and limitations

While some ROS sensing probes function *via* spin-trap mechanisms (*e.g*. TEMPO derived probes) [60] the majority of reported probes in the literature are based on fluorescence response.[61] Historically, the most commonly used fluorescent ROS probes (available through commercial sources) for *in vitro* cell-based assessment of ROS are dihydroethidium (DHE) and 2,7-dichloro dihydrofluorescein (DCFH) which respond to $O_2^{\cdot -}$ and H_2O_2 respectively (Figure 1.7).

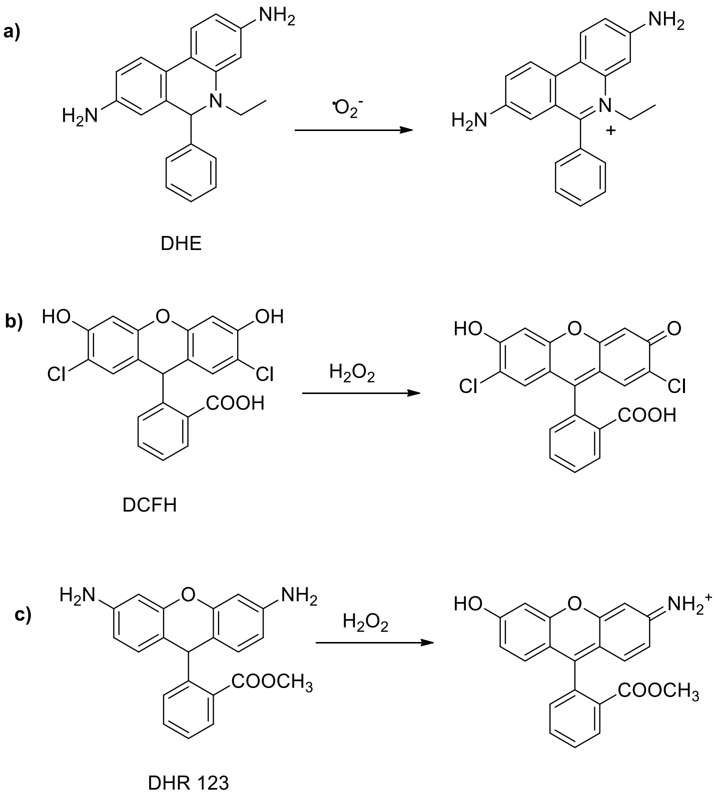

Figure 1.7- a) Conversion of non-fluorescent DHE to fluorescent ethidium (ET, λ_{ex} = 510 nm, λ_{em} = 610nm) in response to superoxide b) Conversion of non-fluorescent DCFH to fluorescent 2,7-2,7-dichlorofluorescein (DCF, λ_{ex} = 498nm, λ_{em} = 522nm) c) Conversion of non-fluorescent DHR 123 to rhodamine 123 (λ_{ex} = 500nm, λ_{em} = 536nm).

The rhodamine-derived ROS probe dihydrorhodamine 123 (DHR 123) is also used routinely for the detection of various ROS species including H_2O_2, $^{\cdot}OH$ and

HOCl. These probes are membrane permeable which make them useful in assessing oxidative burst within cells.[61] Upon $O_2^{\cdot -}$ oxidation, DHE is converted to the fluorescent DNA intercalator ethidium (ET) and the more recently discovered oxidation product hydroxylethidium.[62] Although this probe is frequently employed as an *in vitro* sensor of ROS, there are numerous limitations and challenges associated with its use that also hold true for other mitochondria-targeted probes such as Mitox-red.

Firstly, DHE and its derivatives spontaneously oxidize creating higher background signals and responses that do not precisely correlate with ROS levels.[63] This is also a concern with the use of DCFH and DHR 123.[64] Furthermore, the success of the probe heavily relies on concentrations used in the assay. At higher concentrations of DHE, fluorescence can be seen irrespective of superoxide-induced oxidation and is associated with saturation of mitochondrial nucleic acid binding sites by ET.[65] Importantly, while it is commonly acknowledged that DHE responds exclusively to $O_2^{\cdot -}$, it must be noted that it is also sensitive to forming multiple oxidation products as a result of H_2O_2 associated peroxidases and other ROS species.[66] Chang and coworkers have developed a series of boronate functionalized fluorescein derivatives that are selective for the detection of H_2O_2 making these derivatives attractive alternatives to DCFH (Figure 1.8b).[67]

Recently, there has been considerable interest in developing novel ROS probes with distinct structural features that may help address some issues with presently employed probes.[61] General properties for successful ROS probes include designing agents that are stable and resistant to auto-oxidation, exhibit minimal cytotoxcicity, are membrane permeable and exhibit a drastic change of optical properties upon oxidation so as to minimize background.[68] If mitochondrial targeting is required, cationic lipophllic species are designed to accumulate within the mitochondrial inner membrane which is driven by the negative potential generated by the proton gradient of the mitochondrial membrane (Figure 1.8a).[61c]

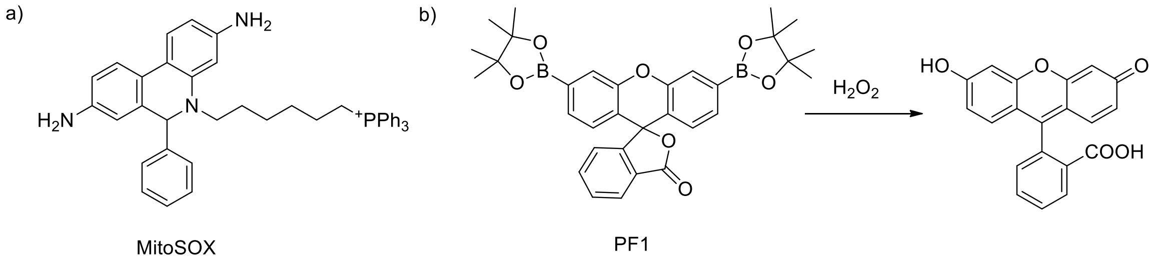

Figure 1.8 a) mitochondria-targeting ROS probe MitoSOX b) boronate probe functionalized fluorescein H_2O_2 probe.

While considerable progress has been made on the development and design of ROS probes, translation to *in vivo* clinical applications have been challenging. In 2009, Kundu *et al.* developed a series of ROS probes based on the reduction of the iminum cation of commercially available cyanine dyes.[69] These probes, known as “hydrocyanines”, are a series of membrane permeable non-fluorescent species that upon selective oxidative hydrogen abstraction by $O_2^{\cdot -}$ or $^{\cdot}OH$, generate fluorescent cationic species that become retained within the ROS active cell. These probes demonstrated the first preclinical example of ROS detection *in vivo* and since then have been evaluated in a number of ROS models.[70]

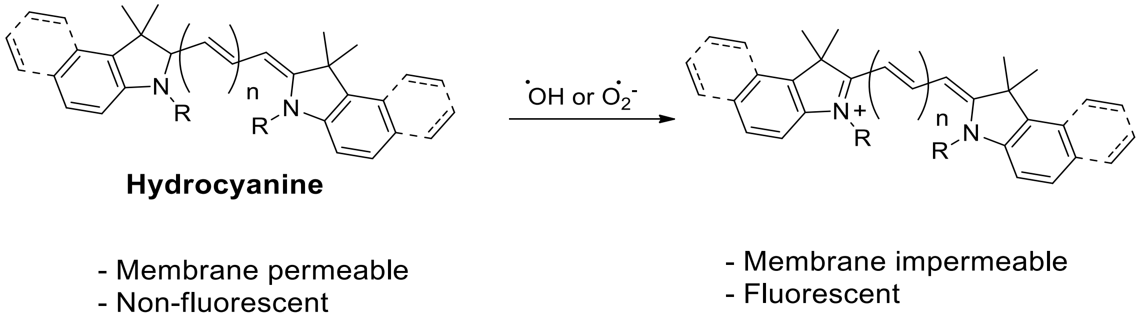

Figure 1.9 General structure of hydrocyanine ROS probes.

Although technological advancements have significantly improved fluorescence response *in vivo*, fluorescent probes continue to suffer from key limitations in detection and quantification (section 1.4). Consequently, a considerable effort has been made to develop ROS probes that are capable of being detected *via* nuclear imaging techniques which would allow for non-invasive and quantitative imaging that is not limited in depth penetration (Figure 1.10).

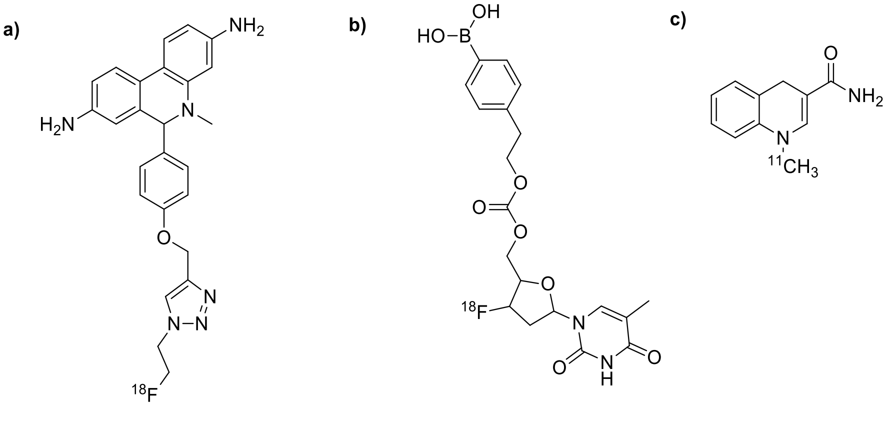

Figure 1.10 PET-ROS probes reported in the literature.

Mach and coworkers have developed the first ^{18}F labeled ROS probe based on a synthesized DHE derivative which was shown to exhibit a two-fold uptake in a ROS cardiac model (Figure 1.10a).[71] Similarly, Chang and coworkers reported a boronic acid that releases the PET tracer [^{18}F]FLT upon exposure to H_2O_2.[72] Recently, Okamura *et al.* have successfully developed a ^{11}C labeled dihydroquinoline ROS probe capable of crossing the blood-brain barrier.[73] While these probes have paved the way for a novel approach towards detecting ROS in living systems, the optimal agent has yet to be developed.

1.4 Thesis objectives, overview and rationale

The long-term goal is to develop molecular imaging probes to assess early RA. These probes can be used as a tool to not only detect the disease at earlier stages, but also to monitor response to treatment, which becomes extremely important considering the severe side effects that may accompany current medications. This thesis describes three main approaches towards imaging RA. The first approach involves the development of a multi-modal OI-PET tracer that targets ROS which is found in the synovial tissue of RA patients. Given the persistence of high ROS levels in different diseases, this probe can also be used in the assessment of infection, other inflammatory diseases, cancer and neurodegenerative diseases. The second approach involves developing similarly “non-targeted” fluorophores and/or “turn-on” ROS probes that show improved properties such as efficient delivery, improved solubility and enhanced “turn-on” capabilities. This approach relies on the angiogenesis pathology linked to multiple pathological conditions. The third approach involves preliminary efforts to create a “targeted” approach involving the development of molecules that could be radiolabeled and specifically target the enzyme TACE which is over-expressed by elevated ROS in the synovium of RA patients.[74]

Given the dominant role of ROS in disease progression and initiation, molecular imaging of ROS is a highly desirable imaging technique that has yet to be addressed clinically. One reason for the lack of these probes is that they are difficult to access. More importantly, the assessment of ROS pathology *via* a multi-modal imaging strategy offers complimentary advantages when OI and PET imaging are integrated. Such a combination can impart improved temporal/spatial resolution provided by OI and deep depth penetration provided by PET.[75] Accordingly, this permits the use of a single agent for various different clinical purposes (*i.e.* the PET labeled agent used for *in vivo* assessments while the “cold” counterpart can be used for image-guided surgeries) and is the main driving force behind the evolution of the successful lymph node draining agent Tilmanocept.[76]

Fluorine-18 (^{18}F) remains the most commonly employed PET isotope as a result of its valuable nuclear/chemical properties such as its ability to possess the shortest positron range (≈ 2.3 mm) resulting in superior resolution when compared to other PET isotopes.[77] For creating ROS probes, the incorporation of fluorine is challenging due to the harsh conditions often involved in the incorporation of ^{18}F and the thermal sensitivity of these chromophores.[78] For these reasons, there are only two examples of ^{18}F-labeled NIR cyanine dyes; one of which involves the synthesis of aryltrifluoroborates and the other of which requires a pre-labeled prosthetic group (described further in Chapter 4). Consequently, before developing an OI-PET ROS probe, several hurdles must be overcome. The specific goals in this context were:

- Development of a straightforward and late-stage ^{18}F labeling strategy for ROS sensitive dyes in which lengthy syntheses and the use of prosthetic groups can be avoided.
- The synthesis of stable precursors that can be readily separated from labeled products.
- To create a probe that does not require conjugation to a targeting ligand.
- Incorporation of ^{18}F in a manner that does not afford bulky substituents which could drastically impede pharmacokinetics/pharmacodynamics.
- Develop a labeling approach with short reaction times.
- Development of a fluorophore that activates in diseased tissue thus minimizing background signals of the optical probe.

These goals were achieved through the development of novel OI-PET probes (Figure 1.11). The target ROS probes were prepared (Chapter 2 and Chapter 3) using various *meso*-chlorinated NIR cyanine dyes where ROS sensing ability of the corresponding hydrocyanines was demonstrated by Kundu *et al*. The incorporated cyclohexyl ring provides additional rigidity and offers advantages in comparison to their “open chained” counterparts including enhanced photostability and quantum yields.[78] The *o*-fluoropyridine functionality was chosen as it is established that labeling at this position is facile and high-yielding.[79] Additionally, this functionality is resistant to metabolic defluorination and has been shown to be successfully retained in cancer cells as compared with corresponding fluoroarene derivatives.[80]

In addition to this approach, there are various other ways to target regions of high ROS pathology including using the "enhanced permeability and retention" (EPR) effect.[81] This relies on the premise that diseased tissue such as that found in RA joints and tumours, experience angiogenesis. This is the underlying principle behind the "Rheumascan" procedure described in section 1.4. The main disadvantage of this procedure is instability and lipophilicity of the contrast agent (*i.e.* ICG) which can result in aggregates, decreasing fluorescence quantum yields. As a result, a subsequent goal having created new ROS probes was to develop a means to address this issue by encapsulation of the fluorophores in F-127 micelles in an effort to improve optical stability and delivery of the agent to the area of interest (Chapter 3).

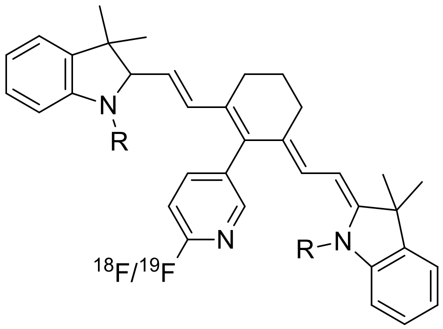

Figure 1.11 General structure of OI-PET ROS probe

This thesis also describes the synthesis of hydroxamic/hydroxamate TACE inhibitors (Chapter 5) that were modified for the purpose of creating targeted imaging agents for RA.[82] Targeting TACE for the purpose of molecularly imaging RA is a unique approach and rationale behind this imaging strategy is outlined below:

- TACE has never been exploited as a MI target and over-expression of this enzyme is an event specific to RA in rheumatology and therefore the envisioned probe will be able to distinguish between other rheumatic diseases.
- The ligands chosen as targeting vectors are small molecule inhibitors with high affinity and specificity to TACE. These radiolabeled compounds are more likely to exhibit faster clearance, rapid uptake and retention in the synovium (pharmacokinetic parameters), in comparison to larger antibodies previously used. This can limit prolonged radiation exposure to the patient.

The preliminary work describes the synthesis and *in vitro* screening of these modified compounds through an established fluorogenic assay. With the success of the ROS probes described in Chapters 2, 3 and 4, further work on optimizing these compounds and creating imaging probes for detecting RA in addition to ROS-active tumours is possible and a key goal of future research.

1.5 References

1. Editorial: Molecular Imaging. ACR, **2000**, *56*, 6, 25-30.
2. M. T Munley, G. C. Kagadis, K. P. McGee, A. S. Kirov, S. Jang, S. Mutic, R. Jeraj, L. Xing, J. D. Bourland, *Med. Phys.*, **2013**, *40*, 101501-1 – 101501-23.
3. M. L. James, S. S. Gambhir, *Physiol. Rev.*, **2012**, *92*, 897–965.
4. F. D. Rollo, *Medicamundi.*, **2003**, *47*, 10–16.
5. B. Tan, D. Piwnica-Worms, L. Ratner, *Curr. Opin. Oncol*., **2000**, *12*, 450-458.
6. A. Rahmim, H. Zaidi, *Nucl. Med. Commun*., **2008**, *29*, 193-207.
7. H. Hong, J. Sun, W. Cai, *Biomark.Insights.*, **2008**, *3*, 435–451.
8. Magdy K.M, 2011, *Basic Sciences of Nuclear Medicine,* Springer Berlin Heidelberg, p379-413.
9. H. A. Nabi, J.M. Zubeldia, *J. Nucl. Med. Technol*., **2002**, *30*, 3–10.
10. D. A. Jaffray, C. Chung, C. Coolens, W. Foltz, H. Keller, C. Menard, M. Milosevic, J. Publicover, I. Yeung, *Semin. Radiat. Oncol.*, **2015**, *25*, 292–304.
11. A. A. M. Van Der Veldt, E. F. Smit, A. A. Lammertsma, *Front.Oncol*., **2013**, *3*, 1–7.
12. J. Culver W. Akers, S. Achilefu, *J. Nucl. Med*., **2008**, *49*, 169–172.
13. V. Ntziachristos, J. Ripoll, L.V. Wang, R. Weissleder, *Nat.Biotechnol*., **2005**, *23*, 313-320.
14. C.H. Contag, M.H. Bachmann, *Annu Rev Biomed Eng*., **2002**, *4*, 235–260.
15. A. Sato, B. Klaunberg, R. Tolwani, *Comp. Med*., **2004**, *54*, 631–634.
16. A. Taruttis, V. Ntziachristos, *Am. J. Roentgenol*., **2012**, *199*, 263–271.

17. J.V. Frangioni*, Curr. Opin. Chem. Biol*., **2003**, *7*, 626-634.
18. A.L. Vahrmeijer, M. Hutterman, J.R. van der Vorst, C.J.H. van der Velde and J.V. Frangioni, *Nat. Rev. Clin.Oncol*., **2013**, *10*, 507-518.
19. H. Kobayashi, M. Ogawa, R. Alford, P. L. Choyke and Y. Urano, *Chem. Rev.*, **2010**, *110*, 2620–2640.
20. T. Fischer, B. Ebert, J. Voigt, R. Macdonald, U. Schneider, A. Thomas, B. Hamm, K.A. Hermann., *Acad. Radiol.*, **2010**, *17*, 375–381.
21. B. Fautrel, A.E. Clarke, F. Guillemin, V. Adam, Y. St-Pierre, T. Panaritis, *Curr. Opin. Rheumatol.,* **2002**, *27*, 121–126.
22. H. Czembirek, M. Boeck, M. Stiskal, *Radiographics*, **2005**, *25***,** 381–398.
23. C. G. Peterfy, *Curr. Opin. Rheumatol.,* **2003**, *15*, 288–295.
24. A. Wunder, R. H. Straub, S. Gay, J. Funk, U. Müller-Ladner, *Rheumatology,* **2005**, *44*, 1341–1349.
25. G. Malviya, F. Conti, M. Chianelli, F. Scopinaro, R. A. Dierckx, A. Signore, *Eur. J. Nucl. Med. Mol. Imaging,* **2010**, *37*, 386–398.
26. M. De Schrijver, K. Streule, R. Senekowitsch, R. Fridrich, *Nucl. Med. Commun.*, **1987**, *8*, 895-908
27. M. H. de Bois, J. W. Arndt, I. Speyer, E. K. Pauwels, F. C. Breedveld, *Scand. J. Rheumatol.,* **1996**, *25*, 155–158.
28. F. Jamar, P. T. Chapman, D. H. Manicourt, D. M. Glass, D. O. Haskard, A.M. Peters, *Br. J. Radiol.,* **1997**, *70*, 473–481.
29. W. Becker, F. Emmrich, G. Horneff, G. Burmester, F. Seiler, A. Schwarz, J.

Kaiden, F. Wolf, *Eur. J. Nucl. Med. Mol. Imaging,* **1990**, *17,* 156-159.

30. R. Kinnie, W. Becker, J. Schwab, G. Horneff, A. Schwarz, J. Kaiden, F. Emmrich, G. Burmester, F. Wolf, *Nucl. Med. Commun.*, **1993,** *14*, 667-675.
31. D. Paran, O. Elkayam, A. Mayo, H. Paran, M. Amit, M. Yaron, D. Caspi, T. Sourasky, M. Hospital, *Ann. Rheum. Dis.,* **2001**, *60*, 888–891.
32. T. Fischer, B. Ebert, J. Voigt, R. Macdonald, U. Schneider, A. Thomas, B. Hamm, K.-G. A. Hermann, *Acad. Radiol.,* **2010**, *17*, 375–381
33. L. L. Gompels, N. H. Lim, T. Vincent, E. M. Paleolog, *Rheumatology,* **2010**, *49*, 1436–1446.
34. W.T. Chen, U. Mahmood, R. Weissleder, C.-H. Tung, *Arthritis Res. Ther.,* **2005**, *7*, 310–317.
35. A. Veihelmann, a G. Harris, F. Krombach, E. Schütze, H. J. Refior, K. Messmer, *Microcirculation,* **1999**, *6*, 281–290.
36. A. Veihelmann, G. Szczesny, D. Nolte, F. Krombach, H. J. Refior, K. Messmer, *Res. Exp. Med.,* **1998**, *198*, 43–54.
37. A. Hansch, O. Frey, I. Hilger, D. Sauner, M. Haas, D. Schmidt, C. Kurrat, M. Gajda, A. Malich, R. Bräuer, W.A. Kaiser, *Invest. Radiol.,* **2004**, *39*, 626–632.
38. P. T. Chapman, F. Jamar, E. T. Keelan, a M. Peters, D. O. Haskard, *Arthritis Rheum.,* **1996**, *39*, 1371–1375.
39. W.F. T. Lai, C.-H. Chang, Y. Tang, R. Bronson, C.-H. Tung, *Osteoarthr. Cartil.,* **2004**, *12*, 239–244.
40. S. G. Werner, H. Langer, P. Schott, M. Bahner, C. Schwenke, G. Lind-albrecht,

F. Spiecker, B. Kurtz, G. R. Burmester and M. Backhaus, *Arthritis Rheum.*, **2013**, *65*, 3036–3044.

41. K. Xu, F. Wang, X. Pan, R. Liu, J. Ma, F. Kong, B. Tang, *Chem. Commun.,* **2013**, *49*, 2554–2556.
42. C. Bremer, S. Werner, H.E. Langer, *Imaging*, **2009**, *28*, 96–100.
43. V. S. Schäfer, W. Hartung, P. Hoffstetter, J. Berger, C. Stroszczynski, M. Müller, M. Fleck and B. Ehrenstein, *Arthritis Res. Ther*., **2013**, *15*, 1-9.
44. a) A. K. N. Schmidt, P. Amstad, P. Cerutti, P. A. Baeuerle, *Chem. Biol.*, **1995**, *2*, 13-22 b) B. D'Autréaux, M. B. Toledano, *Nat. Rev. Mol. Cell Biol.,* **2007**, *8*, 813-824. c) R. Mittler, S. Vanderauwera, N. Suzuki, G. Miller, V. B. Tognetti, K. Vandepoele, M. Gollery, V. Shulaev, F. Van Breusegem, *Trends Plant Sci.,* **2011**, *16*, 300-309 d) B. C. Dickinson, C. J. Chang, *Nat. Chem. Biol.,* **2011**, *7*, 504-511.
45. K. A. Gelderman, M. Hultqvist, L. M. Olsson, K. Bauer, A. Pizzolla, P. Olofsson, R. Holmdahl, *Antioxid. Redox Signaling,* **2007**, *9*, 1541- 1567.
46. Y.W. Yap, M. Whiteman, N. S. Cheung, *Cell. Signal.,* **2007**, *19*, 219-228.
47. a) G. Waris, H. Ahsan, *J. Carcinog.,* **2006**, *5*, 1-8 b) G.Y. Liou, P. Storz, *Free Radic Res*., **2010**, *44*, 479-496.
48. K. Ishikawa, K. Takenaga, M. Akimoto, N. Koshikawa, A. Yamaguchi, H. Imanishi, K. Nakada, Y. Honma, J. Hayashi, *Science*, **2008**, *320*, 661-664.
49. J.M. McCord, I. Fridovich *J. Biol. Chem*., **1968**, *243*, 5753-5760
50. D. Kang, N. Hamasaki, *Clin. Chem. Lab. Med.*, **2003**, *41*, 1281–1288.

51. X. Li, P. Fang, J. Mai, E. T. Choi, H. Wang and X. Yang, *J. Hematol. Oncol.*, **2013**, *6*, 19.
52. G. Loschen, A. Azzi, C. Richter, L. Flohe, *FEBS Lett*., **1974**, *42*, 68-72
53. H. J. Forman, H.J., J.A. Kennedy, *Biochem. Biophys. Res. Commun*., **1974**, *60*, 1044-1050.
54. N. R. Madamanchi, M. S. Runge, *Circ. Res*., **2007**, *100*, 460-473.
55. E. Cadenas, K.J. Davies, *Free Radic. Biol. Med*., **2000**, *29*, 222-230.
56. H. Sies, *Eur.J. Biochem*., **1993**, *215*, 213-219.
57. I.R. Hanna, Y. Taniyama, K. Szocs, P. Rocic, K.K. Griendling, *Antioxid. Redox. Signal*, **2002**, *4*, 899-914.
58. A. J. Scott, K. P. O. Dea, D. O. Callaghan, L. Williams, J. O. Dokpesi, L. Tatton, J. M. Handy, P. J. Hogg, M. Takata, *J. Biol. Chem.*, **2011**, *286*, 35466 –35476.
59. D. A. Hildeman, T. Mitchell, J. Kappler, P. Marrack, *J. Clin. Invest*., **2003**, *111*, 575–581.
60. S. Ben, H. Nakagawa, T. Suzuki, N. Myata, *Bioorg. Med. Chem. Lett*., **2007**, *17*, 2055-2058.
61. a) X. Chen, X. Tian, I. Shin, J. Yoon, *Chem. Soc. Rev*. **2011**, *40*, 4783-4804. b) A. Gomes, E. Fernandes and L. F. C. Lima, *J. Biochem. Biophys. Methods*, **2005**, *65*, 45–80. c) B. C. Dickinson, D. Srikun and C. J. Chang, *Curr. Opin. Chem. Biol*., **2010**, *14*, 50-56.
62. H. Zhao, S. Kalivendi, H. Zhang, J. Joseph, K. Nithipatikom, J. Vasquez-Vivar, B. Kalyanaraman, *Free Radic. Biol. Med*., **2003**, *34*, 1359-1368.

63. B. Halliwell, M. Whiteman, *Br.J. Pharmacol*., **2004**, *142*, 231-255.
64. M. Yazdani, *Toxicol. In vitro.*, **2015**, *30*, 1996–2000.
65. S.L. Budd, R.F. Castilho, D.G. Nicholls, *FEBS Lett*., **1997**, *415*, 21-24.
66. N. Patsoukis, I. Papapostolou, C.D. Georgiou, *Anal. Bioanal. Chem*., **2005**, *381*, 1065-1072.
67. M. C. Y. Chang, A. Pralle, E. Y. Isacoff and C. J. Chang, *J. Am. Chem. Soc.*, **2004**, *126*, 15392–15393.
68. X. Chen, Z. Zhong, Z. Xu, L. Chen and Y. Wang, *Free radical Res*., **2010**, *44*, 587–604.
69. K. Kundu, S. F. Knight, N. Willett, S. Lee, W. R. Taylor, N. Murthy, *Angew. Chem. Int. Ed*., **2009**, *48*, 299-303
70. a) K. M. Poole, C. E. Nelson, R. V Joshi, J. R. Martin, M. K. Gupta, S. C. Haws, T. E. Kavanaugh, M. C. Skala and C. L. Duvall, *Biomaterials*, **2015**, *41*, 166–175. b) J. Kim, W. Choi, Y. H. Kim and G. Tae, *J. Control. Release*, **2011**, *156*, 398–405. c) S. Selvam, K. Kundu, K. L. Templeman, N. Murthy and A. J. García, *Biomaterials*, **2011**, *32*, 7785–7792. d) S. Magalotti, T.P. Gustafson, Q. Cao, D.R. Abendschein, R.A. Pierce, M.Y. Berezin, W.J. Akers, *Mol. Imaging. Biol*., **2013**, *15*, 423-430.
71. W. Chu, A. Chepetan, D. Zhou, K. I. Shoghi, J. Xu, L. L. Dugan, R. J. Gropler, M. a Mintun, R. H. Mach, *Org. Biomol. Chem.,* **2014**, *12*, 4421-4431.
72. V. Carroll, B. W. Michel, J. Blecha, H. Vanbrocklin, K. Keshari, D. Wilson C. J. Chang, *J. Am. Chem. Soc.,* **2014**, *136*, 14742-14745.

73. T. Okamura, M. Okada, T. Kikuchi, H. Wakizaka and M.-R. Zhang, *J. Cereb. Blood Flow Metab.*, **2015**, 1–7.
74. E. Choy, G. Panavi, *New Engl. J.Med.*, **2011**, *344*, 907-916.
75. M. Nahrendorf, E. Keliher, B. Marinelli, P. Waterman, P. F. Feruglio, L. Fexon, M. Pivovarov, F. K. Swirski, M. J. Pittet, C. Vinegoni, R. Weissleder, *Proc. Natl. Acad. Sci. U.S.A*., **2010**, *107*, 7910-7915.
76. S. P. Stroup, C. J. Kane, C. M. James, C. H. Davis, A. M. Wallace, C. K. Hoh, D. R. Vera, *Clin. Exp. Metastasis*, **2012**, *29*, 673–680.
77. M.C. Lasne, C. Perrio, J. Rouden, L. Barre, D. Roeda, F. Dolle and C. Crouzel. *Top. Curr. Chem*, **2002**, *222*, 201-258.
78. H. Lee, J. C. Mason, S. Achilefu, *J. Org. Chem.,* **2006**, *71*, 7862-7865.
79. J. A. McCarron, V. W. Pike, C. Halldin, J. Sandell, J. Sóvágó, B. Gulyas, Z. Cselényi, H. V Wikström, S. Marchais-Oberwinkler, B. Nowicki, F. Dollé, L. Farde, *Mol. Imaging Biol.,* **2004**, *6*, 17-26.
80. G. Bartoli, A. Latrofa, P.E. Todesco, *J. Chem. Soc.-Perkin. Trans. I.,* **1972**, *21*, 2671-2671
81. Y. Matsumura, H. Maeda, *Cancer Res*., **1986**, *46*, 6387-6392.
82. J. L. Gilmore, B. W. King, C. Harris, T. Maduskuie, S. E. Mercer, R.-Q. Liu, M. B. Covington, M. Qian, M. D. Ribadeneria, K. Vaddi, J.M. Trzaskos, R.C. Newton, C.P. Decicco, J.J. Duan, *Bioorg. Med. Chem. Lett.,* **2006**, *16*, 2699–2704.

Chapter 2: A Fluorine-18 Labeled Near-IR Turn-on Dye for Multi-Modal Reactive Oxygen Species (ROS) Detection

Salma Al-Karmi, Silvia A. Albu, Nancy Janzen, Shannon Czorny, Laura Banevicius, Max Nanao, Jon Zubieta, Alfredo Capretta, John F. Valliant

2.1 Preface

The following work contains text and figures that is in preparation for submission to *Chemistry-A European Journal*. Salma Al-Karmi performed and developed the synthetic work, characterization, purification, optical induction studies and all experiments related to radiolabeling. Dr. Silvia Albu aided in the synthetic work and characterization. Nancy Janzen and Shannon Czorny performed the *in vivo* and *in vitro* biological experiments. Laura Banevicius performed preliminary excitation and emission spectra. Dr. Max Nanao and Dr. Jon Zubieta generated crystal structure data. Dr. Alfredo Capretta and Dr. John Valliant are the principle investigators and led the research efforts.

2.2 Introduction

Reactive oxygen species (ROS) are central to all aerobic organisms as they play a pivotal role in signal transduction, immune system control, gene expression and cellular signalling.[1] A homeostatic balance *via* redox regulation of ROS is required to prevent a pro-oxidative cellular state; a phenomenon known as “oxidative stress.” Extensive oxidative destruction brought about by oxidative stress has been implicated in the initiation and progression of multiple diseases including Alzheimer's and Parkinson's disease,[2] cancer,[3] and inflammatory diseases.[4] Consequently, the ability to detect elevated ROS levels *in vivo* has significant value for basic research, drug discovery and patient care.

The majority of ROS sensing probes reported to date are based on fluorescence response.[5,6,7] To overcome limited depth of imaging that is achievable using optical techniques,[7] progress in preparing radiolabeled ROS probes has been made recently.[8,9,10] For example Mach and co-workers reported the synthesis of ^{18}F labeled analogue of the widely used *in vitro* ROS sensing dye dihydroethidium (DHE).[11] More recently, Chang and co-workers reported a novel construct that releases the PET tracer [^{18}F]FLT upon exposure to hydrogen peroxide.[12]

2.3 Objectives

While these probes have a number of attractive features, there is a notable absence of a single construct that can be used for both PET and near-infrared (NIR) imaging of ROS. NIR probes offer superior depth penetration and reduced light scattering compared to other fluorophores. Fortuitously, the reduction of the iminium cation of NIR cyanine dyes has been shown to create sensitive ROS probes, which react *via* oxidative hydrogen abstraction by superoxide and hydroxyl radicals. Reaction with these species "turns-on" the fluorescence and generates a cationic fluorophore that remains in ROS active cells.[7n,13] While select groups have reported ^{18}F labeling of near-IR dyes,[8f,8g] we sought to develop a convenient route to an ^{18}F-labeled, near-IR turn-on type ROS probe. The approach takes advantage of an inexpensive cyanine dye as the starting material and a late-stage fluorination, to ensure ease of access and use for *in vitro* and *in vivo* ROS studies.

2.4 Synthesis, Radiolabeling and Biological Evaluation

To synthesize the target probe, the commercially available dye IR780 iodide was functionalized *via* a Suzuki coupling with 6-fluoropyridin-3-ylboronic acid (Scheme 2.1).[14-18] *o*-Fluoro-pyridine was selected as the prosthetic group, because it is known to be resistant to metabolic defluorination and the ^{18}F analogue can be produced from the corresponding nitropyridine.[19] Radiopharmaceuticals derived from fluoro-pyridines have also shown enhanced uptake and retention in cancer cells compared to analogues derived from fluorobenzene.[20]

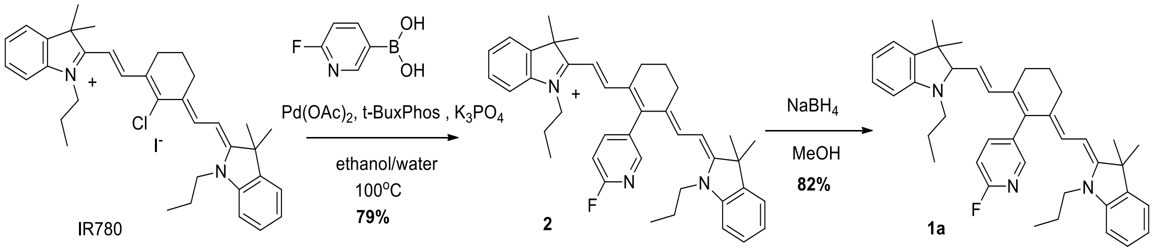

Scheme 2.1 Synthesis of the fluorinated ROS probe **1a** from a commercially available IR780 dye.

Following isolation of **2**, the dye was reduced with sodium borohydride in methanol to afford the ROS probe **1a** in 82% yield. Reduction of the iminium bond was immediately accompanied by a change in colour (green to yellow). Absorption and emission spectra revealed that **2** exhibited excitation and emission maxima at 768 nm and 794 nm respectively, with a Stokes shift of 26 nm, which is comparable to that of other cyanine dyes.[6x] Excitation of **1a** at 768 nm showed no fluorescence in direct contrast to **2** (Figure 1). This drastic change in intensity has been shown to be advantageous where turn-on type probes reduce background signal and maximize signal-to-noise ratios for both *in vitro* and *in vivo* studies.[21]

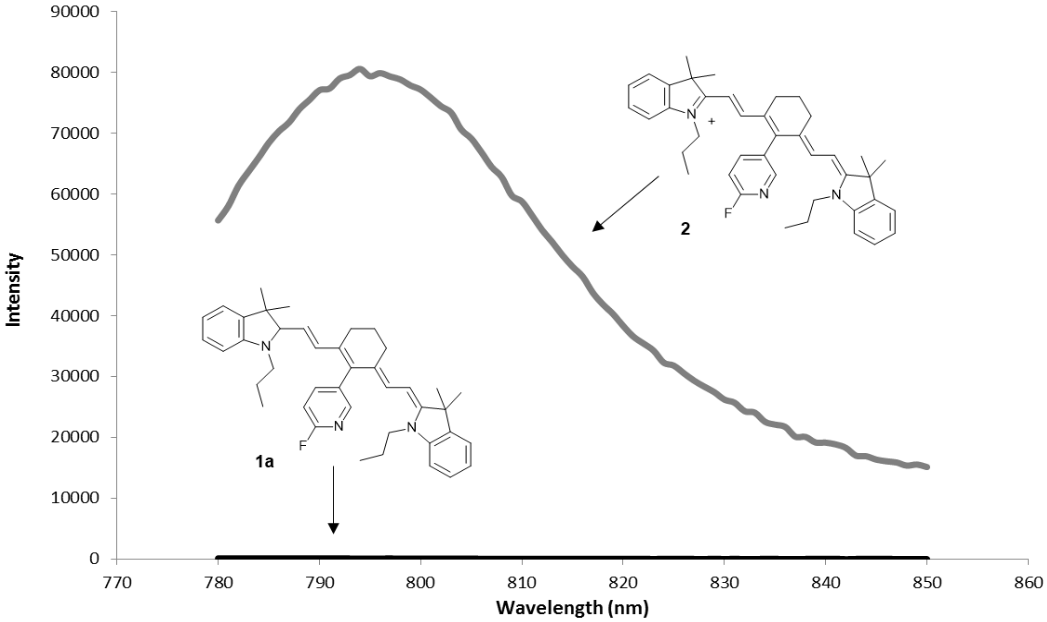

Figure 2.1 Fluorescence emission spectra for **1a** and **2** (40 μM in methanol, λ_{ex} = 768 nm).

DHE, a commonly employed *in vitro* ROS probe,[11] requires careful handling as it is prone to auto-oxidation.[22] A comparison of the stability profile of **1a** with DHE in 20% methanol/PBS buffer (pH=7.4) was performed by placing 40 μM solutions of the probes in a water bath at 37°C, and taking fluorescence measurements over time. The experiments showed that **1a** was stable to auto-oxidation, while DHE experienced a steady increase in fluorescence intensity over 24 h.

Hydrocyanine-based ROS probes have been shown to respond selectively to hydroxyl radicals and superoxide.[7n,13] Using the same assay, the reactivity of **1a** towards a series of different ROS sources and related reagents was evaluated to assess any potential impact of adding the fluorinated prosthetic group. Fluorescence emission at 794 nm (λ_{ex} = 768 nm) was triggered upon treatment with hydroxyl radicals and superoxide (Figure 2.2), which is consistent with other hydrocyanine ROS probes. For the other ROS sources, along with Fe (II) and glutathione (GSH), the emission intensity was similar to the vehicle control. To assess the relative change in intensity upon exposure to ROS, **1a**, and DHE were treated with potassium superoxide (KO_2), and the fluorescence monitored after 1 h. Compound **1a** demonstrated a much greater response than DHE, and there was significantly less background signal for the hydrocyanine in the absence of the radical source. The fluorescence enhancement for **1a** was 21 fold, while for DHE it was less than 2 (1.53).

Fluorescence microscopy studies using PC-3 cells, which are known to generate high concentrations of ROS,[23] were performed using **1a**. The images obtained indicated the dye localized in the cells and that the fluorescence intensity was reduced when the cells were treated with ROS quenchers, NAC and TEMPOL (Appendix 1, Figure S12). Notwithstanding, having demonstrated uptake and retention in PC-3 cells, the cellular toxicity was evaluated noting that **1a** appeared to well tolerated during all microscopy studies. Using an MTT assay, even after incubation for 48 hr, the IC_{50} (65 μM) was higher than that for the cisplatin control

(52 μM) (Appendix 1, Figure S13) and appropriate for a cellular and in vivo imaging probe.

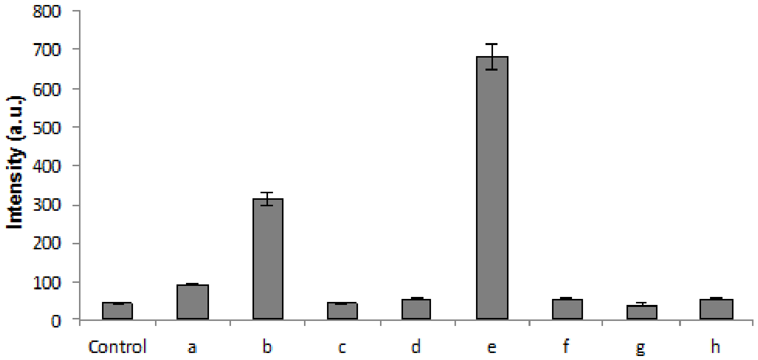

Figure 2.2 Fluorescence response of **1a** (20 μM in 9% methanol/PBS) to various oxidants: a) ·OtBu b) ·OH c) ClO^- d) $^1O_2$ e) O_2^- f) Fe^{2+} g) H_2O_2 h) GSH (λ_{ex} = 768 nm, λ_{em} = 794 nm).

To prepare a suitable precursor for labeling with ^{18}F, a Suzuki coupling with IR780 iodide and 2-nitro-5-pyridineboronic acid pinacol ester **3** (Scheme 2.2) was performed. The product was obtained in 68% yield and the crystal structure of **3** determined after the product was crystallized from an ethanol/water mixture (Appendix 1, Figure S14 and Table S1). The crystal structure was consistent with that proposed for **3**, and showed a fully conjugated backbone where the average sp^2 C-C bond lengths were 1.37 Å (± 0.04). The data is in agreement with previously reported X-ray structures of cyanine dyes.[24,25]

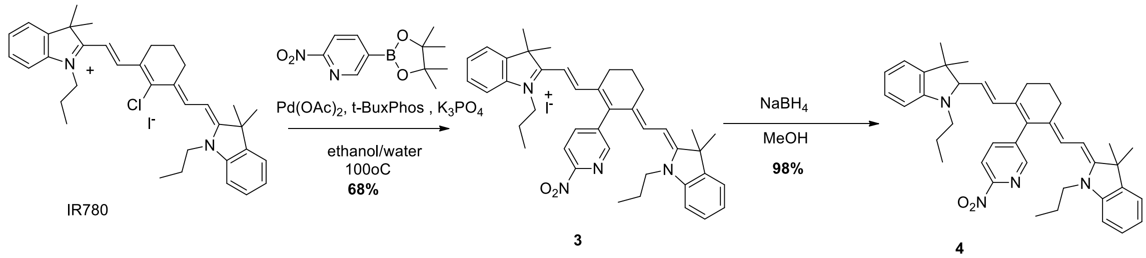

Scheme 2.2 Synthesis of 2-nitropyridines **3** and **4** as precursors for labeling with ^{18}F.

^{18}F labeling (to produce **1b**) was initially performed by subjecting **3** to standard nucleophilic fluorination conditions followed by treatment with methanolic borohydride. Despite attempts to optimize the method, the highest decay corrected radiochemical yield (DCY) obtained was 19%. A more successful route involved direct labeling of **4** at 150 ^{o}C for 4 min, which increased the DCY to 62% (*n* = 5), and further decreased the overall time required for synthesis and purification by approximately 60 min (Scheme 2.3). It is important to note that this approach required strict time control, as prolonged exposure to borohydride resulted in drastically reduced labeling yields.

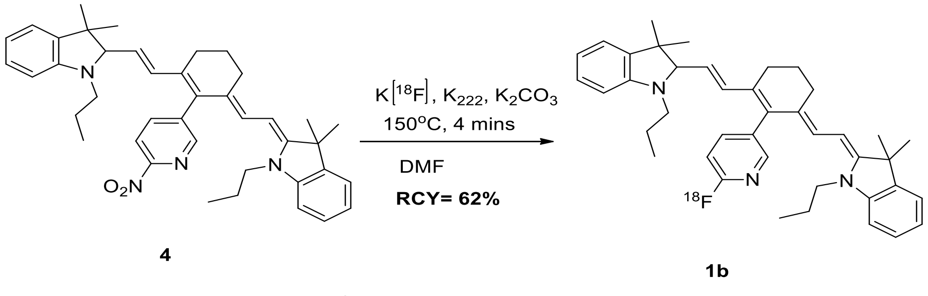

Scheme 2.3 One-step^{18}F radiolabeling of **4** to produce **1b**.

Compound **1b** was purified by reverse phase HPLC and dried under reduced pressure prior to formulation where the total synthesis/purification time was 35 min. The identity of **1b** was confirmed by coinjection with the non-radioactive standard **1a** (Figure 2.3). The specific activity was calculated using a standard curve and was found to be 5.2 GBq/µmol (0.14 Ci/µmol), which is consistent with the modest amount of starting activity used (0.92 GBq). The value is comparable to previously reported ^{18}F BODIPY fluorophores,[8c,8d,8h,9a] but lower than trifluoroborate based dyes[8e,9b] and ^{18}F *o*-pyridine based radiopharmaceuticals, where the latter indicates it is feasible to achieve higher specific activities.[26]

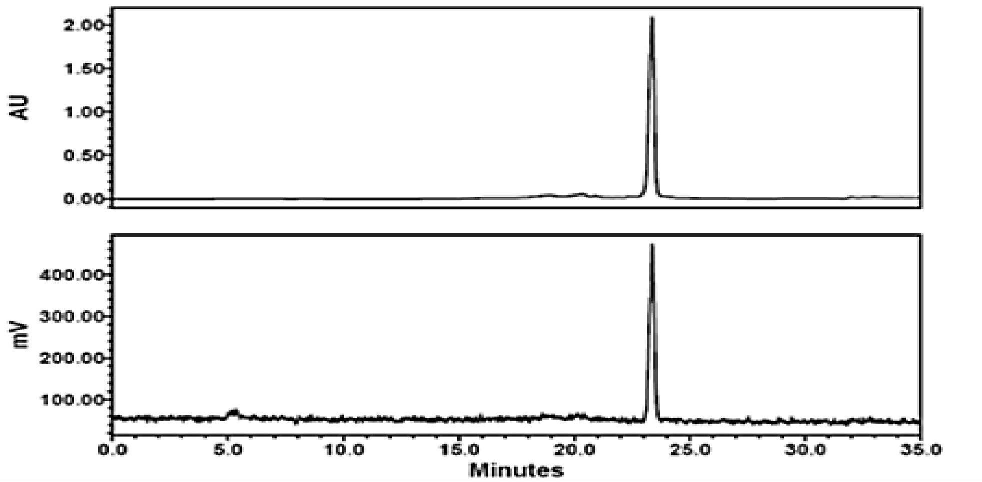

Figure 2.3 UV (top) and gamma HPLC traces of a coinjection of non-radioactive standard **1a** and radiolabeled product **1b**.

The stability of **1b** in 10% ethanol/saline was assessed using HPLC. At 60 min, **1b** remained the dominant product however over time a small peak in the HPLC, corresponding to the retention time of the oxidized fluorophore, was evident. As this is likely due to the presence of radicals generated following radioactive decay,[27] the use of a radical scavenger was explored. Ascorbic acid, at concentrations suitable for preclinical and clinical studies[28] (0.5 mg/mL), was used as an antioxidant and proved to be highly effective as the probe showed no evidence of oxidation out to 150 min (Appendix 1, Figures S19 and S20).

The biodistribution of cyanine dyes including IR780 using fluorescent imaging has been evaluated in a range of different preclinical models.[29] With access to [^{18}F]**1b**, it is possible to use PET imaging to evaluate the *in vivo* distribution of the reduced hydrocyanine dye. PET/CT images at 2 and 4 h showed significant blood pool activity where the heart, lungs and spleen could be readily visualized (Figure 2.4).

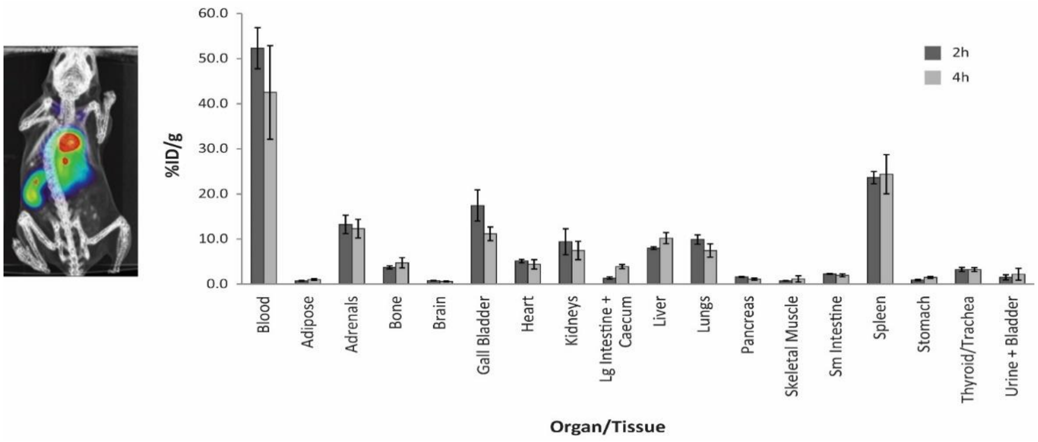

Figure 2.4. PET/CT image (left) of **1b** at 2 h post-injection (PI) (75% max. threshold) and biodistribution data (right) at 2 and 4 h PI, expressed as percent injected dose per gram (%ID/g). Complete biodistribution data and additional images are found in Appendix 1; Table S2, Figure S22.

Quantitative tissue and fluid counting following necropsy was in agreement with the images and confirmed that at 2 h the highest amount of activity was in the blood (52.3 ± 4.6 %ID/g) followed by spleen (23.6 ± 1.4 %ID/g) and gall bladder (17.4 ± 3.4 %ID/g), with activity also present in blood rich organs (heart, lungs, liver). The observed retention of the tracer in the blood pool may be due to binding of **1b** to albumin or red blood cells (RBC's, Chapter 3).[29,30]

To assess the ROS targeting ability of the probe *in vivo*, **1b** was evaluated in a ROS-induced cardiomyopathy model whereby C57BL/6 mice were administered doxorubicin (Dox, 20 mg/ Kg). We observed a significant increase in heart uptake between Dox-treated and control mice at 4 hours post injection of the tracer ($p < 0.05$, Figure 2.5).

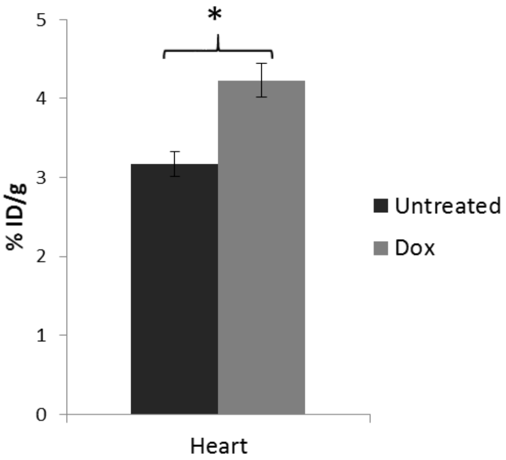

Figure 2.5 Percent injected dose per gram (%ID/g) in the heart of untreated and doxorubicin treated C57BL/6 mice 4 hours post injection of **1b** ($n = 3$, $p < 0.05$).

Compound **1b** exhibited a smaller change as compared to [^{18}F]DHE (1.3 versus 2-fold), which may be attributed to the selectivity of **1b** towards hydroxyl radicals and superoxide whereas DHE is known to react with a wider range of ROS and reactive nitrogen species[31] that are present in Dox-induced cardiomyopathy models.[32,33]

2.4 Summary and Conclusions

In summary, we report a convenient synthetic method for preparation of a ^{18}F-labeled multi-modal PET-turn-on NIR ROS probe. The fluorophore **1a** is synthetically tractable and has a number of advantages over existing ROS sensing probes including its ability to emit in the NIR region upon selective oxidation and is resistant to autooxidation. The PET analogue **1b** can be produced in a single step in reasonable radiochemical yield and exhibits stability in solution. This probe was tested in a doxorubicin cardiac model and demonstrated significant cardiac uptake as compared with untreated mice The work describes the first reported PET and quantitative biodistribution study of a radiolabeled hydrocyanine dye that shows selective *in vitro* and *in vivo* reactivity towards ROS.

2.5 Experimental

Supplementary figures can be found in **APPENDIX 1.**

General considerations. Unless otherwise stated, all chemicals and reagents were purchased and used as received from Sigma-Aldrich without further purification. Solvents were purchased from Caledon Laboratories Ltd. Reactions were monitored using Alugram Sil G/UV$_{254}$ thin layer chromatography (TLC) plates and visualized under ultra-violet light. Column chromatography was performed on a Teledyne Isco Combiflash R_f200® system.

^{1}H and ^{13}C NMR spectra were recorded on Bruker AV 700 or AV 600 spectrometers. ^{1}H chemical shifts are reported in ppm, relative to the residual proton signal of the NMR solvents. Coupling constants (*J*) are reported in Hertz (Hz). ^{13}C chemical shifts are reported in ppm, relative to the carbon signal of the NMR solvents. High resolution mass spectra (HRMS) were obtained on a Waters QToF Ultima Global spectrometer. Reverse phase analytical HPLC was performed using a Waters 2489 HPLC, equipped with a Waters 2489 UV/Vis (λ = 254 nm or 350 nm) and a Bioscan Flow count gamma detector (model 106). Spectra were recorded and processed on Empower 2 software (Waters). The eluents were HPLC grade water containing 0.4% ammonium formate (solvent A) and acetonitrile (solvent B). Analytical HPLC was performed using a Phenomonex Synergi Polar RP column (250 × 4.60 mm, 4 µm). Semi-preparative HPLC was performed using a Phenomonex Synergi Polar RP column (250 × 10.0 mm, 4µm). The flow rate for analytical HPLC was 1 mL/min and 4 mL/min for semi-prep HPLC. The desired products were analyzed/eluted using either a 95 to 5% gradient (solvent A) over 35 min (method A) or a 50% to 5% gradient (solvent A) over 25 min (method B). Fluorescence measurements were obtained using a Tecan® infinity M1000 plate reader while microscopy studies were performed using Olympus Bright Field BX 53 microscope. Cell media and supplements were purchased from Invitrogen (Mississauga, ON), and the PC-3 cell line purchased from ATCC (CRL-1435). Cells were propagated using Ham's F-12 Nutrient Mix, supplemented with 10% fetal bovine serum (FBS) and 1% Penicillin Streptomycin at 37˚C and 5% CO_2 and were not used beyond passage 30. Fluorine-18 was produced using GE-PET trace-10 cyclotron. 18F fluoride was trapped on a QMA cartridge preconditioned with 0.2% $KHCO_3$ and sterile water solution and was eluted off the QMA cartridge using in 2 mL 0.04 mmol/mL K222 solution.

Synthesis of 2

IR780 iodide (25 mg, 0.04 mmol), 6-fluoropyridin-3-ylboronic acid (7.0 mg, 0.05 mmol), $Pd(OAc)_2$ (1.0 mg, 10 mol%) and *t*-BuXPhos (3.0 mg, 20 mol%), were added to a vial equipped with a Teflon® cap and purged under argon for 2 minutes. The contents of the vial were suspended in ethanol (1 mL) and argon bubbled through the solution for 5 min using a long needle. K_3PO_4 (aq) (0.5 mL, 0.2 mM) was added under argon and the vial sealed, covered with aluminum foil and heated at 100^{o}C overnight. The reaction vessel was cooled and the reaction mixture diluted with water (10 mL) and extracted with DCM (2 × 10 mL). The organic phases were combined, dried over anhydrous $MgSO_4$ and concentrated *in vacuo*. The desired product was isolated using a 8 gram flash RediSep® Rf basic alumina column (using 10% MeOH in DCM as the eluent) to afford **2** as a green solid (19 mg, 79%). $R_f = 0.26$ (5% MeOH/DCM). ^{1}H NMR (700 MHz, MeOH-d4): δ 8.12 (d, *J* = 2.4 Hz, 1H), 7.90 (dt, *J* = 7.9, 2.4 Hz, 2H), 7.41-7.36 (m, 5H), 7.27 (d, *J* = 7.9 Hz, 2H), 7.21 (dt, *J* = 7.5, 0.6 Hz, 2H), 7.15 (d, *J* = 14.0 Hz, 2H), 6.25 (d, *J* = 14.0 Hz, 2H), 4.08 (t, *J* = 7.4 Hz, 4H), 2.75 (t, *J* = 6.1Hz, 4H), 2.07 (m, 2H), 1.84 (dd, *J*

= 14.7 Hz, 7.4 Hz, 4H), 1.84 (m, 4H), 1.27 (s, 12H), 1.02 (t, *J* = 7.4 Hz, 6H). ^{13}C NMR (175 MHz, MeOH-d4) δ 173.7, 165.0 (*J* = 241.1 Hz), 157.2, 149.1 (*J* = 14.1 Hz), 148.3, 145.0 (*J* = 8.0 Hz) ,144.0 (*J* = 273.3 Hz) 134.5 (*J* = 4.7 Hz),133.3, 129.8, 126.3, 123.5, 112.1, 111.0 (*J* = 37.1 Hz), 101.6, 50.1, 49.9, 46.5, 28.0, 27.9, 25.8, 22.4, 21.8, 11.6; HRMS (ESI$^+$) for $C_{41}H_{47}N_3$ F calcd 600.3754, obsd 600.3760.

Synthesis of 1a

Compound **2** (10 mg, 0.016 mmol) was dissolved in MeOH (2 mL) in a 30 mL scintillation vial covered with aluminum foil. Freshly prepared $NaBH_4$ in MeOH (1 mL, 0.16 mM) was added dropwise to the green solution, generating a yellow solution. The reaction was stirred at room temperature (RT) for 10 min and the solvent was removed by rotary evaporation. The resulting solid was dissolved in DCM (3 mL) and extracted with water (2 × 3 mL). The organic phase was dried over anhydrous $MgSO_4$ and the solvent was removed by rotary evaporation to afford a bright yellow solid (7.0 mg, 82%). R_f = 0.31 (hexanes). ^{1}H NMR (600 MHz, CD_3CN): δ 7.92 (s, 1H), 7.64 (d, *J* = 7.1 Hz, 1H), 7.13 (m, 1H), 7.09 (dd, *J* = 8.0 Hz *J* = 1.0 Hz, 2H), 7.06 (d, *J* = 7.3 Hz, 2H), 6.98 (dd, *J* = 7.7 Hz, *J* = 1.0 Hz, 2H), 6.95 (d, *J* = 7.2 Hz, 2H), 6.74 (appt, *J* = 7.4 Hz, 2H), 6.64 (d, *J* = 8.0 Hz, 2H), 6.58 (appt, *J* = 7.4 Hz, 2H), 6.41 (d, *J* = 7.7 Hz, 2H), 6.04 (d, *J* = 15.6 Hz, 1H), 5.90 (d, *J* = 12.4 Hz, 1H), 5.70 (dd, *J* = 15.6 Hz, *J* = 9.0 Hz, 1H), 5.49 (d, *J* =12.4 Hz, 1H), 3.56 (t, *J* = 7.3 Hz, 2H), 2.90 (m, 2H), 2.58 (m, 2H), 2.52 (m, 2H), 1.98 (m, 2H), 1.64 (m, 2H), 1.11 (s, 9H), 0.96 (s, 3H), 0.93 (t, *J* = 7.4 Hz, 3H) 0.85 (t, *J* = 7.4 Hz, 3H). δ ^{13}C NMR (150 MHz, CD_3CN) δ 150.4 (*J* = 269.2 Hz), 149.4 (*J* = 13.6 Hz), 146.0, 144.7, 139.6 (*J* = 20.4 Hz) , 137.2, 135.4, 135.1, 132.6, 131.2, 128.7, 128.3, 126.9, 126.6, 122.5 (*J* = 19.1 Hz), 120.2, 109.8 (*J* = 38.9 Hz), 107.8, 107.2, 93.7, 78.8, 48.6,45.9, 44.9, 44.3, 28.2, 27.9, 26.9, 26.2, 25.9, 24.4, 22.9, 20.3, 12.0, 11.7. HRMS (ESI$^+$) for $C_{41}H_{49}N_3F$ calcd 602.3911, obsd 602.3916

Synthesis of 3

IR780 iodide (25.0 mg, 0.04 mmol), 2-nitro-5-pyridineboronic acid pinacol ester (12 mg, 0.05 mmol), $Pd(OAc)_2$ (1.0 mg, 10 mol %) and *t*-BuXPhos (3.0 mg, 20 mol %) were added to a vial equipped with a Teflon® cap and purged under argon for 2 min. The contents of the vial were suspended in absolute ethanol (1 mL) and argon bubbled through the solution for 5 min using a long needle. K_3PO_4 (aq) (0.5 mL, 0.2 mM) was added under argon and the vial sealed, covered with aluminum foil and heated at 100°C overnight. The reaction vessel was cooled and the reaction mixture diluted with water (10 mL) and extracted with DCM (2 × 10 mL). The organic phases were combined, dried over anhydrous $MgSO_4$ and concentrated *in vacuo*. The product was isolated using a 8 gram flash RediSep® Rf basic alumina column (using 20% MeOH in DCM as the eluent) to afford **4** as a green solid (17 mg, 68%). R_f = 0.52 (5 % MeOH/ DCM). ^{1}H NMR (700 MHz, MeOH-d4: δ 8.52 (s, 1H), 8.51 (d, J = 5.4 Hz, 1H), 8.07 (dd, J= 8.2 Hz, 1.8 Hz, 1H), 7.36 (t, J = 7.7 Hz, 2H), 7.32 (d, J = 7.3 Hz, 2H), 7.20 (m, 4H), 6.91 (d, J = 14.0 Hz, 2H), 6.19 (d, J = 14.0 Hz, 2H), 3.99 (t, J = 7.3 Hz, 4H), 2.73 (t, J = 6.1 Hz, 4H), 2.13 (s, 6H), 2.03 (m, 4H), 1.79 (m, 4H), 1.16 (d J = 8.1 Hz, 12H), 0.99 (t, J = 7.4 Hz, 6H). ^{13}C NMR (175 MHz, MeOH-d4 δ 173.5, 157.6, 155.1, 150.2, 147.5, 143.5, 142.9, 142.5, 142.1, 132.8, 129.6, 126.1, 123.2, 119.2, 112.1, 101.5, 49.9, 46.5, 27.8, 27.7, 25.6, 21.9, 21.4, 11.6. HRMS (ESI$^+$) for $C_{41}H_{47}N_4O_2$ calcd 627.3699, obsd 627.3703.

Auto-oxidation study

A 40 µM solution (1 mL) of **1a** (in 20% MeOH/PBS buffer, pH = 7.4) was placed in a water bath at 37°C and the fluorescence intensity readings ($\lambda_{ex}/\lambda_{em}$ = 768 nm/794 nm) of 100 µL aliquots were taken every h for 7 h and once at 24 h. This was repeated for 40 µM solution (1 mL) of dihydroethidium (DHE, $\lambda_{ex}/\lambda_{em}$ = 515 nm/560 nm) for comparison (Figure S9).

Stability studies for 1a

A 30 µM solution of **1a** in 20% MeOH/PBS (1 mL) was incubated at 37°C for 6 h. The solution was analyzed by analytical HPLC after 1 h and 6 h (Figure S10).

Reactivity assay for 1a

Analytes (500 µM, final concentration) were added to a solution of **1a** (final concentration: 20 µM) in 9% MeOH/PBS buffer (pH =7.4) and left at ambient temperature for 1 h, after which fluorescence was measured using a plate reader (λ_{ex} = 768 nm, λ_{em} = 794 nm). KO_2 was added as a solid[34] while hydroxyl radicals were generated *in situ via* the Fenton reaction[35] where H_2O_2 (100 mM) was added to an aqueous solution of iron (II) sulfate heptahydrate (100 mM). *tert*-Butoxyl radical was generated by combining *tert*-butyl hydrogen peroxide (TBHP,100 mM) with Fe^{2+} (100 mM). Singlet oxygen ($^1O_2$) was generated *in situ* by the addition of $NaClO_4$ to H_2O_2.[36]

Reaction with superoxide

To a solution of **1a** (10.0 mg, 0.016 mmol) in 10 mL dry DMSO was added 10 mg of solid KO_2. The reaction was stirred for 1 h at RT. The stock solution was used to make a 50 μM solution in MeOH and 150 μL of this solution was used for fluorescence measurements ($\lambda_{ex}/\lambda_{em}$ = 768 nm/794 nm). The readings were recorded relative to a 150 μL of 50 μM solution of untreated **1a** (Figure S11). The experiment was repeated for (10.0 mg, 0.016 mmol) DHE ($\lambda_{ex}/\lambda_{em}$ = 510 nm/ 595 nm).

Fluorescence microscopy studies

PC-3 cells (2.5 × 10^5 cells/well) were plated on 12 mm round coverslips and incubated with or without 5 mM NAC in Ham's F12 nutrient mixture (Invitrogen, 11765-054), containing 10% FBS and 1% penicillin/streptomycin at 37°C and 5% CO_2 for 24 h. Cells were also pre-treated with or without 5 mM TEMPOL for 30 min or 5 mM NAC for 1 h, prior to addition of **1a.** Test compound was added directly to the growth media and incubated for 30 min at 37°C. Cells were washed twice with PBS, and fixed by incubating in 4% paraformaldehyde for 10 min at RT. Following fixation, cells were washed twice with PBS and once with H_2O. Coverslips were mounted to slides using Everbrite Hardset Mounting Medium containing DAPI, and stored at 4 °C overnight. The cellular fluorescence was acquired on an Olympus Bright field BX53 microscope using a commercially available filter set consisting of a 747 nm excitation filter, and a 800 nm emission filter (Appendix 1, Figure S12)

MTT assay

PC-3 cell viability and proliferation was assessed using a 3-(4,5-dimethylthiazol-2-yl)-2,5-diphenyltetrazolium bromide (MTT) assay (Molecular Probes, V13154). PC-3 cells were plated ($1.0\text{x}10^4$cells/100µL) in growth media and incubated at 37°C under 5% CO_2 atmosphere overnight. **1a** was suspended in 4% DMSO/Ham's F12 Nutrient Mixture buffer and a serial dilution was performed to achieve final concentrations/well of 0.01, 0.1, 1, 10, 100 and 1000µM in triplicate. As a control, cisplatin was added to wells at identical concentrations and conditions. No cell as well as vehicle only controls were also completed in triplicate. The cells were incubated for 48 h at 37^{o}C under 5% CO_2 atmosphere. The media was aspirated off and replaced with fresh growth media containing no phenol red (Invitrogen, 31053). MTT was added (1mM final concentration in each well) and incubated at 37°C for 4 h, after which 100 µL of SDS-0.01M HCl (1 g/mL) was added to each well. The cells were incubated at 37^{o}C overnight and the absorbance was recorded at λ = 570 nm. (Appendix 1, Figure S13)

X-ray crystallography

Data were collected on the ESRF microfocus MX beamline ID23-EH.[37] A crystal of **3** was flash frozen in a gaseous Nitrogen stream at 100K, and oscillation data were collected on a Pilatus3-2M detector (Dectris, Switzerland) at 14.209 keV (0.8726 A). The detector was set to the minimum possible distance, which is limited by the diffractometer and sample changer robotics to 1.06 A at the edge. Higher resolution data can however be collected at the corners of the detectors. No 2θ movement exits on this beamline, and the energy is fixed. 1480, 0.15° oscillations were collected, with 0.04 second exposures, and 99% attenuation of the beam. Data were reduced with XD.[38]

Structure refinement was carried out using the SHELXTL crystallographic software.[39] After assigning all non-hydrogen atoms, the models were refined against F^2 first using isotropic and then using anisotropic thermal displacement parameters. The hydrogen atoms were introduced in calculated positions and then refined isotropically. Neutral atom scattering coefficients along with anomalous dispersion corrections were taken from the International Tables, Vol. C. Images of the crystal structures were generated using CrystalMaker.[40]

Synthesis of 1b

Compound **3** (5.5 mg, 0.007 mmol) was dissolved in 400 µL of MeOH, and 200 µL of a freshly prepared 0.03 mM sodium borohydride solution in MeOH was added slowly. An instant colour change from green to yellow was observed. The reaction was stirred at RT for 30 s after which it was extracted with DCM (2 × 10 mL). The organic phase was dried over anhydrous $MgSO_4$ and the solvent was removed by rotary evaporation to afford the reduced product as a yellow-brown solid (4.9 mg). A solution of K [^{18}F] F-K_{222} complex (0.92 GBq) was transferred to a 5 mL pyrex® reaction vial and dried at 85°C in an oil bath under a stream of nitrogen. Azeotropic drying by the addition of 1 mL portions of CH_3CN was performed over a 20 minute period (total of 6 mL). The reduced precursor was dissolved in 400 µL of dry DMF and added to the $^{18}F/K_{222}$ mixture which was subsequently heated at 150°C for 4 minutes. After cooling to RT the desired product was isolated by semi-preparative HPLC (decay corrected RCY = 62% ± 5, *n* = 5).

For imaging and biodistribution studies, following evaporation under reduced pressure **1b** was formulated in 10% ethanol/2% pluoronic (F-127) in 0.9% sterile saline.

Stability study for 1b

Compound **1b** (19.98 MBq) was suspended in 600 µL of 10% ethanol/saline and incubated at RT. The solution was analyzed by reverse-phase HPLC (Method A) at 60 and 120 minutes (Appendix 1, Figure S19).

Stability was also accessed in the presence of ascorbic acid (Appendix 1, Figure S21). Compound **1b** (21.98 MBq) was suspended in 500 µL of 10% ethanol/saline. To this was added 100 µL of a 0.5 mg/mL aqueous solution of ascorbic acid. The mixture was left to incubate at RT and the solution was analyzed by reverse-phase HPLC at 60 and 150 minutes (Method A, Figure S20).

Specific activity of 1b [41]

Compound **1b** (2.85 MBq) was dried and allowed to decay to background. It was then dissolved in MeOH and the fluorescence intensity at (λ_{ex} 418 nm) measured and compared to a standard curve (Figure S21) determined using known concentrations of **1a** (30 μM, 15 μM, 7.5 μM, 3.7 μM, 1.8 μM, 938 nM, 469 nM, 234 nM). The specific activity was 5.18 GBq/ μmol (0.14 Ci/μmol).

***In vivo* experiments**

All animal studies were approved by the Animal Research Ethics Board at McMaster University. Mice were maintained under Specific Pathogen Free (SPF) conditions in an established animal facility with 12 h light/dark cycles and given food and water libitum. Imaging experiments were performed on healthy female 17-18 week old C57BL/6 mice (Taconic, Germantown, NY, USA). Biodistribution experiments were performed on healthy female 5-6 week old C57BL/6 mice (Charles River Laboratories, Kingston, NY, USA).

PET/CT imaging

Imaging experiments were performed on a healthy female C57BL/6 mouse, 17-18 weeks old. Each mouse was injected with approximately 9.7MBq of the radiotracer **1b** (200μL in 2% pluronic F127/0.9% NaCl) *via* the tail vein. For the PET imaging, mice were anesthetized with 1% isoflurane and strapped to a bed equipped with an electric heating coil (Harvard). The bed is sealed inside of a Biocontainment Cylinder, and a plastic tube with two airlines, each fitted with a filter (PALL Gas Filter with Hydrophobic Glass, 8004022), allowed continuous infusion of anesthetic into the chamber. The cylinder is placed into the gantry of the MOSAIC Animal PET Imaging System (Philips) such that the animal is positioned within the field of view of the scanner. A 60 min list mode acquisition was initiated immediately after injection of the radioactive tracer. Post acquisition, the data was sorted into twelve 5 min images, which were reconstructed with non-attenuation correction and standardized uptake value (SUV) conversion. At later time points, 15 min static acquisitions were acquired. Sinograms were reconstructed with non-attenuation correction and SUV conversion. For the CT images mice were anesthetized using 1% isoflurane and X-ray images acquired using a conebeam X-SPECT scanner (Gamma Medica, Nothridge, USA), with a source voltage of 75 kVp and a current of 165 μA at the McMaster Centre of Preclinical and Translational Imaging. Projection data was acquired with 1024 projection angles (1184x1120 pixels, 0.1 mm pixels) and reconstructed using a Feldkamp cone beam backprojection algorithm in COBRA (Exxim Software, Pleasanton, CA, USA), into 512x512x512 arrays (0.155 mm isotropic voxels). A water-filled tube was included within each scan in order to convert the voxel values to Hounsfield units (HU). CT images were compressed to a 256x256x256 matrix (0.31 mm isotropic voxels) then the CT and PET images were fused, with in-house software developed in Matlab, by a process that maximised mutual information (MI) between the two images.[42] Powell's multidimensional direction set method was used to maximise MI using a one dimensional search algorithm based on golden section search and parabolic interpolation.[43] PET images underwent rigid body transformation until a change of less than 0.01 mm (translation) or 0.01 degrees (rotation) was observed along or around each axis to obtain fusion parameters. During the process, the 82^3 matrix of the PET image was interpolated for comparison to the CT image, and was resampled to a 256^3 matrix when the stop criteria were met. This corresponds to a change in voxel size from 1.463 mm^3 to 0.31 mm^3. When maximized MI was reached, the result was visually inspected to confirm fusion quality. Imaging analysis was completed using AMIDE software. (Appendix 1, Figure S22)

Biodistribution studies

Biodistribution studies were performed on healthy female C57BL/6 mice, 5-6 weeks old (*n* = 3 per time point, at t = 2h and 4h post-injection; an additional mouse remained under anesthetic for 1h post-injection). Mice were injected with approximately 0.7MBq of **1b** (200µL in 2% pluronic F127/0.9% NaCl) *via* the tail vein. At the specified timepoints, animals were anesthetized with 3% isoflurane and euthanized by cervical dislocation. Blood, adipose, adrenals, bone (femur), brain, gall bladder, heart, kidneys, large intestine and caecum (with contents), liver, lungs, pancreas, skeletal muscle, small intestine (with contents), spleen, stomach (with contents), thyroid/trachea, urinary bladder + urine and tail were collected, weighed and counted in a Perkin Elmer Wizard 1470 Automatic Gamma Counter. Decay correction was used to normalize organ activity measurements to time of dose preparation, for data calculations with respect to injected dose (*i.e*. %ID/g). (Appendix 1, Table S2)

2.6 References

1. a) A. K. N. Schmidt, P. Amstad, P. Cerutti, P. A. Baeuerle, *Chem. Biol.,* **1995**, *2*, 13-22. b) B. D'Autréaux, M. B. Toledano, *Nat. Rev. Mol. Cell Biol.,* **2007**, *8*, 813-824. c) R. Mittler, S. Vanderauwera, N. Suzuki, G. Miller, V. B. Tognetti, K. Vandepoele, M. Gollery, V. Shulaev, F. Van Breusegem, *Trends Plant Sci.,* **2011**, *16*, 300-309. d) B. C. Dickinson, C. J. Chang, *Nat. Chem. Biol.* **2011**, *7*, 504-511.
2. Y.W. Yap, M. Whiteman, N. S. Cheung, *Cell. Signal.,* **2007**, *19*, 219-228.
3. a) G. Waris, H. Ahsan, *J. Carcinog.,* **2006**, *5*, 1-8. b) G.Y. Liou, P. Storz, *Free Radic Res.*, **2010**, *44*, 479-496.
4. K. A. Gelderman, M. Hultqvist, L. M. Olsson, K. Bauer, A. Pizzolla, P. Olofsson, R. Holmdahl, *Antioxid. Redox Signaling,* **2007**, *9*, 1541-1567.
5. X. Chen, X. Tian,I. Shin, J. Yoon, *Chem. Soc. Rev*., **2011**, *40*, 4783-4804.
6. a) B. C. Dickinson, C. Huynh, C. J. Chang, *J. Am. Chem. Soc.*, **2010**, *132*, 5906-5915 b) N. Karton-Lifshin, E. Segal, L. Omer, M. Portnoy, R. Satchi-Fainaro, D. Shabat, *J. Am. Chem. Soc.,* **2011**, *133*, 10960-10965. c) M. C. Y. Chang, A. Pralle, E. Y. Isacoff, C. J. Chang, *J. Am. Chem. Soc.,* **2004**, *126*, 15392-15393. d) N. Karton-Lifshin, E. Segal, L. Omer, M. Portnoy, R. Satchi-Fainaro, D. Shabat, *J. Am. Chem. Soc.,* **2011**, *133*, 10960-10965. e) B. C. Dickinson, Y. Tang, Z. Chang, C. J. Chang, *Chem. Biol.,* **2011**, *18*, 943-948 f) B. C. Dickinson C. J. Chang, *J. Am. Chem. Soc.,* **2008**, *130*, 9638-9639. g) Z. Lou, P. Li, Q. Pan, and K. Han, *Chem. Commun.,* **2013**,

49, 2445-2447. h) F. Si, Y. Liu, K. Yan, and W. Zhong, *Chem. Commun.*, **2015**, *51*, 7931-7934. i) G. C. Van De Bittner, E. A. Dubikovskaya, C. R. Bertozzi, C. J. Chang, *Proc. Natl. Acad. Sci. U.S.A*., **2010**, *107*, 21316-21321. j) A. T. Wrobel, T. C. Johnstone, A. Deliz Liang, S. J. Lippard, P. Rivera-Fuentes, *J. Am. Chem. Soc.,* **2014**, *136*, 4697-4705. k) S. Sato, M. Tsunoda, M. Suzuki, M. Kutsuna, K. Takido-uchi, M. Shindo, H. Mizuguchi, H. Obara, H. Ohya, *Spectrochim. Acta. A. Mol. Biomol. Spectrosc.,* **2009**, *71*, 2030-2039. l) N. B. Yapici, S. Jockusch, A. Moscatelli, S. R. Mandalapu, Y. Itagaki, D. K. Bates, S. Wiseman, K. M. Gibson, N. J. Turro, L. Bi, *Org. Lett.,* **2012**, *14*, 50-53. m) Q. Xu, K.-A. Lee, S. Lee, K. M. Lee, W.-J. Lee, and J. Yoon, *J. Am. Chem. Soc.,* **2013**, *135*, 9944-9949. n) J. Yin, Y. Kwon, D. Kim, D. Lee, G. Kim, Y. Hu, J.-H. Ryu, J. Yoon, *J. Am. Chem. Soc.*, **2014**, *136*, 5351-5358. o) K. Xu, M. Qiang, W. Gao, R. Su, N. Li, Y. Gao, Y. Xie, F. Kong, B. Tang, *Chem. Sci.,* **2013**, *4*, 1079-1086. p) D. Oushiki, H. Kojima, T. Terai, M. Arita, K. Hanaoka, Y. Urano, T. Nagano, *J. Am. Chem. Soc.,* **2010**, *132*, 2795-2801 q) J. Wang, C. He, P. Wu, J. Wang, C. Duan, *J. Am. Chem. Soc.,* **2011**, *133*, 12402-12405.r) K. Pu, A. J. Shuhendler, J. Rao, *Angew. Chem. Int. Ed.,* **2013**, *52*, 10325-10329. s) N. G. Zhegalova, G. Gonzales, M. Y. Berezin, *Org. Biomol. Chem.,* **2013**, *11*, 8228-8234. t) E. W. Miller, A. E. Albers, A. Pralle, E. Y. Isacoff, C. J. Chang, *J. Am. Chem. Soc.,* **2005**, *127*, 16652-16659. u) Y. Koide, Y. Urano, S. Kenmoku, H. Kojima, T. Nagano, *J. Am. Chem. Soc.,* **2007**, *2*, 10324-10325. v) M. C. Y.

Chang, A. Pralle, E. Y. Isacoff, C. J. Chang, *J. Am. Chem. Soc.,* **2004**, *126*, 15392-15393. w) L. E. McQuade, J. Ma, G. Lowe, A. Ghatpande, A. Gelperin, S. J. Lippard, *Proc. Natl. Acad. Sci. U.S.A.,* **2010**, *107*, 8525-8230. x) L. Yuan, W. Lin, S. Zhao, W. Gao, B. Chen, L. He, S. Zhu, *J. Am. Chem. Soc.,* **2012**, *134*, 13510-13523.

7. a) K. Setsukinai, Y. Urano, K. Kakinuma, H. J. Majima, T. Nagano, *J. Biol. Chem.,* **2003**, *278*, 3170-3175. b) N. Soh, K. Makihara, E. Sakoda, T. Imato, *Chem. Commun*., **2004**, *5*, 496-497. c) N. Soh, Anal. *Bioanal. Chem*., **2006**, *386*, 532–543. d) N. Soh, K. Makihara, T. Ariyoshi, D. Seto, T. Maki, H. Nakajima,K. Nakano T. Imato, *Anal. Sci*., **2008**, *24*, 293-296. e) S. E. Page, K. T. Wilke, V. C. Pierre, *Chem. Commun*., **2010**, *46*, 2423-2425. f) L. Yuan, W. Lin, J. Song, *Chem. Commun.,* **2010**, *46*, 7930-7932. g) P. Li, T. Xie, X. Duan, F. Yu, X. Wang, B. Tang, *Chem.Eur. J*., **2010**, *16*, 1834-1840. h) G. M. Ganea, P. E. Kolic, B. El-Zahab, I. M. Warner, *Anal. Chem*., **2011**, *83*, 2576-2581. i) J.-Y. Kim, W. I. Choi, Y. H. Kim, G. Tae, *J. Control. Release,* **2011**, *156*, 398-405. j) W. T. Huang, W. Y. Xie, Y. Shi, H. Q. Luo, N. B. Li, *J. Mater.Chem*., **2012**, *22*, 1477-1481. k) F. Liu, T. Wu, J. Cao,H. Zhang,M. Hu, S. Sun, F. Song, J. Fan, J.Wang, X. Peng, *Analyst*, **2013**, *138*, 775-778. l) M. Kim, S.-K. Ko, H. Kim, I. Shin, J. Tae, *Chem. Commun.,* **2013**, *49*, 7959-7961. m) N. B. Yapici, S. Jockusch, A. Moscatelli, S. R. Mandalapu, Y. Itagaki, D. K. Bates, S. Wiseman, K. M. Gibson, N. J. Turro, L. Bi, *Org.*

Lett., **2012**, *14*, 50-53. n) K. Kundu, S. F. Knight, N. Willett, S. Lee, W. R. Taylor, N. Murthy, *Angew. Chem. Int. Ed*., **2009**, *48*, 299-303.

8. a) S. Liu, D. Li, Z. Zhang, G. K. S. Prakash, P. S. Conti, Z. Li, *Chem. Commun*., **2014**, *50*, 7371-7373. b) E. J. Keliher, J. a Klubnick, T. Reiner, R. Mazitschek, R. Weissleder, *ChemMedChem.,* **2014**, *9*, 1368-1373. c) J. A. Hendricks, E. J. Keliher, D. Wan, S. a Hilderbrand, R. Weissleder, R. Mazitschek, *Angew. Chem. Int. Ed.,* **2012**, *51*, 4603-4606. d) S. Liu, T.-P. Lin, D. Li, L. Leamer, H. Shan, Z. Li, F. P. Gabbaï, P. S. Conti, *Theranostics*, **2013**, *3*, 181-189. e) Z. Liu, Y. Li, J. Lozada, P. Schaffer, M. J. Adam, T. J. Ruth, D. M. Perrin, *Angew. Chem. Int. Ed.,* **2013**, *52*, 2303-2307. f) R. Ting, T. a Aguilera, J. L. Crisp, D. J. Hall, W. C. Eckelman, D. R. Vera, R. Y. Tsien, *Bioconjug. Chem.,* **2010**, *21*, 1811-1819. g) T. Priem, C. Bouteiller, D. Camporese, X. Brune, J. Hardouin, A. Romieu, P.Y. Renard, *Org. Biomol. Chem.,* **2013**, *11*, 469-479. h) Z. Li, T. Lin, S. Liu, C. Huang, T. W. Hudnall, F. P, Gabbai, P. S. Conti, *Chem. Commun.,* **2011**, *47*, 9324-9326.
9. a) T. K. Heinrich, V. Gottumukkala, E. Snay, P. Dunning, F. H. Fahey, S. Ted Treves, A. B. Packard, *Appl. Radiat. Isot.,* **2010**, *68*, 96-100.b) R. Ting, J. Lo, M. J. Adam, T. J. Ruth, D. M. Perrin, *J. Fluor. Chem.,* **2008**, *129*, 349-358. c) R. Ting, C. W. Harwig, J. Lo, Y. Li, M. J. Adam, T. J. Ruth, D. M. Perrin, *J. Org. Chem.,* **2008**, *73*, 4662-4670.
10. J. Culver, W. Akers, S. Achilefu, *J. Nucl. Med.,* **2008**, *49*, 169-172.

11. W. Chu, A. Chepetan, D. Zhou, K. I. Shoghi, J. Xu, L. L. Dugan, R. J. Gropler, M. a Mintun, R. H. Mach, *Org. Biomol. Chem.,* **2014**, *12*, 4421-4431.
12. V. Carroll, B. W. Michel, J. Blecha, H. Vanbrocklin, K. Keshari, D. Wilson C. J. Chang, *J. Am. Chem. Soc.,* **2014**, *136*, 14742-14745.
13. J. J. Gao, K. H. Xu, B. Tang, L. L. Yin, G. W. Yang, and L. G. An, *FEBS J.,* **2007**, *274*, 1725-1733.
14. H. Lee, J. C. Mason, S. Achilefu, *J. Org.Chem*., **2006**, *71*, 7862-7865.
15. H. S. Choi, K. Nasr, S. Alyabyev, D. Feith, J. H. Lee, S. H. Kim, Y. Ashitate, H. Hyun, G. Patonay, L. Strekowski, M. Henary, J. V Frangioni, *Angew. Chem. Int. Ed*., **2011**, *50*, 6258-6263.
16. M. Y. Berezin, K. Guo, W. Akers, R. E. Northdurft, J. P. Culver, B. Teng, O. Vasalatiy, K. Barbacow, A. Gandjbakhche, G. L. Griffiths, S. Achilefu, *Biophys. J.,* **2011**, *100*, 2063-2072.
17. J. Yin, Y. Kwon, D. Kim, D. Lee, G. Kim, Y. Hu, J.-H. Ryu, J. Yoon, *J. Am. Chem. Soc.,* **2014**, *136*, 5351-5358.
18. K. Xu, F. Wang, X. Pan, R. Liu, J. Ma, F. Kong, B. Tang, *Chem. Commun.,* **2013**, *49*, 2554-2556.
19. J. A. McCarron, V. W. Pike, C. Halldin, J. Sandell, J. Sóvágó, B. Gulyas, Z. Cselényi, H. V Wikström, S. Marchais-Oberwinkler, B. Nowicki, F. Dollé, L. Farde, *Mol. Imaging Biol.,* **2004**, *6*, 17-26.

20. a) G. Bartoli, A. Latrofa, P.E. Todesco, *J. Chem. Soc.-Perkin. Trans. I.,* **1972**, *21*, 2671-2671. b) Y. Chen, M. Pullambhatla, C. A. Foss, Y. Byun, S. Nimmagadda, S. Senthamizhchelvan, G. Sgouros, R. C. Mease, M. G. Pomper, *Clin. Cancer Res*., **2011**, *17*, 7645-7653.
21. H. Kobayashi, M. R. Longmire, M. Ogawa, P. L. Choyke, S. Kawamoto, *Lancet Oncol*., **2010**, *11*, 589-595.
22. S. Dikalov, K. K. Griendling D. G. Harrison, *Hypertension,* **2007**, *49*, 717-727.
23. a) B. Kumar, S. Koul, L. Khandrika, R. B. Meacham, H. K. Koul, *Cancer Res.,* **2008**, *68*, 1777-1785. b) H. Hu, Y. Chai, L. Wang, J. Zhang, H. J. Lee, S.-H. Kim, J. Lü, *Mol. Cancer Ther*., **2009**, *8*, 2833-2843.
24. P. Bouit, E. Di Piazza, B. Le Guennic, C. Aronica, L. Toupet, C. Andraud, O. Maury, *J. Am. Chem. Soc*., **2010**, *132*, 4328-4335.
25. X. Peng, F. Song, E. Lu, Y. Wang, W. Zhou, J. Fan, Y. Gao, *J. Am.Chem.Soc.,* **2005**, *127*, 4170-4171.
26. a) J. Ballinger, B.M. Bowen, G. Firnau, E.S. Garnett, F.W. Teare. *Int. J. Appl. Radiat. Isot*., **1984**, *35*, 1125-1128. b) D. Denoyer, I. Greguric, P. Roselt, O. C. Neels, N. Aide, S. R. Taylor, A. Katsifis, D. S. Dorow, R. J. Hicks, *J. Nucl. Med.,* **2010**, *51*, 441-447. c) H. Liu, S. Liu, Z. Miao, Z. Deng, B. Shen, X. Hong, Z. Cheng, *J. Med. Chem.,* **2013**, *56*, 895-901.
27. I. Velikyan, *Molecules*, **2015**, *20*, 12913-12943.

28. D. T. Chien, A. K. Szardenings, S. Bahri, J. C. Walsh, F. Mu, *J. Alzheimer's Dis*., **2014**, *38*, 171-184.
29. a) X. Yi, F. Yan, F. Wang, W. Qin, G. Wu, X. Yang, C. Shao, L. Chung, J. Yuan, *Med. Sci. Monit*., **2015**, *21*, 511-517. b) N. S. James, Y. Chen, P. Joshi, T. Y. Ohulchanskyy, M. Ethirajan, L. Strekowski, R. K. Pandey, *Theranostics*, **2013**, *3*, 692-702. c) X. Yang, C. Shi, R. Tong, W. Qian, H. E. Zhau, R. Wang, G. Zhu, J. Cheng, V. W. Yang, T. Cheng, M. Henary, L. Strekowski, L. W. K. Chung, *Clin. Cancer Res*., **2010**, *16*, 2833-2844 d) S. Onoe, T. Temma, Y. Shimizu, M. Ono, H. Saji, *Cancer Med.,* **2014**, *3*, 775-786.
30. P. J. Sims, A. S. Waggoner, C. Wang, J. F. Hoffman, *Biochemistry*, **1974**, *13*, 3315-3330.
31. A. Gomes, E. Fernandes, J. L. F. C. Lima, *J. Biochem. Biophys. Methods,* **2005**, *65*, 45-80.
32. a) P. Mukhopadhyay, M. Rajesh, S. Bátkai, V. Patel, Y. Kashiwaya, L. Liaudet, O. V. Evgenov, K. MacKie, G. Haskó, P. Pacher, *Cardiovasc. Res.,* **2010**, *85*, 773-784. b) P. Mukhopadhyay, M. Rajesh, S. Bátkai, Y. Kashiwaya, G. Haskó, L. Liaudet, C. Szabo and P. Pacher, *Am. J. Physiol. Heart Circ. Physiol*., **2009**, *296*, 1466-1488. c) F. Shen, S. Chu, A. K. Bence, B. Bailey, X. Xue, P. A. Erickson, M. H. Montrose, W. T. Beck and L. C. Erickson, *J. Pharmacol. Exp. Ther.,* **2008**, *324*, 95-102. d) Z. Fu, J. Guo, L. Jing, R. Li, T. Zhang and S. Peng, *Toxicol. In Vitro.,* **2010**, *24*, 1584-1591.

d) Y. Zhang, Y. M. Kang, C. Tian, Y. Zeng, L. X. Jia, X. Ma, J. Du, H. H. Li, *PLoS One,* **2011**, *6*, 1-9.

33. D. M. Weinstein, M. J. Mihm, J. A. Bauer, *J. Pharmacol. Exp. Ther.,* **2000**, *294*, 396-401.
34. a) K. Kundu, S. F. Knight, N. Willet, S. Lee, W. R. Taylor, N. Murthy *Angew. Chem. Int. Ed.,* **2009**, *48*, 299-303. b) A. E. Albers, V. S. Okreglak, C. J. Chang *J.Am.Chem.Soc*., **2006**, *128*, 9640-9641. c) L. Yuan, W. Lin, J. Song *Chem.Commun.,* **2010**, *46*, 7930-7932.
35. H. H. Fenton *Chem. News*, **1876**, 33, 190-190.
36. K. Xu, X. Liu, B. Tang, G. Yang, An, L. *Chem. Eur. J*., **2007**, *13*, 1411-1416.
37. D. Flot, T. Mairs, T. Giraud, M. Guijarro, M. Lesourd, V. Rey, D. van Brussel, C. Morawe, C. Borel, O. Hignette, J. Chavanne, D. Nurizzo, S. McSweeney, E. Mitchell. *J. Synchrotron Radiat*., **2010**, *17*, 107-118.
38. W. Kabsch *Acta Crystallogr. D Biol. Crystallogr.,* **2010**, *66*, 125-132.
39. SHELXTL PC, version 6.12, Bruker-AXS Inc., Madison, WI, **2002**
40. CrystalMaker: A Crystal and Molecular Structures Program. CrystalMaker Software Ltd., Oxford, England (www.crystalmaker.com).
41. Z. Liu, Y. Li, J. Lozada, P. Schaffer, M. J. Adam, T. J. Ruth, D. M. Perrin, *Angew. Chem. Int. Ed. Engl.*, **2013**, *52*, 2303-2307.
42. F. Maes, A. Collignon, D. Vandermeulen, G. Marchal, P. Suetens, *IEEE Trans Med Imaging*, **1997**, *16*, 187-198.

43. W. Press, S. A Teukolsky W. T. Vetterling B. P. Flannery, Methods in *Multidimensions. Numerical Recipes in C: The Art of Scientific Computing*. 3rd ed. Cambridge: Cambridge University Press. **2007**, p 509–515.

Chapter 3: Biological Studies on First Generation Fluorinated-near-IR Probes

3.1 Introduction

The biological properties of probes **1a**/**1b** and **2a**/**2b** (Chapter 2) were further investigated including assessing differences in their distribution *in vivo*. The high blood residence time of **1b** led to speculation that the agent may be binding to red blood cells (RBCs) or serum albumin and as such, may be useful as a blood-pool agent capable of assessing hypervascularity. Such an agent can be valuable in evaluating inflammatory diseases[1] (such as RA), cancer[2], HIV[3] and lymph-node draining.[4]

Cyanine dyes such as ICG and other fluorescent dyes such as Evans blue have been known to bind serum albumin.[4a,5,6] It is this feature that aids in the delivery of the agents to the area of interest.[7] Further advantages of albumin binding agents include improved pharmacokinetics and circulation, and prevention of premature clearance of the probe.[7] ICG itself has been known to show enhanced fluorescence while bound to albumin in comparison to the free dye.[8] Despite these advantages, the intravenous use of ICG is limited in part by the instability of the fluorophore in solution.[4a] Accordingly, ICG forms multiple degradation products both *in vitro* and *in vivo* which promotes rapid excretion by the liver and bile duct.[4a,4e]

Radiolabelled ligands for the assessment of blood pool volume have been sought after in an effort to address limitations associated with fluorescence imaging. Clinically, ^{99m}Tc labeling of RBCs is one of the most common ways of assessing blood pool activity.[9] However, this method suffers from poor image quality and requires drawing the patient's blood prior to administration, which present risks, both to the patient and healthcare provider.[10] To improve image quality, many attempts have been made to create PET blood pool agents. This includes ^{11}C or ^{15}O labeling of RBCs *via* gaseous carbon monoxide, which requires elaborate instrumentation due to the route of administration involving inhalation by the patient.[11] Albumin labeling is an attractive alternative to RBC mediated blood volume imaging. Currently, the only albumin-derived radiopharmaceutical approved by the FDA is $^{131/125}$I-labelled HSA.[12] Preclinical PET imaging has since been performed on ^{68}Ga, ^{62}Cu, ^{64}Cu and ^{18}F labelled HSA.[12,13-16] Notwithstanding, many HSA radiopharmaceuticals require pre-conjugation of a labeled prosthetic group to the protein prior to administration. Other concerns include *in vivo* stability of the complex, less than ideal circulation and high concentration of the tracer in the liver or lungs, which are known to possess a large albumin space.[17]

Another approach used to extend the half-life of a probe and improve it's targeting efficiency is the encapsulation of the agent in a micelle. This approach is especially useful for hydrophobic optical probes as it has been shown to improve in *vivo* stability, hydrophilicity and clearance.[18] Specifically, encapsulation of cyanine dyes into micelles and nanoparticles have been shown to increase quantum yield by 450-fold in an aqueous environment and an increase of circulatory half life by 95-fold.[19] These agents can accumulate in pathological tissue experiencing angiogenesis *via* the EPR effect where retention of these probes are as a consequence of poor lymphatic drainage at pathological sites.[20, 21] This strategy can therefore improve delivery, while also enhancing *in vivo* stability, half-life and uptake.[18]

Additionally, such probes can be used in theranostics and offer an opportunity to precisely target diseased tissue.[21] NIR fluorophores (such as ICG) amplify heat generation within targeted tissue and generate cytotoxic heat upon NIR excitation.[22] Thus cyanine dyes (such as ICG, IR780 and IR783) and other NIR probes have been encapsulated in micelles and successfully employed as photosensitizers in photothermal therapy (PTT) and photoacoustic imaging (PAI) in addition to acting as improved NIR imaging agents.[19,23-28]

3.2 Objectives

This chapter describes studies investigating two complementary approaches in imaging angiogenesis. First, as an extension of Chapter 2, a comparison is made in the *in vivo* biodistribution and imaging data of PET agents **1b** and **2b** in healthy C57BL/6 mice. This study will provide valuable information on whether the biological behaviour of the probes is comparable and whether the presence of the iminium cation is necessary for blood retention of the tracer. Furthermore, a comparison of these studies will determine whether tracer **1b** undergoes oxidation *in vivo* and thus provides valuable insight on the stability of the probe. Additional *in vivo* experiments where the blood of the animal is analyzed will determine whether the probe resides in the blood plasma or bound to RBCs.

In the second approach, encapsulation of synthesized NIR fluorinated fluorophores in pluronic F-127 micelles is discussed. Anticipated advantages of this approach include improved solubility in aqueous solutions, enhanced photochemical properties and improved *in vivo* half-life. Furthermore, many cyanine dyes are plagued by problems associated with toxicity and micelle encapsulated dyes are known to decrease or even prevent these toxic effects.[18] Therefore, potentially higher concentrations of these micelles can effectively be used in a theranostic approach for imaging and treatment of diseases possessing hypervascularity. Pluronic F-127 polymers have been approved by the FDA and exhibit well-documented safety profiles. Successful F-127 encapsulated agents can therefore be translated to human use.[29]

3.3 Biodistribution, Imaging and Blood Binding Studies of PET tracers ***1b*** *and* ***2b***

Compounds **1b** and **2b** were radiolabeled directly as described in Chapter 2. Due to their hydrophobicity, these tracers exhibited poor solubility and transfer efficiency which resulted in problematic i.v. administration in mice. For this reason, it was necessary to explore various biocompatible formulations prior to any *in vivo* studies (Table 3.1). The most successful formulation (entry 12) was also used for tracer **2b**, but this agent demonstrated considerablly less transfer efficiency than **1b** (< 8%). This difference in behaviour may be attributed to attraction of the cation to the negatively charged surface of the glass vial. To validate this, SigmaCote® was used to neutralize the surface of the glass prior to formulation which resulted in an increase in transfer efficiency (≈ 30%). The addition of ethanol to the formulation was necessary as it was later found that this not only aided in transfer of the agent but also improved the stability of the compound, which in its absence would degrade due to radiolysis (Figure 3.1).

Entry	Buffer	Additive	% Transfer
1	Saline	-	3
2	PBS	-	3
3	Saline	10% EtOH	
4	Saline	5% BSA	25
5	Saline	10% PEG-400	4
6	Saline	10% CD	12
7	Saline	5% BSA,	25
8	Saline	0.01% Tween	5
9	PBS	10% ETOH, 10% CD	13
10	PBS	10% EtOH, 10% PEG 400	7
11	PBS	10% EtOH, 1% DMSO	12
12	Saline	2% F-127, 10% EtOH	50
13	Saline	2% F-127	44

Table 3.1 Various biocompatible formulations explored for **1b** and corresponding transfer efficiencies. CD = β-cyclodextrin. % transfer is defined as (initial radioactivity in vial / final radioactivity measured after transfer) × 100.

Biodistribution studies performed on **1b** showed high retention of the tracer in the blood out to 4 hours (Table 3.2, 53% and 42% ID/g at 2 and 4 hours respectively). Organs possessing a large blood volume such as the spleen and liver showed high uptake which remained relatively constant over the duration of the study. The high uptake in the gall bladder suggests the tracer is being cleared *via* the hepatobiliary system. The modest activity in the skeleton implies some defluorination of the tracer, but is quite surprising given that ortho-fluoropyridines are known to be quite resilient *in vivo*.[30] PET/CT images confirmed the biodistribution data where the tracer was retained in the circulatory system for the duration of the study and blood-rich organs especially ventricles of the heart were clearly visualized.

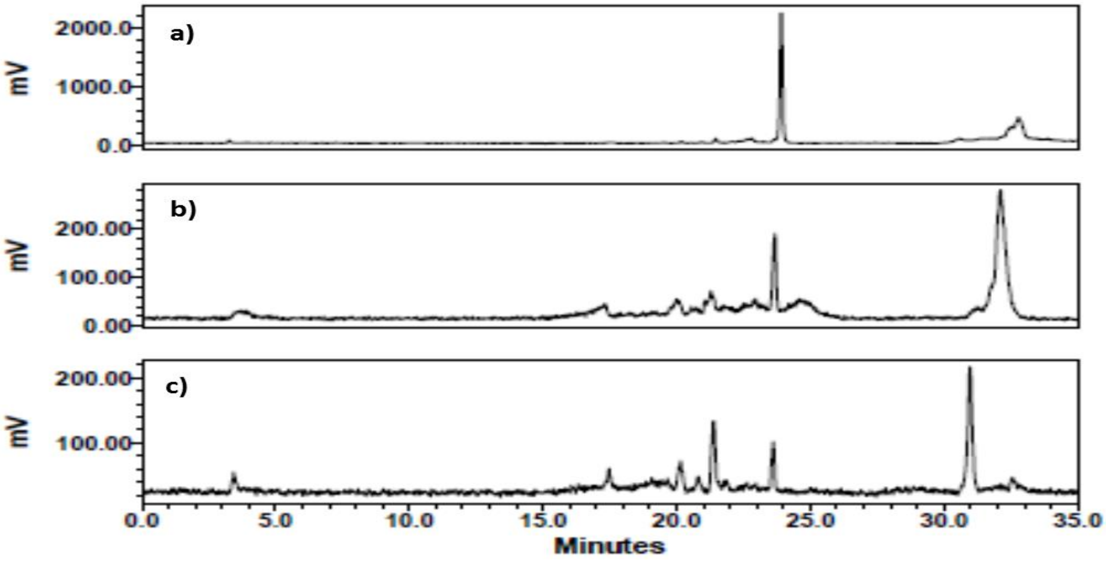

Figure 3.1 γ-Traces of **1b** a) after 0.5 hours formulated in 10% ethanol, 2% pluronic F-127 in saline b) formulated in 2% pluronic F-127/saline 1-hour post formulation c) formulated in 2% pluronic F-127/saline 2 hours post formulation.

The biodistribution pattern of **1b** bears a remarkable resemblance to existing blood-pool agents, especially those related to serum albumin. For example, studies on ^{125}I labeled albumin demonstrated considerable uptake in organs with high albumin accumulation namely the adrenals, spleen, heart and liver with obvious high retention in the blood.[31]

%ID/g	n=3		n=3	
	2h		4h	
Organ/Tissue	Avg	SEM	Avg	SEM
Blood	52.32	4.57	42.51	10.38
Adipose	0.72	0.07	1.02	0.2
Adrenals	13.25	2.04	12.29	2.07
Bone	3.7	0.36	4.73	1.12
Brain	0.76	0.06	0.59	0.12
Gall Bladder	17.45	3.45	11.16	1.51
Heart	5.14	0.38	4.39	1.04
Kidneys	9.41	2.86	7.46	2.04
Lg Intestine + Caecum	1.33	0.25	3.87	0.49
Liver	7.98	0.31	10.21	1.22
Lungs	9.89	1.03	7.44	1.48
Pancreas	1.59	0.12	1.13	0.24
Skeletal Muscle	0.72	0.05	1.17	0.67
Sm Intestine	2.27	0.1	1.95	0.35
Spleen	23.63	1.36	24.37	4.35
Stomach	0.92	0.15	1.5	0.22
Thyroid/Trachea	3.24	0.47	3.22	0.45
Urine + Bladder	1.5	0.57	2.2	1.3

Table 3.2 Biodistribution of **1b** after intravenous injection into healthy C57BL/6 mice, sacrificed at 2 and 4 h. Data is expressed in % injected dose/gram of tissue or fluid (%ID/g).

The long circulation time of the tracer suggests that the compound is bound to the blood tightly and that the resulting complex is stable. This feature is highly desirable in a blood pool agent as many agents tend to suffer from stability issues resulting in rapid clearance.[13,32] For example ^{18}F and ^{11}C labeled RBCs showed 23-53% decrease in blood pool activity after 60 minutes.[33] Another example involving ^{67}Cu labeled albumin showed complete clearance of the tracer from the blood in just 10 minutes.[15] Given the lipophilicity of **1b** (log P ≈ 10), it may be possible that the agent is preferentially binding to the hydrophobic pocket (in site IIA) of albumin which is dominated by strong hydrophobic interactions.[34] Thorarensen *et al.* [35] developed a very high affinity fluorescent albumin binder that possesses common functionalities to **1b** (Figure 3.2). In fact, the binding of indole containing compounds to albumin are well-documented and the literature notes various examples.[36]

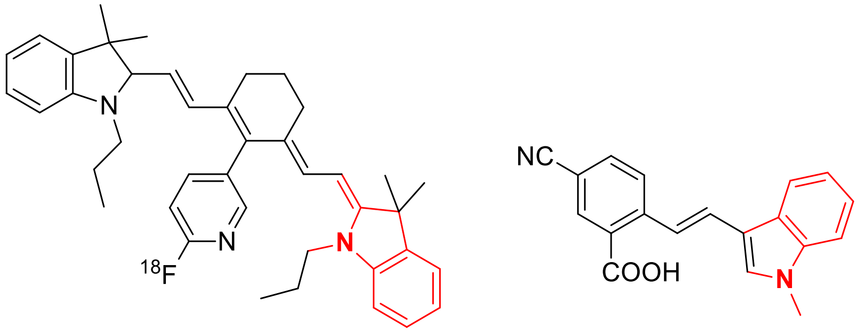

1b

6

Figure 3.2 Common structural features between **1b** and potent HSA binder **6** (400 ± 100 nm).

To determine definitively whether the tracer resided in the blood plasma or RBCs, blood studies were performed where the tracer was injected in mice and the blood collected. Whole blood was centrifuged and activity in the supernatant and RBC were counted (Figure 3.3). This experiment showed that 97% of the activity was found in the blood plasma and not RBC's, further supporting that the tracer may be binding to serum albumin.

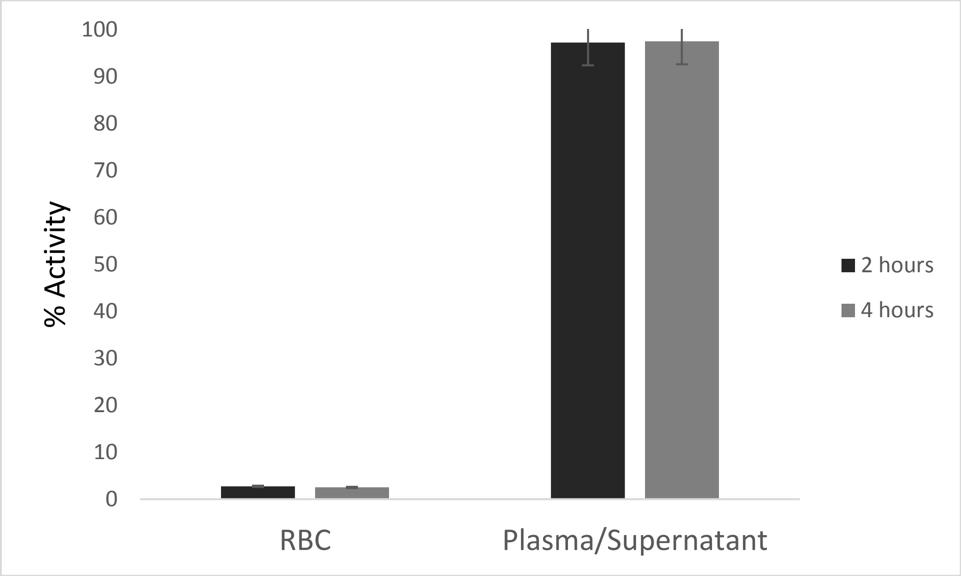

Figure 3.3 Percent activity for compound **1b** in red blood cells and plasma post centrifugation of perfused blood.

To rule out the possibility that the added surfactant may have promoted the observed prolonged circulation,[37] biodistribution studies and PET/CT imaging were performed on **2b** using the same formulation (Figure 3.4 and 3.5). The distribution of radioactivity in tissues drastically varied from that seen with **1b**. At 2 hours, an average of 7.51% ID/g was seen in the blood and blood pool activity decreased to 0.6% ID/g at the 4-hour time point. Comparatively less activity was found in blood rich and albumin-accumulating organs such as the adrenals, the spleen and the liver. At 4 hours, higher amounts of activity were detected in the gall bladder and large intestine suggesting the tracer was clearing *via* the hepatobiliary system. This finding differs from **1b** which showed very little clearance from the blood and only slight variation in organ distribution between 2 and 4-hour time points. This data is in agreement with the PET/CT image which highlights the gallbladder and large intestine as the predominant visualized organs (Figure 3.5).

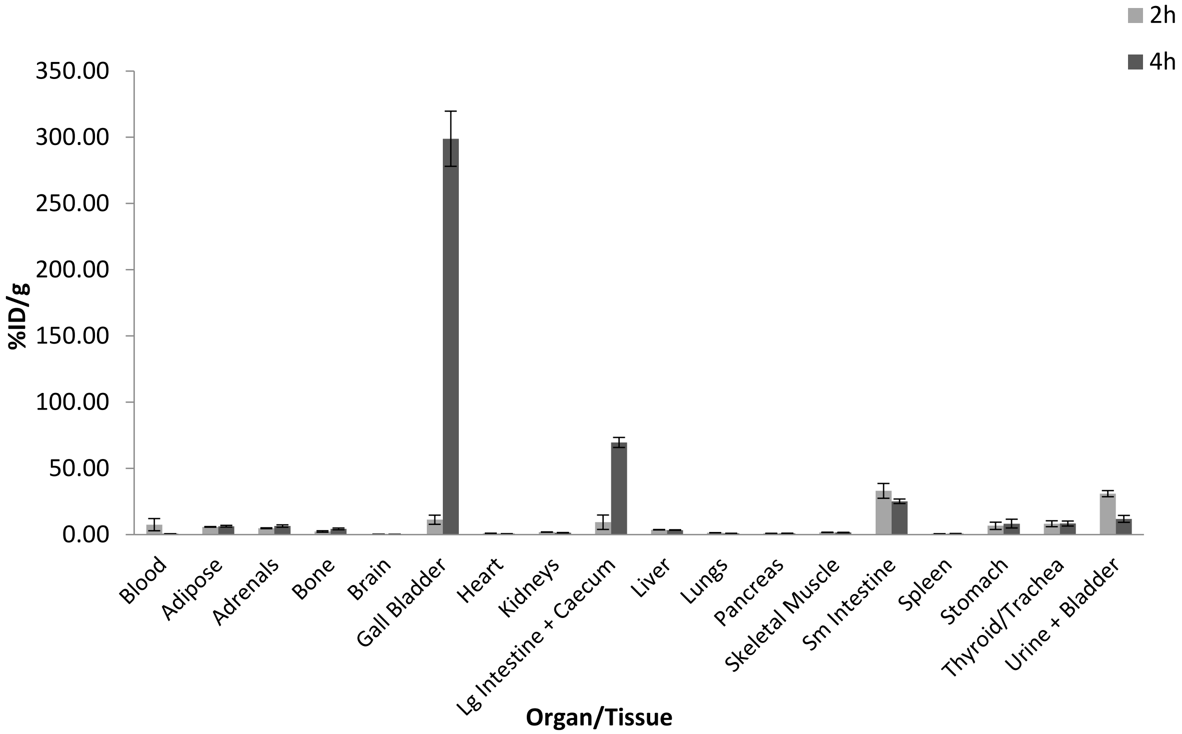

Figure 3.4 Biodistribution for **2b** after intravenous injection into healthy C57BL/6 mice, sacrificed at 2 and 4 h. Data is expressed as percent injected dose per gram of tissue or fluid (%ID/g).

This data suggests that **2b** either does not bind to components of the blood or does so very weakly as compared to **1b**, though it has been previously noted that the related dye IR780 exhibits affinity to albumin.[38] It is strongly inferred through this data that the presence of the iminium ion is responsible for this change in *in vivo* behaviour. This study was repeated with **2b** and it was shown that any activity observed in the blood similarly resided in the blood plasma (data not shown). In comparison to **1b** (and in agreement with the *in vivo* studies) much less activity was observed in the blood for **2b**, further demonstrating that this tracer does not bind as strongly to components in the blood plasma. In agreement with the above data, the carcass showed appreciatively less activity than those that received **1b** further confirming that **2b** clears at a sufficiently higher rate.

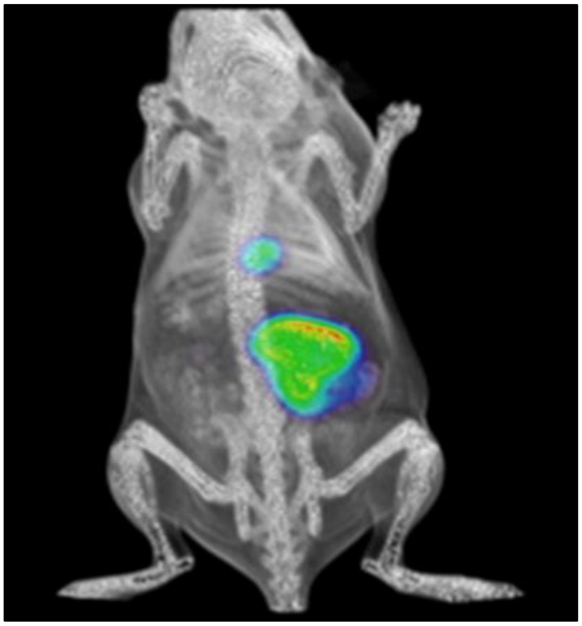

Figure 3.5 Reconstructed PET/CT image at 2 hours post intravenous injection of **2b** in a healthy C57BL/6 mouse.

To confirm that the compound is capable of binding albumin, fluorescence studies were performed on **1a**. Binding of fluorophores to albumin is typically accompanied by an increase in fluorescence intensity, indicative of the dye being enclosed by a non-polar environment.[39] **1a** at a final concentration of 20 μM, was incubated with various concentrations of HSA. The compound exhibited an enhancement of fluorescence intensity with increasing concentrations of HSA, suggestive of a binding interaction between **1b** and HSA (Figure 3.6). Further, at higher concentrations (not shown for clarity), no observable difference in fluorescence intensity was observed, indicating saturation of binding sites on the protein.[39]

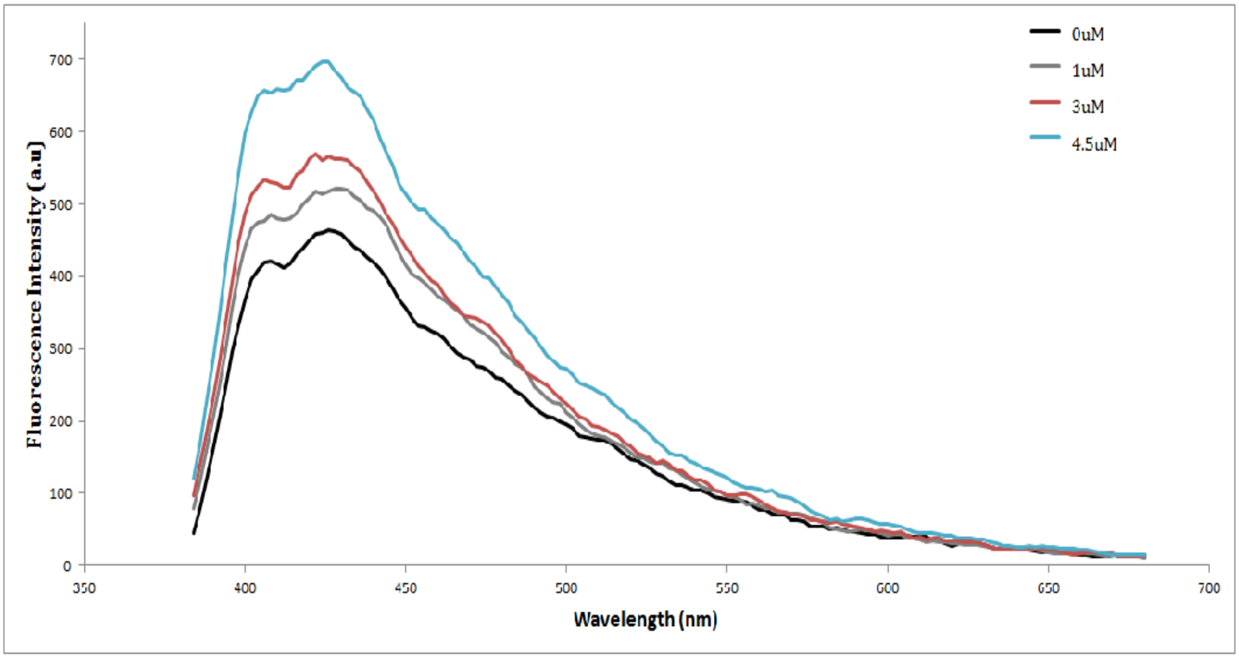

Figure 3.6 Fluorescence intensity spectra upon incubation of **1a** (λ_{ex} = 412 nm, 20 μM final concentration) with varying concentrations of HSA (0-4.5 μM). Some HSA concentrations were omitted from the plot for clarity.

3.4. The synthesis, characterization and assessment of encapsulated NIR fluorinated dyes in pluronic F-127 micelles

Synthesized NIR dyes **2** and **7** were encapsulated in micelles using F-127 pluronic coblock polymers. IR780 iodide was also encapsulated to serve as a reference standard for *in vivo* imaging studies. This reference was chosen for several reasons. Firstly, IR780 iodide as a free dye has been known to accumulate in tumours.[40] This implies that upon dissociation from the micelles, uptake into the tumour can be observed. Secondly, lipophilic fluorophores, such as IR780 have previously been bound to nanocarriers and shown promise in both imaging and PTT/PAI/PDT therapy.[21,38] Importantly, IR780 loaded nanoparticles have also been shown to exhibit stronger intensity in tumours than the free unbound dye.[38] Studies involving IR780 encapsulated micelles led to the development of nanoimaging agent LipImage™, where the encapsulated dye is similar in structure to IR780.[26] Thirdly, our synthesized dyes emit within the same range as IR780 but exhibit enhanced fluorescence intensity in comparison (described in Chapter 4).

In addition to the encapsulation of the NIR dyes, ROS probe **1a** was also encapsulated with the ultimate goal of improving the aqueous solubility of the probe which proved to be problematic in the *in vitro* / *in vivo* studies. As, previously mentioned, the micelles can behave as an EPR mediated delivery system. Once delivered to the area of interest, the encapsulated probe (**1a**) could be released, potentially promoting the oxidation of **1a** to **2a** in areas experiencing elevated ROS. Hydrocyanine functionalized pluronic F-127 micelles have been utilized previously with great success.[13]

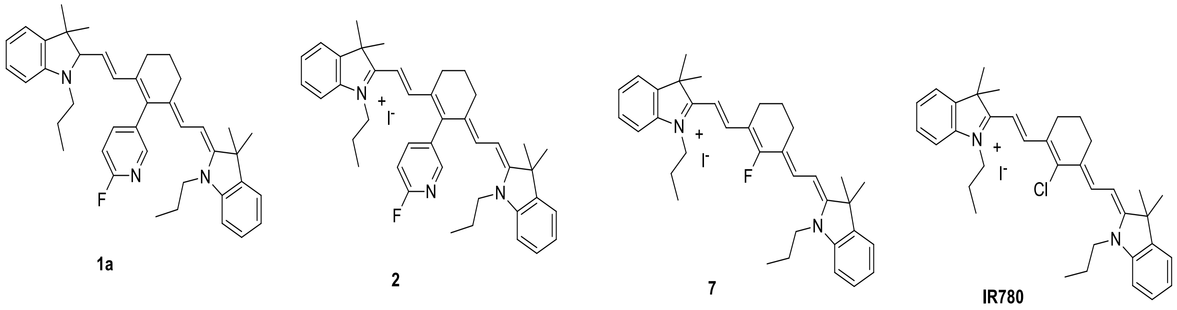

1a **2** **7** **IR780**

Figure 3.7 Structures of dyes encapsulated in F-127 pluronic micelles.

The micelle encapsulation of the dyes were carried out using a solvent evaporation method as reported by Sreejith *et al.* [24] and subsequently purified by dialysis. This method generated monodisperse micelles as shown by experimental PDI values (≤ 0.2) determined by DLS. The average hydrodynamic micelle diameter was also determined at 37°C to be between 19-32 nm for all encapsulated dyes (Figure 3.8).

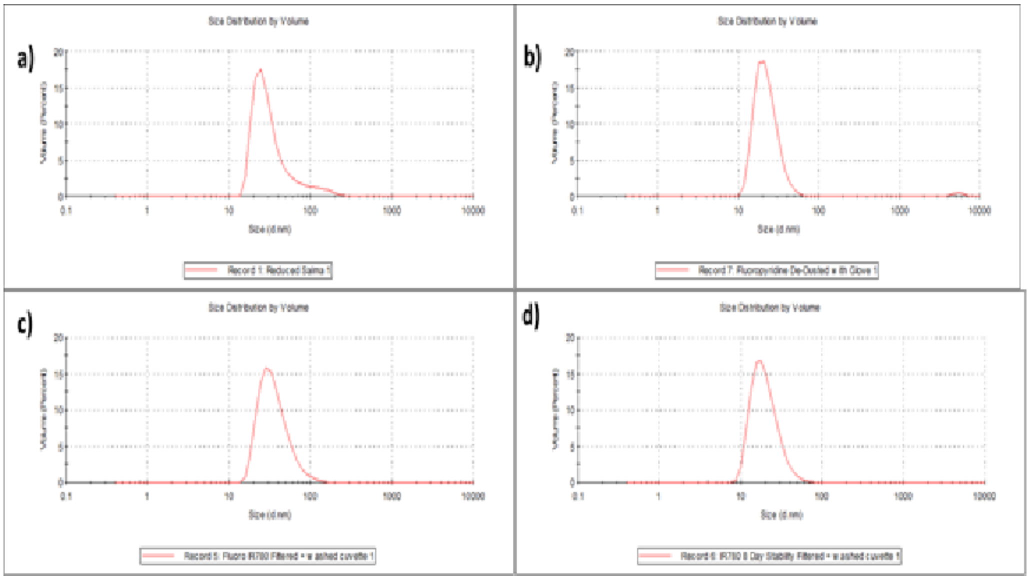

Figure 3.8 DLS data showing hydrodynamic diameter in PBS buffer (pH = 7.4) for a) **1a** b) **2a** c) **7** and d) IR780.

Determination of the diameter by intensity and volume resulted in consistent average diameters. TEM images revealed uniform spherical structures with comparable diameters as those determined by DLS (Figure 3.9). The size of the micelles are very dependent on the preparation procedure and are usually governed by the organic solvent that is used, the addition sequence and concentration of polymer used.[41]

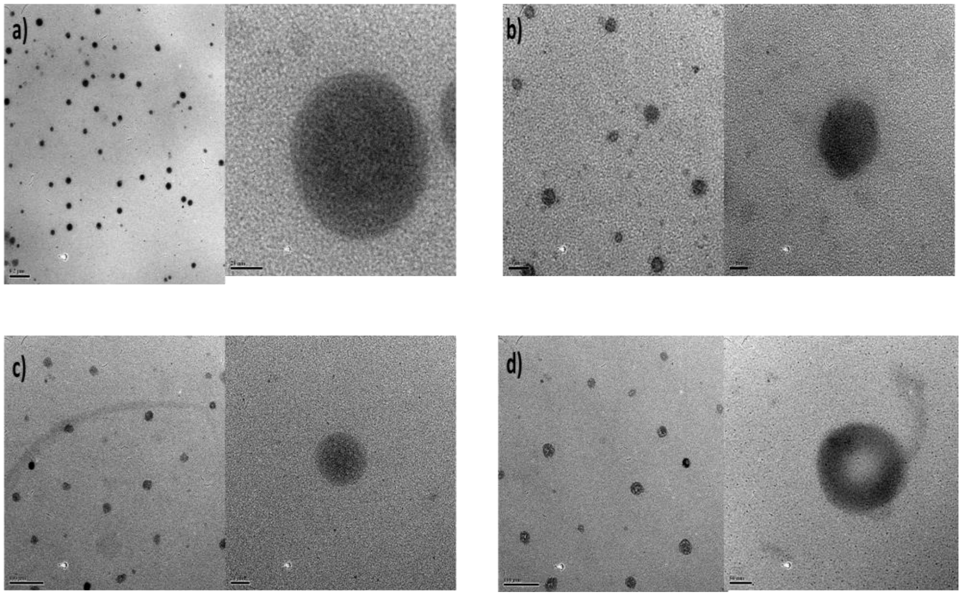

Figure 3.9 TEM images of a)**1a** b) **2** c) **7** and d) IR780 encapsulated micelles in PBS (pH= 7.4).

The average diameter of the micelles are in agreement with some previously reported fluorophore encapsulated F-127 micelles[23,42] but sufficiently smaller than other fluorophore-encapsulated micelles reported in the literature.[24] Micelle size is an important feature for optimizing distribution [41,43] where several studies have shown that nanoparticles >100 nm demonstrate inadequate penetration and accumulation in hypovascular tumours.[44,45] In their study of drug encapsulated micelles, Cabral *et al.* have shown a significant trend between therapeutic targeting and the relative size of polymeric micelles. Micelles that were 30 nm demonstrated complete tumour suppression, those that were 50 nm showed reduced tumour growth and that 100 nm in size failed to supress tumour growth.[43] The inconsistency can be explained by the fact that smaller micelles < 50 nm are capable of traveling to distant blood vessels, permitting homogenous drug distribution, while larger micelles are unable to efficiently penetrate the tumour. Differences are also seen in accumulation in non-target organs, where larger micelles accumulated more in the liver and non-target organs.[22,24,43] Additionally, micelles possessing diameters between 10-100 nm are less likely to be prematurely cleared by the reticuloendothial system, permitting an enhanced EPR effect.[46]

The entrapment efficiency (EE) and drug loading (DL) were assessed by lyophilizing samples and releasing encapsulated fluorophores by dissolving in a known volume of organic solvent (DMSO or methanol). Absorbance readings were taken and compared to a standard curve fitted to a linear regression model. EE and DL were calculated based on equations 3.1 and 3.2. Table 3.3 summarizes DL, EE and various other properties associated with the micelles.

$$DL\ (wt\ \%) = mass\ of\ encapsulated fluorophore \\ /\ mass\ of\ fluorophores\ loaded\ \ into\ micelles \times 100\ \ (\mathbf{3.1})$$

$$EE\ (\%) = \quad mass\ of\ fluorophore\ loaded\ into\ micelles \\ /\ mass\ of\ fluorophore\ initially\ added \times 100\ \ (\mathbf{3.2})$$

As shown, the EE and DL efficiencies were quite low. Smaller diameter size and lower EE/DL have been shown to be a factor of higher concentrations of polymer used in the preparation of the micelles.[23] The method of preparation of these micelles was adapted from Sreejith *et al.* and no EE and DL values were reported for comparison. Low DLs and EEs like the ones obtained have previously been reported and can be increased by modifying the micelle encapsulation procedure.[47] These low values can also be linked with the high lipophilicities of these fluorophores which is known to influence encapsulation efficacy.[46]

Fluorophore	PDI	Average Size (nm)	EE (%)	DL (%)
1a	ND	37.7	40	2.4
2	0.12	26.6	1.1	0.02
7	0.24	30.8	21.6	0.43
IR780	0.25	28.4	8.5	2.3

Table 3.3 Average micelle diameters, % EE, % DL and PDI values for fluorophore encapsulated micelles (ND = not determined).

Micelle stability was initially assessed with samples that were left in PBS at 4°C for 12 days. Specifically, DLS was used to evaluate whether aggregates or changes in diameter could be observed. The micelles showed no changes in PDI and hydrodynamic diameter and no aggregation was observed. Dispersed micelles in PBS were also frozen overnight at -78°C and thawed to perform DLS. Similarly, the micelles showed no change in these properties and aggregation was not observed.

The optical properties of the NIR fluorophore encapsulated micelles were assessed and compared with that of the free dyes. As expected, a red shift in excitation and emission maxima was observed signifying the presence of encapsulated micelles.[23] The fluorescence spectrum of the encapsulated micelles (in PBS) and the corresponding free dyes (in 7% DMSO/PBS) is shown in Figure 3.10. The free fluorophores exhibit fluorescence quenching in aqueous solution, most likely due to aggregation of the dyes.[48]

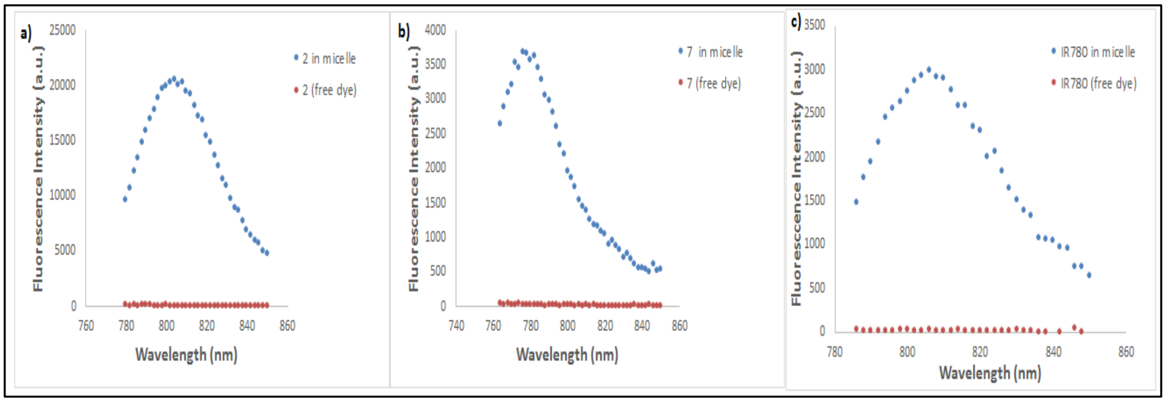

Figure 3.10 Fluorescence emission scan for encapsulated NIR fluorophores (in PBS) and free dyes (in 7% DMSO/PBS) at a concentration of 14.5 μM. a) emission spectrum of **2** (λ_{ex} = 770 nm) b) emission spectrum of **7**(λ_{ex} = 754 nm) c) emission spectrum of IR780 (λ_{ex} = 776 nm).

The stability of the micelles were further evaluated in the presence of BSA (Figure 3.11). The micelles were incubated in 5 % BSA in PBS at 37^{o}C for 1 hour and an emission spectrum was recorded. As a comparison, micelles suspended in PBS in the absence of BSA were also incubated at 37^{o}C. While emission maxima remained the same as for micelles that were not incubated with BSA, the fluorescence intensity was significantly enhanced (Figure 3.11). Kim *et al* also observed this variation in intensity when their ICG encapsulated F-127 micelles were incubated with serum albumin.[23] Micelles constructed from non-ionic polymers (such as pluronic) have been shown to exhibit stability to blood components and have previously demonstrated favourable biodistribution patterns.[41] Generally, micelles composed of a PEG shell prevent recognition by the immune system and offer prolonged blood circulation necessary for efficient tumour accumulation.[41]

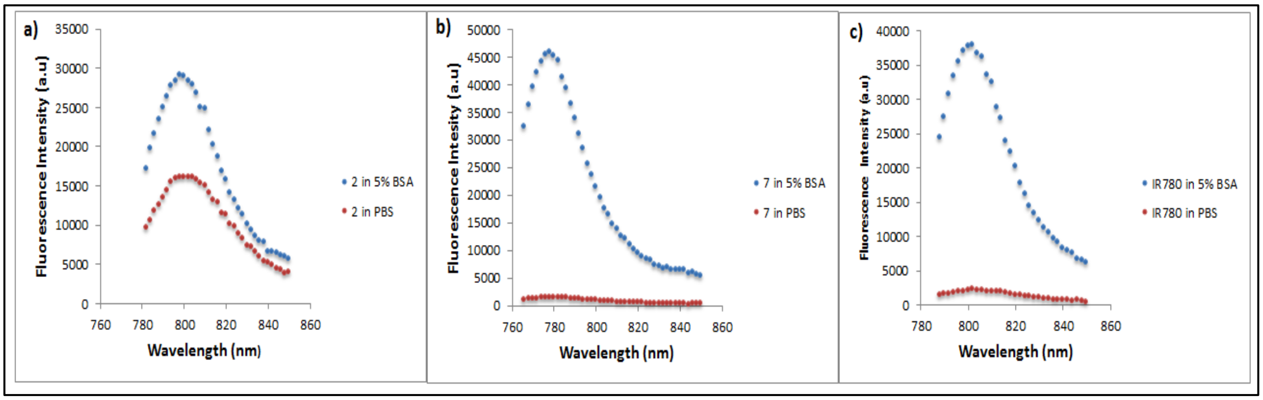

Figure 3.11 Fluorescence emission scan for encapsulated NIR fluorophores incubated at 37°C in the presence and absence of 5% BSA a) emission spectrum of **2** (λ_{ex} = 770 nm) b) emission spectrum of **7** (λ_{ex} = 754 nm) c) emission spectrum of IR780 (λ_{ex} = 776 nm).

It is unclear what led to the change in fluorescence intensity since both micelle stability and albumin bound fluorophores result in enhanced quantum yields. ICG itself (in addition to various other albumin-binding dyes) demonstrates enhanced fluorescence intensity when bound to albumin.[49] It has also been reported that PEGylated polymers directly interact with serum albumin *via* hydrogen bonds.[50] These interactions need not be destructive to the micelles as many have reported micelle stability in the presence of BSA for several hours.[51,] It may be possible that interactions that occur between the polymer and albumin result in enhanced stabilization of the micelle-fluorophore assembly.

In Chapter 2, the toxicity of **1a** was assessed and found to have a comparable IC_{50} to cisplatin. Micelle encapsulation has been known to significantly decrease the cytotoxicity of therapeutic agents, such as doxorubicin.[18b] To evaluate toxicity, an MTT assay was performed on **1a** encapsulated in micelles where the average IC_{50} was found to be 2.4 mM (Figure 3.12). In comparison, the parent compound exhibited an IC_{50} of 52.0 µM, which was comparable to that of cisplatin (65.1 µM). Taken together, the data suggests that the encapsulated probe exhibits considerably less cytotoxicity as compared to the parent compound.

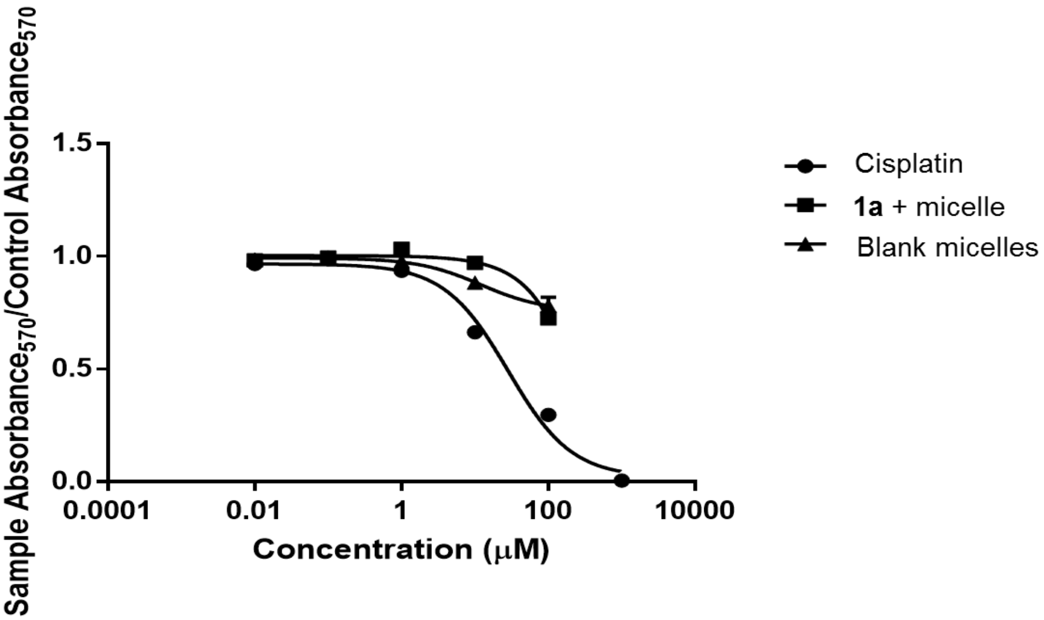

Figure 3.12. MTT assay of PC-3 cell viability, with various concentrations of F-127 encapsulated **1a**, cisplatin and blank (empty) micelles.

To evaluate the *in vivo* properties of the micelles, preliminary studies of encapsulated **1a** were performed in a CD1 mouse bearing a PC-3 xenograph tumour. The mouse was injected with 100 µM of the dye and imaged 24 hours post injection. The mouse was imaged at two different wavelengths (λ_{ex} / λ_{em} = 418 nm/ 478 nm for **1a** and λ_{ex} / λ_{em} = 768 nm/ 794 nm for **2**) followed by *ex vivo* imaging of organs at those same wavelengths (Figure 3.13). The *in vivo* images obtained show no evidence of accumulation at the tumour and *ex vivo* imaging confirmed this at both wavelengths. Under NIR imaging, the liver, kidneys and intestines were the major organs detected.

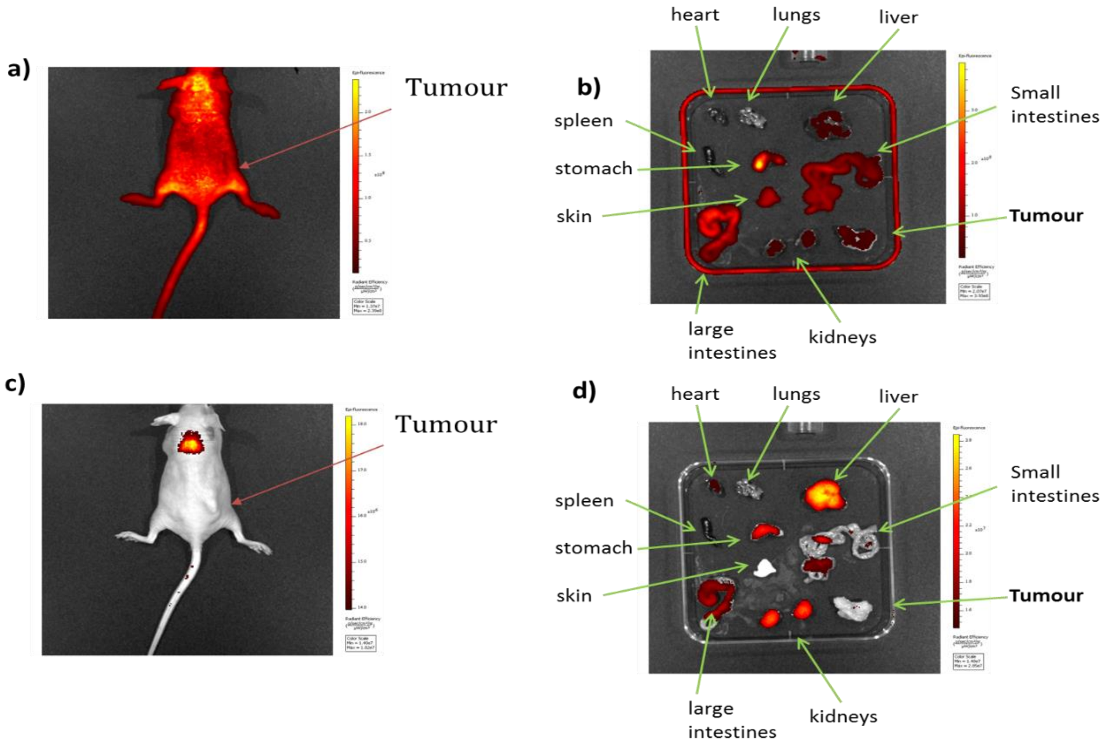

Figure 3.13. *in vivo* and *ex vivo* IVIS images 24 hours post 10 µg injection of **1a** encapsulated micelles a) *in vivo* image at $\lambda_{ex} / \lambda_{em}$ = 418 nm/ 478 nm b) *ex vivo* image at $\lambda_{ex} / \lambda_{em}$ = 418 nm/ 478 nm. c) *in vivo* image at $\lambda_{ex} / \lambda_{em}$ = 768 nm/ 794 nm d) *ex vivo* image at $\lambda_{ex} / \lambda_{em}$ = 768 nm/ 794 nm.

At $\lambda_{ex} / \lambda_{em}$ = 418 nm/478 nm, the major organ visualized was the stomach. Although some fluorescence was detected in the tumour at this wavelength, this signal was not above levels observed in the skin which served as background. One potential reason for the lack of tumour uptake is the prolonged age and large size of the tumour. Larger tumours behave very differently from growing, active tumours as they are known to possess decreased rates of cell proliferation and down regulation of apoptosis.[53] Further, PC-3 tumours possess low vascularity and thus assessment of this probe in other highly vascular tumours is worthwhile. [54]

3.5 Summary and Conclusions

This chapter focused on assessing the biological properties of the ROS probe described in Chapter 2. A biodistribution study with the oxidized form suggests that the reduction of the iminium bond is responsible for the strong retention of the tracer in the blood. Blood studies on the ROS probe demonstrate that a substantial amount of the activity in the blood resides in the blood plasma (97%). Furthermore, preliminary fluorescence measurements indicate that **1a** may bind albumin.

This chapter also describes the encapsulation of three cyanine fluorophores and a hydrocyanine dye in F-127 pluronic micelles. These micelles proved to be stable 2 weeks in solution and showed significantly higher fluorescence than the corresponding “free” dyes in aqueous solution. When incubated with albumin, the micelles show enhanced fluorescence intensity, which may be due to stabilization of the micelles, or disassembly of the micelle and subsequent interaction of the free dye with albumin.

3.6 Experimental

PET/CT imaging

Imaging experiments were performed using a 18 week old healthy female C57BL/6 mouse. The mouse was injected with approximately 1.7 MBq of the radiotracer **2b** (200μL in 2% pluronic F127/0.9% NaCl) *via* the tail vein. For PET imaging, mice were anesthetized with 1% isoflurane and strapped to a bed equipped with an electric heating coil (Harvard). The bed was sealed inside of a Biocontainment Cylinder, and a plastic tube with two airlines, each fitted with a filter (PALL Gas Filter with Hydrophobic Glass, 8004022), which allowed continuous infusion of anesthetic into the chamber. The cylinder was placed into the gantry of the MOSAIC Animal PET Imaging System (Philips) such that the animal is positioned within the field of view of the scanner. A 60 min list mode acquisition was initiated immediately after injection of the radioactive tracer. Post acquisition, the data was sorted into twelve 5 min images, which were reconstructed with non-attenuation correction and standardized uptake value (SUV) conversion. At later time points, 15 min static acquisitions were acquired. Sinograms were reconstructed with non-attenuation correction and SUV conversion. For the CT images, mice were anesthetized using 1% isoflurane and X-ray images acquired using a conebeam X-SPECT scanner (Gamma Medica, Nothridge, USA), with a source voltage of 75 kVp and a current of 165 μA at the McMaster Centre of Preclinical and Translational Imaging. Projection data was acquired with 1024 projection angles (1184 x 1120 pixels, 0.1 mm pixels) and reconstructed using a Feldkamp cone beam backprojection algorithm in COBRA (Exxim Software, Pleasanton, CA, USA), into 512 x 512 x512 arrays (0.155 mm isotropic voxels). A water-filled tube was included within each scan in order to covert the voxel values to Hounsfield units (HU). CT images were compressed to a 256x256x256 matrix (0.31 mm isotropic voxels then the CT and PET images were fused, with in-house software developed in Matlab, by a process that maximised mutual information (MI) between the two images.[55] Powell's multidimensional direction set method was used to maximise MI using a one dimensional search algorithm based on golden section search and parabolic interpolation.[56] PET images underwent rigid body transformation until a change of less than 0.01 mm (translation) or 0.01 degrees (rotation) was observed along or around each axis to obtain fusion parameters. During the process, the 823 matrix of the PET image was interpolated for comparison to the CT image, and was resampled to a 2563 matrix when the stop criteria were met. This corresponds to a change in voxel size from 1.463 mm3 to 0.31 mm3. When maximized MI was reached, the result was visually inspected to confirm fusion quality. Imaging analysis was completed using AMIDE software.

Biodistribution studies

Biodistribution studies were performed on 5-6 weeks old healthy female C57BL/6 mice, (*n* = 3 per time point, at t = 2h and 4h post-injection; an additional mouse remained under anesthetic for 1h post-injection). Mice were injected with approximately 0.7MBq of **2b** (200μL in 2% pluronic F127/0.9% NaCl) *via* the tail vein. At the specified timepoints, animals were anesthetized with 3% isoflurane and euthanized by cervical dislocation. Blood, adipose, adrenals, bone (femur), brain, gall bladder, heart, kidneys, large intestine and caecum (with contents), liver, lungs, pancreas, skeletal muscle, small intestine (with contents), spleen, stomach (with contents), thyroid/trachea, urinary bladder, urine and tail were collected, weighed and counted in a Perkin Elmer Wizard 1470 Automatic Gamma Counter. Decay correction was used to normalize organ activity measurements to time of dose preparation, for data calculations with respect to injected dose (*i.e*. %ID/g)

Blood studies

Blood studies were performed using healthy female 5-6 week old C57BL/6 mice, (*n* = 3 per time point, at t = 2h and 4h). Mice were injected with approximately 0.7MBq of **1b** (200µL in 2% pluronic F127/0.9% NaCl) *via* the tail vein. 1mL of blood from each mouse was collected via cardiac puncture while under anesthetic and the total radioactivity was recorded using a dose calibrator. 0.9% NaCl was added to the blood in a 3:1 ratio and the sample was triturated with 0.9% NaCl. Samples were then centrifuged at 600g for 10 minutes. The supernatant was collected and the radioactivity of each fraction was counted in a Perkin Elmer Wizard 1470 Automatic Gamma Counter. Pellets were resuspended in 0.9% NaCl, triturated and centrifuged as before. The remaining radioactivity in the supernatant was counted and added to the previous supernatant wash. Data was expressed as % total radioactivity in the blood sample.

General method for micelle encapsulation of the fluorophores

A solvent evaporation method was performed as described previously.[24] The dye (5 mg) was weighed and dissolved in a 100 mg/mL solution of pluronic F-127 polymer in DCM (total volume: 5 mL). An equal volume of PBS buffer (pH = 7.4) was added to the organic solvent and the mixture was stirred overnight in a 50 mL uncapped round bottom flask. The following day, any remaining DCM was evaporated and the aqueous solvent containing the dispersed micelles was filtered through a 0.2 µm syringe filter. The aqueous mixture was dialysed (Fisherbrand® cellulose dialysis tubing, nominal MW 12,000-14,000) against water for 24 hours.

Determination of loading efficiency and content

Lyophilized samples were weighed and suspended in 1 mL DMSO to release encapsulated fluorophores. Micelles containing no fluorophores were used as a blank. The concentration of the fluorophores was determined using a standard curve. Samples were excited at 780, 766 and 794 nm for dyes **2**, **7** and IR780 respectively. Absorbance readings were used to determine concentration from the equation of a line where the squared correlation coefficient were 0.999, 0.998 and 0.997 for **2**, **7** and IR780 respectively. The concentrations used ranged from 0.2-30 µM. From this data, % DL and % EE were determined.

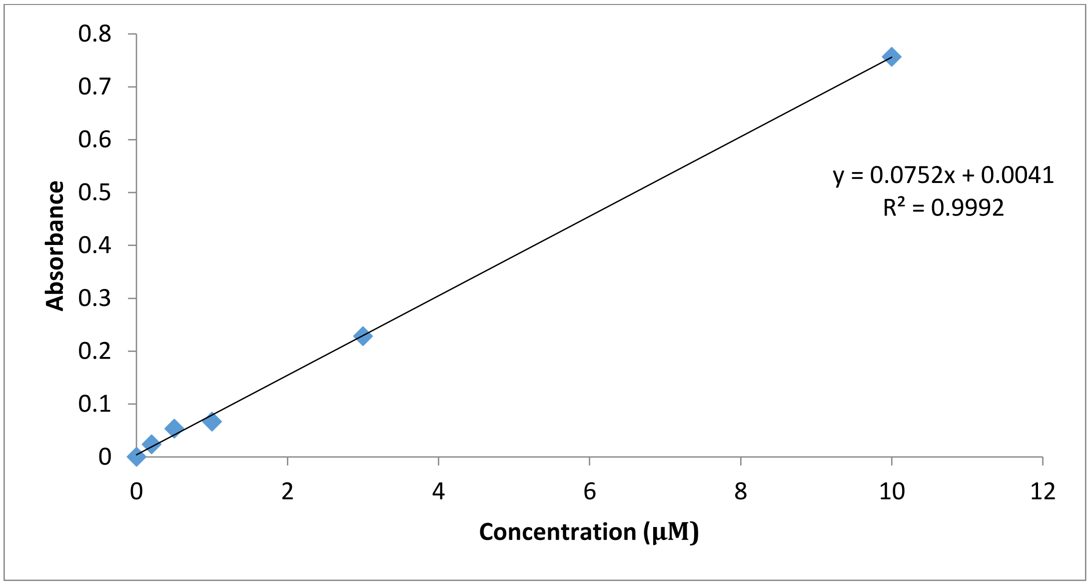

Figure 3.14 Standard curve of absorbance versus concentration of **2** in DMSO.

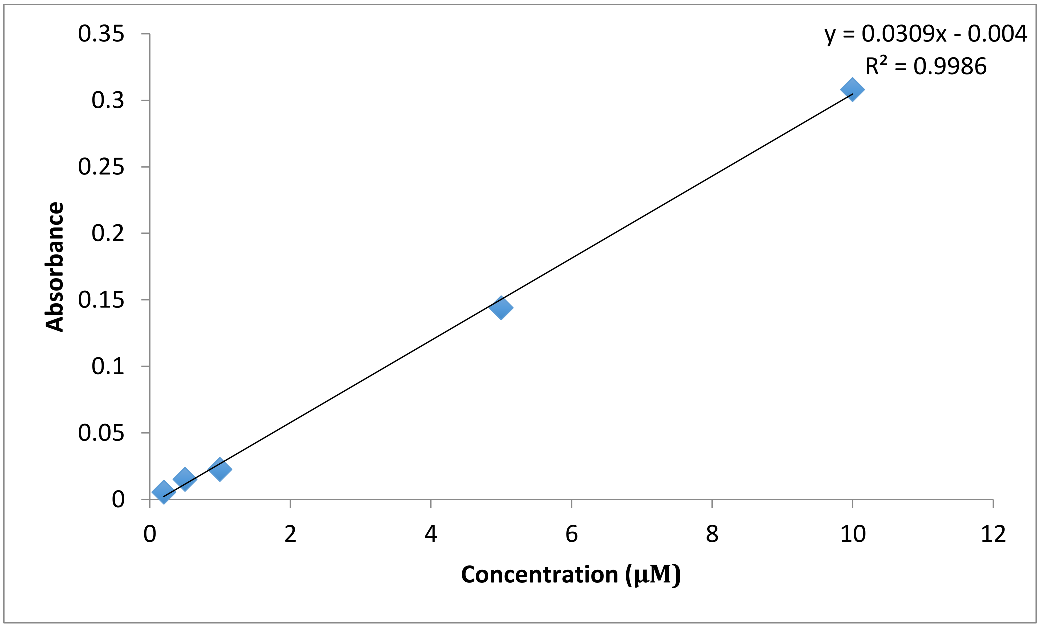

Figure 3.15 Standard curve of absorbance versus concentration of **7** in DMSO.

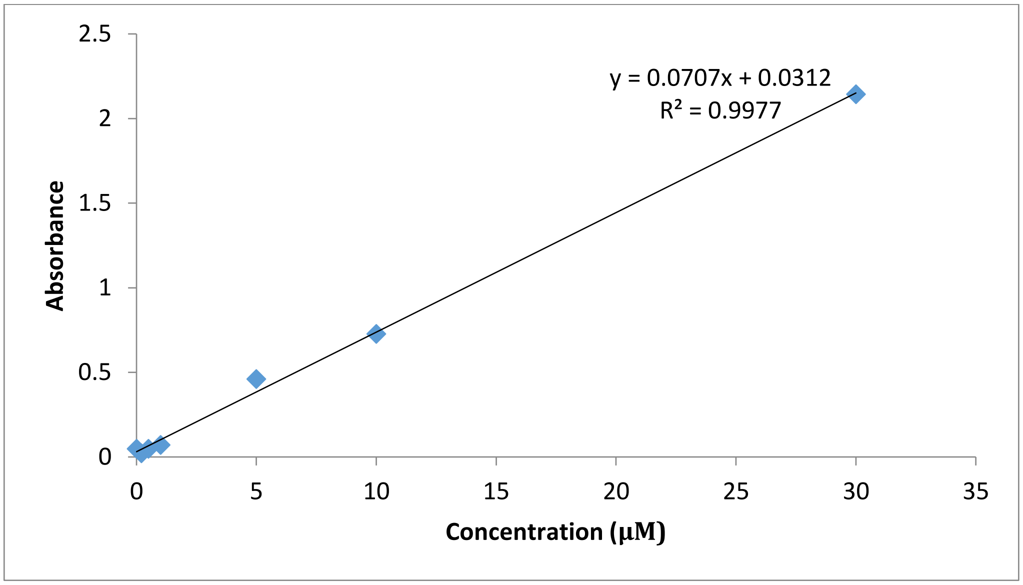

Figure 3.16 Standard curve of absorbance versus concentration of **IR780** in DMSO.

Micelle size determination

Average hydrodynamic diameters and PDI were determined by DLS (Malvern Zetasizer Nano ZS). 1 mg/ mL solutions in PBS buffer (pH = 7.4) were used for the analysis. The readings were taken at 37^{o}C and PDI were reported. Zeta potentials could not be reported due to incompatibility of the probe with the pluronic suspension. Assessment of aggregation and changes in diameter size was assessed after being suspended in PBS (pH = 7.4) for 8 or 12 days at 4^{o}C.

TEM image acquisition

A droplet of a diluted sample (≈ 10 μM) in PBS buffer was placed onto a copper grid (300 mesh) and air dried. The sample was analyzed using a FEI Titan 80-300 LB microscope and average diameters were determined on Image J™ software.

Fluorescence and absorbance measurements

Emission and excitation spectra of encapsulated fluorophores were measured at a concentration of 14.5 µM in PBS buffer. Micelles containing no fluorophores were used as a blank. All optical readings were taken by aliquoting 100 µL of the solutions into a 96-well plate and read using a Tecan® infinity M1000 plate reader.

Stability studies

Micelles at a concentration of 7.25 µM were suspended in 5% BSA/PBS or in the absence of BSA (total volume: 2 mL). The solutions were incubated in a water bath at 37^{o}C for 1 hour. Samples were excited at 780, 766 and 794 nm for dyes **2**, **7** and IR780 respectively and the emission spectrum was obtained. PBS or empty micelles in PBS were used as the blank.

MTT assay

PC-3 cell viability and proliferation was assessed using a 3-(4,5-dimethylthiazol-2-yl)-2,5-diphenyltetrazolium bromide (MTT) assay (Molecular Probes, V13154). PC-3 cells were plated (1.0×10^{4} cells/100µL) in growth media and incubated at 37°C under 5% CO2 atmosphere overnight. **1a** was suspended in 4% DMSO/Ham's F12 Nutrient Mixture buffer and a serial dilution was performed to achieve final concentrations/well of 0.01, 0.1, 1, 10, 100 and 1000µM in triplicate. As a control, cisplatin was added to wells at identical concentrations and conditions. No cell as well as vehicle only controls were also completed in triplicate. The cells were incubated for 48 h at 37^{o}C under 5% CO2 atmosphere. The media was aspirated off and replaced with fresh growth media containing no phenol red (Invitrogen, 31053). MTT was added (1 mM final concentration in each well) and incubated at 37°C for 4 h, after which 100uL of SDS-0.01MHCl (1g/mL) was added to each well. The cells were incubated at 37^{o}C overnight and the absorbance was recorded at λ = 570 nm.

In vivo and *ex vivo* fluorescence imaging

A male CD1 mouse bearing a subcutaneous PC-3 xenograph tumour was injected with 10 µg (in a volume of 200 µL) of **1a** encapsulated F-127 micelles in PBS. The mouse was imaged (λ_{ex} / λ_{em} = 418 nm/ 478 nm and λ_{ex} / λ_{em} = 768 nm/ 794 nm) on a IVIS Lumina II at 24 hours and immediately euthanized by cervical dislocation under 2% isofluorane anesthesia. Major organs and the tumour were extracted and imaged on an IVIS system.

3.7 References

1. C. Fiehn, F. Kratz, G. Sass, U. Muller-Ladner, E. Neumann, *Ann. Rheum. Dis*., **2008**, *67*, 1188-1191.
2. a) K. Chen, J. Xie, X. Chen, *Mol.Imaging*, **2009**, *8*, 65-73. b) J. Prakash, R. Bansal, E. Post, A. de Jagger-Krikken, M.N. Lub de Hooge, K. Poelstra, *Neoplasia*, **2009**, *11*, 1348-1385. c) P.K. Dubey, D. Singodia, R.K. Verma, S.P. Vyas, *J. Pharm. Pharmacol*., **2011**, *63*, 33-40. d) M.G. Anhorn, S. Warner, J. Kreuter, K. Langer, H. von Briesen, *Bioconjugate Chem*., **2008**,

19, 2321-2331. e) K. Low, M. Wacker, S. Wagner, K. Langer, H. von Breisen, *Nanomedicine*, **2011**, *7*, 454-463.

3. D. Xie, C. Yao, L. Wang, C.A. Stoddart, R.G., Ptak, W. Min, J. Xu, J. Xiao, M. Huang, B. Chen, B. Liu, X. Li, H. Jiang, *Antimicrob. Agents Chemother*., **2010**, *54*, 191-196.
4. a) C.A. Davies-Venn, B. Angermiller, N. Wilganowski, P. Ghosh, B.R. Harvey, G. Wu, S. Kwon, M.B. Aldrich, E.M. Sevick-Muraca, *Mol. Imaging Biol*., **2012**, *14*, 301-314. b) Y. Wang, L. Lang, P. Huang, Z. Wang, O. Jacobson, D.O. Kiesewetter, I.U. Ali, G. Teng, G. Niu, X. Chen, *Proc. Natl. Acad. Sci. U.S.A*., **2015**, *112*, 208-213. c) S.T. Proulx, P. Luciani, S. Derzsi, M. Rinderknecht, V. Mumprecht, J.C. Leroux, M. Detmar, *Cancer Res*., **2010**, *15*, 7053-7062.
5. G.R. Cherrick, S.W. Stein, C.M. Leevy, C.S. Davidson, *J. Clin. Investig*., **1960**, *39*, 592-600.
6. R.A. Rawson, *Am. J. Physiol*., **1942**, *138*, 708-717.
7. T. Peters, Jr., *All about Albumin: Biochemistry, Genetics, and Medical Applications*, Academic Press, San Diego, 1996.
8. R. Philip, A. Penzkofer, W.B. Baumler, R.M. Szeimies, C. Adels, *J. Photochem. Photobiol. A*, **1996**, *96*, 137-148.
9. J.A. Ponto, *J. Nucl. Med. Technol*., **1981**, *9*, 150-153.
10. J. R. Herance, J. D. Gispert, S. Abad, V. M. Victor, D. Pareto, È. Torrent, S. Rojas, *Contrast Media Mol. Imaging,* **2013**, *8*, 375–81.

11. K.J. Kearfott, *J. Nucl. Med*., **1982**, *23*, 1031-1037.
12. G. Niu, L. Lang, D.O. Kiesewetter, Y. Ma, Z. Sun, Z., N. Guo, J. Guo, C. Wu, X. Chen, *J. Nucl. Med.*, **2014**, *55*, 1150-1156.
13. J. Hoffend, W. Mier, J. Schumacher, K. Schmidt, A. Dimitrakopoulou-Strauss, L.G. Strauss, M. Eisenhut, R. Kinscherf, U. Haberkorn, *Nucl. Med. Biol*., **2005**, *32*, 287-292.
14. H. Okazawa, Y. Yonekura, Y. Fujibayashi, H. Yamauchi, K. Ishizu, S. Nishizawa, Y. Magata, N. Tamaki, H. Fukuyama, A. Yokoyama, J. Konishi, *J. Nucl. Med*., **1996**, *37*, 1080-1085.
15. C.J. Anderson, P.A. Rocque, C.J. Weinheimer, M.J. Welch, *Nucl. Med. Biol*., **1993**, *20*, 461-467.
16. a) Y. Wang, L. Lang, P. Huang, Z. Wang, O. Jacobson, D. O. Kiesewetter, I. U. Ali, G. Teng, G. Niu, X. Chen, *Proc. Natl. Acad. Sci. U. S. A.,* **2014**, *112*, 208–213. b) C.R. Fischer, V. Groehn, J. Reber, R. Schibli, S.M. Ametamey, C. Müller, *Mol. Imaging Biol.*, **2013**, *15*, 649–654.
17. K.M. Subramanian, *J. Nucl. Med*., **1991**, *32*, 480-482.
18. a) X.M. Yi, F.L. Wang, W.J. Qin, X.J. Yang, J.L. Yuan, *Int. J. Nanomedicine,* **2014**, *9*, 1347–1365. b) A. M. Butt, M. C. I. M. Amin, H. Katas, N. Sarisuta, W. Witoonsaridsilp, R. Benjakul, *J. Nanomater.,* **2012**, *2*, 1-12.
19. X. Wu, W. Zhu, *Chem. Soc. Rev.,* **2015**, *44*, 4179–4184.

20. H. Maeda, H. Nakamura, J. Fang, *Adv. Drug Deliver. Rev.,* **2013**, *65*, 71–79.
21. H. Maeda, *J Control Release*, **2012**, *164*, 138–144.
22. C. L. Peng, Y. H. Shih, P. C. Lee, T. M. H. Hsieh, T. Y. Luo, M. J. Shieh, *ACS Nano,* **2011**, *5*, 5594–5607.
23. T. H. Kim, Y. Chen, C. W. Mount, W. R. Gombotz, X. Li, S. H. Pun, *Pharm. Res.*, **2010**, *27*, 1900–1913.
24. S. Sreejith, J. Joseph, M. Lin, N. V. Menon, P. Borah, H. J. Ng, Y. X. Loong, Y. Kang, S. W.-K. Yu, Y. Zhao, *ACS Nano,* **2015**, *9*, 5695–5704.
25. Z. M. Hudson, D. J. Lunn, M. A. Winnik, I. Manners, *Nat. Commun.,* **2014**, *5*, 1–8.
26. A. Jacquart, M. Keramidas, J. Vollaire, R. Boisgard, G. Pottier, E. Rustique, F. Mittler, F. P. Navarro, J. Boutet, J. L. Coll, I. Texier, *J Biomed Opt.*, **2013**, *18*, 101311-1-101311-9.
27. Y. Shi, S. Kunjachan, Z. Wu, F. Gremse, D. Moeckel, M. van Zandvoort, F. Kiessling, G. Storm, C. F. van Nostrum, W. E. Hennink, T. Lammers, *Nanomedicine.,* **2015**, *10*, 1111–1125.
28. T. Lei, R. Manchanda, A. Fernandez-Fernandez, Y.C. Huang, A.J. Mcgoron, *Beilstein J Nanotech*., **2014**, 5, 313-322.
29. W. Zhang, K. Gilstrap, L.Wu, K.C. Bahadur Remant, M.A. Moss, Q. Wang, X. Lu, X. He, *ACS Nano*, **2010**, *4*, 6747-6759.
30. a) G. Bartoli, A. Latrofa, P.E. Todesco, *J. Chem. Soc.-Perkin. Trans. I.*,

1972, *21*, 2671-2671. b) Y. Chen, M. Pullambhatla, C. A. Foss, Y. Byun, S. Nimmagadda, S. Senthamizhchelvan, G. Sgouros, R. C. Mease, M. G. Pomper, *Clin. Cancer Res*., **2011**, *17*, 7645-7653.

31. A.A. Mallick, A. Ischizaka, K.E. Stephens, J.R. Hatherill, H.D. Tazelaar, T.A. Raffin, *Chest*, **1989**, *95*, 1114-1120.
32. C.J. Mathias, M.J. Welch, M.A. Green, H. Diril, C.F. Meares, R.J. Gropler, S.R. Bergmann, *J. Nucl. Med*., **1991**, *32*, 475-480.
33. O. Gheysens, V. Akurathi, R. Chekol, T. Dresselaers, S. Celen, M. Koole, D. Dauwe, B. J. Cleynhens, P. Claus, S. Janssens, et al., *EJNMMI Res.,* **2013**, *3*, 1-11.
34. M. Nairat, A. Konar, M. Kaniecki, V. V. Lozovoy, M. Dantus, *Phys. Chem. Chem. Phys.,* **2015**, *17*, 5872–5877.
35. A. Thorarensen, R. W. Sarver, F. Tian, A. Ho, D. L. Romero, K. R. Marotti, *Bioorg. Med. Chem. Lett.,* **2007**, *17*, 4646–9.
36. T. J. Dengler, G. M. Robertz-Vaupel, H. J. Dengler, *Eur. J. Clin. Pharmacol.,* **1992**, *43*, 491–499.
37. Z. Liu, D. Liu, L. Wang, J. Zhang, N. Zhang, *Int. J. Mol. Sci.,* **2011**, *12*, 1684–1696.
38. a) C. Yue, P. Liu, M. Zheng, P. Zhao, Y. Wang, Y. Ma, L. Cai, *Biomaterials,* **2013**, *34*, 6853–6861.b) C. Jiang, H. Cheng, A. Yuan, X. Tang, J. Wu, Y. Hu, *Acta Biomater.,* **2015**, *14*, 61–69.

39. E. D. Moody, P. J. Viskari, C. L. Colyer, *J. Chromatogr. B Biomed. Sci. Appl.*, **1999**, *729*, 55–64.
40. a) S. Onoe, T. Temma, Y. Shimizu, M. Ono, H. Saji, *Cancer Med.,* **2014**, *3*, 775-786. b) Wang, F.; Shao, C.; Chung, L. W. K. *Med. Sci. Monit*., **2015**, 511–517.
41. H. Cabral, Y. Matsumoto, K. Mizuno, Q. Chen, M. Murakami, M. Kimura, Y. Terada, M. R. Kano, K. Miyazono, M. Uesaka, Nishiyama, N., Kataoka, K., *Nat. Nanotechnol.,* **2011**, *6*, 815–823.
42. Y. Zhang, M. Jeon, L. J. Rich, H. Hong, J. Geng, Y. Zhang, S. Shi, T. E. Barnhart, P. Alexandridis, J. D. Huizinga, M. Seshadari, W. Cai, C. Kim, J.F. Lovell, *Nat. Nanotechnol.,* **2014**, *9*, 631–638.
43. J. Wang, W. Mao, L.L. Lock, J. Tang, M. Sui, W. Sun, H. Cui, D. Xu, Y. Shen, *ACS Nano,* **2015**, *9*, 7195–7206.
44. P.S. Uster, P.K. Working, J. Vaage, *Int. J. Pharm*., **1998**, *162*, 77-86.
45. M. R. Kano, Y. Bae, C. Iwata, Y. Morishita, M. Yashiro, M. Oka, T. Fujii, A. Komuro, K. Kiyono, M. Kaminishi, et al., *Proc. Natl. Acad. Sci. U. S. A.,* **2007**, *104*, 3460–3465.
46. a) H. Liu, S. Farrell, K. Uhrich, *J. Control. Release*, **2000**, *68*, 167-174. b) S.M. Moghimi, C.J. Porter, I.S. Muir, L. Illum, S.S. Davis, *Biochem. Biophys. Res. Commun*., 1991, 177, 861-866. c) F. Yuan, M. Dellian, D. Fukumura, M. Leunig, D.A. Berk, V.P. Torchilin, R.K. Jain, *Cancer Res*., **1995**, 55,

3752-3756. d) S. Stolnik, L. Illum, S.S. Davis, *Adv. Drug Deliv. Rev*.,**1995**, *16*, 195-214.

47. T. Miller, G. Van Colen, B. Sander, M. M. Golas, S. Uezguen, M. Weigandt, A. Goepferich, *Pharm. Res.,* **2013**, *30*, 584–595.
48. D. S. Conceição, D. P. Ferreira, L. F. Vieira Ferreira, *Int. J. Mol. Sci.,* **2013**, *14*, 18557–18571
49. B. Botz, K. Bölcskei, A. Kemény, Z. Sándor, V. Tékus, G. Sétáló, J. Csepregi, A. Mócsai, E. Pintér, L. Kollár, Z. Helyes, *J. Biomed. Opt.,* **2015**, *20*, 016022.
50. C. Ragi, M.R. Sedaghat-Herati, A.A. Ouameur, H.A. Tajmir-Riahi, *Biopolymers*, **2005**, *78*, 231-236.
51. J. Lu, S. C. Owen, M. S. Shoichet, *Macromolecules*, **2011**, *44*, 6002–6008.
52. I. Pepić, J. Lovrić, A. Hafner, J. Filipović-grčić, *Drug Dev. Ind. Pharm*., **2014**, *40*, 944-951.
53. B. Åkerblom, G. Zang, Z. W. Zhuang, G. Calounova, M. Simons, M. Welsh, *Mol. Oncol.,* **2012**, *6*, 333–346.
54. M. D. Angelica, Y. Fong, *Mol. Cancer Ther.,* **2013**, *12*, 787-798.
55. F. Maes, A. Collignon, D. Vandermeulen, G. Marchal, P. Suetens, *IEEE Trans Med Imaging*, **1997**, *16*, 187-198.
56. W. Press, S.A. Teukolsky, W.T. Vetterling, B.P. Flannery, *Methods in Multidimensions. Numerical Recipes in C: The Art of Scientific Computing*. 3rd ed. Cambridge: Cambridge University Press. **2007**, p.509.

Chapter 4: Synthesis of Second Generation Fluorinated Near-Infrared Dyes

4.1 Introduction

The partition coefficient (log P) of a given pharmaceutical is a strong predictor of a compound's *in vivo* pharmacokinetic/pharmacodynamics (PK/PD) properties.[1] This coefficient can effectively correlate with a drug's absorption, distribution, metabolism and excretion (ADME) properties.[2] In the case of radiopharmaceuticals, which are generally administered *via* intravenous injection, endothelial absorption properties are less relevant. Instead, the processes of distribution, metabolism and excretion are of critical importance. Generally, compounds that are lipophilic demonstrate higher plasma binding and therefore, greater overall distribution.[2] Similarly, lipophilic compounds more readily diffuse through the cell membrane, which is especially important for agents that are required to bind to intracellular targets.[2]

In addition to exhibiting higher permeability, lipophilic agents tend to be rapidly metabolized by the liver but exhibit slow renal excretion due to passive tubular reabsorption in the kidneys.[3] Poor renal excretion is especially amplified with compounds that are bound to the plasma as a result of inefficient glomerular filtration.[3] Radiopharmaceuticals that are too lipophilic are also more likely to exhibit non-specific binding.[4] Thus it is often very difficult to define an "optimal" log P value.

Generally, the incorporation of fluorine in pharmaceuticals has been known to improve therapeutic efficacy and allow for favourable PK/PD properties.[5] Additional advantages include the high polarity of the carbon-fluorine bond which contributes to its strength (estimated at 130 Kcal/mol) and thus its relative *in vivo* stability.[6] Although fluorine is often used to replace hydrogen in biomolecules, fluorine is sterically similar to the hydroxyl group and can effectively replace this functionality. Hydrogen and hydroxyl substitutions have afforded clinically relevant radiotracers best exemplified by the development of [^{18}F] DOPA and [^{18}F] FDG.

Besides the number of advantages associated with the incorporation of fluorine onto bioactive molecules, a number of fluorinated fluorophores (more specifically, rhodamine and fluorescein derivatives) have been known to possess enhanced optical properties over their non-fluorinated counterparts.[7] For example, the development of a fluorinated fluorescein analogue led to the commercialization of "Pennsylvania Green," a brighter and more photostable derivative (Figure 4.1).[7a]

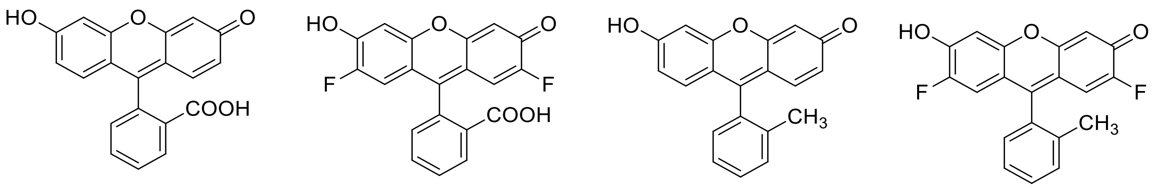

Fluorescein Oregon Green Tokyo Green Pennsylvania Green

Figure 4.1 Fluorinated fluorescein derivatives and their non-fluorinated counterparts.

Similarly, Wurthner *et al* have shown that the synthesis of fluorinated perylene bisimides accessed *via* halogen exchange (HALEX), resulted in analogues possessing superior quantum yields in comparison to the corresponding chlorinated and brominated dyes (Scheme 4.1).[8]

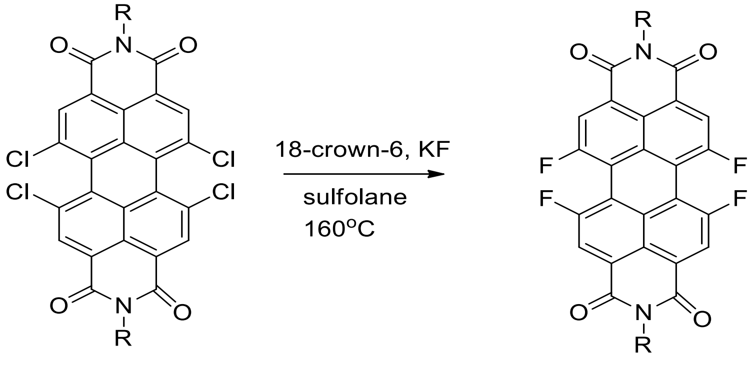

1

2

Scheme 4.1 HALEX reaction performed on chlorinated perylene bidimide producing fluorinated dye **2**.

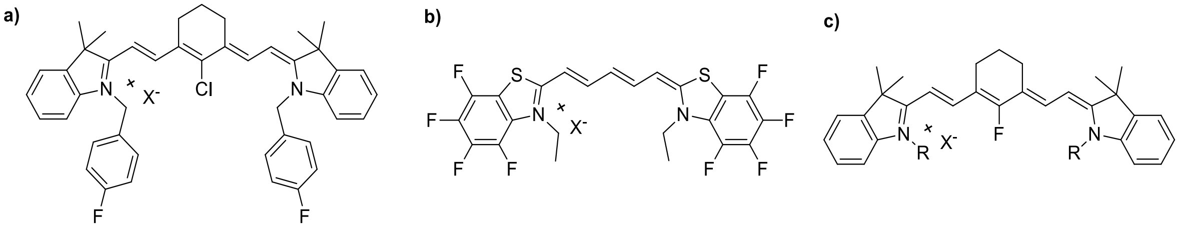

3

4

Not reported

Figure 4.2 Fluorinated cyanine dyes reported in the literature a) fluorination *via* alkylation at the indole nitrogen[9a] b) fluorinations at the aryl ring position c) fluorination at the cyclohexyl position has not been reported.[9b]

Fluorination of fluorophores have been limited in number, mainly due to difficulties in making the synthetic transformation.[7e] The literature reports only a select few examples of fluorinated NIR cyanine dyes (Figure 4.2). Fluorinations at the N-alkyl positions and aryl positions both resulted in highly fluorescent/photostable derivatives by comparison to their non-fluorinated counterparts.[9] Even more challenging is the accessibility of ^{18}F labeled fluorophores due to the relatively short half-life of the radioisotope. Although there are numerous accounts of [^{18}F] BODIPY fluorophores attainable *via* isotopic exchange, there are only two known examples of ^{18}F labeled cyanine dyes to date (Figure 4.3).

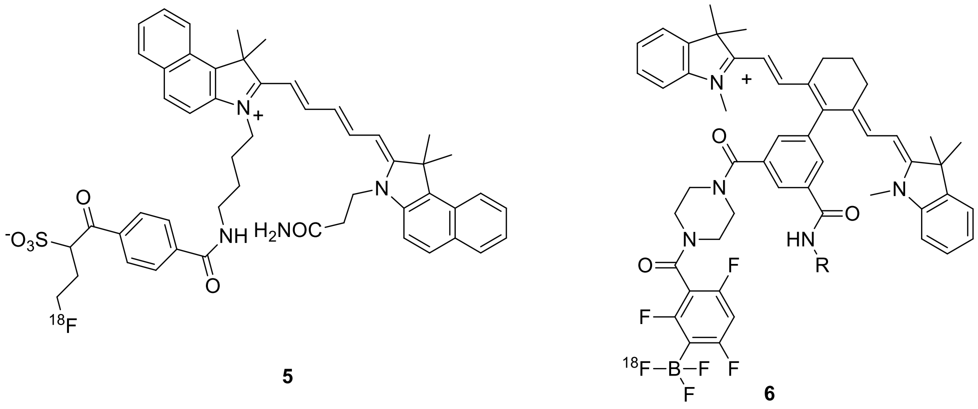

5

6

Figure 4.3 ^{18}F labeled cyanine dyes reported in the literature.

Priem *et al.* developed the fluorinated dye **5** (Figure 4.3) *via* a prelabeled prosthetic group which required multiple steps to synthesize prior to conjugating it to the dye.[10] Ting *et al.* obtained **6** by incorporating a “boron trap” that was conjugated to the dye *via* a bulky linker.[11] Building on the chemistry developed in Chapter 2, introduction of fluorine by direct substitution of the chlorine on IR780 and creating the corresponding hydrocyanine ROS probe could result in probes with favourable optical properties. Further, translation of this fluorination to ^{18}F labeling would be a desirable approach to accessing PET agents capable of emiting in the NIR from commercially available *meso*-chlorine containing dyes, without the need for a prosthetic group.

4.2 Objectives

The goal was to develop the means to synthesize and evaluate fluorinated NIR dyes structurally analogous to that synthesized in Chapter 2. In an effort to improve *in vivo* clearance, a new class of derivatives were designed to be less hydrophobic with considerably lower partition coefficients. This includes the synthesis of a sulfonated derivative and an analogue with a shorter N-alkylated chain (*i.e*. methyl versus propyl). Varying the length of N-alkyl chains on cyanine dyes in particular has been shown to dramatically influence the biodistribution.[12,13,14] Accordingly, the development of a radiolabeled cyanine dye with variable N-alkyl chains is desirable to further optimize the ROS probe described in Chapter 2.

As a complementary strategy, a method for the direct fluorination of IR780 iodide was developed. There are a number of motivations behind being able to create a fluorinated analogue of IR780. Firstly, the exchange of chlorine with fluorine is likely to be accompanied by an increase in lipophilicity, an attribute that is known to promote uptake of IR780 in preclinical tumour models.[12] Secondly, the synthetic strategy can also be used to create a new class of ^{18}F labeled NIR probes potentially in a single step. In addition to the new chemistry, the optical properties of the fluorinated dyes were determined.

4.3 Synthesis, Characterization and Radiolabeling of NIR Turn-on ROS Sensors with variable partition coefficients

Given the results described in Chapter 2, attempts were made to prepare a less hydrophobic ROS probe. To this end, fluorophore **7** was synthesized in a 61% yield using the optimized Suzuki coupling conditions described in Chapter 2 (Scheme 4.2). Commercially available IR783 was used as starting material where the sulfonated derivative **7** was found to have a calculated clog P of ≈ 3.7. Reduction of **7** using methanolic sodium borohydride was attempted but isolation of **8** proved to be difficult. Attempts to scale up the synthesis to facilitate isolation of the product were unsuccessful.

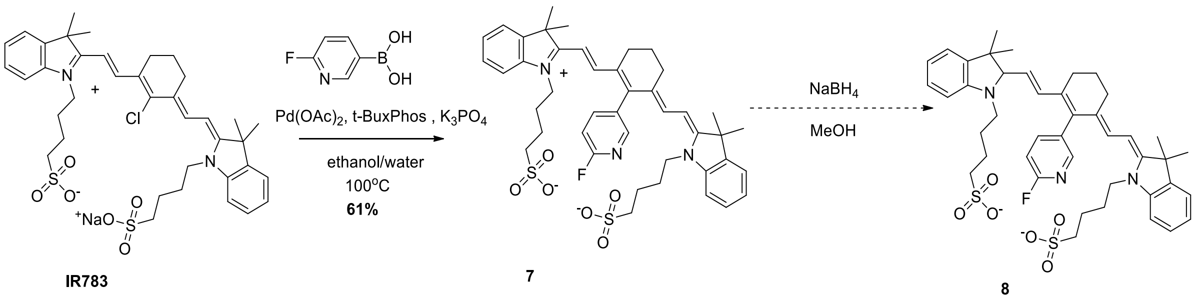

Scheme 4.2 Synthesis of fluorophore **7** *via* Suzuki coupling with 6-fluoropyridin-3-yl)boronic acid and structure of anticipated ROS probe **8**.

Purification of this material by reverse phase chromatography (*e.g.* C18 Sep-Pak cartridges and HPLC) resulted in impure and/or decomposed material. The ^{1}H NMR of **8** was acquired by reducing **7** in MeOH-d4 which revealed the presence of vinyl protons in varying chemical environments, indicative of reduction of the iminum bond and the absence of symmetry brought about by loss of extended conjugation (Figure 4.4).

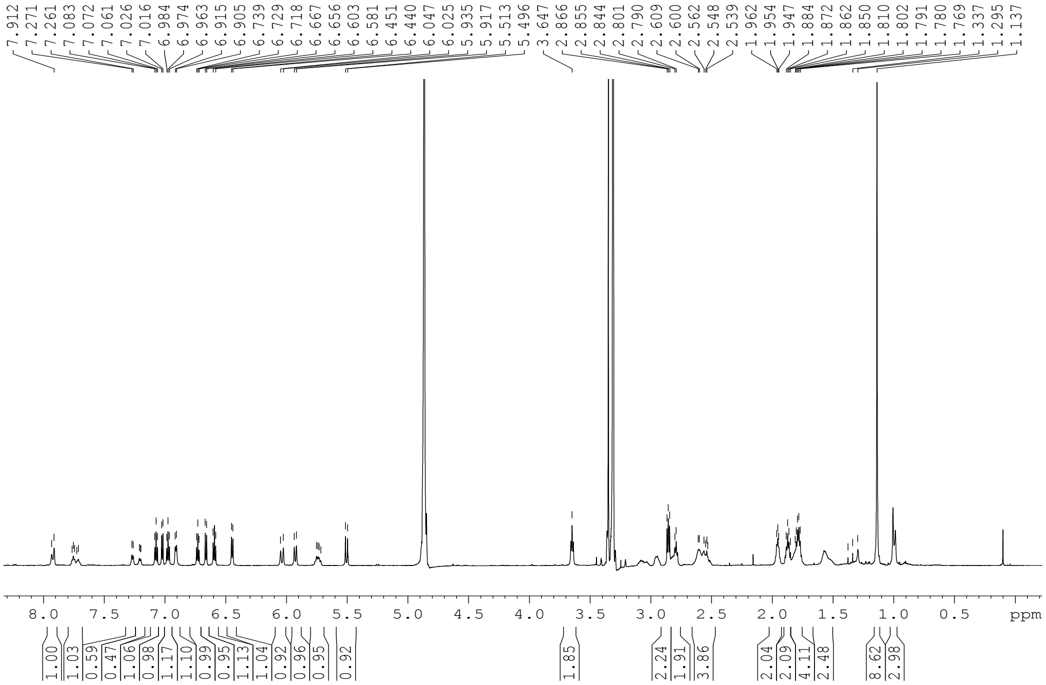

Figure 4.4 ^{1}H NMR of **8** derived from borohydride reduction of **7** in MeOH-d4

The excitation and emission spectra were collected in order to determine whether functionalization at this position influenced the NIR emitting properties (Figure 4.5). Functionalization of cyanine dyes specifically at the *meso* position has been known to be accompanied by changes in the photophysical properties, notably in the appearance of hypsochromic shifts.[15] These studies revealed that **7** experiences an excitation maximum at λ_{ex} 766 nm and an emission maximum of λ_{em} 796 nm. The functionalization resulted in comparable values to the parent compound IR783 (λ_{ex} 766 nm, λ_{em} 798 nm).

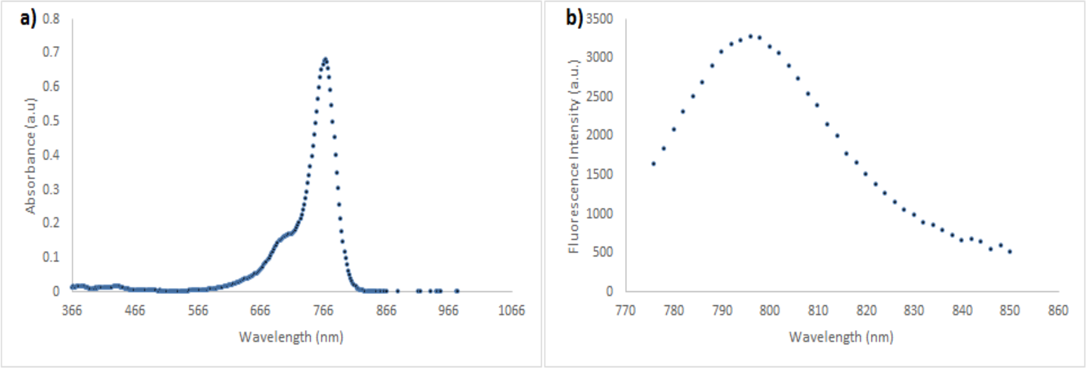

Figure 4.5 a) Absorbance spectrum of **7** (40 µM in methanol) b) Corresponding excitation spectrum (λ_{ex} = 766 nm).

Due to challenges in isolating **8** an alternative strategy was pursued. Previously employed Suzuki coupling conditions were used to synthesize fluorophore **9a** and fluorescent intermediate **10** using commercially available intermediate IR775 chloride. This scaffold possesses two less ethyl groups by comparison to IR780 and a calculated clog P value of 11.2. Reduction of the iminium cation using previously established conditions resulted in **11a** and radiolabeling precursor **12** (Scheme 4.3). This probe exhibits no overall charge and the cationic intermediate generated from elevated ROS concentrations permits intracellular entrapment of the probe.[12a]

Excitation and emission scans of a solution of **9a** in methanol revealed that the fluorophore exhibited maxima at 762 nm and 788 nm respectively giving a Stokes shift of 26 nm (Figure 4.6). This Stokes shift value is comparable to other cyanine dyes reported in the literature[16] and is identical to that reported for the previously synthesized ROS probe described in Chapter 2.

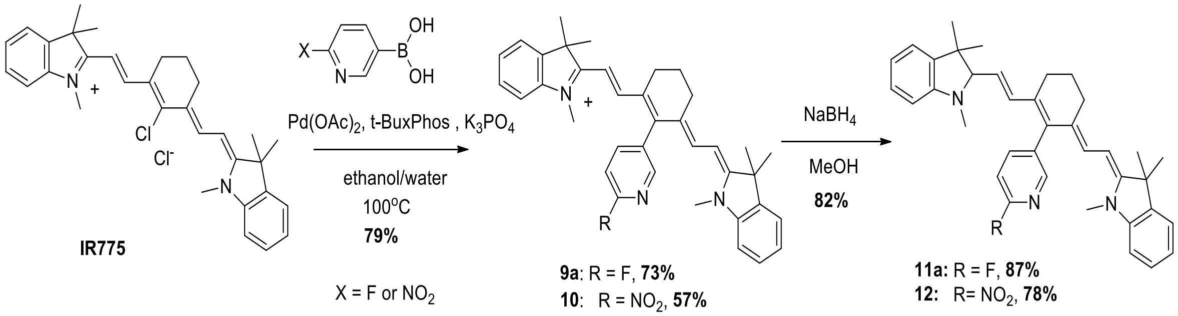

Scheme 4.3 Synthesis of ROS probe **11a** and radiolabeling precursor **12**.

Excitation of the reduced probe **11a** at 758 nm showed negligible fluorescence (Figure 4.7). The cyanine dye **9a** exhibits a 35-fold increase in fluorescence intensity as compared to **11a** at this excitation wavelength. This contrasting difference in intensity is a significant trait for “turn on” probes where background signals can be considerably reduced for *in vitro* and *in vivo* studies.[17]

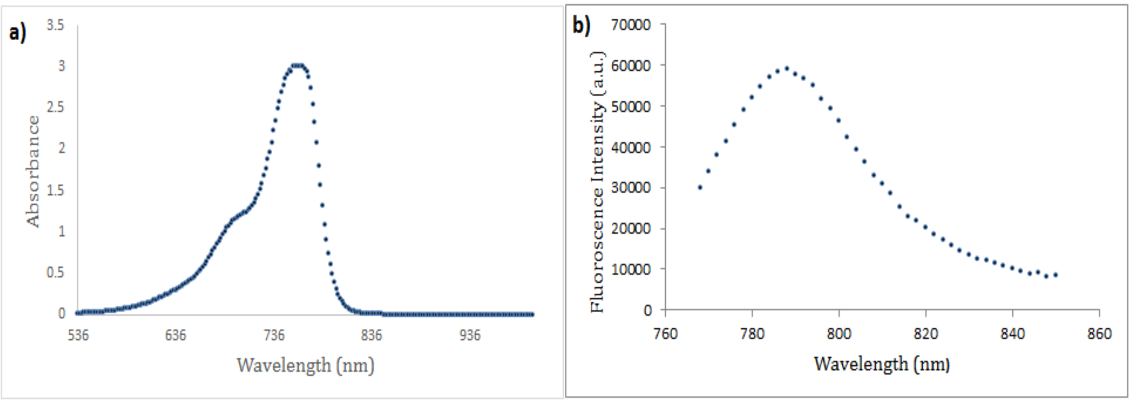

Figure 4.6 a) Absorbance spectrum of **9a** (40 µM in methanol) b) Corresponding excitation spectrum (λ_{ex} = 762 nm).

The radiolabeling precursor **12** was synthesized by subjecting **10** to methanolic borohydride and stirring for a few seconds at room temperature. The reduction of the iminium bond was kinetically more favourable than the reduction of the nitro group. Tailoring reaction conditions resulted in preferential reduction of the iminium bond and retention of the nitro group. Altering reaction conditions such as reaction time or borohydride concentrations resulted in complete reduction of the nitro functionality which was detrimental to radiolabeling yields. The nitro functionality was used over the more labile trimethylammonium triflate leaving group as attempts to synthesize this precursor required a greater number of synthetic steps, and resulted in poor yields and challenging purification protocols (data not shown).

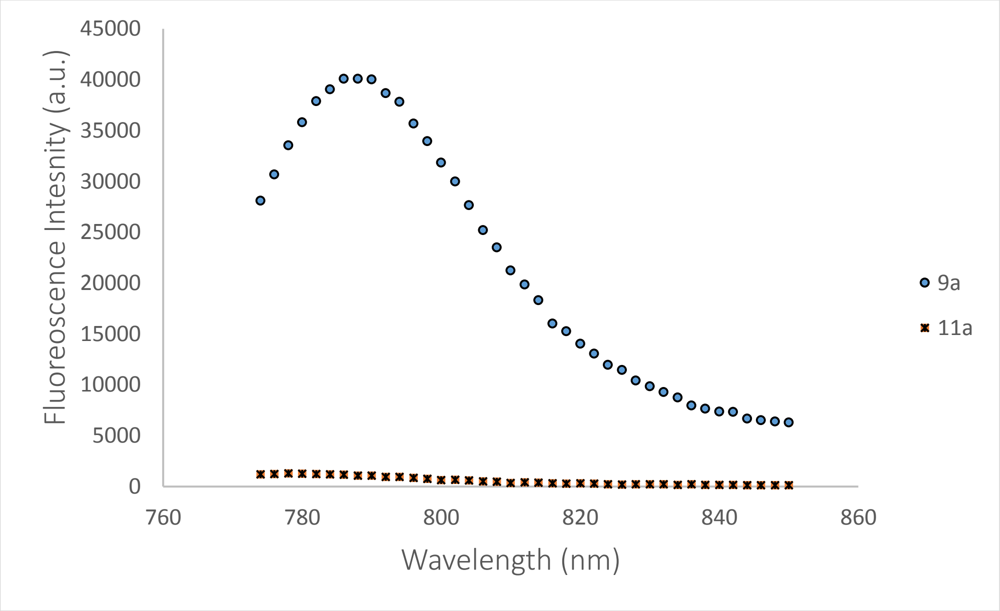

Figure 4.7 Emission spectrum of 40 µM solutions of **9a** and **11a** in methanol (λ_{ex} = 762 nm).

^{18}F radiolabeling of **12** was performed in one step, analogously to the ROS probe reported in Chapter 2. The total synthesis/purification time (excluding the drying step) was 35 minutes (RCY = 65% decay-corrected, *n* = 3). Stability studies performed on **11b** (in 10% ethanol in 0.9% saline) revealed that this probe was more susceptible than the probe described in Chapter 2 to radiolysis brought about by positron-induced ROS formation (Figure 4.8).

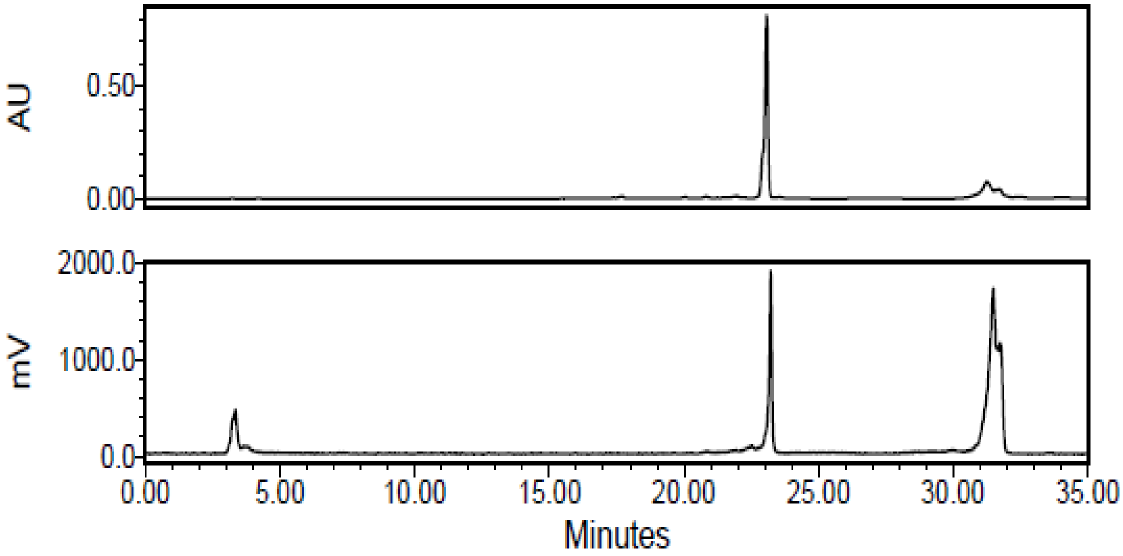

Figure 4.8 HPLC chromatograms after formulation of **11b** in 10% ethanol/0.9% saline showing stability profile of carrier added mixture. UV trace of **11a** (top) and γ-trace (bottom) revealing presence of **9b** and the appearance of a new unidentified peak at 31 minutes.

Reinjection shortly after formulation revealed a prominent peak at 31 minutes along with **11b**, which was not observed for the previous probe until left in the formulation for 60 minutes. This issue was resolved by the addition of a 0.5 mg/mL solution of ascorbic acid to the formulation which resulted in stabilization of the tracer for up to 4 hours at room temperature (Figure 4.9).

With the stability of **11b** resolved, the probe can be evaluated in various *in vivo* preclinical tumour or ROS models. This radiotracer can be contrasted with the previously established probe described in Chapter 2 and compared to the biodistribution of its oxidized form to determine the *in vivo* stability. These biological studies are essential in determining whether the chain length has an effect on the overall biodistribution.

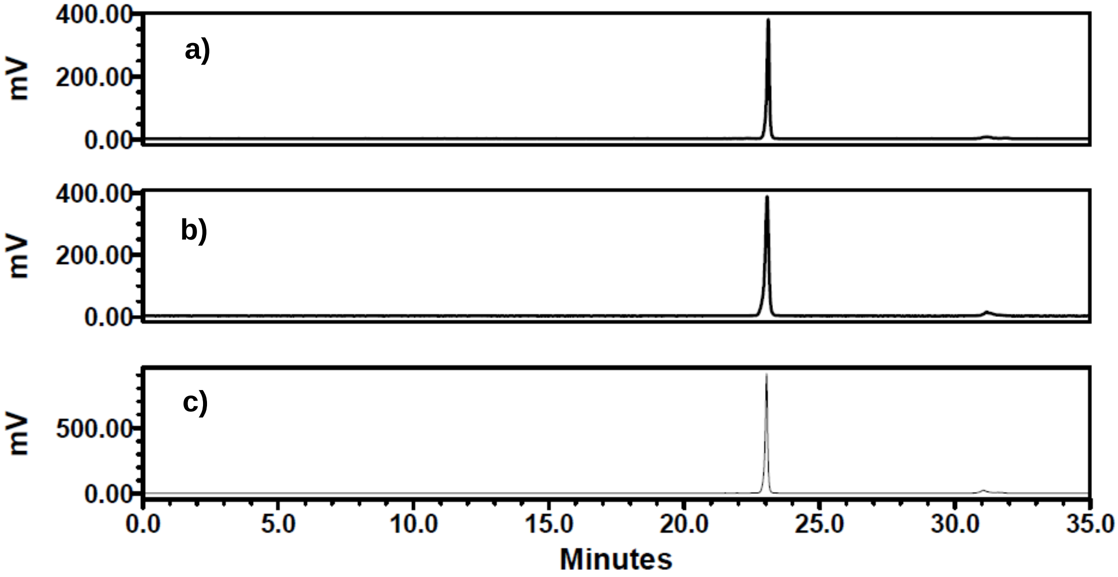

Figure 4.9 γ-HPLC chromatograms following the incubation of **11b** in 10% ethanol/saline in the presence of ascorbic acid (0.5 mg/mL) a) initial injection b) 2 hours c) 4 hours.

4.4 Synthesis, Characterization and Biological evaluation of a Fluorinated Analogue of IR780

4.4.1 Synthesis and Reaction Optimization

As previously discussed, fluorinated dyes are often associated with favourable photochemical properties but accessibility of these probes is limited due to synthetic challenges associated with many fluorination reactions. A nucleophilic fluorination strategy is desirable due to its potential application in ^{18}F PET chemistry. Cyanine dyes bearing a *meso* chlorine functionality have been shown to undergo reactions with nucleophiles as a result of the delocalization of electrons on the backbone of the molecule, leading to an electron-deficient π- system.[18,19] There is considerable debate over the exact mechanism of nucleophilic displacement and it is thought that cyanine dyes undergo these transformations *via* one of two mechanisms.[20] The first mechanism is an addition-elimination mechanism facilitated by the cationic charge on the molecule (Figure 4.10a). The second possible mechanism involves a $S_{NR}1$ pathway whereby a single electron transfer (SET) is initiated by the nucleophile (Figure 4.10b, equation 1). This process involved dissociation of R-Cl to the radical cation $R^{\cdot+}$ (equation 2) and reaction of this species with the nucleophile (Nu) generates a radical intermediate (equation 3). This intermediate behaves as an electron donor for the propagation process (equation 4).

Displacement of the chloride to synthesize a fluorinated analogue is expected to be particularly challenging due to the poor nucleophilicity of the fluoride anion. Additionally, as expected with typical halogen exchange (HALEX) reactions, harsh conditions such as elevated temperatures and long reactions times are often required.[21] This poses a challenge for application to cyanine dyes as prolonged heating has been known to promote decomposition products.[19] Accordingly, fluorination *via* transition metal catalysis may aid in decreasing reaction times and/or temperatures.

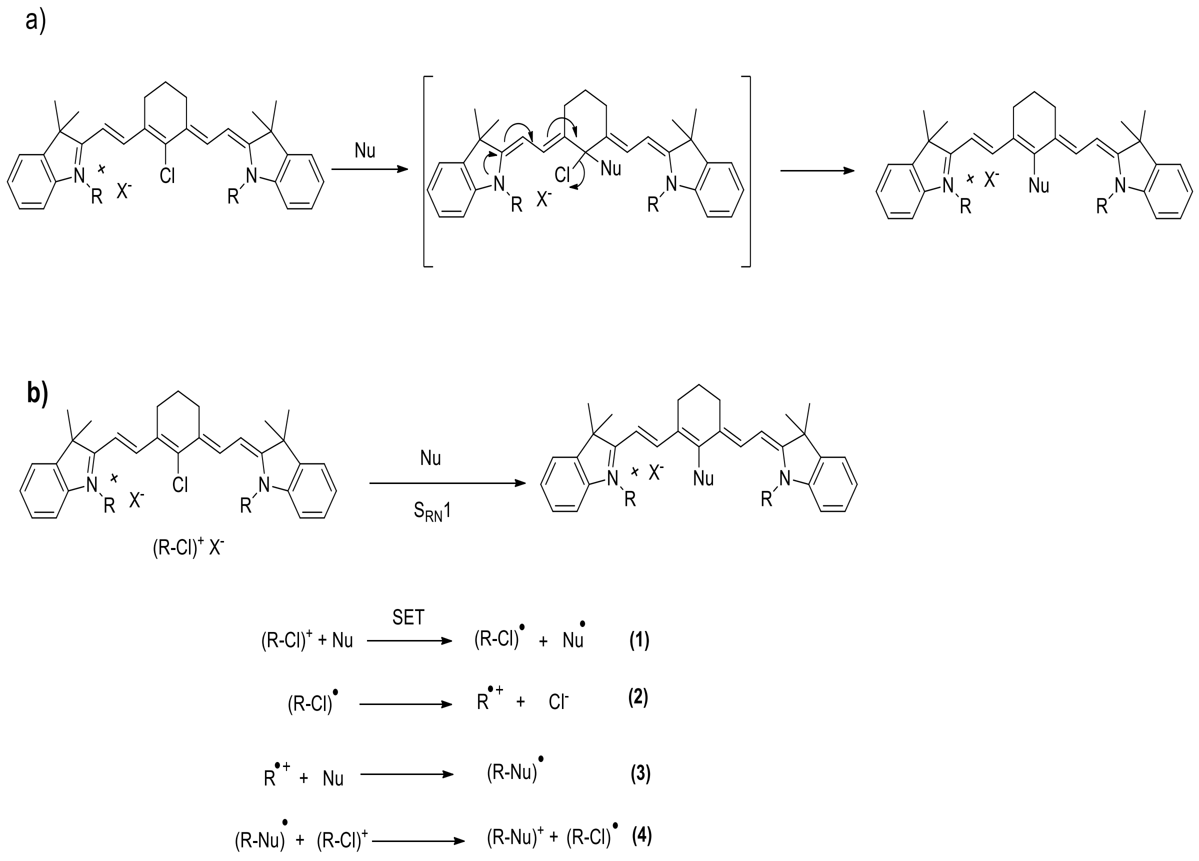

Figure 4.10 Proposed mechanisms for nucleophilic substitution at the center of *meso* chlorinated cyanine dyes a) addition-elimination reaction b) single electron transfer (SET) mechanism.

There has been a great interest in the use of transition metal catalysis (such as copper[22] and palladium[23]) for the conversion of aryl/vinyl (pseudo) halides to their corresponding fluorinated products. Initially, the fluorination of IR780 was attempted under standard conditions in the absence of transition metal catalysts using DMSO as the solvent and KF as the fluoride source (Table 4.1, entries 1,2, 4,5). These reactions resulted in poor yields, recovery of starting material or the formation of a byproduct.

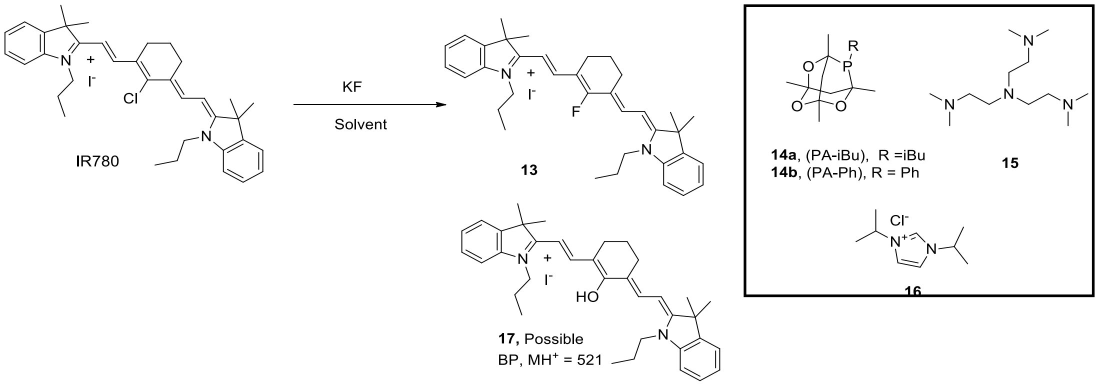

Entry	Temperature (^{o}C)	Base	Solvent	Catalyst/additive	Yield (%)
1	150	K_2CO_3	DMSO	18-crown-6	-
2	150	K_3PO_4	DMSO	18-crown-6	5%
3	150	-	DMSO	18-crown-6, CuI	30%
4	150	K_2CO_3	DMSO	K_{222}	2%
5	150	K_3PO_4	DMSO	K_{222}	11%
6	150	-	DMSO	18-crown 6, $Cu(OTf)_2$	54%
7	80	-	DMSO	18-crown-6, CuI	12%
8	80	CsF	DMSO	18-crown-6, CuI	NR
9	80	CsF	CH_3CN	18-crown-6, CuI	NR
10	80	CsF	t-BuOH	-	NR
11	150	K_2CO_3	DMSO	18-crown-6	25%
12	150	K_2CO_3	DMSO	**14a**, CuI	20%
13	150	K_3PO_4	DMSO	CuI	30%
14	150	Cs_2CO_3	DMSO	CuI	BP/NR
15	150	K_3PO_4	DMSO	**14a**, CuI	65%
16	150	K_3PO_4	DMSO	**14b**, CuI	32%
17	150	K_3PO_4	DMSO	**14a**, $Cu(OTf)_2$	68%
18	150	K_3PO_4	DMSO	Cu $(OTf)_2$	16%
19	150	K_3PO_4	DMSO	**16**, CuI	48%
20	150	K_3PO_4	DMSO	**15**, CuI	BP
21	150	K_3PO_4	DMSO	**15**, $Cu(OTf)_2$	BP
22	150	K_3PO_4	DMSO	$Pd(OAc)_2$, *t*-BuXPhos	BP

Table 4.1 HALEX conditions for the fluorination of IR780. BP= by-product; NR = no reaction.

Interestingly, the use of phase transfer catalysts in the absence of additional base and in the presence of copper (I) resulted in higher yields (entry 3).

Similarly, the addition of stoichiometric additives commonly employed in nucleophilic fluorination reactions such as t-BuOH[24] (entry 10) and TBAF[25] (not shown) resulted in no conversions. The latter may be due to catalyst poisoning brought about by the iodide counterion.[25] The reaction required a minimum of 140°C for it proceed which is typical of HALEX reactions.[26] The addition of base increased the yields, where K_3PO_4 afforded greater yields than K_2CO_3 (entry 4 and 5). This finding is in agreement with a previous report.[23b] Interestingly, employing Cs_2CO_3 resulted in either no reaction or the generation of a byproduct (entry 13 versus entry 14). The choice of the base has been reported to be important in stabilizing the catalyst complex.[23b]

CsF as both the source of fluoride and the base showed no conversion to the product (entries 8 and 9). As an alternative KF was used as the fluoride source because it is inexpensive and less hygroscopic than other fluoride sources, which adds to the practicality of the reaction.[23b] Unlike the fluorination of alkyl triflates reported by Lalic, the use of dried KF was not necessary for this reaction to occur.[22d] However, due to the hygroscopic nature of the solvent (DMSO) it is thought that the identity of the byproduct may be **17**. A peak in the MS spectrum of the crude reaction mixture (521) corresponds to the molecular weight of structure **17**.

The use of palladium catalysts in combination with bulky, phosphine ligands has been explored for fluorination of aryl/vinyl (pseudo) halides.[23] Buchwald has shown through mechanistic studies that the use of the bulky phosphine monodendate ligands facilitates C-F reductive elimination reactions which are known to be the rate determining step in these type of cross-coupling transformations.[23a,23b,23d] Furthermore, the use of such ligands suppresses the favourable formation of the P-F bond. For this reason, fluorination was attempted using Pd catalysts in combination with monodendate phosphine ligands (for example, entry 22). This resulted in the formation of what is believed to be **17**. The results suggest that with this catalyst system hydroxylation is preferential over the desired fluorination (see below for further details).

Conversions to **13** were more successful with copper catalysis. No significant difference in yields were observed in employing Cu (I) versus Cu (II) catalysts (entries 15 and 17). This is contrary to findings reported by Lu *et al.*, where they noted a remarkable difference in Cu (I) and Cu (II) catalysts in hydroxyl-trifluoromethylation reactions.[27] The use of copper catalysts in combination with N-heterocylic carbenes (NHC) has been successful in high yielding fluorination of alkyl triflates using KF as the fluoride source under mild conditions.[22d] We used NHC source **16** in combination with CuI where the reaction afforded **13** in a 48% yield (entry 19). Reducing temperatures resulted in no conversions (data not shown). Interestingly, the use of the diamine ligand **15**, known to form strong and stable Cu complexes[28], resulted in poor yields of the fluorinated product (entry 20 and 21). This may suggest that this reaction does not proceed in a typical cross-coupling type mechanism, where the stabilization of a Cu (III) complex is necessary for the catalytic cycle.[29] Dang *et al.* have suggested that the use of a copper complex may promote a phase transfer catalysis in the organic solvent and thus improve the nucleophilicity of the fluoride.[22d] In their study, the use of TEMPO as a radical scavenger ruled out the possibility of a radical mechanism reaction.

Although phosphine ligands are more commonly employed with Pd catalysts, previous employment of Cu-monodendate phosphine complexes (including those derived from PA) have been successful in performing various transformations[27,30] including 1,4 hydroxytrifluoro methylations.[27] This reaction like the one described here is also dependent on the base used (entry 12 and entry 15).

It is important to note that the use of a ligand is not absolutely necessary to achieve the desired transformation (entry 13), but does improve yields. Mechanistic studies on allylic/vinylic fluorinations suggest that the metal binds to the alkyl ligand generating an intermediate much like that observed in the Heck-Mizoroki reaction.[31] Copper is known to form stable complexes with alkenes.[29,31] Therefore, it is plausible that one or more of the vinyl groups present on IR780 may participate in copper complexation, facilitating the formation of the C-F bond. The proposed mechanism involves Cu ligation to the alkene to form a Cu (III) intermediate **18** where halide exchange can take place. This is then followed by nucleophilic attack and subsequent β-elimination (Figure 4.11). This mechanism relies on the ability of the metal to ligate to the alkene which would significantly weaken the alkyl bond and facilitate the reaction by decreasing the demanding energy barrier. This may further explain why reactions with strongly binding ligand **15** preferred the formation of the byproduct (**17**) which could have prevented metal-ligation to the alkene.

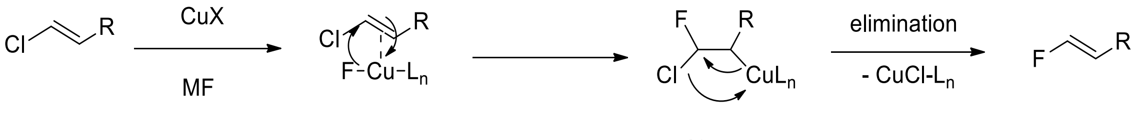

18

19

Figure 4.11 Proposed mechanism for copper catalyzed fluorination of IR780 *via* Cu (III) intermediate **19**.

The optimal reaction conditions required stoichiometric amounts of copper catalyst, equal equivalents of base and 0.5 eq of the PA ligand (see Appendix 2 for supporting characterization of this compound). Potassium fluoride was used in 10-fold excess and the reaction was complete within 30 minutes of heating at 150^{o}C. Decreasing temperatures below 140^{o}C resulted in no reaction. Reactions left overnight at 80^{o}C also resulted in the formation of **17**. Preliminary investigations on substrate scope demonstrate that this reaction can be translated to other cyanine dyes, such as IR783 and IR775 as determined by HRMS. However, isolation of the desired products are complicated by the presence of byproducts or starting materials which often coelute with the product and thus complete characterization of these particular dyes is still required.

4.4.2 Optical properties and Biological evaluation

The optical properties of **13** were assessed at a concentration of 40 µM and compared to IR780 iodide under similar conditions. The absorption and emission maxima observed for **13** exhibited a hypsochromic shift by 20 and 26 nm respectively. Such hypsochromic shifts have been observed for previously synthesized fluorinated dyes.[8,32] Absorbance shifts to lower wavelengths often result in the formation of photostable probes and ones that are less prone to photodegradation.[32] The emission profile of **13** also demonstrated a 4-fold increase in fluorescence intensity as compared to IR780 (Figure 4.12).

ROS probe hydro-IR780 has been shown to increase sensitivity of commercial HRP ELISA assays by two orders of magnitude.[33] To further assess whether the sensitivity of **13** was translatable *in vitro*, IR780 and **13** were reduced to synthesize the corresponding hydrocyanines which were then evaluated in a PC-3 cell assay (Scheme 4.4).

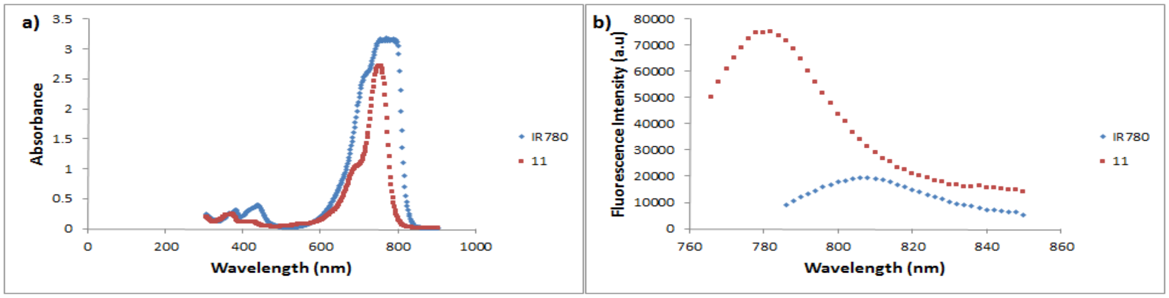

Figure 4.12 Absorbance and emission profiles of IR780 iodide (λ_{ex} = 776 nm, λ_{em} = 808 nm) and **11** (λ_{ex} = 756 nm, λ_{em} = 782 nm) at a concentration of 40 µM in acetonitrile a) absorbance spectrum b) emission spectrum.

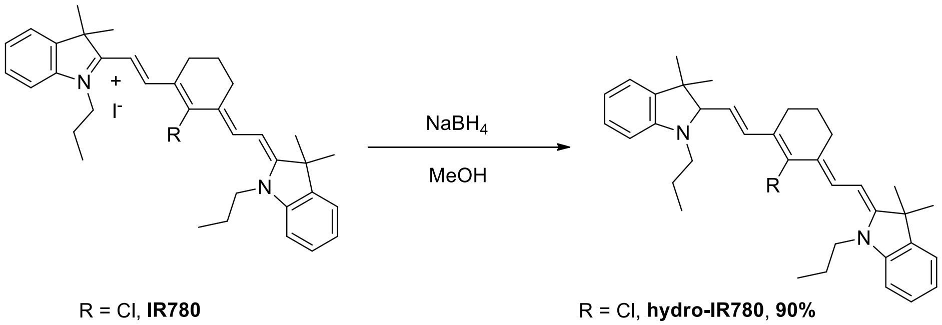

R = Cl, **IR780**
R = F, **13**

R = Cl, **hydro-IR780**, **90%**
R = F, **20, 82%**

Scheme 4.4 Sodium borohydride reduction of cyanine dyes to afford hydrocyanines hydro-IR780 and **20**.

Compound **20** and hydro-IR780 were incubated with PC-3 cells at concentrations of 100, 150 and 200 μM for 120 minutes after which the fluorescence was measured (Figure 4.13). At each concentration, **20** showed a 2-2.5 fold increase in fluorescence intensity when incubated with PC-3 cells as compared to hydro-IR780 ($p < 0.001$).

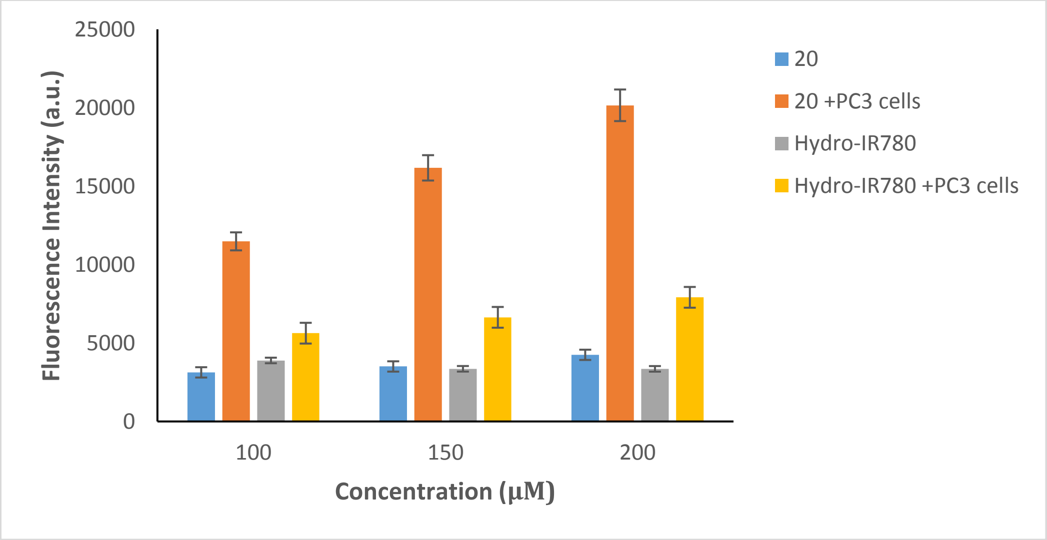

Figure 4.13 PC-3 cell assay study: fluorescence response of **20** and hydro-IR780 after a 120 minute incubation period with PC-3 cells ($p < 0.001$).

Turn-on ratios (fluorophore incubated with PC-3 cells versus untreated fluorophore) for **18** were between 3.6 and 4-fold where by comparison, hydro-IR780 exhibited a 1.4-2.3-fold increase at all concentrations tested. The enhanced fluorescence response implies that lower concentrations of the probe **18** can be used to assess ROS activity *in vitro and in vivo*.

4.4.3 Attempted radiolabeling of IR780 iodide

Copper-assisted ^{18}F labelings have been successfully performed on aryl iodides[34] (*via* formation of ^{18}F trifluoromethylated products), aryl iodonium salts[35] and aryl boronic esters.[36] These reactions, as the one described, are highly dependent on the substrate used. We attempted the labeling using 5 mg (0.007 mmol) of IR780 iodide. After azeotropic drying, 1mg of CuI was added to the vial followed by the addition of the dye in dry DMSO and the reaction was heated to 160^{o}C for 4 minutes.

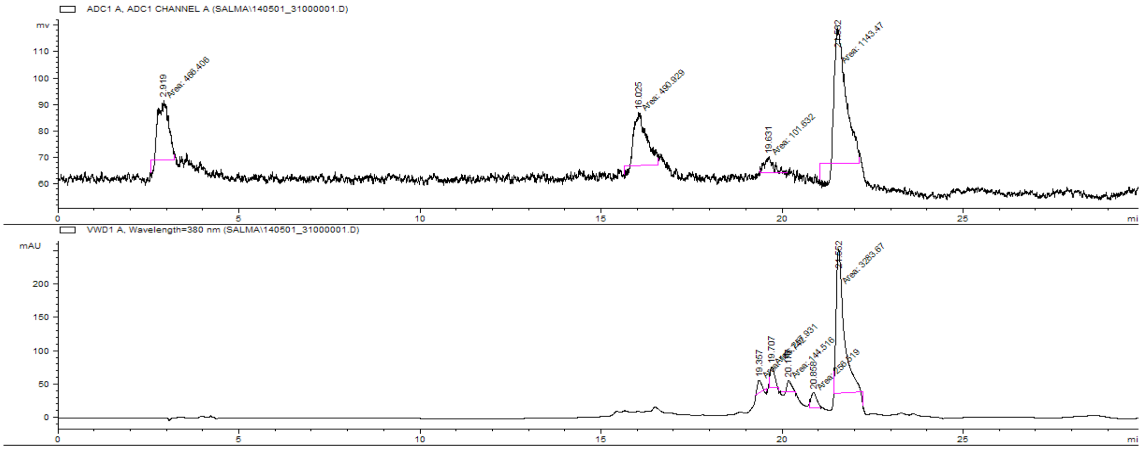

Figure 4.14 Crude HPLC chromatograms: UV trace (bottom) and γ-trace (top) revealing peak that corresponds to the retention time of **13**.

The crude chromatogram showed the appearance of a radioactive peak at 22 minutes corresponding to the retention time of IR780 iodide and the desired product **13**. The reaction however, was very difficult to reproduce, after multiple attempts and variable reaction conditions.

4.5 Summary and Conclusions

This chapter describes the synthesis of fluorine containing cyanine dyes. The main aim was to develop a synthetic platform that would allow access to fluorescent probes, with the ultimate goal of developing ^{18}F labeled multi-modal probes. The synthesis of structural analogues of the probe described in Chapter 2 was established, including one example which possessed a shorter N-alkyl chain. This analogue was successfully radiolabeled and stability studies demonstrated this probe was stable in solution at 4 hours in the presence of a formulation containing ascorbic acid. These probes also retained emission wavelengths in the NIR. Further, a fluorinated analogue of IR780 was successfully developed *via* an optimized transition-metal catalyzed HALEX reaction. Although the radiolabeling of this probe was not reproducible, the corresponding reduced ROS probe showed enhanced fluorescence both in solution and in a PC-3 cell assay in comparison to hydro-IR780. The sensitivity of this probe is a favourable trait and can be advantageous during *in vitro* and *in vivo* studies.

4.6 Experimental

Supplementary figures can be found in **APPENDIX 2**

Synthesis of 7

IR783 (29 mg, 0.04 mmol), 6-fluoropyridin-3-ylboronic acid (7.0 mg, 0.05 mmol), $Pd(OAc)_2$ (1.0 mg, 10 mol%) and *t*-BuXPhos (3.0 mg, 20 mol%), were added to a vial equipped with a Teflon® cap and purged under argon for 2 minutes. The contents of the vial were suspended in ethanol (1 mL) and argon bubbled through the solution for 5 min using a long needle. K_3PO_4 (aq) (0.5 mL, 0.2 mM) was added under argon and the vial sealed, covered with aluminum foil and heated at 100^{o}C overnight. The reaction vessel was cooled and the reaction mixture diluted with water (2 mL) and directly loaded onto a RediSep® Rf 18C reverse phase column (using 30% water in acetonitrile as the eluent) to afford **5** as a green solid (19 mg, 61%). ^{1}H NMR (700 MHz, MeOH-d4) δ 8.12 (d, *J* = 2.2 Hz, 1H), 7.90 (td, J_1 = 7.9 Hz, J_2 = 2.3 Hz, 1 H), 7.38 (m, 5H), 7.30 (d, *J* = 7.8 Hz, 2H), 7.19 (t, *J* = 7.4 Hz, 2H), 7.14 (d, *J* = 13.9 Hz, 2H), 6.29 (d, *J* = 13.9 Hz, 2H), 4.15 (t, *J* = 7.1 Hz, 4H), 2.87 (t, *J* = 7.3 Hz, 4 H), 2.78 (t, *J* = 6.1 Hz, 4H), 2.07 (m, 2H), 1.96 (m, 4H), 1.91 (m, 4H), 1.26 (s, 12H). 13C NMR (175 MHz, MeOH-d4) δ 173.5, 164.9 (*J* = 241.1 Hz), 157.2, 149.1 (*J* = 14.1 Hz), 148.4, 145.0 (*J* = 7.8 Hz), 142.8 (*J* = 250.1 Hz), 134.6 (*J* = 4.2 Hz), 133.7, 129.9, 126.2, 123.4, 112.1, 110.1 (*J* = 37.3 Hz), 101.2, 51.8, 50.0, 44.8, 28.0, 27.9, 27.2, 25.8, 23.6, 22.4 HRMS (ESI+) for $C_{43}H_{49}FN_3O_6S_2$ calcd. 786.3047 Obsd: 786.3030

Synthesis of 9a

IR775 chloride (20 mg, 0.04 mmol), 6-fluoropyridin-3-ylboronic acid (7.0 mg, 0.05 mmol), Pd(OAc)$_2$ (1.0 mg, 10 mol%) and *t*-BuXPhos (3.0 mg, 20 mol%), were added to a vial equipped with a Teflon® cap and purged under argon for 2 minutes. The contents of the vial were suspended in ethanol (1 mL) and argon bubbled through the solution for 5 min using a long needle. K_3PO_4 (aq) (0.5 mL, 0.2 mM) was added under argon and the vial sealed, covered with aluminum foil and heated at 100^{o}C overnight. The reaction vessel was cooled and the reaction mixture diluted with water (10 mL) and extracted with DCM (2 × 10 mL). The organic phases were combined, dried over anhydrous $MgSO_4$ and concentrated *in vacuo*. The desired product was isolated using a 8 gram flash RediSep® Rf basic alumina column (using 10% MeOH in DCM as the eluent) to afford **2** as a green solid (17 mg, 73%) ^{1}H NMR (600 MHz, MeOH-d4) δ 8.11 (s, 1H), 7.89 (td, J_1 = 7.9 Hz, J_2 = 2.5 Hz), 7.39 (m, 5H), 7.26 (d, *J* = 7.9 Hz, 2H), 7.21 (td, J_1 = 7.5 Hz, J_2 = 0.7 Hz, 2H), 7.15 (d, *J* = 14.0 Hz, 2H), 6.23 (d, *J* = 14.0 Hz, 2H), 3.60 (s, 6H), 2.77 (t, *J* = 6.2 Hz, 4H), 2.07 (m, 2H), 2.01 (s, 1H), 1.72 (d, *J* = 8.1 Hz, 1H), 1.27 (s, 12 H). ^{13}C NMR (150 MHz, MeOH-d4) δ 174.2, 164.9 (*J* = 241.2 Hz), 157.1, 149.1 (*J* = 14.1 Hz), 148.3, 144.9 (*J* = 7.8 Hz), 143.2 (*J* = 329.9 Hz), 134.5 (*J* = 3.6 Hz), 133.3, 129.8, 126.2, 123.3, 111.8, 110.1 (*J* = 37.2 Hz), 101.6, 31.6, 27.9, 27.7 25.8, 22.3. HRMS (ESI+) for $C_{37}H_{39}FN_3$ calcd. 544.3128 Obsd: 544.3141.

Synthesis of 10

IR775 chloride (20 mg, 0.04 mmol), 2-nitro-5-pyridineboronic acid pinacol ester (12 mg, 0.05 mmol), $Pd(OAc)_2$ (1.0 mg, 10 mol %) and *t*-BuXPhos (3.0 mg, 20 mol %) were added to a vial equipped with a Teflon® cap and purged under argon for 2 min. The contents of the vial were suspended in absolute ethanol (1 mL) and argon bubbled through the solution for 5 min using a long needle. K_3PO_4 (aq) (0.5 mL, 0.2 mM) was added under argon and the vial sealed, covered with aluminum foil and heated at 100^{o}C overnight. The reaction vessel was cooled and the reaction mixture diluted with water (10 mL) and extracted with DCM (2 × 10 mL). The organic phases were combined, dried over anhydrous $MgSO_4$ and concentrated *in vacuo*. The product was isolated using a 8 gram flash RediSep® Rf basic alumina column (using 20% MeOH in DCM as the eluent) to afford **4** as a green solid (14 mg, 57%). ^{1}H NMR (600 MHz, MeOH-d4) δ 8.61 (d, *J* = 8.1 Hz, 1H), 8.57 (d, *J* = 2.1 Hz, 1H), 8.20 (dd, *J* = 8.1 Hz, 1H), 7.37 (d, *J* = 7.4 Hz, 4H), 7.26 (d, *J* = 7.8 Hz, 2H), 7.21 (m, 2H), 6.99 (d, *J* = 14.0 Hz, 2H), 6.26 (d, *J* = 14.0 Hz, 2H), 3.61 (s, 6H), 2.79 (t, *J* = 6.21 Hz, 4H), 2.10 (m, 2H), 1.22 (d, *J* = 5.9 Hz, 12H). ^{13}C NMR (150 MHz, MeOH-d4) δ 174.3, 157.9, 155.3, 150.6, 147.8, 144.2, 143.5, 143.1, 142.1, 133.2, 129.8, 126.4, 123.3, 119.2, 111.9, 101.9, 31.6, 27.8, 27.7, 25.8, 22.3. HRMS (ESI+) for $C_{37}H_{39}N_4O_2$ calcd. 571.3073 Obsd: 571.3080.

Reduction of **9a** was performed in accordance with the method used for the ROS probe described in chapter 2. Briefly, compound **9a** (9 mg, 0.016 mmol) was dissolved in MeOH (2 mL) in a 30 mL scintillation vial covered with aluminum foil. Freshly prepared $NaBH_4$ in MeOH (1 mL, 0.16 mM) was added dropwise to the green solution, generating a yellow solution. The reaction was stirred at room temperature (RT) for 10 min and the solvent was removed by rotary evaporation. The resulting solid was dissolved in DCM (3 mL) and extracted with water (2 × 3 mL). The organic phase was dried over anhydrous $MgSO_4$ and the solvent was removed by rotary evaporation to afford a bright yellow solid.

Spectroscopic studies

Fluorescence measurements were obtained using a Tecan® infinity M1000 plate reader. Briefly, the dyes were suspended in MeOH or CH_3CN to make a stock solution of known concentration which was used to make up a 40 μM solution. 150 μL of the solution were deposited into a 96-well plate which were used for excitation/emission readings. These values were subtracted from an equal volume of the blank (pure solvent).

Radiolabeling Procedure

Compound **10** (4.2 mg, 0.007 mmol) was dissolved in 400 μL of MeOH, and 200 μL of a freshly prepared 0.03 mM sodium borohydride solution in MeOH was added slowly. An instant colour change from green to yellow was observed. The reaction was stirred at RT for 30 s after which it was extracted with DCM (2 × 10 mL). The organic phase was dried over anhydrous $MgSO_4$ and the solvent was removed by rotary evaporation to afford the reduced product as a yellow-brown solid (3.1 mg). A solution of K [^{18}F] F-K_{222} complex (0.92 GBq) was transferred to a 5 mL pyrex® reaction vial and dried at 85^{o}C in an oil bath under a stream of nitrogen. Azeotropic drying by the addition of 1 mL portions of CH_3CN was performed over a 20-minute period (total of 6 mL). The reduced precursor was dissolved in 400 µL of dry DMF and added to the $^{18}F/K_{222}$ mixture which was subsequently heated at 150^{o}C for 4 minutes. After cooling to RT the desired product was isolated by semi-preparative HPLC (decay corrected RCY = 62% ± 5, *n* = 3).

Stability profile of 11b

Compound **11b** (19.98 MBq) was suspended in 600 µL of 10% ethanol/saline and incubated at RT. The solution was analyzed immediately after formulation by reverse-phase HPLC (95%water/CH_3CN gradient).

Stability was also asessed in the presence of ascorbic acid. Compound **11b** (21.98 MBq) was suspended in 500 µL of 10% ethanol/saline. To this was added 100 µL of a 0.5 mg/mL aqueous solution of ascorbic acid. The mixture was left to incubate at RT and the solution was analyzed by reverse-phase HPLC at 2 and 4 hours.

Synthesis of 13

IR780 (25 mg, 0.04 mmol), KF (23 mg, 0.4 mmol), $Cu(OTf)_2$ (14 mg, 0.04 mmol), **12a** (2mg, 0.0007 mmol) and K_3PO_4 (8.5 mg, 0.04 mmol) were added to a vial equipped with a Teflon® cap and purged under argon for 2 minutes. The contents of the vial were suspended in DMSO (600 µL) and the vial was sealed and heated to 150^{o}C for 30 minutes. The reaction vessel was cooled and the mixture was diluted with water (10 mL) and extracted with DCM (2 × 10 mL). The organic phases were combined, dried over anhydrous $MgSO_4$ and concentrated *in vacuo*.

The desired product was isolated using a 8 gram flash RediSep® Rf basic alumina column (using 3% MeOH in DCM as the eluent) to afford **11** as a blue-green solid (17 mg, 68%). ^{1}H NMR (600 MHz, CD_2Cl_2) δ 8.05 (d, *J* = 14.2 Hz, 2H), 7.37 (m, 4H), 7.24 (t, *J* = 7.4 HZ, 2H), 7.11 (d, *J* = 8.0 Hz, 2H), 6.05 (d, *J* = 14.2 Hz, 2H), 4.07 (t, *J* = 7.2 Hz, 4H), 1.97 (m, 2H), 1.89 (q, J_1 = 7.4 Hz, J_2 = 7.4 Hz, 4H), 1.67 (s, 12H), 1.24 (m, 2H), 1.07 (t, *J* = 7.4 Hz, 6H) ^{13}C NMR (150 MHz, MeOH-d4) δ 172.2, 142.5, 141.0, 140.1 (J = 12.3 Hz), 128.9, 125.3, 122.3, 116.9, 110.9, 100.0, 49.4, 46.3, 41.2, 28.3, 24.6, 21.0, 11.9 HRMS (ESI+) for $C_{36}H_{44}N_2F$ calcd. 523.3489 Obsd: 523.3503.

PC-3 cell assay

The PC-3 cell line purchased from ATCC (CRL-1435). Cells were propagated using Ham's F-12 Nutrient Mix supplemented with 10% fetal bovine serum (FBS) and 1% Penicillin Streptomycin at 37˚C and 5% CO_2 and were not used beyond passage 30. Hydro IR780 and **20** were prepared in DMSO to a concentration of 5 mM immediately before use. PC-3 cells (8.5×10^4 cells/well) were loaded on a 96 well plate and allowed to attach overnight. Growth media was removed and cells were washed twice with 0.2mL of PBS. 0.2mL of 0 µM, 100 µM, 150 µM and 200 µM of TA in 20.5mM HEPES pH 7.5 was loaded onto the cells including no cell and vehicle only controls. The plate was incubated for 2h at 37˚C and 5% CO_2. Fluorescence was measured (λ_{ex} / λ_{em} = 756 nm/782 nm for **20**, λ_{ex} / λ_{em} = 768 nm/ 794 nm for hydro-IR780) using a Tecan Infinite M1000. Cells were lysed with 0.05mL of 1% Triton X-100 and incubated at 37˚C for 30min with gentle shaking.

A sample from each well was collected and the amount of protein was determined using the Pierce BCA Protein Assay Kit in order to normalize each sample by µg of protein.

4.7 References

1. a) C. A. Lipinski, F. Lombardo, B. W. Dominy, P. J. Feeney, *Adv. Drug Deliv., Rev.,* **1997**, *23*, 3–25. b) P. D. Leeson, B. Springthorpe, *Nat. Rev. Drug Discov.,* **2007**, *6*, 881–890.
2. M. S. Alavijeh, M. Chishty, M. Z. Qaiser, A. M. Palmer, *NeuroRx,* **2005**, *2*, 554–571.
3. P.G. Barash, B.F. Cullen, R.F. Stoelting, M. Cahalan, C. Stock, R. Ortega, *Clinical Anesthetia*, sixth edition., Lippincott Williams & Wilkins, 2013.
4. G. S. Sundaram, D. Dhavale, J. L. Prior, J. Sivapackiam, R. Laforest, P. Kotzbauer, V. Sharma, *EJNMMI Res.,* **2015**, *5*, 33, 1-13.
5. D. M. Lemal, *J. Org. Chem.,* **2004**, *69*, 1-11.
6. B.E. Smart, *Molecular Structure and Energetics*; Liebman,J. F., Greenberg, A., Eds.; VCH Publishers: Deerfield Beach, FL, 1986.
7. a) L. F. Mottram, S. Boonyarattanakalin, R. E. Kovel, B. R. Peterson, *Org. Lett.,* **2006**, *8*, 581–584. b) Y. Urano, M. Kamiya, K. Kanda, T. Ueno, K. Hirose, T. Nagano, *J. Am. Chem. Soc.,* **2005**, *127*, 4888–4894.c) C. C. Spagnuolo, W. Massad, S. Miskoski, G. O. Menendez, N. A. García, E. A. Jares-Erijman, *Photochem. Photobiol.,* **2009**, *85*, 1082–1088. d) J. Liu, Z.

Diwu, *Bioorg. Med. Chem. Lett.,* **2001**, *11*, 2903–2905. e) Z. R. Woydziak, L. Fu, B. R. Peterson, *J. Org. Chem.,* **2012**, *77*, 473–481.

8. F. Würthner, P. Osswald, R. Schmidt, T. E. Kaiser, H. Mansikkamäki, M. Könemann, *Org. Lett.,* **2006**, *8*, 3765–3768.
9. a) X. Chen, X. Peng, A. Cui, B. Wang, L. Wang, R. Zhang, *J. Photochem. Photobiol. A Chem.,* **2006**, *181*, 79–85. b) B. R. Renikuntla, H. C. Rose, J. Eldo, A. S. Waggoner, B. A. Armitage, *Org. Lett.,* **2004**, *6*, 909–912.
10. T. Priem, C. Bouteiller, D. Camporese, X. Brune, J. Hardouin, A. Romieu, P.-Y. Renard, *Org. Biomol. Chem.,* **2013**, *11*, 469–479.
11. R. Ting, T. A. Aguilera, J. L. Crisp, D. J. Hall, W. C. Eckelman, D. R. Vera, R. Y. Tsien, *Bioconjug. Chem.,* **2010**, *21*, 1811–1819.
12. a) S. Onoe, T. Temma, Y. Shimizu, M. Ono, H. Saji, *Cancer Med.,* **2014**, *3*, 775–786. b) C. Zhang, T. Liu, Y. Su, S. Luo, Y. Zhu, X. Tan, S. Fan, L. Zhang, Y. Zhou, T. Cheng, C. Shi, *Biomaterials,* **2010**, *31*, 6612–6617. c) X. Tan, S. Luo, D. Wang, Y. Su, T. Cheng, C. Shi, *Biomaterials,* **2012**, *33*, 2230–2239.
13. J. Y. Kim, W. Il Choi, Y. H. Kim, G. Tae, *J. Control. Release,* **2011**, *156*, 398–405.
14. B.C. Dickinson, D. Srikun, C.J. Chang, *Curr. Opin. Chem. Biol*., **2010**, 14, 50-56.
15. a) E. Delaey, F. Laar, A. Vos D, Kamuhabwa, P. Jacobs, P. Witte, *J Photochem Photobiol B.,* **2000**, 55, 27-36. b) J. Kulbacka, a Pola, D.

Mosiadz, A. Choromanska, P. Nowak, M. Kotulska, M. Majkowski, A. Hryniewicz-Jankowska, L. Purzyc, J. Saczko, *Biochem. Biokhimia.,* **2011**, *76*, 473–479.

16. L. Yuan, L., W. Lin, S. Zhao, W. Gao, B. Chen, L. He, S. Zhu, *J. Am. Chem. Soc.,* **2012**, *134*, 13510–13523.
17. H. Kobayashi, M. R. Longmire, M. Ogawa, P. L. Choyke, S. Kawamoto, *Lancet Oncol.,* **2010**, *11*, 589–595.
18. a) T. Gorecki*, G.* Patonay*, L.* Strekowski*, R.* Chin*, N.* Salazar*, J*. *Heterocycl*. *Chem*. ***1996****, 33, 1871*-1876. b) L. Strekowsi, M. Lipowska, G. Patonay, *J. Org. Chem*., **1992**, *57*, 4578-4580.
19. H. Lee, J.C. Mason, S. Achilefu, *J. Org. Chem*., **2006**, *71*, 7862–7865.
20. L. Strekowski, M. Lipowska, G. Patonay, *J. Org. Chem.,* **1992**, *57*, 4578-4580.
21. T. D. Sheppard, *Org. Biomol. Chem.,* **2009**, *7*, 1043–1052.
22. a) P. S. Fier, J. F. Hartwig, *J. Am. Chem. Soc.,* **2012**, *134*, 5524–5527. b) A. Casitas, M. Canta, M. Solà, M. Costas, X. Ribas, *J. Am. Chem. Soc.,* **2011**, *133*, 19386–19392. c) Z. Zhang, F. Wang, X. Mu, P. Chen, G. Liu, *Angew. Chem. Int. Ed.,* **2013**, *52*, 7549–7553. d) H. Dang, M. Mailig, G. Lalic, *Angew. Chem. Int. Ed.,* **2014**, *53*, 6473–6476.
23. a) A. C. Sather, H. G. Lee, V. Y. De La Rosa, Y. Yang, P. Müller, S. L. Buchwald, *J. Am. Chem. Soc.,* **2015**, *137*, 13433-13438. b) H. G. Lee, P. J. Milner, S. L. Buchwald, *J. Am. Chem. Soc.,* **2014**, *136*, 3792–3795. c) M. H.

Katcher, A. Sha, A. G. Doyle, *J. Am. Chem. Soc.,* **2011**, *133*, 15902–15905. d) T. Noël, T. J. Maimone, S. L. Buchwald, *Angew. Chemie Int. Ed.,* **2011**, *50*, 8900–8903.

24. D. W. Kim, H.-J. Jeong, S. T. Lim, M.-H. Sohn, J. a Katzenellenbogen, D. Y. Chi, *J. Org. Chem.,* **2008**, *73*, 957–962.
25. C. L. Liotta, H. P. Harris, *J. Am. Chem. Soc*., **1974**, *96*, 2250 –2252.
26. B. T. Worrell, J. E. Hein, V. V Fokin, *Angew. Chem. Int. Ed.,* **2012**, *51*, 11791–11794.
27. D.F. Lu, C.-L. Zhu, H. Xu, *Chem. Sci.,* **2013**, *4*, 2478-2482.
28. W. Tang, Y. Kwak, W. Braunecker, N. V. Tsarevsky, M. L. Coote, K. Matyjaszewski, *J. Am. Chem. Soc.,* **2008**, *130*, 10702–10713.
29. B. J. Bellott, G. S. Girolami, *Organometallics,* **2009**, *28*, 2046–2052.
30. a) J. Won, D. Noh, J. Yun, J. Y. Lee, *J. Phys. Chem. A,* **2010**, *114*, 12112–12115. b) V. V. Grushin, *Acc. Chem. Res.,* **2010**, *43*, 160–171. c) K. Okuro, M. Furuune, M. Enna, M. Miura, M. Nomura, *J. Org. Chem.,* **1993**, *58*, 4716–4721.
31. D.Steinborn, *Fundamentals of Organometallic Catalysis*; 1st ed.; Wiley-VCH: Weinheim, Germany, 2012.
32. H. Muramatsu, A. Okumura, K. Shibata, M. Matsui, *Chem. Ber*., **1994**, *127*, 1627–1632.
33. A. P. Acharya, P. M. Nafisi, A. Gardner, J. L. Mackay, K. Kundu, S. Kumar, N. Murthy, *Chem. Commun.,* **2013**, *49*, 10379–10381.

34. M. Huiban, M. Tredwell, S. Mizuta, Z. Wan, X. Zhang, T. L. Collier, V. Gouverneur, J. Passchier, *Nat. Chem.,* **2013**, *5*, 941–944.

35. N. Ichiishi, A.F. Brooks, J.J. Topczewski, M.E. Rodnick, M.S. Sanford, P.J. H Scott, *Org. Lett*., **2014**, *16*, 3224-3227.

36. M. Tredwell, S. M. Preshlock, N. J. Taylor, S. Gruber, M. Huiban, J. Passchier, J. Mercier, C. Génicot, V. Gouverneur, *Angew. Chem. Int. Ed.,* **2014**, *53*, 7751–7755.

Chapter 5: Towards the Synthesis and Evaluation of TACE Inhibitors as Potential Molecular Imaging Probes for Rheumatoid Arthritis

5.1 Introduction

TNF-α converting enzyme (TACE or ADAM 17) belongs to a class of enzymes known as ADAM enzymes (A disintegrin and metalloproteinase), which are a close relative of another prominent class of peptidases known as matrix metalloproteases (MMPs). TNF-α converting enzyme is a transmembrane glycoprotein that behaves as a sheddase enzyme and exists as a metalloprotease where zinc is tightly bound by free cysteine residues.[1] The importance of metalloproteases in human physiology and their active involvement in biochemical processes is emphasized by the fact that metalloproteases make up 33% of the proteases encoded by the human genome.[2] Inhibiting over-active TACE can disable proinflammatory effects of TNF-α by inhibiting the process by which *pro*-TNF-α is converted to s- TNF-α. TACE catalyzes this conversion by hydrolyzing the Ala 76 and Val 77 bond, shedding the 17 KDa protein responsible for the proinflammatory cascade of events.[3] TACE has become a very sought after clinical target, as it is responsible for the processing of 90% of TNF-α.[4] The enzyme is also actively involved in processing various ligands such as EGF and β-APP which are directly involved in the development of cancer and Alzheimer's disease respectively, making it an especially significant therapeutic target (Figure 5.1).[5]

The over-expression of the cytokine TNF-α is seen as the chief initiator of the proinflammatory response and has also been linked to many pathological conditions including Crohn's disease[6], ulcerative colitis[6], cancer[7] and Alzheimer's disease.[8] The clinical significance of TNF-α blockage has been shown to dramatically improve patient prognosis in several disease states.[3] One notable example demonstrated that TACE inhibition reverts the breast cancer malignant phenotype in the T4-2 cell line to morphology characteristic of non-malignant cells.[9]

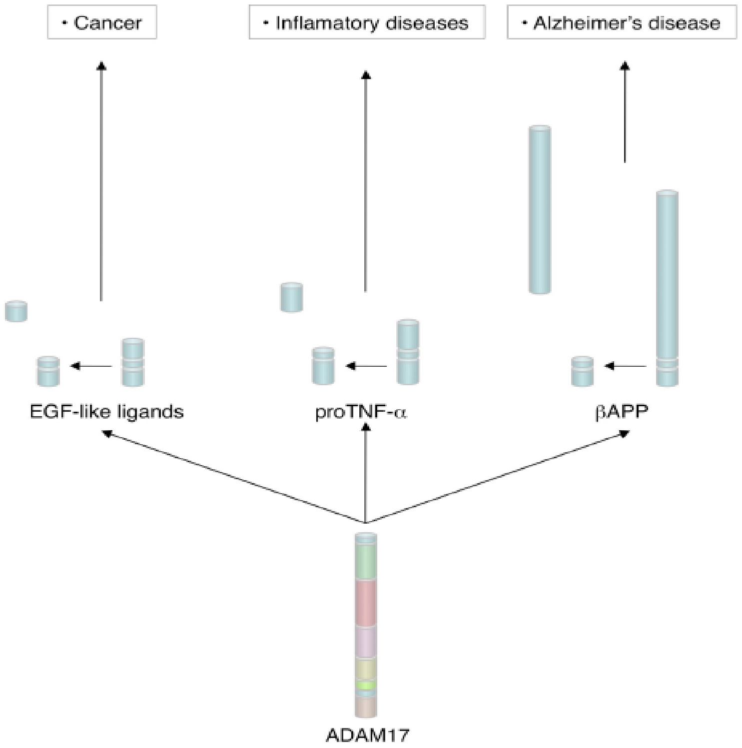

Figure 5.1 Schematic showing the various ligands processed by TACE/ADAM17 and its involvement with multiple disease states.[5]

Currently, TNF-α inhibition has been accomplished by the use of therapeutic biologics such as adalimumab (Humira®). Small-molecule inhibition of TACE resulted in failed clinical trials due to severe musculoskeletal side effects.[10] This is thought to be attributed to the non-selective nature of these drugs which are capable of also inhibiting MMP-1 and/or MMP 14.[11] The inability to achieve selective targeting of TACE is one of the reasons for the lack of availability of these drugs.

5.2 Objectives

In nuclear imaging, toxicity is less often observed due to the low mass dose of the tracer used (nmol to pmol). Molecular imaging of the inflammatory process can provide an early detection and therapeutic monitoring tool that can be used in place of conventional anatomical imaging modalities which can prevent late-stage irreversible bone damage.[12] Recent studies have shown the feasibility of molecularly imaging RA using ^{99m}Tc labeled anti-TNF-α antibodies infliximab[12,13] and adalimumab.[13] The scintigraphic images obtained in these studies have demonstrated the importance of early detection and therapeutic intervention where reversing the molecular events responsible for pathological progression may be feasible. While radiolabeled monoclonal antibodies demonstrate rapid uptake exclusively in diseased tissue, this particular strategy is expensive and generally exhibits poor pharmacokinetics as a result of the relatively large size of the probe.

Radiolabeled analogues of TACE inhibitors may be an effective means for the molecular imaging of RA. TACE has never been used for such a purpose but it is localized and over expressed in the synovium of RA patients.[4] TACE inhibitors[14,15] that were selected as platforms to create new tracers were reported as being highly potent and selective ligands (Figure 5.2). These inhibitors possess hydroxamates/hydroxamic acids, which provide potency by binding zinc in the active site and a quinolone that imparts selectivity towards TACE.[16] Inhibitor **1** is a sulfone-based TACE inhibitor that possesses a prominent reverse hydroxamate functionality, which was reported to be less prone to hydrolysis *in vivo*. TACE inhibitor **2** was pursued as a result of its metabolic stability, its affinity in whole blood assays and fast clearance rate.

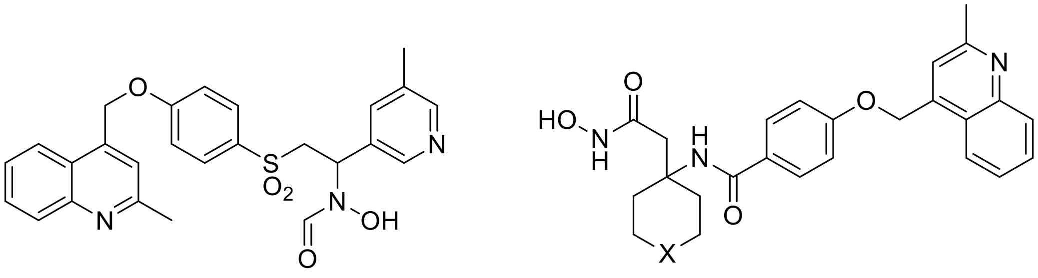

1

2

IC_{50}= 2.8nM

2a: X = O, K_i = 0.35 nM*
2b: X = $-NCH_2CH_2F$, IC_{50} = 2.6 nM*

* in vitro assay performed on pTACE

Figure 5.2 Structures of two selective and high affinity TACE inhibitors being pursued as targeting vectors for probe development.

The goal was to synthesize non-radioactive derivatives of these compounds and to test the analogues in an established TACE assay to ensure structural modifications retain TACE activity. Following successful validation, radiolabeling precursors would be synthesized in order to produce the radiotracer for *in vitro* and *in vivo* screening.

5.3 Synthesis and in vitro validation of TACE inhibitors

Work began by synthesizing inhibitors **1, 2a** and **2b** to validate the *in vitro* testing of the synthesized compounds as well as to provide tractable synthetic methods prior to structural modification of the scaffold. The syntheses of some intermediates were modified from the original reported procedures. The synthesis of **1** began with the construction of the P1' substituent fragment of the inhibitor (Scheme 5.1).

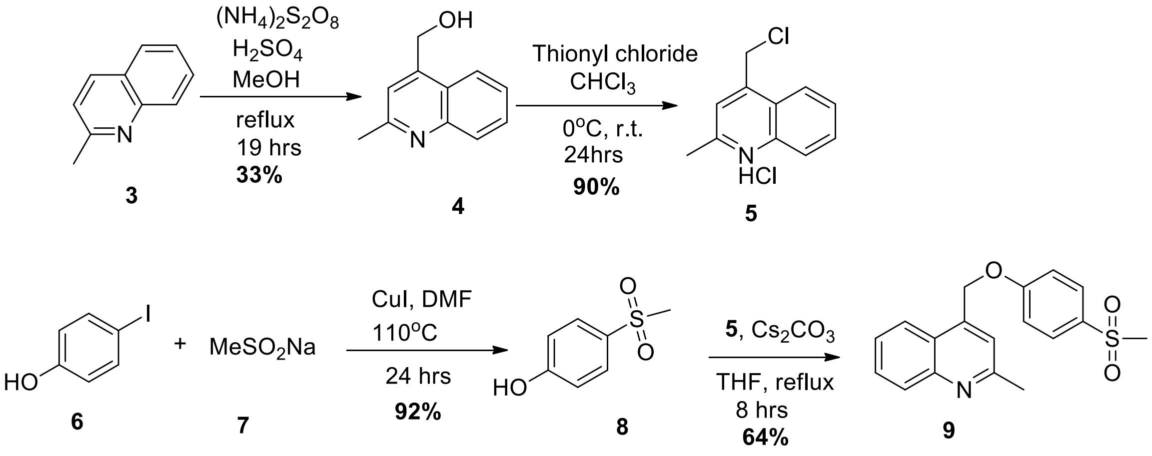

Scheme 5.1 Synthesis of P1' fragment of TACE inhibitor.

Quinalidine **3** underwent alpha-hydroxyalkylation[17] in the presence of ammonium peroxydisulphate to yield 33% of alcohol **4**. Treatment of **4** with thionyl chloride afforded **5** which was coupled to sulfone **8** in the presence of cesium carbonate as the base. Sulfone **8** was synthesized in a 92% yield *via* a nucleophilic copper-assisted displacement[18] reaction with commercially available **7**. Coupling of **5** and **8** in the presence of cesium carbonate afforded **9** in a 64% yield.

Scheme 5.2 displays conditions for the completed synthesis of **1**. Incorporation of the 3-methyl pyridine functionality was accomplished through a Julia coupling[19] with ester **11** derived from commercially available nicotinic acid **10**. The ester was used as the electrophile due to failed attempts or low yields associated with the synthesis using the corresponding aldehyde. Ketone **12** was then reduced using sodium borohydride in methanol and the corresponding alcohol **13** was subsequently dehydrated to give **14** in a 78% yield.

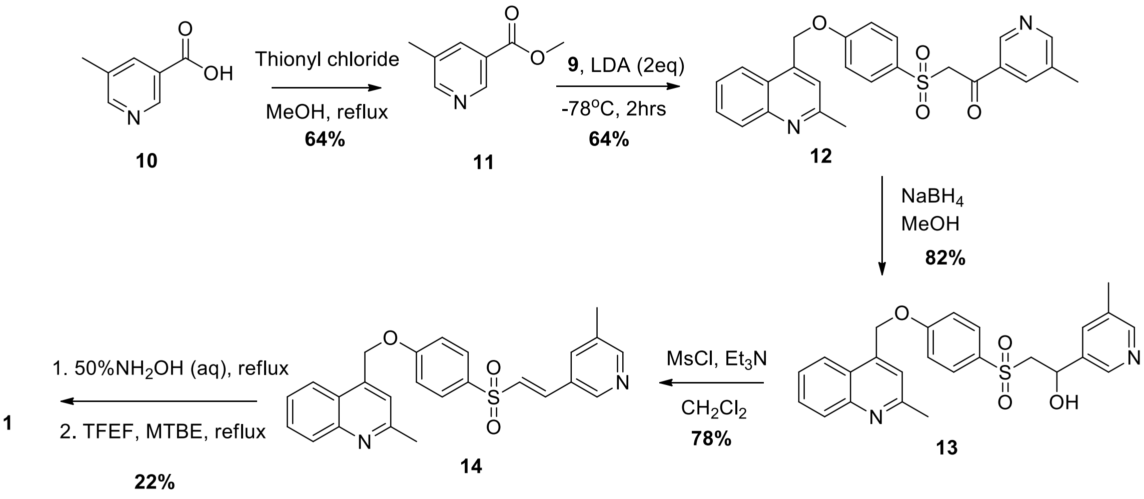

Scheme 5.2 Synthesis of TACE inhibitor **1**.

The synthesis of **1** was then completed in a two-step manner, where **14** was used to produce the hydroxylamine, followed by prompt formylation. Initially, a "mixed-anhydride" method of formylation was attempted but it was found that both the nitrogen and oxygen of the hydroxylamine were formylated. Various attempts at selective formylation failed, including the use of 2,2,2-trifluoroethylformate (TFEF) as the formylating agent.[20] Other routes to **1** were pursued including the synthesis of the oxime *via* ketone **12**, which could be used to directly synthesize the hydroxylamine, but these were unsuccessful (not shown). Similarly, reacting **13** with O,N-Boc protected hydroxylamine in a Mitsunobu reaction failed to afford the corresponding protected hydroxylamine[21] (not shown).

Scaffold **2** was synthesized using the conditions shown in scheme 5.3. Quinoline intermediates **17a/17b** were prepared in a similar manner to that of the previously described **9**. The pyran/piperidine functionality was introduced by initially performing a Horner-Wadsworth-Emmons olefination[22] with commercially available reagents **19a/19b** to afford **20a** and **20b** in a 78 and 57% yield respectively. Conjugate addition of **20a/20b** led to the transesterified amines **21a/21b** which were coupled to **18a/18b** through a PYBOP promoted peptide coupling. Originally, the goal was to synthesize **2** directly from esters **22** where standard conditions[23, 24] called for the presence of a strong base and that the reaction be performed at ambient temperature as reported in the original communication.[15] Performing the reaction under these conditions resulted in only recovery of the starting material and/or the corresponding carboxylic acids (**23a-23d**), with no evidence of the anticipated hydroxamic acids. This led to a microwave assisted approach where the reaction was performed in either basic methanol[25] or aqueous solution.

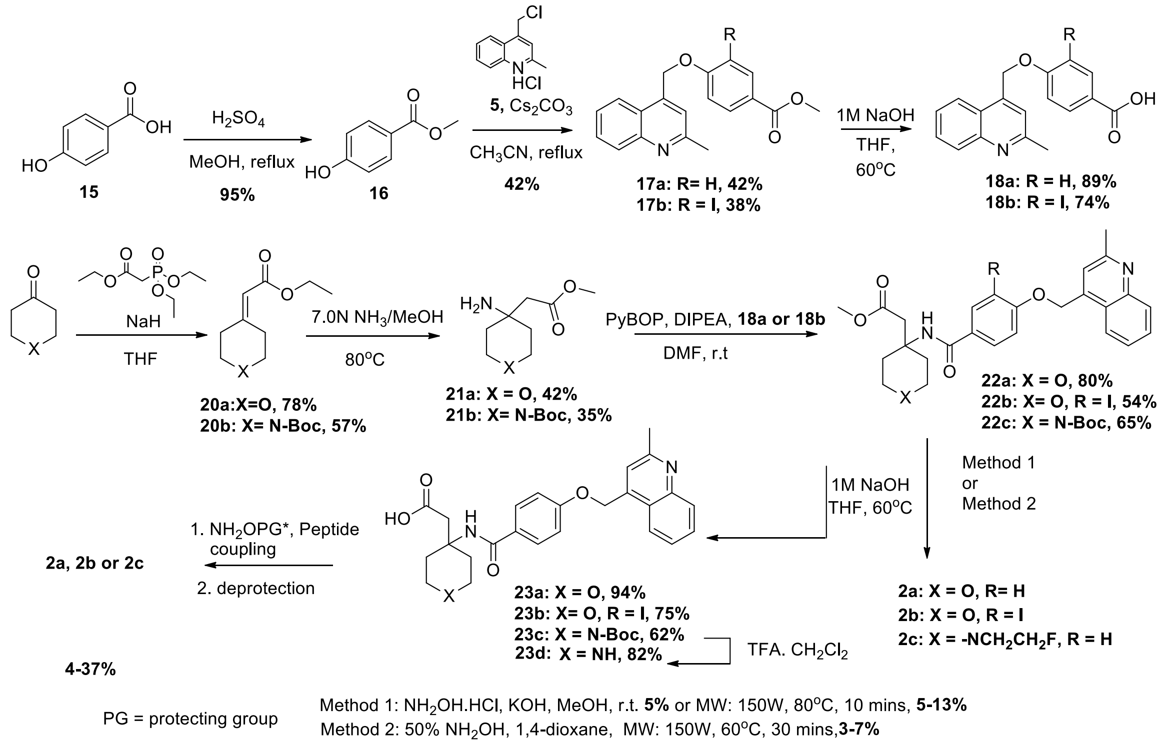

Scheme 5.3 Synthesis of TACE inhibitors **2a**, **2c** and derivative **2b**.

Both conditions yielded very little of the hydroxamic acid with the majority of the reaction mixture consisting of the starting ester. Consequently, we performed the conversion in two steps, with the initial hydrolysis of the esters followed by a peptide coupling with commercially available O-protected hydroxylamines, which in some cases, were cleaved *in situ* and afforded **2** in a 48% yield. O-Protected tert-butyldimethyl silyl hydroxylamines and O-tetrahydropyranyl hydroxylamines provided highest product yields, with the former protecting group cleaving *in situ*.

2b and **2c** were synthesized as non-radioactive standards with the intention of creating SPECT and PET radiotracers respectively. Compound **2c** was previously assessed in an *in vitro* assay using porcine TACE and was found to have an IC_{50}

of 2.5 nM.[15] For comparison, TACE activity of **2a**, **2b** and **2c** were tested in an established fluorogenic assay against human recombinant TACE.[26] Marimastat, a broad-spectrum inhibitor was used as a positive control for the assay (Figure 5.3).

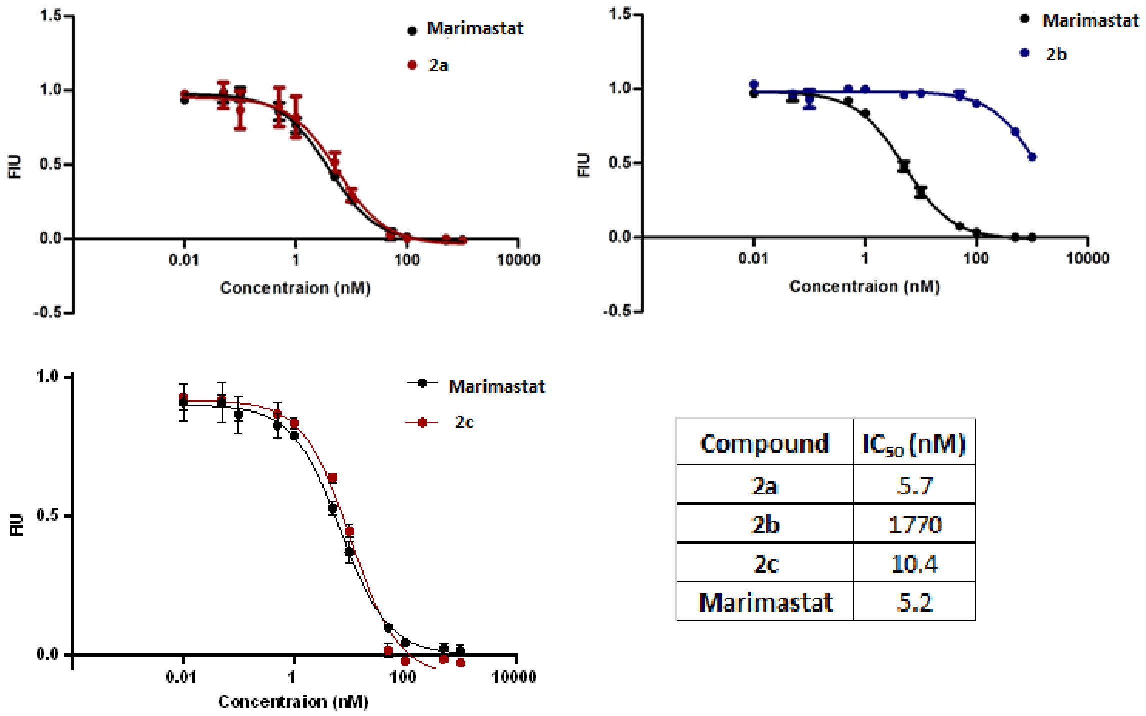

Compound	IC_{50} (nM)
2a	5.7
2b	1770
2c	10.4
Marimastat	5.2

Figure 5.3 IC_{50} curves for **2a**, **2b**, **2c** and positive control marimastat using an established fluorogenic assay.[26] All experiments were performed in triplicate.

While **2a** and **2c** exhibited low nanomolar inhibitory activity, **2b** demonstrated that introduction of iodine at the P1' substituent resulted in a dramatic loss of potency. This led us to pursue the fluorine-18 analogue of **2c**. Initially, we envisioned a direct ^{18}F labeling *via* the synthesis of alcohol **24**. Tosylation was perfomed on the protected hydroxamic acid to avoid decomposition *via* the Lossen rearrangement.[27] Unsuccessful attempts at mesylating and tosylating under various reaction conditions led to pursuing an indirect labeling approach strategy (Scheme 5.5). Boc-protected **23c** was coupled to O-tertbutyl protected hydroxylamine to afford **27**. The Boc protecting group was selectively cleaved in TFA/dichloromethane to afford precursor **28** in a 46% yield (Scheme 5.5).

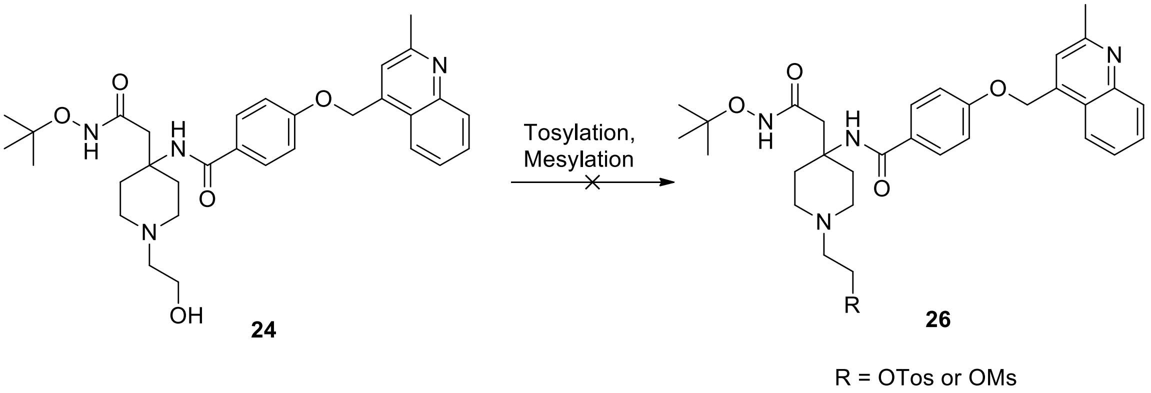

Scheme 5.4 Attempted mesylation/tosylation of **24** in an effort to produce labeling precursor **26**.

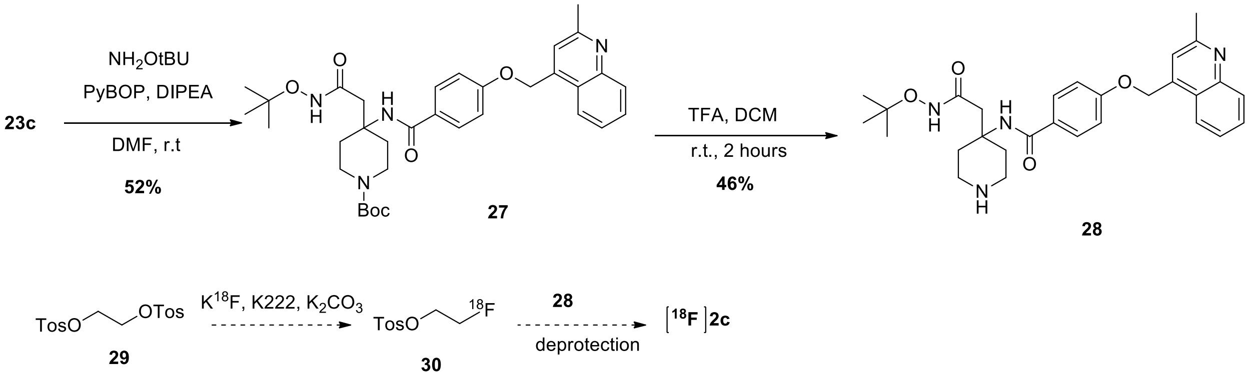

Scheme 5.5 Synthesis of intermediate **28** and proposed method for subsequent ^{18}F labeling *via* alkylation.

Given the success of the work on the ROS probes described in previous chapters, and the challenges in the synthesis of the TACE probes the project was halted at this stage. Going forward the ditosylate **29** can be labeled to afford **30** which can subsequently be used to alkylate **28** and following deprotection, would afford the desired radiotracer. Previous reports have shown successful ^{18}F labeling of hydroxamic acid containing MMP inhibitors *via* nucleophilic substitution, having been performed on both O-*t*Bu protected and naked hydroxamic acids.[28] Due to the thermal demand of the alkylation reaction, intermediate **28** is necessary in order to prevent O-alkylation of the hydroxamic acid.

5.4 Summary and Conclusions

The synthesis of model TACE ligands was achieved however labeling the products was not pursued further. Modified synthesis of two known TACE inhibitors both of which exhibited low nanomolar affinity towards human recombinant TACE was achieved. Radiolabeling precursors were synthesized and can be used to synthesize the desired tracers. The related iodinated compound that was synthesized was not pursued further due to its micromolar affinity.

5.5 Experimental

Synthesis of (2-methylquinolin-4-yl) methanol (**4**)[29]

To a solution of 2-methylquinoline (1.50 g, 10.4 mmol) and ammonium peroxodisulfate (4.76 g, 20.8 mmol) in methanol/water (21 mL/ 16 mL) was added 0.65 mL of concentrated sulfuric acid and the mixture was heated under reflux overnight. The reaction mixture was cooled to room temperature and the methanol was removed under reduced pressure. The pH of the residue was adjusted to pH

10 by addition of saturated sodium carbonate solution and the resulting solution was extracted with chloroform (100 mL). The organic layer was washed with brine, dried over anhydrous sodium sulphate and reduced under pressure to afford a white solid (0.59 g, 33%). ^{1}H NMR (700MHz, $CDCl_3$) δ 8.05 (d, J = 8.4 Hz, 1H), 7.90 (d, J = 8.2 Hz, 1H), 7.69 (ddd, J_1 = 1.2, J_2 = 6.8, J_3 = 8.2 Hz, 1H), 7.51 (ddd, J_1 = 1.2, J_2 = 6.8, J_3 = 8.2 Hz, 1H), 7.50 (s, 1H), 5.20 (d, J = 5.2 Hz, 2H), 2.75 (s, 3H).^{13} C NMR (175MHz, $CDCl_3$) δ 159.4, 147.9, 145.8, 129.5, 129.4, 124.2, 122.7, 119.2, 61.9, 25.6.

Synthesis of 4-chloro-2-methylquinoline hydrochloride (5)[29]

To a solution of **4** (0.97 g, 5.6 mmol) in dry dichloromethane (10 mL/ 5 mL) was added thionyl chloride (0.81 mL, 11.2 mmol) dropwise at 0°C. After the addition was complete, the reaction was left to stir at room temperature for 15 hours. The reaction mixture was then concentrated under reduced pressure and the residue was washed with EtOAc and concentrated to obtain a light orange solid which was used with no further purification (1.15 g, 90%).

Synthesis of 4-(methylsulfonyl) phenol (8)

Copper (I) iodide (0.64 g, 3.2 mmol) was added to a pre-gassed solution of 4-iodophenol (2.3mmol, 0.50g) in DMF (7.5 mL). The mixture was purged with argon for 10 minutes and stirred at r.t for 1 minute. Sodium methanesulfinate (0.14 g, 2.3 mmol) was added, the reaction mixture purged with argon, sealed and heated at 110 °C for 72 hours. Following this, the mixture was diluted with water (40 mL) and extracted with EtOAc (45 mL × 2). The organic phases were combined and washed with brine, dried over sodium sulphate and concentrated under reduced pressure. The crude oil was purified by flash chromatography (10% EtOAc/hexanes) and concentrated under reduced pressure to afford a white solid (0.36 g, 92%). ^{1}H NMR (700MHz, DMSO-d$_6$) δ 10.56 (br s, 1H), 7.72 (d, *J* = 8.7 Hz, 2H), 6.94 (d, *J* = 8.7 Hz, 2H), 3.32 (s, 3H), 3.10 (s, 3 H).^{13} C NMR (175MHz, DMSO-d$_6$) 161.9, 130.8, 129.3, 115.7, 44.1.

Synthesis of 2-methyl-4-((4-(methylsulfonyl)phenoxy)methyl)quinoline (9)

Cesium carbonate (0.94 g, 2.9 mmol) was added to a solution of **4** (0.68 g, 2.9 mmol) and **7** (0.50 g, 2.9 mmol) in acetonitrile (25 mL). The solution was heated under reflux over night after which the reaction mixture was filtered and the solvent removed *in vacuo*. The crude was purified by flash chromatography (50% EtOAc/ hexanes) and concentrated to afford a white solid (0.60 g, 64%). ^{1}H NMR (700MHz, DMSO-d$_6$) δ 8.11 (d, *J* = 7.7 Hz, 1H), 7.98 (d, *J* = 8.2 Hz, 1H), 7.89 (d, *J* = 8.9 Hz, 2H), 7.75 (ddd, J_1 = 1.2, J_2 = 6.8, J_3 = 8.2 Hz, 1H), 7.59 (ddd, J_1 = 1.2, J_2 = 6.8, J_3 = 8.2 Hz, 2H), 7.38 (d, *J* = 8.9 Hz, 2H), 5.74 (s, 2H), 3.18 (s, 3H), 2.67 (s, 3H).^{13} C NMR (175MHz, DMSO-d$_6$) δ 161.8, 158.6, 147.4, 141.5, 133.2, 129.4, 129.3, 128.8, 125.9, 123.7, 120.2, 115.5, 66.7, 43.9, 24.9.

Synthesis of methyl 5-methylnicotinate (11)

5-methylnicotonic acid (80.0 mg, 0.6 mmol) was dissolved in 3 mL of methanol and thionyl chloride (0.09 mL, 1.2 mmol) was added slowly dropwise at 0°C. The reaction was warmed to room temperature, and then refluxed for 18 hours. The ethanol was removed by evaporation and the residue was diluted with DCM (7 mL). The pH was adjusted to 10 with aqueous 1M NaOH and the resulting solution was extacted with ether (10 mL). The organic layer was washed with brine (10 mL) and dried over anhydrous $MgSO_4$. The solvent was removed under pressure and the crude mixture was purified by flash chromatography (40% EtOAc/hexanes) to afford a colourless oil (58.0 mg, 64%). ^{1}H NMR (700 MHz, $CDCl_3$) δ 9.04 (s, 1H), 8.61 (s, 1H), 8.11 (s,1H), 3.94 (s, 3H), 2.40 (s, 3H), ^{13}C NMR (175 MHz, $CDCl_3$) δ 166.1, 153.9, 148.0, 137.7, 133.3, 125.8, 52.5, 18.4.

Synthesis of 1-(5-methylpyridin-3-yl)-2-(4-((2-methylquinolin-4 yl)methoxy) pheny lsulfonyl)ethanone (12)

To a 50 mL oven dried round bottom flask was added **8** (70.0 mg, 0.2 mmol) and the flask was evacuated and backfilled with argon several times. The solid was dissolved in dry THF (5 mL) and the flask was cooled to -78^{o}C by means of a dry ice bath. LDA (2.0 M in THF/heptane/ethylbenzene, 0.21 mL, 0.4 mmol) was added *via* a syringe drop wise under argon. After the addition, the mixture was left to stir for 1 hour at -78^{o}C after which a solution of **11** (70.0 mg, 0.4 mmol) in dry THF (5 mL) was added drop wise under argon at this temperature. The reaction was then stirred for an additional hour at room temperature after which it was quenched with water (10mL) and extracted with EtOAc (10 mL × 2). The organic phase was dried over anhydrous $MgSO_4$, concentrated *in vacuo* and the residue was purified by flash chromatography (5% MeOH/DCM) to afford a bright orange solid (57.0 mg, 64%). HRMS (ESI$^+$) for calculated for $C_{25}H_{22}N_2O_4S$ 447.1379, found: 447.1379.

Synthesis of 1-(5-methylpyridin-3-yl)-2-(4-((2-methylquinolin-4-yl)methoxy) phenylsulfonyl)ethanol (14)

To a solution of **12** (0.12 g, 0.28 mmol) in 12 mL methanol was added $NaBH_4$ (0.02 g, 0.56 mmol) at 0^{o}C. The reaction was warmed to room temperature and stirred for 2 hours after which it was quenched with acetone and the solvent was removed under vacuum. The residue was purified by flash chromatography (10% MeOH/DCM) to furnish **14** as a white solid (0.10 g, 84%).

Synthesis of N-hydroxy-N-(1-(5-methylpyridin-3-yl)-2-(4-((2-methylquinolin-4-yl)methoxy)phenylsulfonyl) ethyl) formamide (1)

To a solution of **14** (30.0 mg, 0.07 mmol) in THF (2 mL) was added NH_4OH (50% wt. in water, 0.5 mL) and the reaction was refluxed at 80^{o}C for 2 hours. The THF was evaporated and the residue was diluted with water (10 mL) and extracted with EtOAc (12mL ×2). The organic phase was dried over anhydrous $MgSO_4$ and concentrated to give a white solid. The hydroxylamine was used in the next step without further purification.

To a solution of the hydroxylamine in MTBE (2 mL) was added 2,2,2-trifluoroethylformate[20] (0.04 mL, 0.4 mmol). The reaction was refluxed for 16 hours after which the MTBE was removed by rotary evaporation. The residue was purified by reverse phase C-18 column chromatography to afford a white solid (6.0 mg, 22%).

Synthesis of ethyl 2-(2H-pyran-4(3H,5H,6H)-ylidene)acetate (20a)

To a suspension of sodium *t*-butoxide (0.67 g, 7.04 mmol) in dry THF was added triethylphosphonoacetate (1.26 Ml, 6.4 mmol) dropwise at 0°C. After the addition was complete, the mixture was stirred for 30 minutes at room temperature after which **18** (6.40 mmol, 0.6mL) in 4mL dry THF was added dropwise. The reaction was left to stir at room temperature for 16 hours. The reaction mixture was quenched with water and extracted with EtOAc (35 mL × 2). The organic phase was dried over anhydrous $MgSO_4$ and the solvent was removed under pressure. The crude was purified by flash chromatography to give a light yellow oil (0.40 g, 82%). ^{1}H NMR (700 MHz, $CDCl_3$) δ 5.68 (s, 1H), 4.15 (q, *J* = 7.1 Hz, 2H), 3.76 (m, 2H), 3.72 (m, 2H), 2.99 (m, 2H), 2.32 (m, 2H), 1.27 (m, 3H). ^{13} C NMR (175 MHz, $CDCl_3$) δ 166.6, 157.3, 114.7, 69.2, 68.6, 59.9, 37.7, 31.2,14.4.

Synthesis of tert-butyl 4-(2-ethoxy-2-oxoethylidene)piperidine-1-carboxylate (20b) was prepared as above to afford a white solid (0.98 g, 57%). ^{1}H NMR (700MHz, $CDCl_3$) δ 5.69 (s, 1H), 4.14 (q, *J* = 7.0 Hz, 2H), 3.46 (m, 4H), 2.26 (m, 2H), 1.46 (s, 9H), 1.26 (t, J = 7.0 Hz, 3H).^{13} C NMR (175MHz, $CDCl_3$) δ 166.4, 157.9, 154.7, 115.4, 79.9, 59.9, 36.5, 29.6, 28.5,14.4.

Synthesis of methyl 4-hydroxybenzoate (17a)

To a 50 mL round bottom flask was added 4-hydroxybenzoic acid (2.00 g, 14.5 mmol) in methanol (13 mL). To this solution was added concentrated sulfuric acid (2 mL) and the reaction was refluxed overnight. The mixture was allowed to cool to room temperature and Na_2CO_3 was added to neutralize the reaction mixture. The methanol was removed under reduced pressure and the residue was taken up in dichloromethane (100 mL) and extracted with water (70 mL × 3). The organic phase was dried under anhydrous $MgSO_4$ and concentrated to give a white solid (2.09 g, 95%). ^{1}H NMR (700MHz, $CDCl_3$) δ 7.95 (d, *J* = 8.5 Hz, 2H), 6.86 (d, *J* = 8.6 Hz, 2H), 5.26 (br s, 1H), 3.89 (s, 3H).^{13} C NMR (175MHz, $CDCl_3$) δ 167.1, 159.9, 132.1, 122.9, 115.3, 52.1.

Synthesis of methyl-3-iodo-4-(2-methylquinolin-4-yl)methoxy)benzoate (17b)

Prepared in accordance with the method described for the synthesis of **17a**. (0.41 g, 95%) ^{1}H NMR (700MHz,$CDCl_3$) δ 8.50 (s, 1H), 8.10 (d, *J* = 8.3 Hz, 1H), 8.10 (m, 1H), 8.02 (d, *J* = 8.5 Hz, 1H), 7.64 (s, 1H), 7.56 (m, 1H), 6.94 (d, *J* = 8.61 Hz, 2H), 5.63 (s, 2H), 3.90 (s, 3H), 2.78 (s, 3H).^{13} C NMR (175MHz, $CDCl_3$) δ 141.5, 131.80, 123.8, 122.53, 116.5, 111.5, 86.0, 52.4, 29.8. HRMS (ESI$^+$) for $C_{19}H_{16}INO_3$ Calcd. 434.0253, Obsd. 434.0240.

Synthesis of methyl 2-(4-aminotetrahydro-2H-pyran-4-yl)acetate (21a)

7.0M NH_3/MeOH (2 mL) was added *via* a syringe to a vial containing **19** (0.10 g, 0.67 mmol). The vial was sealed and heated at 80ºC for 24 hours. The mixture was left to cool to room temperature and the solvent was removed by rotary evaporation. The residue was passed through a plug of silica and eluted in 10% MeOH/DCM. The filtrate was concentrated to afford a light yellow oil which was used with no further purification (49.0 mg, 42%)

Synthesis of 4-((2-methylquinolin-4-yl)methoxy)benzoic acid (18a)[15]

Ester **17** (0.28 g, 0.9 mmol) was diluted in a 1:1 THF/1 M NaOH solution (3 mL) and heated at 60^{o}C for 16 hours. The mixture was cooled and acidified using an aqueous 1 M HCl solution. The resulting white precipitate formed was filtered off, washed with water and dried in dessicator overnight. The resulting carboxylic acid **18a** was used with no further purification. (0.23 g, 89%).

Syntheis of 2-(4-(3-iodo-4-((2-methylquinolin-4-yl)methoxy) benzamido) tetrahydro-2H-pyran-4-yl)acetic acid (18b)

Prepared in accordance with procedure described for synthesis of **18a**. (50.0 mg, 90%) ^{1}H NMR (700 MHz, MeOH-d4) δ 8.45 (d, *J* = 8.5 Hz, 1H), 8.32 (d, *J* = 8.5 Hz, 1H), 8.29 (s, 1H), 8.23 (d, *J* = 8.5 Hz, 1H), 8.11 (m, 1H), 7.94 (m, 1H), 7.92 (m, 1H), 7.35 (d, *J*= 8.5 Hz, 1H), 6.00 (s, 2H), 3.78 (m, 2H), 3.71 (m, 2H), 3.03 (s, 3H), 2.94 (s, 2H), 2.46 (d, *J* = 13.6 Hz, 2H), 1.84 (m, 2H), ^{13} C NMR (175MHz, MeOH-d4) δ 174.1, 169.1, 160.1, 159.4, 140.0, 132.3, 130.7, 125.8, 125.5, 122.0, 113.2, 86.3, 68.6, 64.7, 54.0, 42.9, 35.9, 30.7, 21.8. HRMS (ESI$^+$) for $C_{25}H_{25}IN_2O_5$: Calcd. 561.0886, Obsd. 561.0886.

Synthesis of methyl2-(4-(4-((2-methylquinolin-4 yl)methoxy)benzamido) tetra hydro-2H-pyran-4-yl)acetate (22a)

To a solution of **18a** (0.13 g, 0.44 mmol) in DMF (2 mL) was added PYBOP (0.23 g 0.44 mmol) and DIPEA (0.15 mL, 0.88 mmol) at 0^{o}C. After 5 minutes of stirring at this temperature, a solution of the amine **21a** (80.0 mg, 0.44 mmol) in DMF (1 mL) was added *via* syringe. The reaction was stirred at 0ºC for 15 minutes and then warmed to room temperature where it was left stirring for 18 hours after which it was diluted with water and extracted with EtOAc (15 mL × 3). The organic layers were combined, dried over anhydrous $MgSO_4$ and concentrated *in vacuo*. The residue was purified by silica gel column chromatography (75% EtOAc/ hexanes) and the fractions were concentrated to afford **21** as a white solid (0.16 g, 83%). ^{1}H NMR (700 MHz, MeOH-d4) δ 8.12 (d, J = 7.8 Hz, 1H), 8.01 (d, J = 8.3 Hz, 1H), 7.79 (dd, J = 8.8 Hz, 2H), 7.78 (ddd, J_1 = 1.2, J_2 = 6.8, J_3 = 8.3 Hz, 1H), 7.62 (m, 2H), 7.17 (d, J = 8.8 Hz, 2H), 5.69 (s, 2H), 3.77 (m, 2H), 3.72 (m, 2H), 2.73 (s, 3H), 2.97 (s, 2H), 2.42 (d, J = 12.9 Hz, 2H), 1.82 (m, 2H).^{13} C NMR (175 MHz, MeOH-d4) δ 172.6, 170.8, 160.4, 160.3, 148.5, 144.8, 131.0, 129.0, 127.5, 125.6, 124.5, 121.5, 120.4, 120.0, 115.6, 67.8, 53.9, 51.9, 43.2, 24.7.

Synthesis of **22b** and **22c** as described for the synthesis of **22a**: (0.15 g, 65%).^{1}H NMR (700 MHz, MeOH-d4) δ 8.12 (d, J = 7.8 Hz, 1H), 8.01 (d, J = 8.3 Hz, 1H), 7.79 (dd, J = 8.8 Hz, 2H), 7.78 (ddd, J_1 = 1.2, J_2 = 6.9, J_3 = 8.3 Hz, 1H), 7.62 (m, 2H), 7.17 (d, J = 8.8 Hz, 2H), 5.69 (s, 2H), 3.77 (m, 2H), 3.72 (m, 2H), 2.97 (s, 2H), 2.73 (s, 3H), 2.42 (d, J = 13.0 Hz, 2H), 1.80-1.83 (m, 2H), ^{13}C NMR (175 MHz, MeOH-d4) δ 172.6, 170.8, 160.4, 160.3, 148.5, 144.8, 131.0, 129.0, 127.5, 125.6, 124.5, 121.5, 120.4, 120.0, 115.6, 67.8, 53.9, 51.9, 43.2, 24.7.

Synthesis of 2-(4-(4-((2-methylquinolin-4-yl)methoxy)benzamido)tetrahydro-2H-pyran-4-yl)acetic acid (23a)

Prepared in accordance with the method described for hydrolysis of **18**. ^{1}H NMR (700 MHz, MeOH-d4) δ 8.43 (d, *J* = 8.5 Hz, 2H), 8.17 (d, *J* = 8.5 Hz, 1H), 8.12 (m, 2H), 7.94 (m, 4H), 7.85 (d, *J* = 8.8 Hz, 2H), 7.25 (d, *J* = 8.8 Hz, 2H), 5.93 (s, 2H), 3.78 (m, 2H), 3.72 (m, 2H), 2.99 (s, 3H), 2.95 (s, 2H), 2.46 (d, *J* = 13.4 Hz, 2H),1.83 (m, 2H).^{13} C NMR (175 MHz, MeOH-d4) δ 174.1, 170.5, 130.6, 130.5, 130.4, 125.7, 125.6, 121.6, 115.7, 67.3, 64.6, 53.8, 42.9, 35.9, 21.5.

Synthesis of 2-(4-(3-iodo-4-((2-methylquinolin-4-yl)methoxy)benzamido) tetrahydro -2H-pyran-4-yl) acetic acid (23b)

Prepared in accordance with procedure described for synthesis of **17**. (50.0 mg, 90%) ^{1}H NMR (700 MHz, MeOH-d4) δ 8.45 (d, *J* = 8.5 Hz, 1H), 8.32 (d, *J* = 8.5, 1H), 8.29 (s, 1H), 8.23 (d, *J* = 8.5 Hz, 1H), 8.11 (m, 1H), 7.94 (m, 1H), 7.92 (m, 1H), 7.35 (d, *J* = 8.5 Hz, 1H), 6.00 (s, 2H), 3.78 (m, 2H), 3.71 (m, 2H), 3.03 (s, 3H), 2.94 (s, 2H), 2.46 (d, *J* = 13.6 Hz, 2H), 1.85 (m, 2H). ^{13} C NMR (175MHz, MeOH-d4) δ 174.1, 169.1, 160.1, 159.4, 140.0, 132.3, 130.7, 125.8, 125.5, 122.0, 113.2, 86.3, 68.6, 64.7, 54.0, 42.9, 35.9, 30.7, 21.8. HRMS (ESI$^+$) for $C_{25}H_{25}IN_2O_5$ calcd. 561.0886, Obsd. 561.0886.

Synthesis of N-(4-(2-(hydroxyamino)-2-oxoethyl)tetrahydro-2H-pyran-4-yl)-4-((2-methylquinolin-4-yl)methoxy)benzamide (2a)

Method 1:

Carboxylic acid **23a** (90.0 mg, 0.2 mmol) was suspended in DMF (1.5 mL) and to this was added HOBt. H_2O (30.0 mg, 0.2 mmol), NH_2-OTBDMS (14.0 mg, 0.2 mmol). The solution was cooled to 0^{o}C and EDC.HCl (40.0 mg, 0.2mmol) was added slowly to the stirring mixture. The reaction was left stirring at this temperature for 15 minutes and then warmed to room temperature. After 18 hours the mixture was diluted with water (2 mL) and extracted with EtOAc (3 mL × 3). The organic layers were combined, dried over anhydrous $MgSO_4$ and the solvent was removed by rotary evaporation. The resulting residue was resuspended in a minimum amount of water/acetonitrile and purified by means of a reverse phase C18 column (provided by Teledyne Technologies inc., RediSep® Rf, 5.5g) (43% acetonitrile/ water) to afford the free hydroxamic acid as a white solid (89.0 mg, 48%).

Method 2:

Compound **22a** (43.0 mg, 0.09mmol) was added to a microwave vial equipped with a stir bar and diluted in 1,4-dioxane (0.5 mL) and an equal volume of 50% aqueous hydroxylamine solution. The vial was capped and subjected to microwave irradiation (60^{o}C, 150W) for 30 minutes. The reaction was diluted with EtOAc (2 mL) and washed with water. The organic layer was dried over anhydrous magnesium sulfate and the solvent was removed by rotary evaporation. The residue was purified in the manner described in method 1. (10.0 mg, 25%). ^{1}H NMR (700 MHz, MeOH-d4) δ 8.12 (d, *J* = 7.9 Hz, 1H), 8.01 (d, *J* = 8.4 Hz, 1H), 7.82, (d, *J* = 8.8 Hz, 2H), 7.77 (m, 1H), 7.61 (m, 2H), 7.16 (d, *J* = 8.8 Hz, 2H), 5.69 (s, 2H), 3.76 (m, 2H), 3.72 (m, 2H), 2.72 (s, 2H), 2.69 (s, 2H), 2.47 (d, *J* = 13.6 Hz, 2H), 1.82 (m, 2H).^{13} C NMR (175 MHz, MeOH-d4) δ 170.6, 169.4, 162.3, 160.4, 148.5, 144.8, 131.0, 130.5, 130.0, 129.0, 127.5, 124.5, 121.6, 115.6, 67.8, 64.7, 54.3, 41.5, 35.9, 28.7, 24.7. HRMS (ESI$^+$) for $C_{25}H_{28}N_3O_5$ Calcd.,450.2029, Obsd.

450.2026. **2b** and **2c** prepared in accordance with method 1 for synthesis of **2a**. **2b :**(4.0 mg, 57%,) ^{1}H NMR (700 MHz, MeOH-d4) δ 8.31 (d, *J* = 2.1 Hz, 1H), 8.15 (d, *J* = 8.3 Hz, 1H), 8.02 (d, *J* = 8.4 Hz, 1H), 7.88 (d, *J* = 2.1 Hz, 1H), 7.87 (d, *J* = 2.1 Hz, 1H), 7.80 (s, 1H), 7.79 (ddd, J_1 = 1.3, J_2 = 6.9, J_3 = 8.3 Hz, 1H), 7.64 (m, 1H), 7.24 (d, *J* = 8.6 Hz, 1H), 5.77 (s, 2H), 3.76 (m, 2H), 3.70 (m, 2H), 2.75 (s, 3H), 2.68 (s, 2H), 2.46 (d, *J* = 13.6 Hz, 2H), 1.82 (m, 2H).^{13} C NMR (175 MHz, MeOH-d4) δ 169.4, 169.1, 160.6, 160.4, 148.4, 144.4, 140.1, 131.8, 131.1, 130.5, 129.0, 127.6, 125.4, 124.6, 121.6, 112.9, 86.4, 68.8, 64.7, 54.5, 41.4, 35.9, 24.9. HRMS (ESI$^+$) for $C_{25}H_{26}IN_3O_5$ Calcd. 576.0995 Obsd. 576.0972 **2c**:^{1}H NMR (600 MHz, DMSO-d_6) δ 8.12 (d, *J* = 8.3 Hz, 2H), 7.97 (d, *J* = 8.3 Hz, 1H), 7.81 (d, *J* = 8.7 Hz, 2H), 7.78 (m, 1H), 7.58 (m, 2H), 7.19 (d, *J* = 8.7 Hz, 2H), 5.68 (s, 2H), 4.53 (m ,1H), 4.46 (m, 1H), 2.73 (s, 3H), 2.66 (s, 3H), 2.55 (m, 4H), 2.44 (d, *J* = 12.1Hz, 2H), 2.28 (m, 2H), 1.74 (s, 1H), 1.62 (m, 2H).^{13} C NMR (150 MHz, DMSO-d_6) 166.4, 166.0, 160.0, 158.6, 147.4, 141.9, 129.4, 129.3, 128.8, 125.9, 123.8, 123.7, 120.1, 114.2, 82.4, 81.5, 66.3, 57.7, 57.6, 52.8, 49.4, 33.1, 24.9. HRMS (ESI$^+$) for $C_{27}H_{32}FN_4O_4$ Obsd. 495.2408 Calcd. 495.2423

5.6 References

1. M. L. Moss, J. M. White, M. H. Lambert, R. C. Andrews, *Drug Discov. Today,* **2001**, *6*, 417–426.
2. P. A. Kenny, *Differentiation.,* **2007**, *75*, 800–808.
3. S. A. Doggrell, *Expert. Opin. Investig. Drugs,* **2002**, *11*, 1003–1006.

4. I. M. Clark, A. E. Parker, *Expert. Opin.Ther. Targets,* **2003**, *7*, 19–34.
5. J. Arribas, C. Esselens, *Curr. Pharm. Des*., **2009**, *15*, 2319-2335.
6. R.C. Newton, C.P. Decicco, *J. Med. Chem*., **1999**, *42*, 2295-2314.
7. a) B.B. Aggarwal, S. Shishodia, S.K. Sandur, M. K. Pandey, G. Sethi, *Inflammation,* **2006**, *72*, 1605–1621. b) K. Liu, C. Qin, Z. Wang, S. Liu, X. Cui, D. Zhang, *Asian Pac. J. Cancer Prev.*, **2012**, *13*, 847-850.
8. R. Medeiros, R.D. Prediger, G.F. Passos, P. Pandolfo, F.S. Duarte, J.L. Franco, A.L. Dafre, G. Di Giuanta, C.P. Figueiredo, R.N. Takahashi, M.M. Campos, J.B. Calixto, *J. Neuro. Sci*., **2007**, 27, 5394-5404.
9. P.A. Kenny, M.J. Bissel, *J. Clin. Invest*., **2007**, *117*, 337-345.
10. a) P.D. Brown, *Exp. Opin. Invest. Drugs*, **2000**, *9*, 2167-2177. b) T. Shaw, J.S. Nixon, K.M. Bottomley, *Exp. Opin. Invest. Drugs* 2000, *9*, 1469-1478. c) S. Elliot, T. Cawston, *Drugs Aging*, **2001**, *18*, 87-99.
11. V. Aranapakam, J.M. Davis, G.T. Grosu, J. Baker, J. Ellingboe, A. Zask, J.I. Levin, V.P. Sandanayaka, M. Du, J.S. Skotnicki, J.F. DiJoseph, A. Sung, M.A. Sharr, L.M. Killar, T. Walter, G. Jin, R. Cowling, J. Tillett, W. Zhao, J. McDevitt, Z.B. Xu, *J. Med. Chem.,* **2003**, *46*, 2376-2396.
12. M. Chianelli, C. D’Alessandria, F. Conti, R. Priori, G. Valesini, A. Annovazzi, A. Signore, *Q. J. Nucl. Med. Mol. Imaging.,* **2006**, *3*, 217-225.
13. G. Malviya, F. Conti, M. Chianelli, F. Scopinaro, R. A. Dierckx, A. Signore, *Eur. J. Nucl. Med. Mol. Imaging,* **2010**, *37*, 386–398.

14. N. Kamei, T. Tanaka, K. Kawai, K. Miyawaki, A. Okuyama, Y. Murakami, Y. Arakawa, M. Haino, T. Harada, M. Shimano, *Bioorg. Med. Chem. Lett.,* **2004**, *14*, 2897–2900.
15. J. L. Gilmore, B. W. King, C. Harris, T. Maduskuie, S. E. Mercer, R.Q. Liu, M. B. Covington, M. Qian, M. D. Ribadeneria, K. Vaddi, et al., *Bioorg. Med. Chem. Lett.,* **2006**, *16*, 2699–2704.
16. a) P. R. Murumkar, S. DasGupta, S. R. Chandani, R. Giridhar, M. R. Yadav, *Expert. Opin. Ther. Pat.,* **2010**, *20*, 31–57. b) J.W. Skiles, N.C. Gonnella, A.Y. Jeng*, Curr. Med. Chem*., **2004**, *11*, 2911-2977.
17. M.H. Palmer, P.S. McIntyre, *Tetrahedron Lett*., **1968**, *17*, 2147-2150.
18. H. Abe, H. Suzuki, *Tetrahedron Lett.,* **1995**, *36*, 6239–6242.
19. M. Julia, J.M. Paris, *Tetrahedron Lett*., **1973**, *14*, 4833-4836.
20. D. R. Hill, C.N. Hsiao, R. Kurukulasuriya, S. Wittenberger, *Org. Lett.*, **2002**, *4*, 111-113.
21. D. W. Knight, M. P. Leese, *Tetrahedron Lett.,* **2001**, *42*, 2593–2595.
22. a) W. Wadsworth, *Org. React.*, **1977**, *25*, 73-253. b) L. Horner, H.M.R. Hoffmann, H. G. Wippel, *Ber.,* **1958**, *91*, 61-63. c) W.S. Wadsworth Jr., W.D. Emmons, *J. Am. Chem. Soc.,* **1961**, *83*, 1733-1738.
23. M.C. Pirrung, J.H.L. Chau, *J. Org. Chem.,* **1995**, *60*, 8084-8085.
24. E. Thouin, W.D. Lubell, *Tetrahedron Lett.,* **2000**, *41*, 457-460.
25. A. Mordini, G. Reginato, F. Russo, M. Taddei, *Synthesis,* **2007**, *20*, 3201–3204.

26. G. Jin, X. Huang, R. Black, M. Wolfson, C. Rauch, H. Mcgregor, G. Ellestad, R. Cowling, *Anal. Biochem.,* **2002**, *275*, 269 –275.
27. W. Lossen, *Eur. J. Org. Chem*., *161*, 347-362.
28. S. Wagner, H.-J. Breyholz, M. P. Law, A. Faust, C. Höltke, S. Schröer, G. Haufe, B. Levkau, O. Schober, M. Schäfers, K. Kopka, *J. Med. Chem.,* **2007**, *50*, 5752–5764.
29. T. Harada, M. Haino, A. Okuyama, Y. Arakawa, Y. Murakami, *Eur.Patent No*. 02767899.4 (23 June, 2004).

Chapter 6: Conclusions and Future Work

The current diagnostic imaging methods used in clinical practice to identify and characterize RA are severely limited. Radiography is the most widely used imaging modality but is generally most effective for late-stage disease where there is bone erosion and deformities.[1,2] Existing medications in contrast are most effective when they are used to treat this disease at an early stage.[3] Molecular imaging can be used not only as a diagnostic tool, but also as a means to monitor therapeutic response and aid in drug discovery. For this reason, the development of molecular imaging probes for RA can directly impact patient prognosis by aiding in therapeutic treatment plans and decreasing the severe side-effects often associated with RA treatment.

This thesis describes three strategies towards molecular imaging of RA. The first approach involves the development of a hybrid optical-PET probe that responds to ROS. This probe is currently the first reported example of a NIR turn-on optical-PET probe (Chapter 2). The PET agent exhibited a biodistribution pattern reminiscent of albumin-related blood-pool imaging agents, which are capable of accumulating in tissues exhibiting hypervascularity. The fluorescent counterpart is significantly more stable than the commonly employed ROS probe DHE and has been shown to specifically react with superoxide and hydroxyl radicals. Such a probe would be valuable not only in assessing RA, but also for cancer and cardiac ischemia.

The second approach involves the development of NIR fluorinated fluorophores that were encapsulated in F-127 micelles. One of the synthesized fluorophores is a *meso*-fluorinated dye that was prepared *via* a HALEX reaction. This fluorophore is the first example of a *meso* fluorinated cyanine dye that shows enhanced fluorescence response both in solution and in a PC-3 cell assay in comparison to the commercially available chlorinated analogue (IR780). The micelle encapsulated fluorophores also show enhanced fluorescence in the encapsulated micelles and are completely soluble in aqueous buffer. Stability studies show no evidence of aggregation in solution up to two weeks which is advantageous for general use and longer term storage of the agent. These micelles have the ability to localize in hypervascular diseased tissue found in RA where the fluorophore is expected to accumulate based on the EPR effect.

The third approach involved the development of a targeted probe that binds to the metalloprotease TACE. This enzyme is heavily involved in RA (and other diseases such as cancer) initiation and progression. The preliminary data presented describes the synthesis and *in vitro* evaluation of two hydroxamic acids, one of which exhibits an average IC_{50} of 10 nM. Given the success of the work on the ROS probes this work was not advanced beyond development and screening of the lead candidates.

6.1 Future work and Preliminary Results

The immediate future work is to evaluate the ROS probes developed during the course of this work in different preclinical models. In particular evaluation of the micelle entrapped dyes appears to be the most viable route to achieving the desired target- to-non-target ratio. For the albumin binding probe, work should focus on evaluating the compound *in vivo* compared to labeled albumin or other albumin binding agents including ^{18}F Evan's blue, which was recently reported.[4]

An additional avenue of future research is to prepare more water soluble ^{18}F-labeled cyanine and hydrocyanine dyes. The ^{18}F labeling of cyanine fluorophores is challenging due to the sensitive nature of the dye to the typically harsh reaction conditions used during labeling. Further, the labeling of ROS-sensitive probes is made more difficult by stability issues arising from radiation-induced radical formation in solution. Currently, there are two known examples of ^{18}F cyanine dyes: one based on isotopic exchange at the center of a "boron trap",[5] and the other which employed a pre-labeled prosthetic group.[6] Through the work described in this thesis, it has been shown that the introduction of the *o*-nitropyridine functionality onto commercially available *meso*-chlorinated dyes can be accomplished by a robust Suzuki coupling reaction.^{18}F labeling can be achieved in good yield in one step by heating the precursors for a very short period of time (4 minutes). To assess whether this was translatable to other structurally similar dyes, the same procedures were used to prepare a related probe derived from IR775 chloride (Chapter 4), resulting in comparable RCYs. Given that minor structural variations on cyanine fluorophores have resulted in dramatic differences in biodistribution patterns,[7,8] detailed exploration of various structural analogues in a number of preclinical models is required (Figure 6.1). Further, given the blood binding ability of the first generation ROS probe, this probe can be assessed in a model that assesses lymphatic drainage to determine whether it can be useful in lymph node mapping.

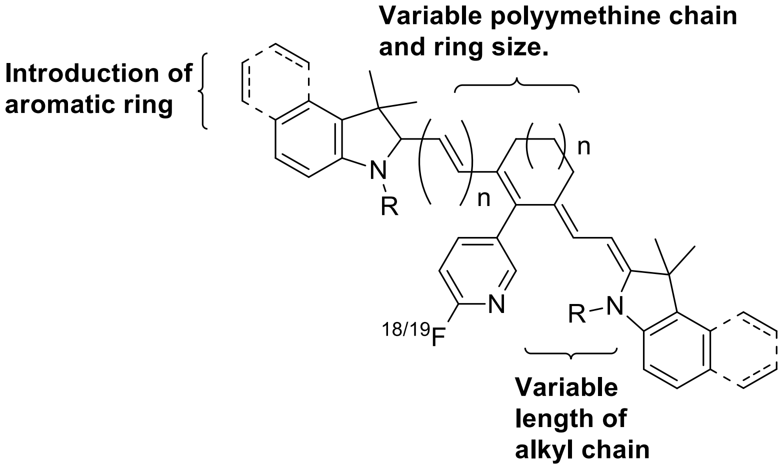

Figure 6.1 Structural modifications that can be made on the cyanine dye scaffold for assessment in preclinical models.

While there are imaging agents targeted at MMP enzymes[9] and the related cytokine TNF-α[10], the enzyme TACE has not been targeted to date for molecular imaging purposes. One challenge may be that the current known small-molecule TACE inhibitors possess sensitive hydroxamic acid functionalities that are prone to hydrolyze/degrade *in vivo* or under certain reaction conditions.[11] Consequently, ^{18}F labeling of compounds possessing this functionality may be more efficiently achieved *via* a prosthetic group approach. The azide-alkyne Huisgen cycloaddition[12] is commonly exploited in ^{18}F labeling reactions due to the rapid and facile nature of the reaction. Ester **2** was synthesized as an intermediate for the purpose of generating the corresponding hydroxamic acid **4a**. It has been previously demonstrated that functionalization at the piperidine nitrogen of this scaffold is tolerable in that inhibitory activity is not drastically altered.[13] **4a** must first be assessed for activity in an *in vitro* assay to confirm that the triazole ring does not negatively impact inhibitory activity.

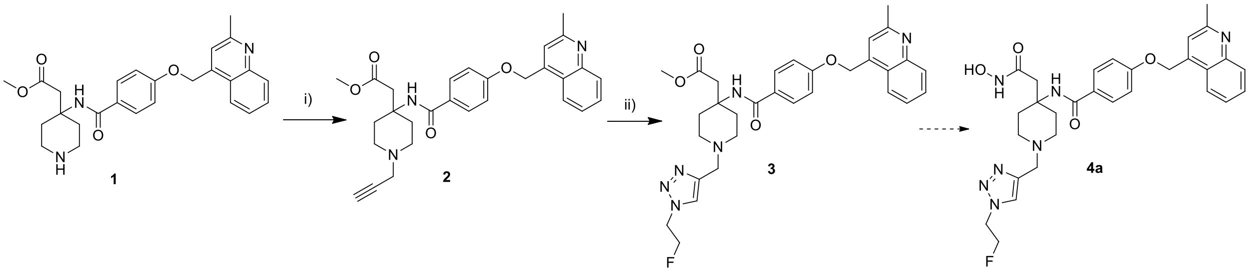

Scheme 6.1 Synthesis of precursors for the synthesis of potential TACE inhibitor **4**. i) Propargyl bromide, NaH, THF, r.t, 30 min, **66%**. ii) 1-azido-2-fluoroethane, sodium ascorbate, Cu (II) acetate, DMF, r.t., 1 hour, **36%**.

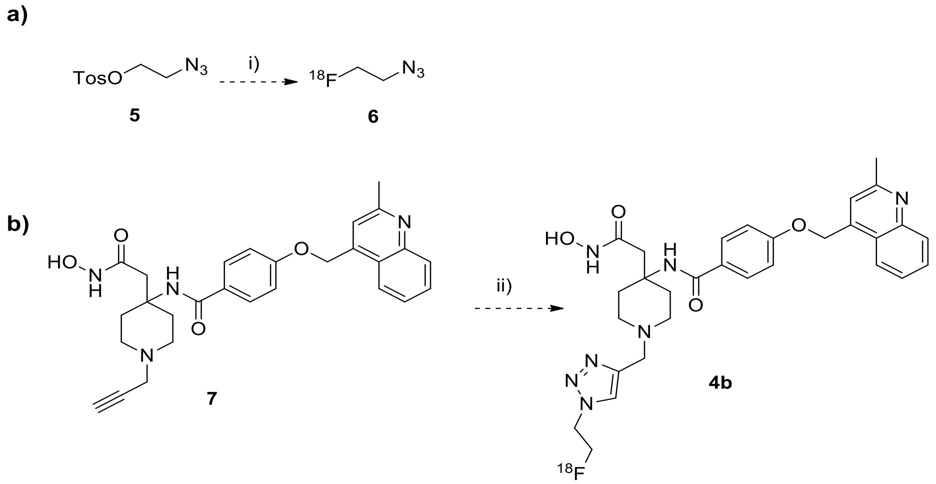

Scheme 6.2 Prosthetic group radiolabeling strategy for the synthesis of **4b**. a) Synthesis of ^{18}F-ethyl azide i) K [^{18}F], K_2CO_3, K_{222}. b) Conjugation of radiolabeled prosthetic group via the click reaction ii) Cu(II) catalyst, sodium ascorbate.

^{18}F labeling can be performed by first synthesizing the tosylate **5** and then subjecting this to conventional nucleophilic fluorination conditions. The product **6** can be reacted with intermediate **7** to generate the anticipated product. As a proof of concept, tracer **4b** can be assessed in various tumour cell lines, such as MCF-7 which are known to show enhanced TACE activity.[14]

6.2 Experimental

Synthesis of **2**

Compound **1** (0.11 g, 0.25 mmol) was dissolved in dry THF (4 mL) and carefully added to an oven-dried 25 mL flask containing a slurry of NaH (60% dispersion in mineral oil, 70.0 mg, 1.7 mmol) in THF (4 mL). Propargyl bromide (80% wt solution in toluene, 0.15 mL, 1.0 mmol) was slowly added to the mixture *via* a syringe and after addition, the mixture was stirred at r.t for 30 min. The reaction was quenched with brine and extracted with EtOAc (2 × 20 mL). The organic phases were combined, dried over anhydrous $MgSO_4$ and concentrated *in vacuo*. The desired product was isolated using a 4 gram flash RediSep® Rf silica gel column (30% MeOH/DCM) to afford **2** as a white solid (80.0 mg, 66%). ^{1}H NMR (700 MHz, MeOH-d4): δ 8.10 (d, *J* = 8.5 Hz, 1H), 8.00 (d, *J* = 8.5 Hz, 1H), 7.78, (d, *J* = 8.7 Hz, 2H), 7.76 (m, 1H), 7.60 (m, 2H), 7.16 (d, *J* = 8.7 Hz, 2H), 5.69 (s, 2H), 3.60 (s, 2H), 3.35 (s,3H), 3.31 (m, 4H), 2.93 (s, 1H), 2.76 (d, *J* = 12.3 Hz, 2H), 2.62 (t, *J* = 11.4 Hz, 2H), 1.95 (s, 3H), 2.54 (d, *J* = 12.3 Hz, 2H), 1.82 (m, 2H), ^{13} C NMR (175 MHz, MeOH-d4) δ 172.6, 170.7, 162.3, 160.4, 148.5, 144.8, 131.0, 130.4, 130.1, 129.0, 127.5, 125.6, 124.5, 121.5, 115.6, 78.9, 75.5, 67.7, 53.9, 51.9, 47.3, 34.7, 24.7. HRMS (ESI$^+$) for $C_{29}H_{32}N_3O_4$ Calcd. 486.2393 Obsd. 486.2417.

6.3 References

1. H. Czembirek, M. Boeck, M. Stiskal, *Radiographics*, **2005**, *25*, 381–398.
2. C.G. Peterfy, *Curr. Opin. Rheumatol.,* **2003**, *15*, 288–295.
3. M. Chianelli, C. D'Alessandria, F. Conti, R. Priori, G. Valesini, A. Annovazzi, A. Signore, *Q. J. Nucl. Med. Mol. imaging.,* **2006**, *50*, 217–225.
4. Y. Wang, L. Lang, P. Huang, Z. Wang, O. Jacobson, D. O. Kiesewetter, I. U. Ali, G. Teng, G. Niu, X. Chen, *Proc. Natl. Acad. Sci. U. S. A.,* **2014**, *112*, 208–213.
5. T. Priem, C. Bouteiller, D. Camporese, X. Brune, J. Hardouin, A. Romieu, P.Y. Renard, *Org. Biomol. Chem.,* **2013**, *11*, 469–479.
6. R. Ting, T.A. Aguilera, J. L. Crisp, D. J. Hall, W. C. Eckelman, D. R. Vera, R. Y. Tsien, *Bioconjug. Chem.,* **2010**, *21*, 1811–1819.
7. S. Onoe, T. Temma, Y. Shimizu, M. Ono, H. Saji, *Cancer Med.,* **2014**, *3*, 775–786.
8. C. Zhang, T. Liu, Y. Su, S. Luo, Y. Zhu, X. Tan, S. Fan, L. Zhang, Y. Zhou, T. Cheng, C. Shi, *Biomaterials,* **2010**, *31*, 6612–6617.
9. a) S. Wagner, H.-J. Breyholz, M. P. Law, A. Faust, C. Höltke, S. Schröer, G. Haufe, B. Levkau, O. Schober, M. Schäfers, K. Kopka, *J. Med. Chem.,* **2007**, *50*, 5752–64. b) N. Matusiak, A. Waarde, R. Bischoff, R. Oltenfreiter, C.

Wiele, R. A. Dierckx, P. H. Elsinga, *Curr Pharm Des.,* **2013**, *19*, 4647–4672. c) M. Schäfers, O. Schober, S. Hermann, *J. Nucl. Med.,* **2010**, *51*, 663–666. d) S. Wagner, H. J. Breyholz, A. Faust, C. Holtke, B. Levkau, O. Schober, M. Schafers, K. Kopka, *Curr. Med. Chem.,* **2006**, *13*, 2819–2838.

10. a) M. Chianelli, C. D'Alessandria, F. Conti, R. Priori, G. Valesini, A. Annovazzi, A. Signore, *Q J Nucl Med Mol Imaging.,* **2006**, *3*, 217-225. b) P. Barrera, W. J. Oyen, O. C. Boerman, P. L. van Riel, *Ann Rheum Dis.,* **2003**, *62*, 825–828.
11. A. Massaro, A. Mordini, G. Reginato, F. Russo, M. Taddei, *Synthesis,* **2007**, 20, 3201–3204.
12. R. Huisgen, *Proc. Chem. Soc*., **1961**, 357-396.
13. J. L. Gilmore, B. W. King, C. Harris, T. Maduskuie, S. E. Mercer, R.-Q. Liu, M. B. Covington, M. Qian, M. D. Ribadeneria, K. Vaddi, J.M. Trzaskos, R.C. Newton, C.P. Decicco, J.J. Duan, *Bioorg. Med. Chem. Lett.,* **2006**, *16*, 2699–2704.
14. a) McGowan, P. M.; Ryan, B. M.; Hill, A. D. K.; McDermott, E.; O'Higgins, N.; Duffy, M. J. *Clin. Cancer Res.,* **2007**, *13*, 2335–2343. b) B. B. S. Zhou, M. Peyton, B. He, C. Liu, L. Girard, E. Caudler, Y. Lo, F. Baribaud, I. Mikami, N. Reguart, G. Yang, Y. Li, W. Yao, K. Vaddi, A.F. Gazdar, S.M. Friedman, D.M. Jablon, R.C. Newton, J.S. Fridman, J.D. Minna, P.A. Scherle, *Cancer Cell.,* **2006**, *10*, 39–50.

APPENDIX 1

Figures:

Figure S1 ^{1}H NMR spectrum of **2** (700 MHz, MeOH-d4)

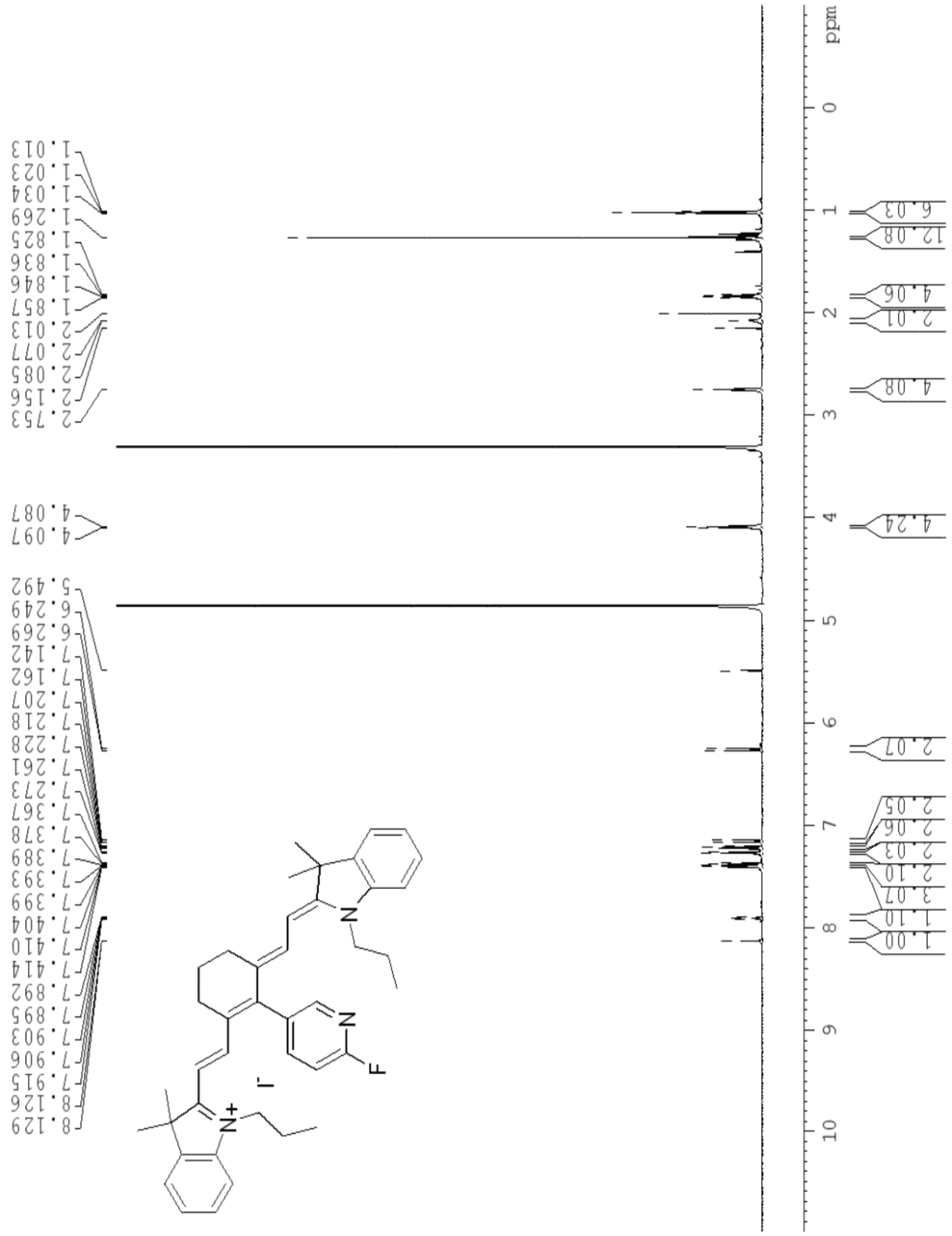

Figure S1-1 Expansion of the ^{1}H NMR of **2** (700 MHz, MeOH-d4)

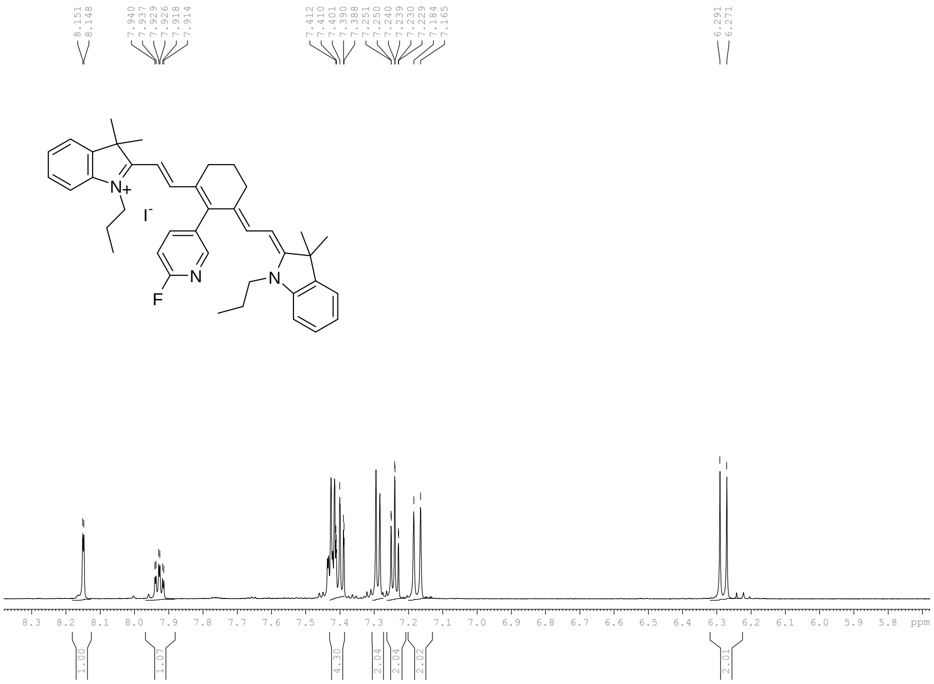

Figure S1-2 Expansion of the ^{1}H NMR of **2** (700 MHz, MeOH-d4)

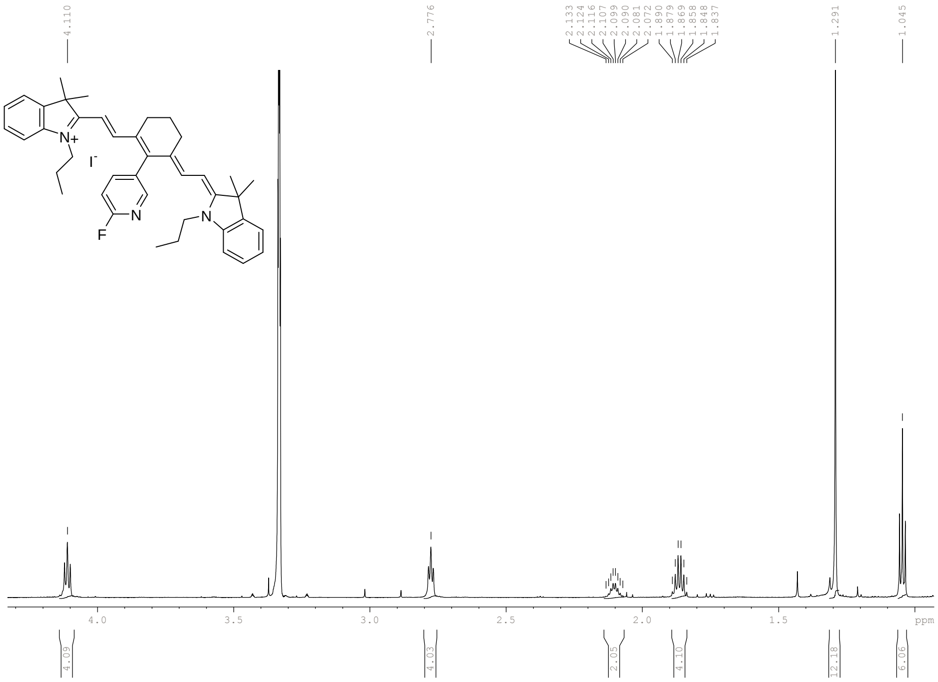

Figure S2. ^{13}C NMR spectrum of **2** (150 MHz, MeOH-d4)

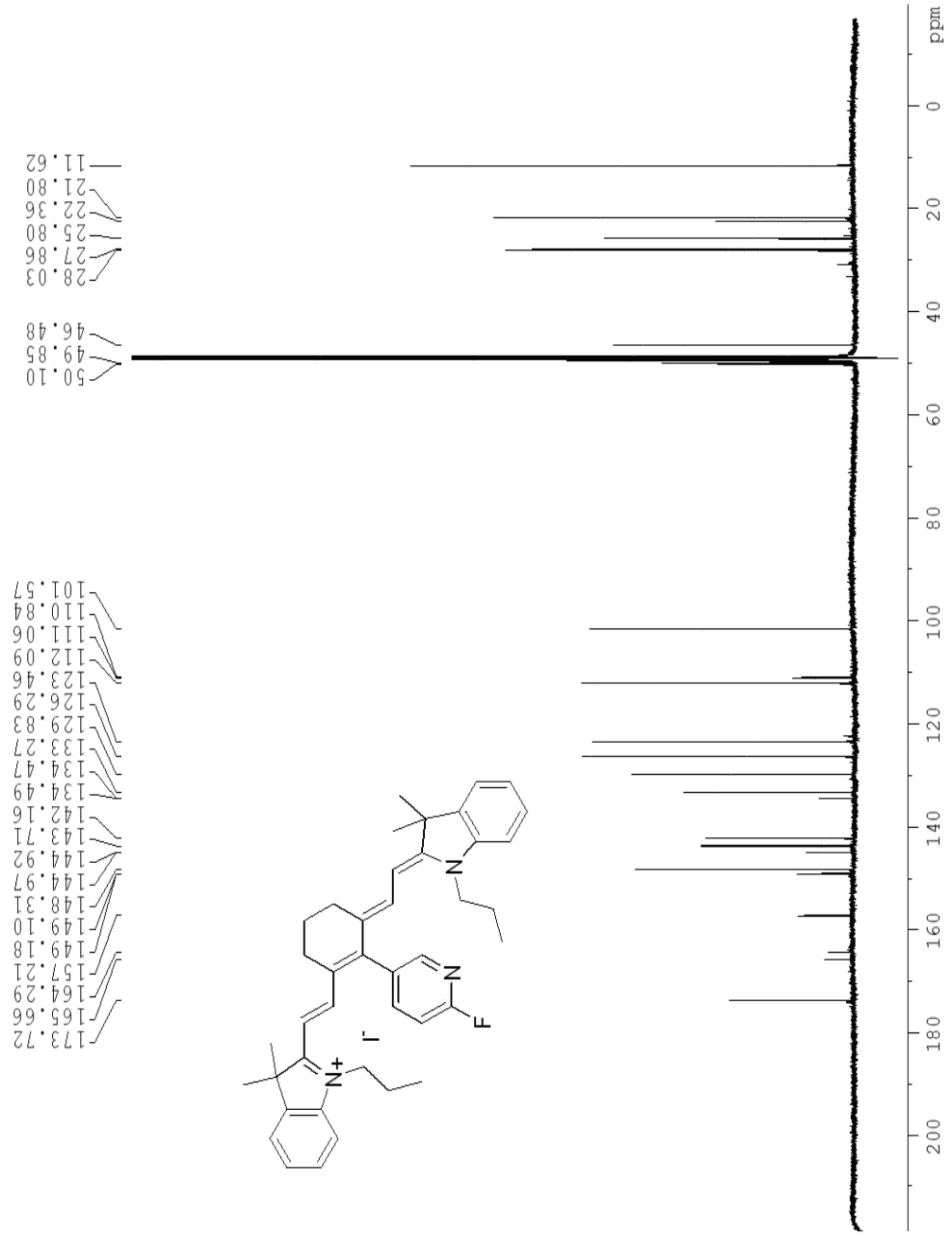

Figure S2-1. Expansion of the ^{13}C NMR spectrum of **2** (150 MHz, MeOH-d4)

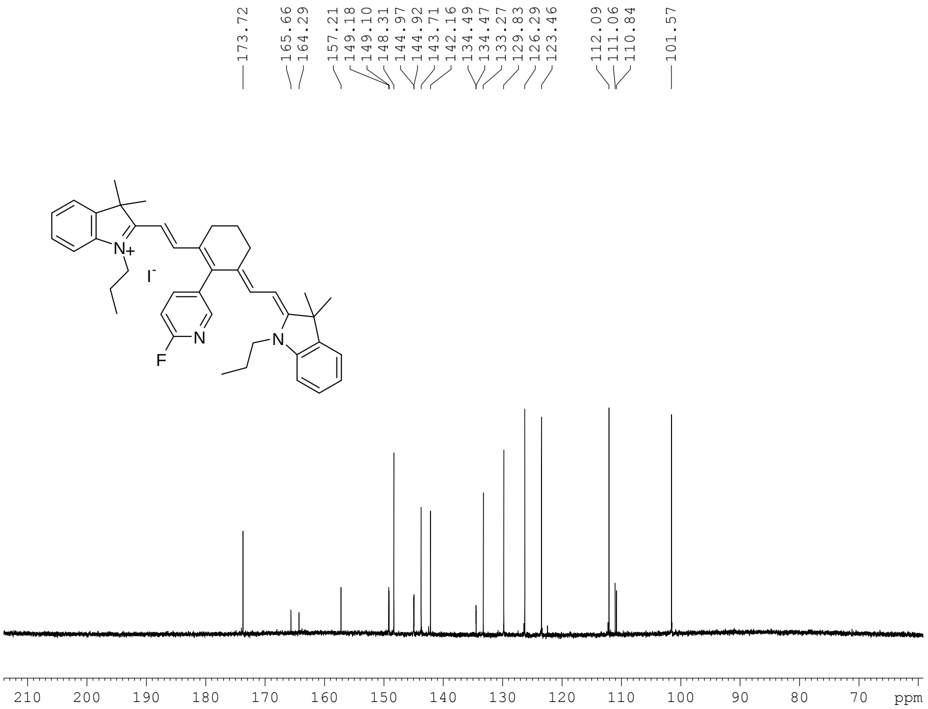

Figure S2-2. Expansion of the ^{13}C NMR spectrum of **2** (150 MHz, MeOH-d4)

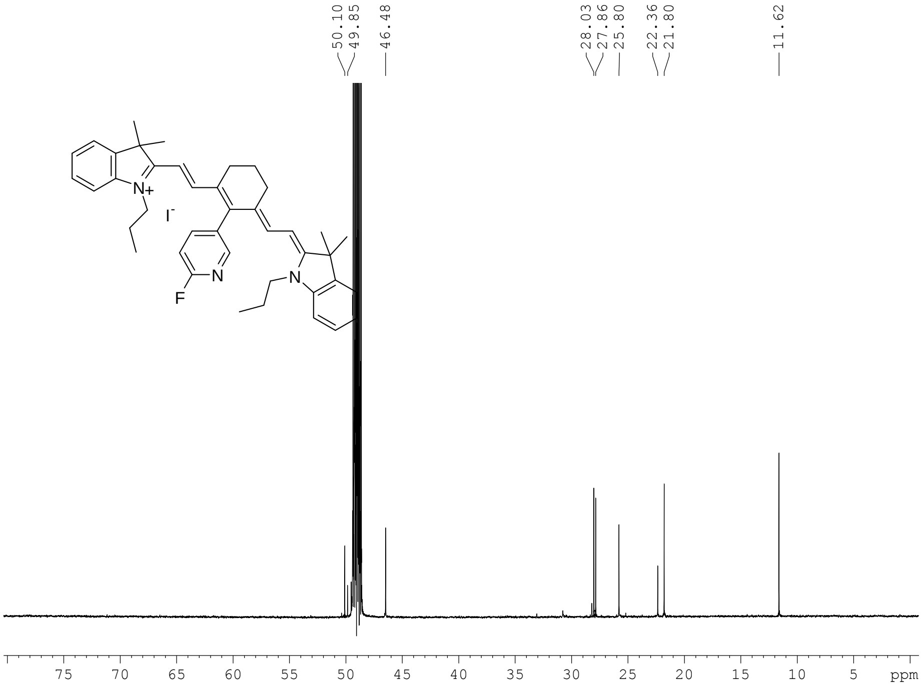

Figure S3. COSY spectrum of **2** (700 MHz, MeOH-d4)

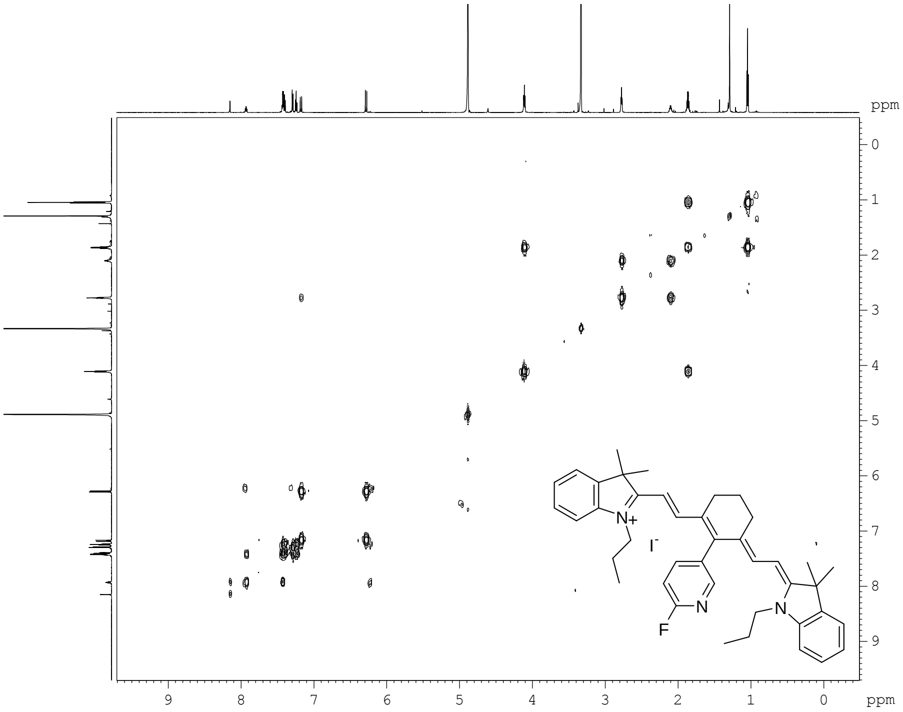

Figure S4. HRMS of **2** (ESI$^+$)

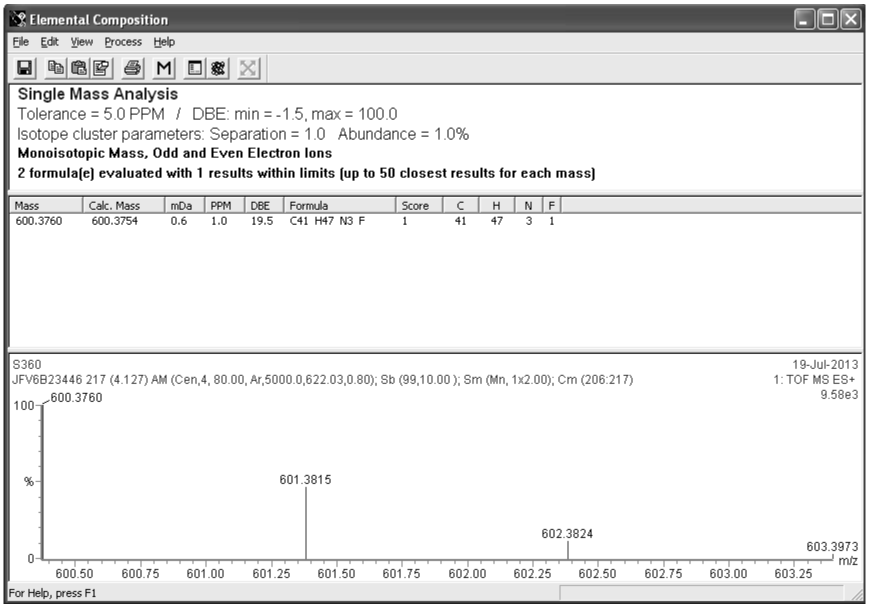

Single Mass Analysis

Tolerance = 5.0 PPM / DBE: min = -1.5, max = 100.0

Isotope cluster parameters: Separation = 1.0 Abundance = 1.0%

Monoisotopic Mass, Odd and Even Electron Ions

2 formula(e) evaluated with 1 results within limits (up to 50 closest results for each mass)

Mass	Calc. Mass	mDa	PPM	DBE	Formula	Score	C	H	N	F
600.3760	600.3754	0.6	1.0	19.5	C41 H47 N3 F	1	41	47	3	1

S360 19-Jul-2013

JFV6B23446 217 (4.127) AM (Cen,4, 80.00, Ar,5000.0,622.03,0.80); Sb (99,10.00); Sm (Mn, 1x2.00); Cm (206:217) 1: TOF MS ES+

9.58e3

Figure S5. ^{1}H NMR spectrum of **1a** (700 MHz, CD_3CN)

Figure S5-1. Expansion of the ^{1}H NMR spectrum of **1a** (700 MHz, CD_3CN)

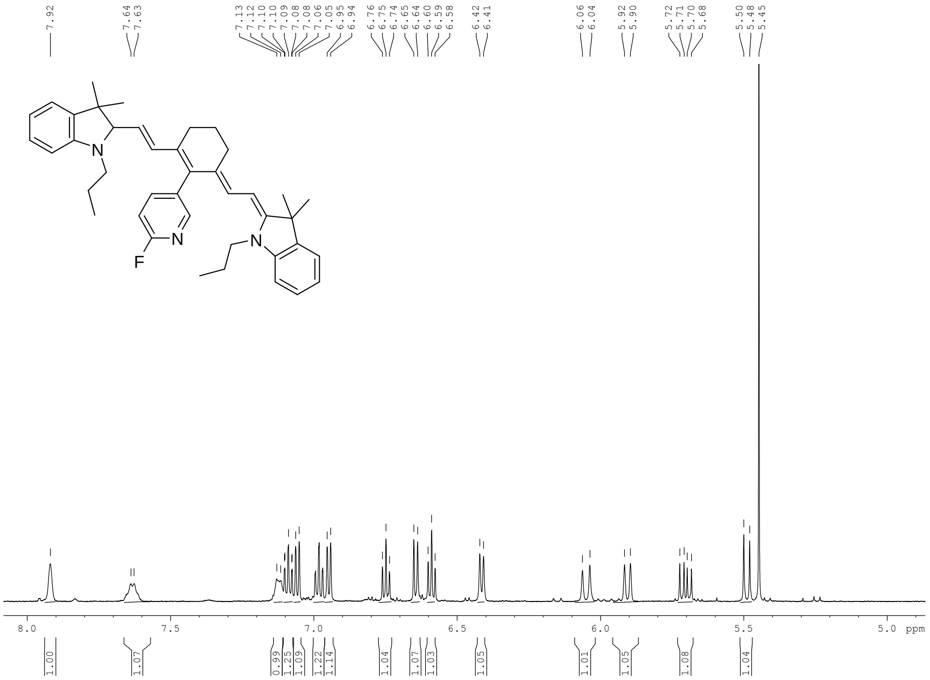

Figure S5-2. Expansion of the ^{1}H NMR spectrum of **1a** (700 MHz, CD_3CN)

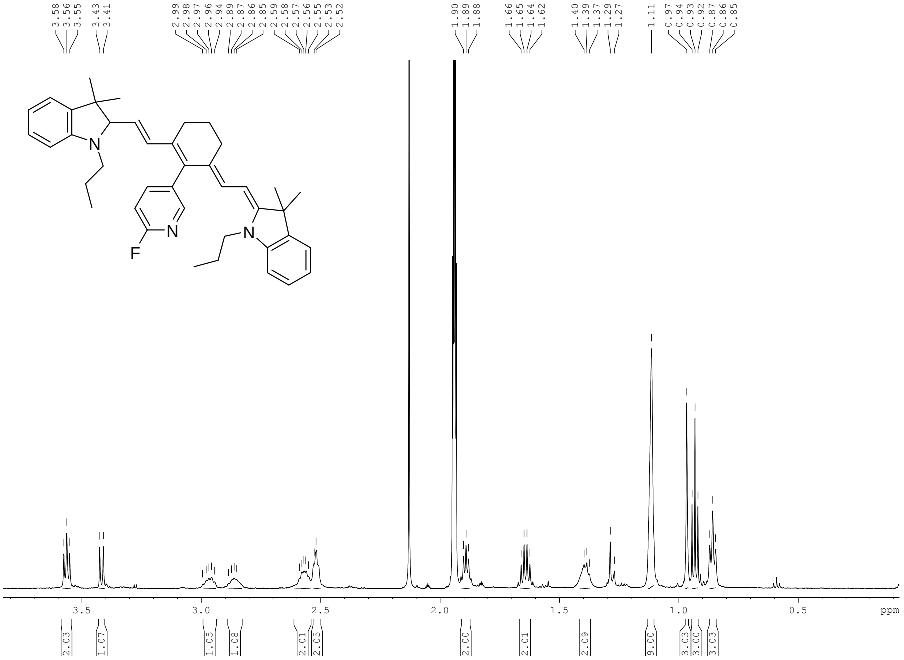

Figure S6. ^{13}C NMR spectrum of **1a** (150 MHz, CD_3CN)

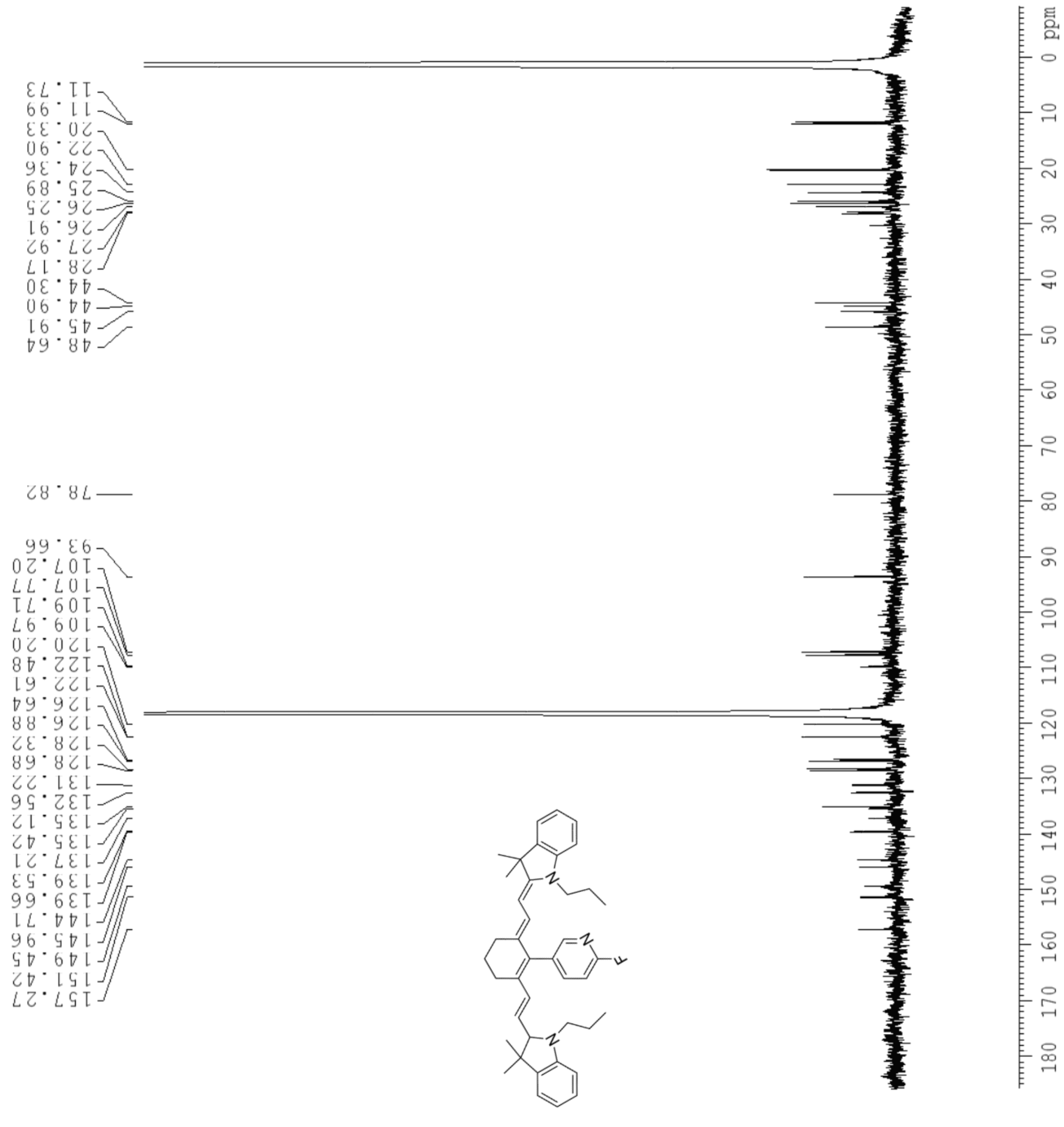

Figure S6-1. Expansion of the ^{13}C NMR spectrum of **1a** (150 MHz, CD_3CN)

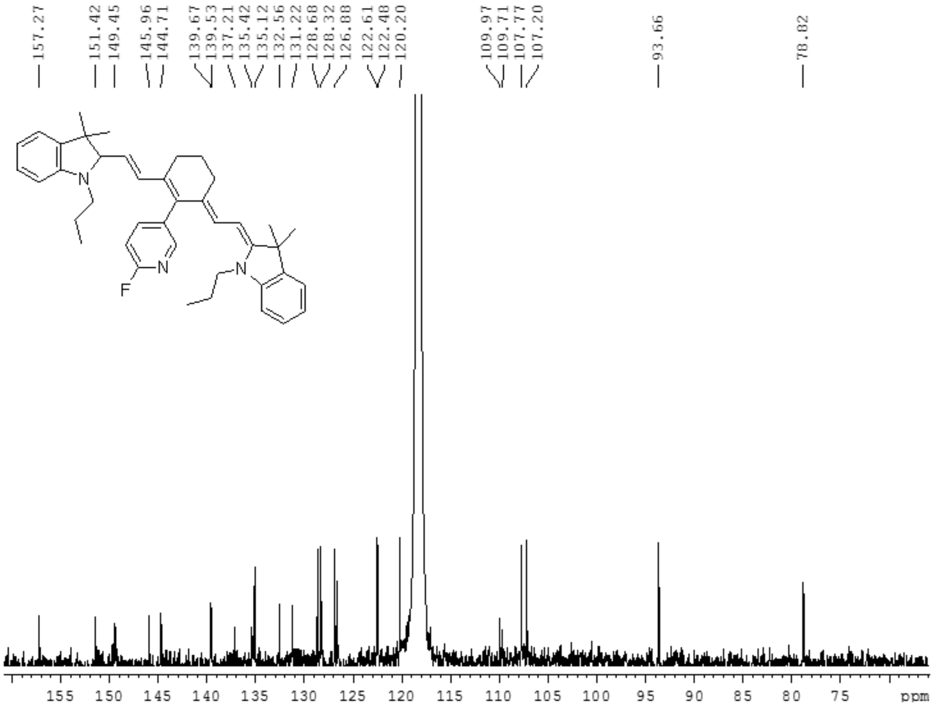

Figure S6-2. Expansion of the ^{13}C NMR spectrum of **1a** (150 MHz, CD_3CN)

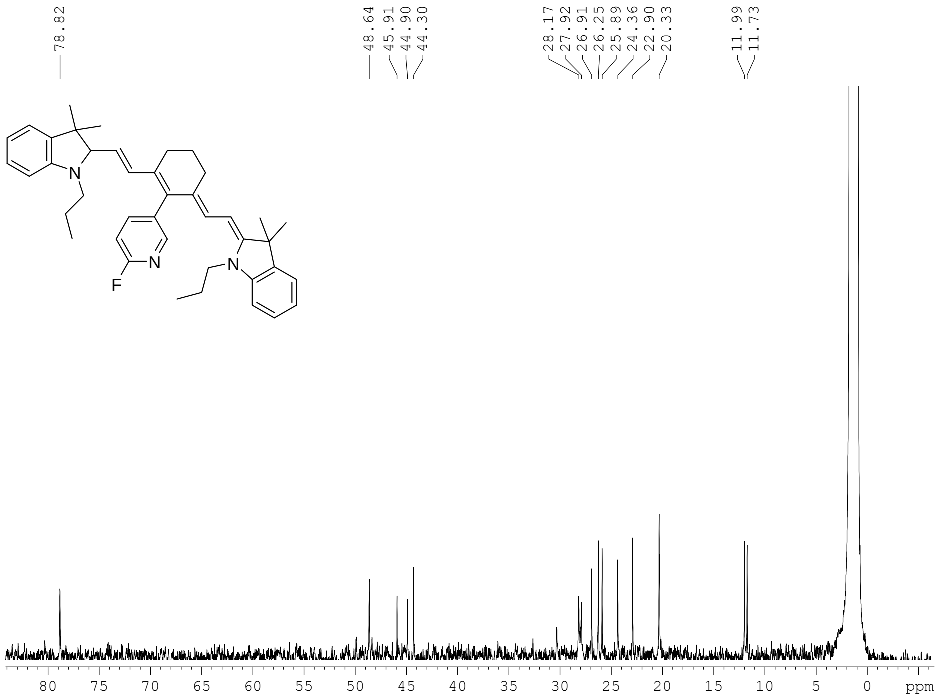

Figure S7. COSY spectrum of **1a** (700 MHz, CD_3CN)

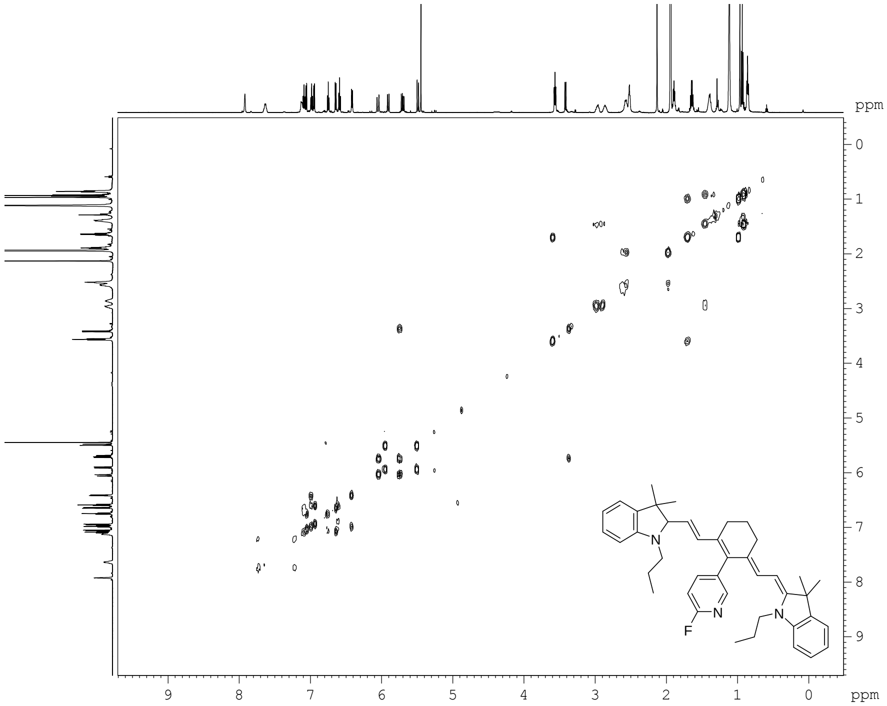

Figure S8. HRMS of **1a** (ESI^+)

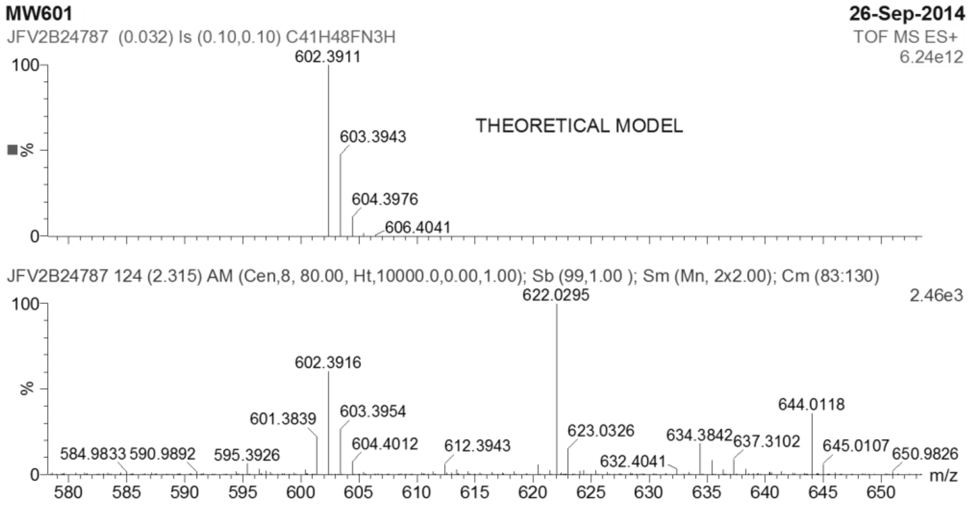

Figure S9. Stability profile of **1a** ($\lambda_{ex}/\lambda_{em}$ = 768 nm/794 nm) and dihydroethidium (DHE, $\lambda_{ex}/\lambda_{em}$ = 515 nm/560 nm) at a concentration of 40 µM in 20% MeOH/PBS (pH= 7.4). Probes were incubated at 37°C and fluorescence readings were taken at the specified time intervals.

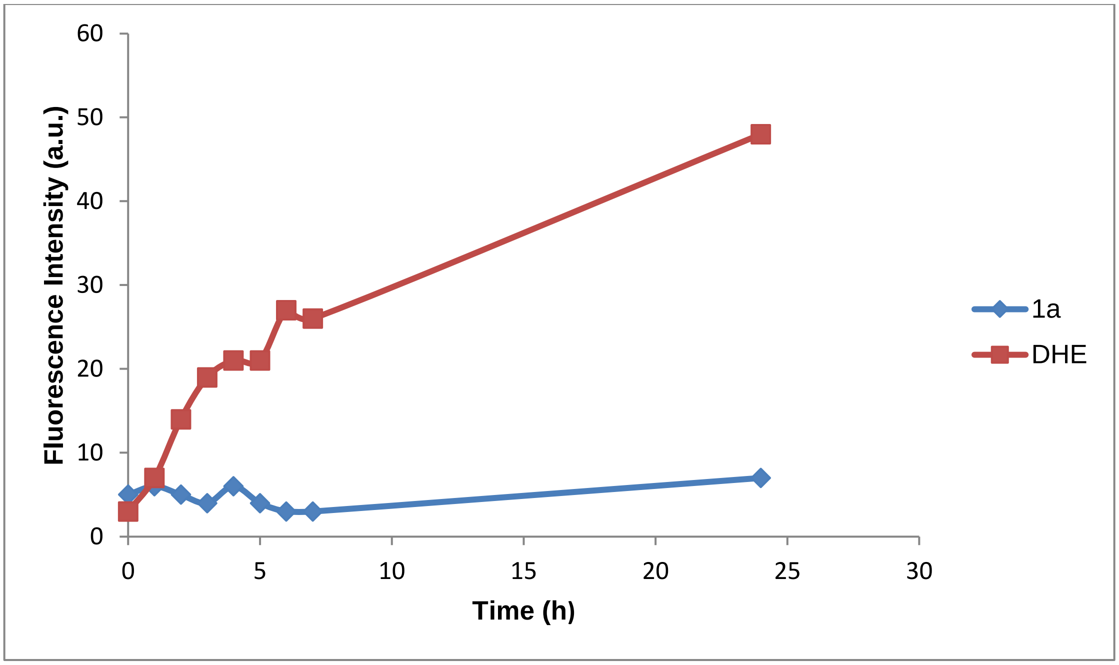

Figure S10. UV HPLC (λ = 254 nm) chromatograms of **1a** in 20% MeOH/PBS after incubation at 37°C at 1 and 6 h (Method B).

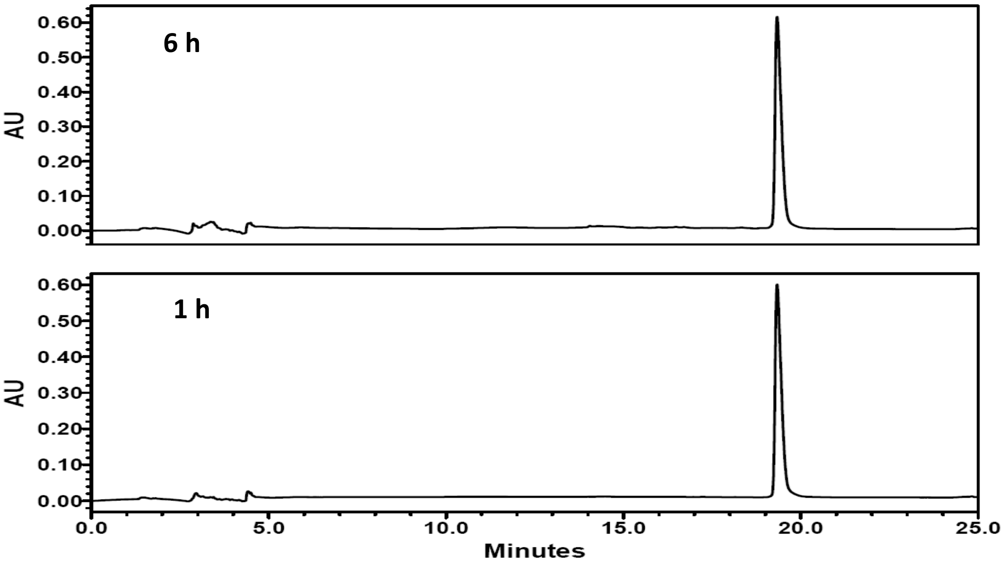

Figure S11. Fluorescence intensity of **1a**, and DHE (50 µM in MeOH) in the absence (no induction) and presence (induction) of KO_2, after 1 h at RT.

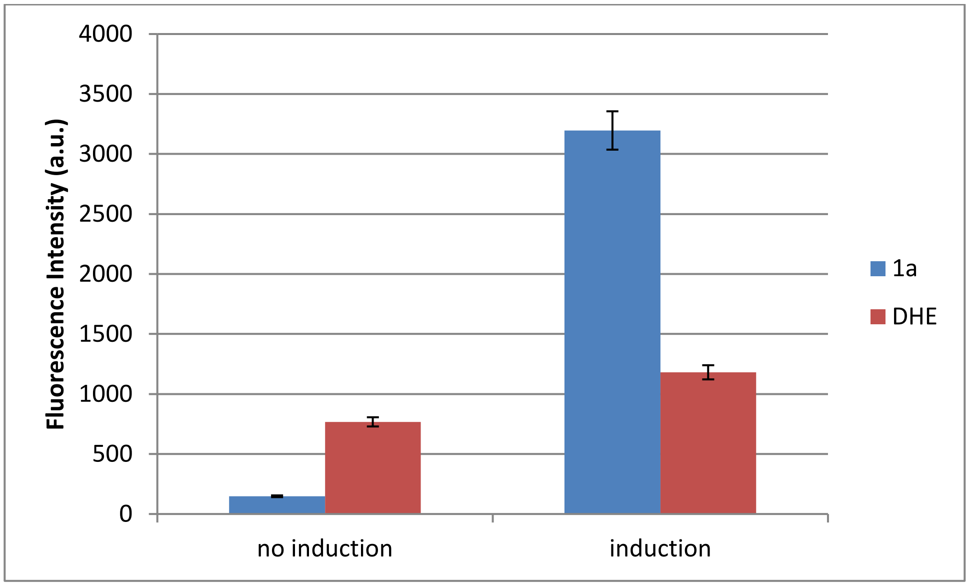

Figure S12. Fluorescence microscopy images of PC-3 cells treated with a) 50 µM **1a** (1% DMSO) for 0.5 h following treatment with 0.8% saline for 0.5 h b) 50 µM **1a** (1% DMSO) for 0.5 h following treatment with 5 mM TEMPOL (0.8% saline) for 0.5 h c) control image following treatment with 0.8% saline for 1 h and 1% DMSO for 0.5 h d) 50 µM **1a** (1% DMSO) for 0.5 h following treatment with 0.8% saline for 1h e) 50 µM **1a** following treatment with 5 mM NAC for 1h (f) Brightfield image. TEMPOL = 4-hydroxy-2,2,6,6-tetramethylpiperidin-1-oxyl; NAC = N-acetyl-L-cysteine. Note that we found this assay highly variable.

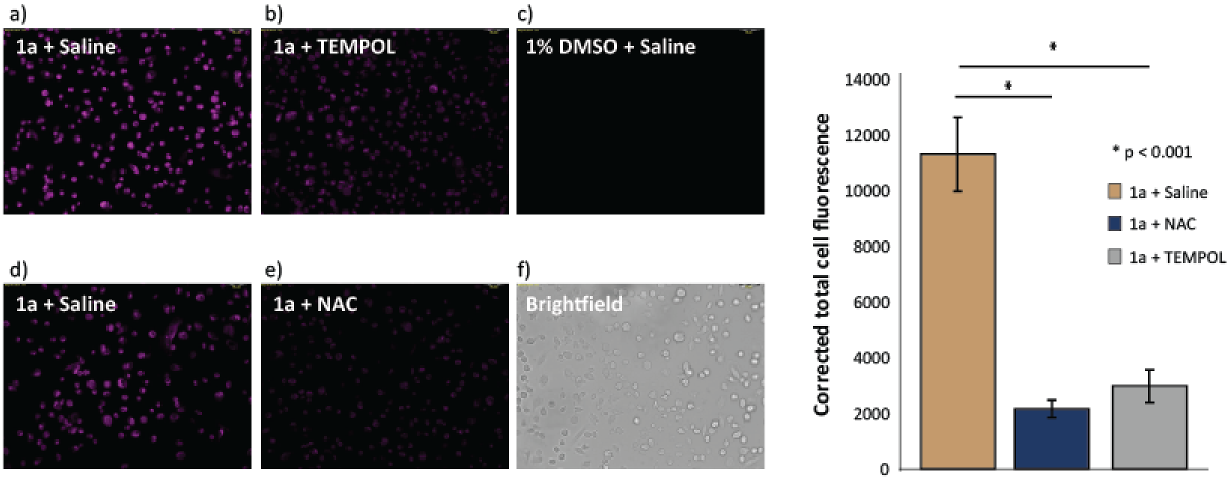

Figure S13. MTT assay of PC-3 cell viability, with various concentrations of **1a** or cisplatin.

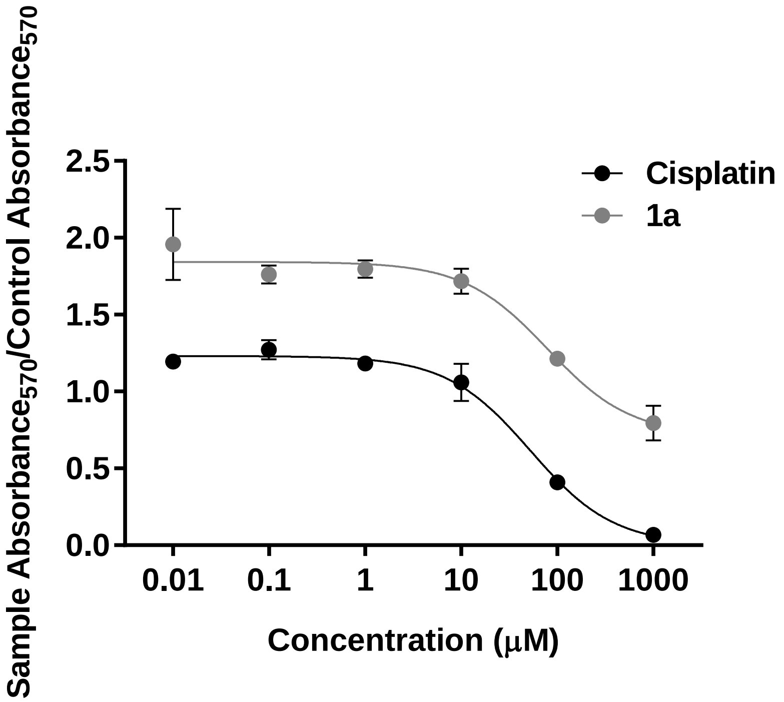

Figure S14. ORTEP projection for **3** (50% thermal ellipsoid probability). Hydrogen atoms and counter ion were omitted for clarity.

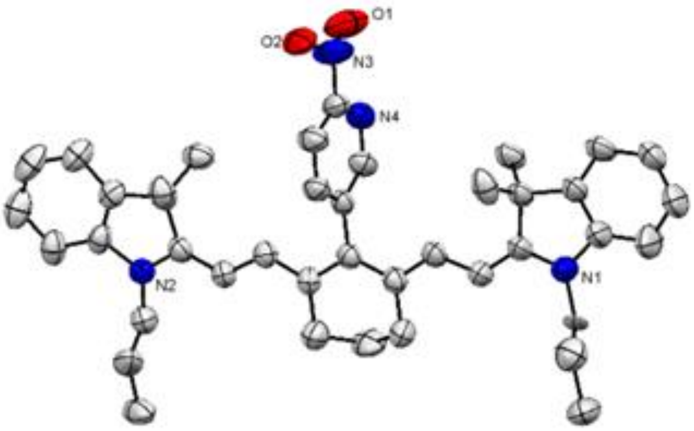

Figure S15. ^{1}H NMR spectrum of **3** (700 MHz, MeOH-d4)

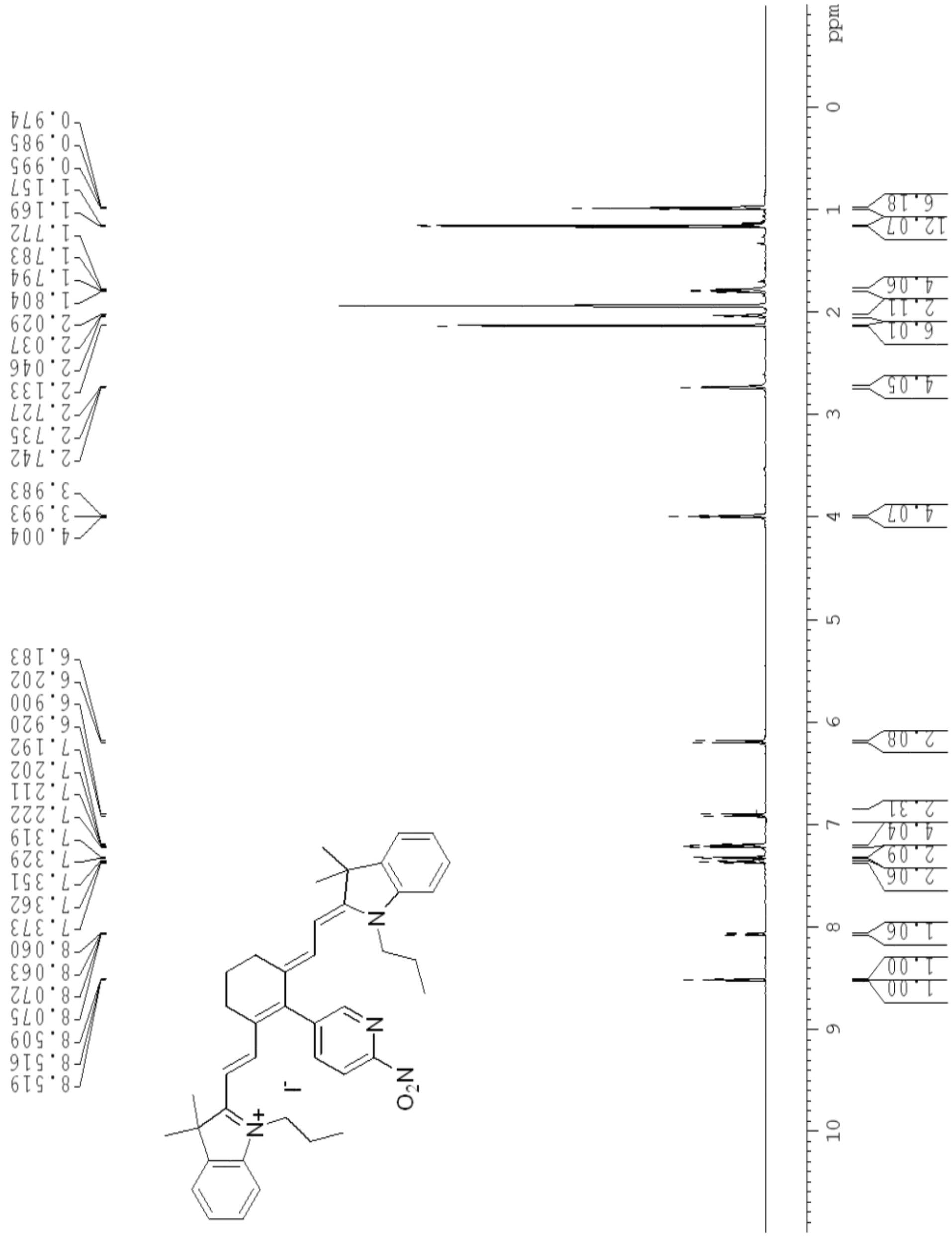

Figure S15-1. Expansion of the ^{1}H NMR spectrum of **3** (700 MHz, MeOH-d4)

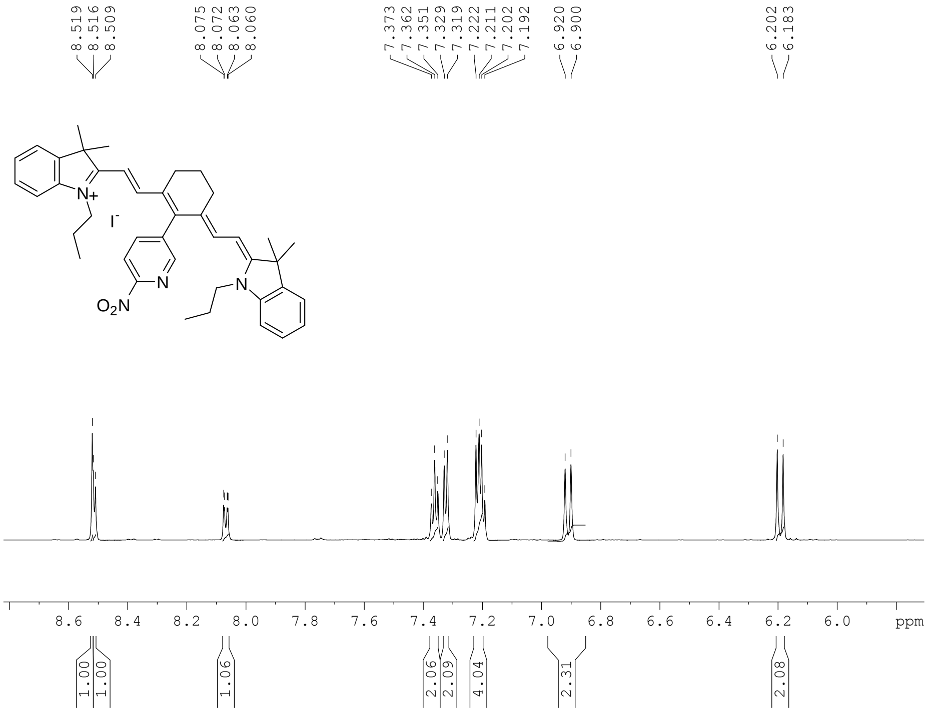

Figure S15-2. Expansion of the ^{1}H NMR spectrum of **3** (700 MHz, MeOH-d4)

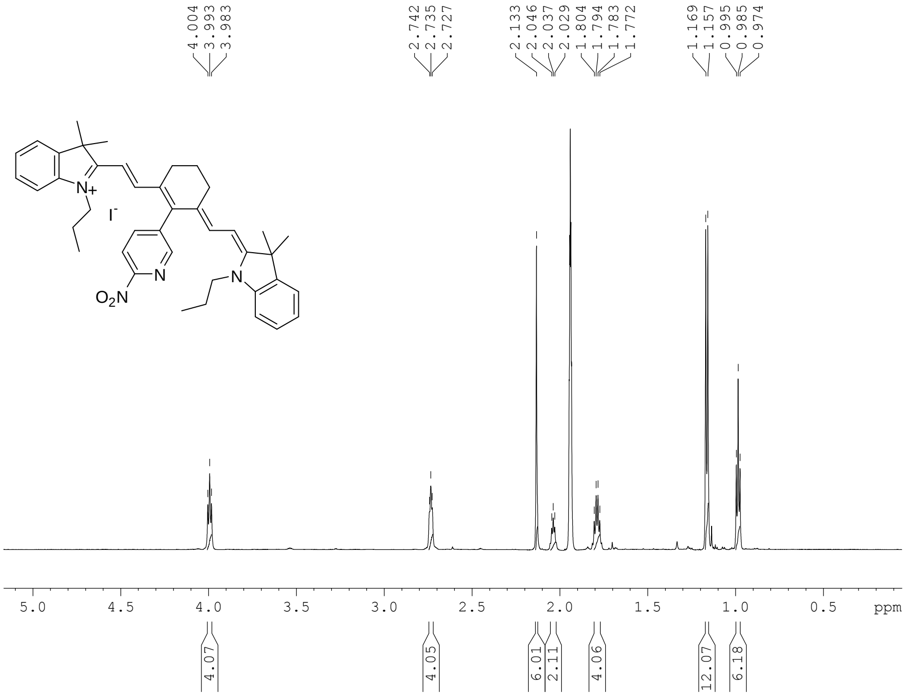

Figure S16. ^{13}C NMR spectrum of **3** (150 MHz, MeOH-d4)

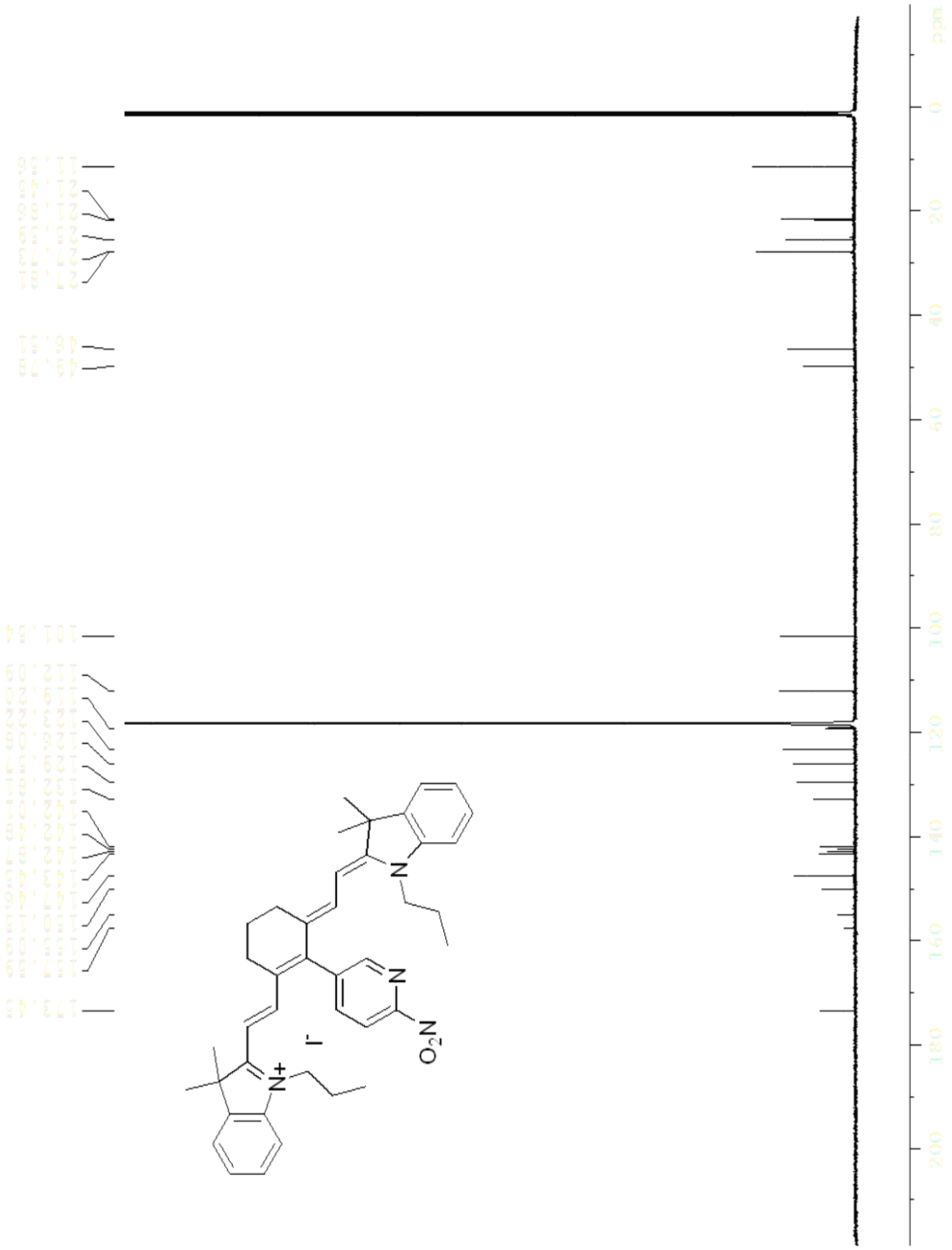

Figure S16-1. Expansion of the ^{13}C NMR spectrum of **3** (150 MHz, MeOH-d4)

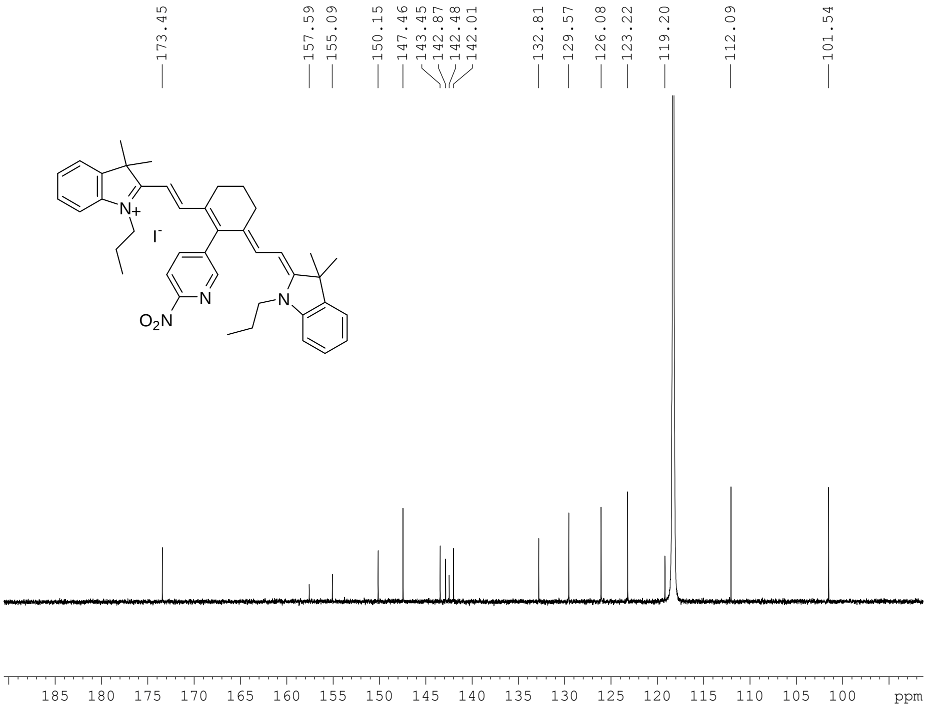

Figure S16-2. Expansion of the ^{13}C NMR spectrum of **3** (150 MHz, MeOH-d4)

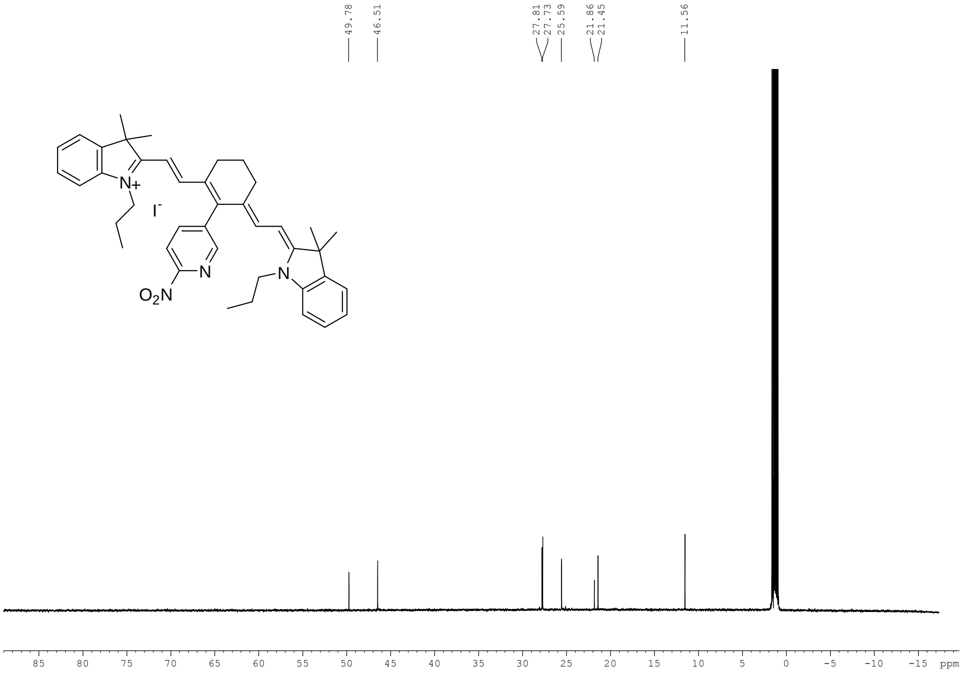

Figure S17. COSY spectrum of **3** (700 MHz, MeOH-d4)

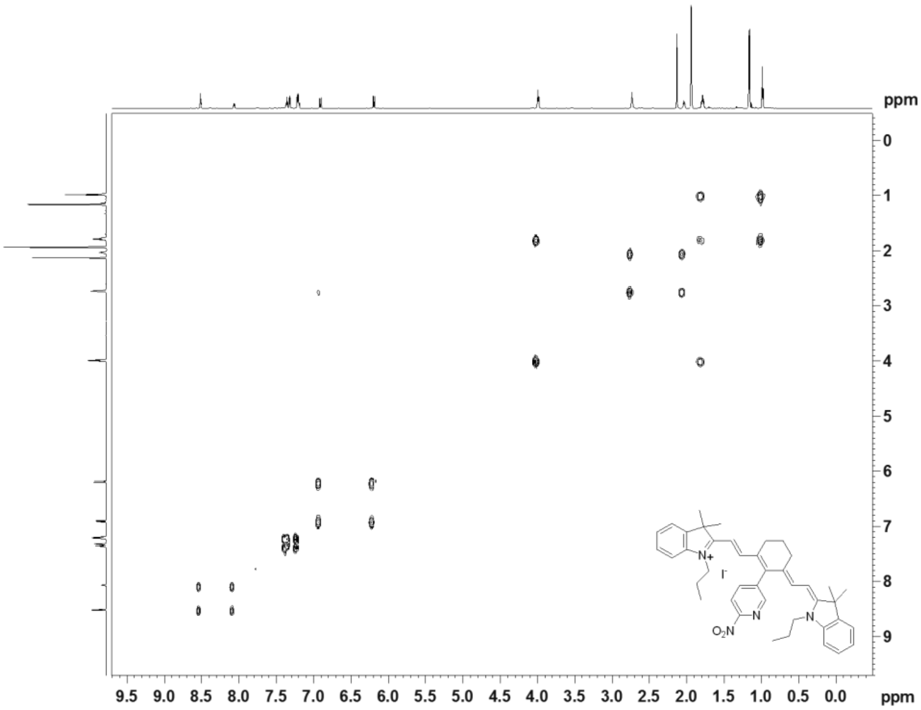

Figure S18. HRMS of **3** (ESI$^+$)

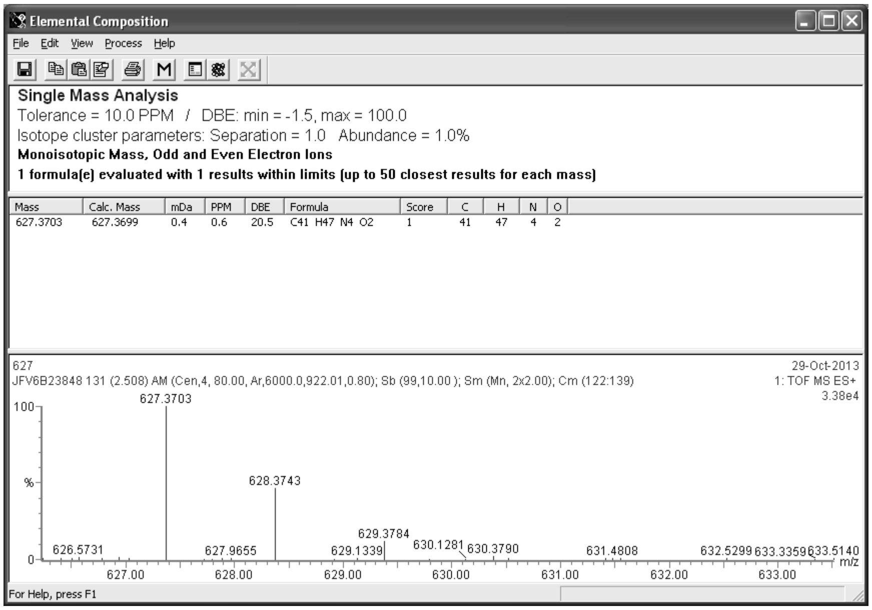

Single Mass Analysis
Tolerance = 10.0 PPM / DBE: min = -1.5, max = 100.0
Isotope cluster parameters: Separation = 1.0 Abundance = 1.0%
Monoisotopic Mass, Odd and Even Electron Ions
1 formula(e) evaluated with 1 results within limits (up to 50 closest results for each mass)

Mass	Calc. Mass	mDa	PPM	DBE	Formula	Score	C	H	N	O
627.3703	627.3699	0.4	0.6	20.5	C41 H47 N4 O2	1	41	47	4	2

627
JFV6B23848 131 (2.508) AM (Cen,4, 80.00, Ar,6000.0,922.01,0.80); Sb (99,10.00); Sm (Mn, 2x2.00); Cm (122:139)
29-Oct-2013
1: TOF MS ES+
3.38e4

Figure S19. γ-HPLC chromatograms following the incubation of **1b** 10% ethanol/saline for 60 and 120 min (Method A).

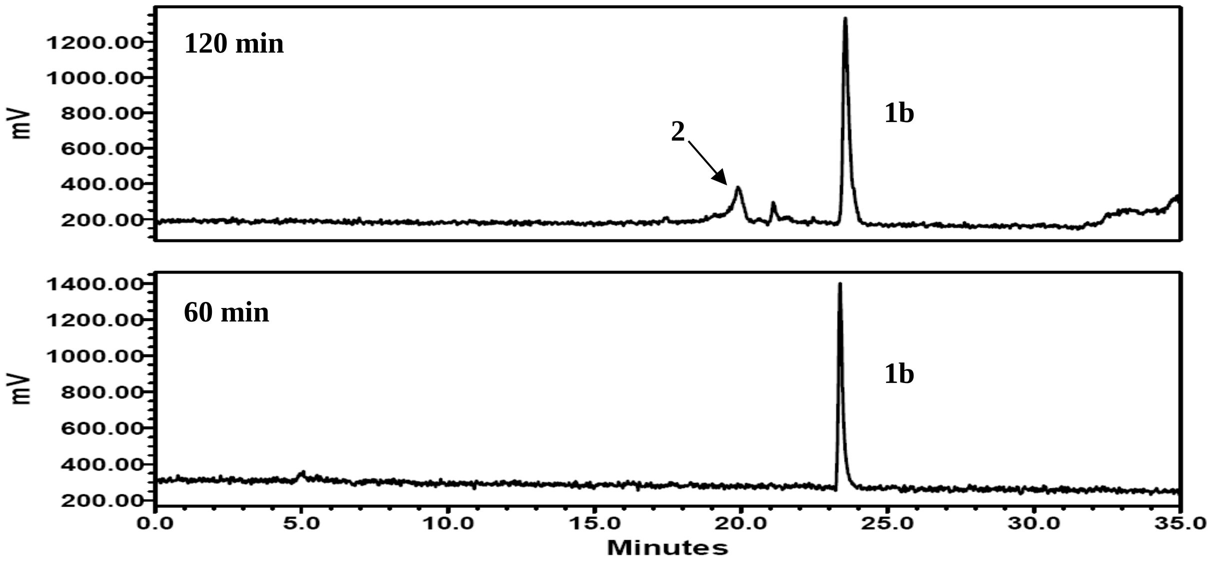

Figure S20. γ-HPLC chromatograms following the incubation of **1b** in 10% ethanol/saline in the presence of ascorbic acid (0.5 mg/mL) for 60 and 120 min (Method A).

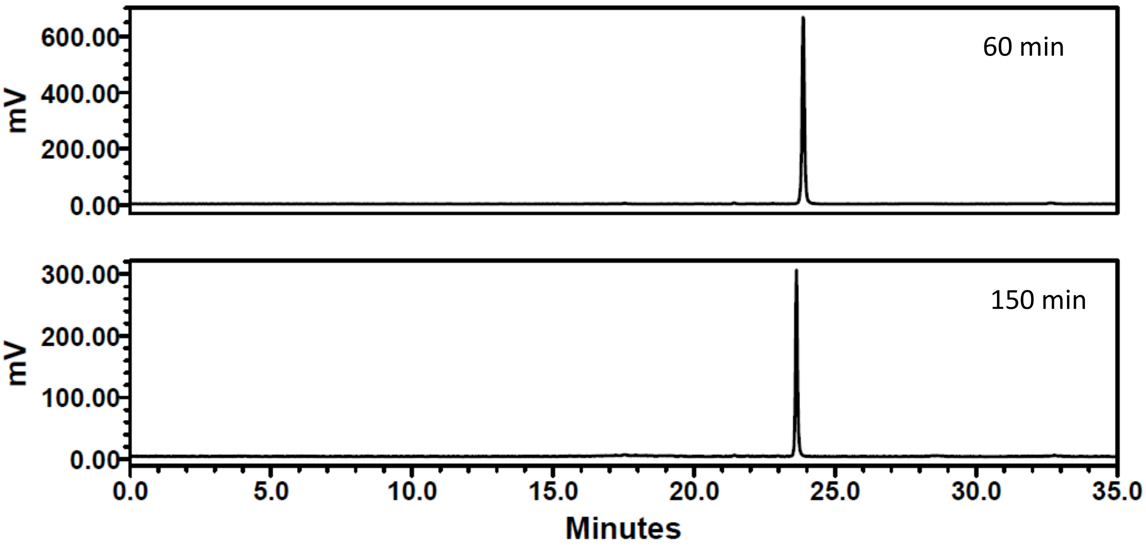

Figure S21. Standard curve of fluorescence intensity versus concentration of **1a**.

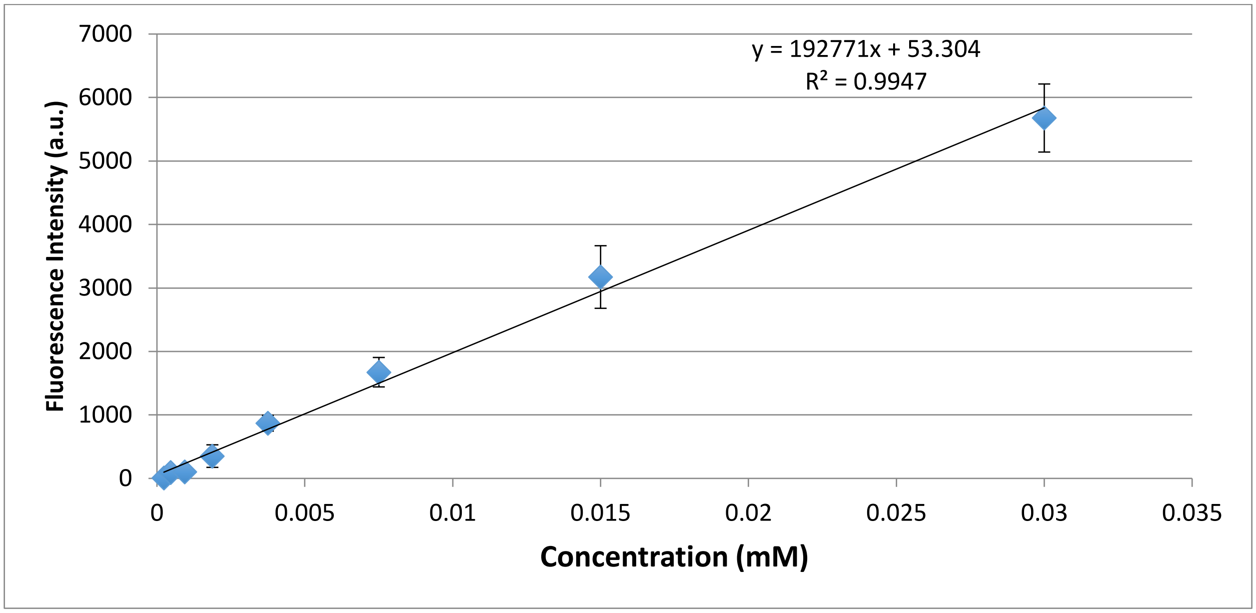

Figure S22. Reconstructed PET/CT images at 1,2 and 4 h post intravenous injection of **1b** in a healthy C57BL/6 mouse.

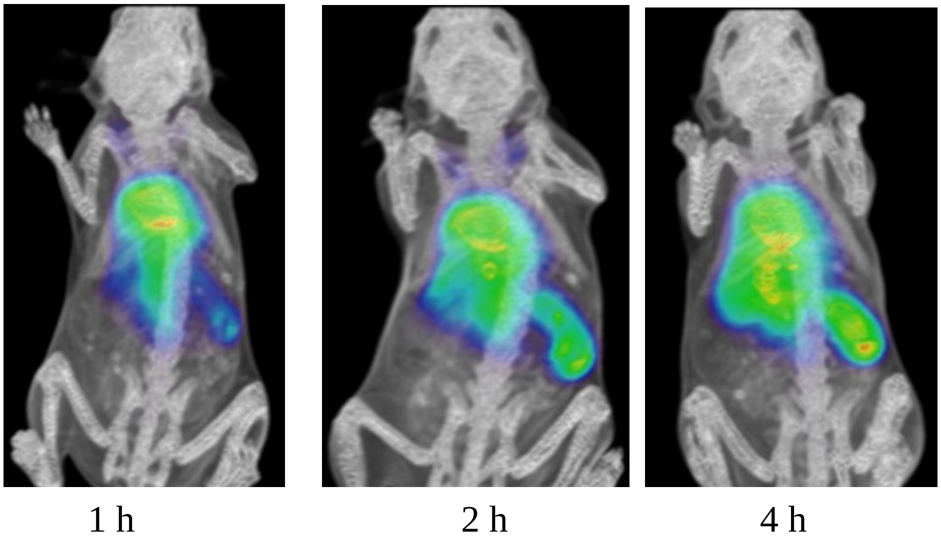

Tables:

Table S1. X-ray Crystallography Data for **3**

Space group crystal system	Monoclinic
Space group name	$P2_1/c$
Cell length A	19.880 (4)
Cell length B	6.0200 (12)
Cell length C	33.220 (7)
α	90
β	91.15 (3)
γ	90
Cell volume (A^3)	3974.9 (14)
Z	6
T (K)	293 (2)
λ (Synchrotron) (Å)	0.8726
D ($g.cm^{-3}$)	1.25 (2)
θ_{max}	24.5°
Parameters	566

Table S2. Biodistribution of **1b** after intravenous injection into healthy C57BL/6 mice, sacrificed at 2 and 4 h. Data is expressed in % injected dose/gram of tissue or fluid (%ID/g).

%ID/g	n=3		n=3	
	2 h		4 h	
Organ/Tissue	avg	SEM	avg	SEM
Blood	52.32	4.57	42.51	10.38
Adipose	0.72	0.07	1.02	0.20
Adrenals	13.25	2.04	12.29	2.07
Bone	3.70	0.36	4.73	1.12
Brain	0.76	0.06	0.59	0.12
Gall Bladder	17.45	3.45	11.16	1.51
Heart	5.14	0.38	4.39	1.04
Kidneys	9.41	2.86	7.46	2.04
Lg Intestine + Caecum	1.33	0.25	3.87	0.49
Liver	7.98	0.31	10.21	1.22
Lungs	9.89	1.03	7.44	1.48
Pancreas	1.59	0.12	1.13	0.24
Skeletal Muscle	0.72	0.05	1.17	0.67
Sm Intestine	2.27	0.10	1.95	0.35
Spleen	23.63	1.36	24.37	4.35
Stomach	0.92	0.15	1.50	0.22
Thyroid/Trachea	3.24	0.47	3.22	0.45
Urine + Bladder	1.50	0.57	2.20	1.30

APPENDIX 2

Figure S1. ^{1}H NMR spectrum of **7** (700 MHz, MeOH-d4)

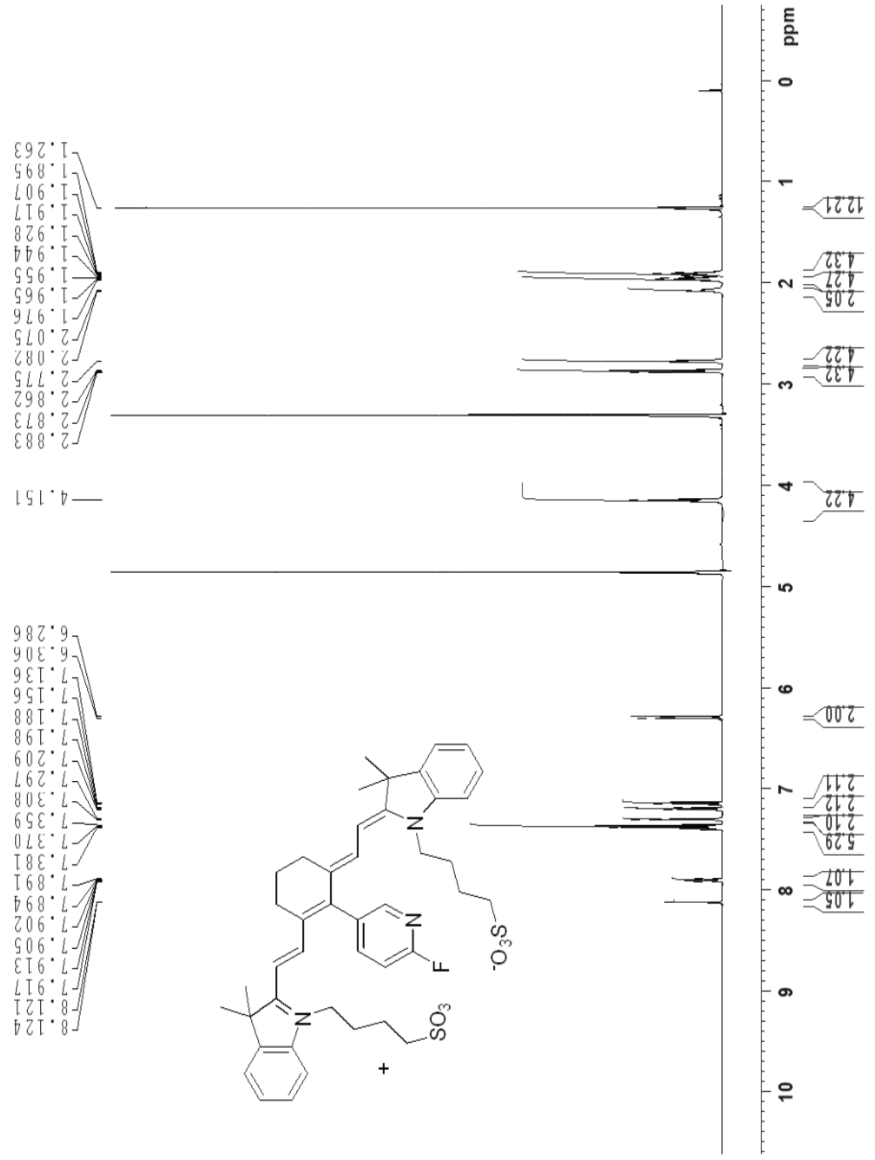

Figure S2. ^{13}C NMR spectrum of **7** (175 MHz, MeOH-d4)

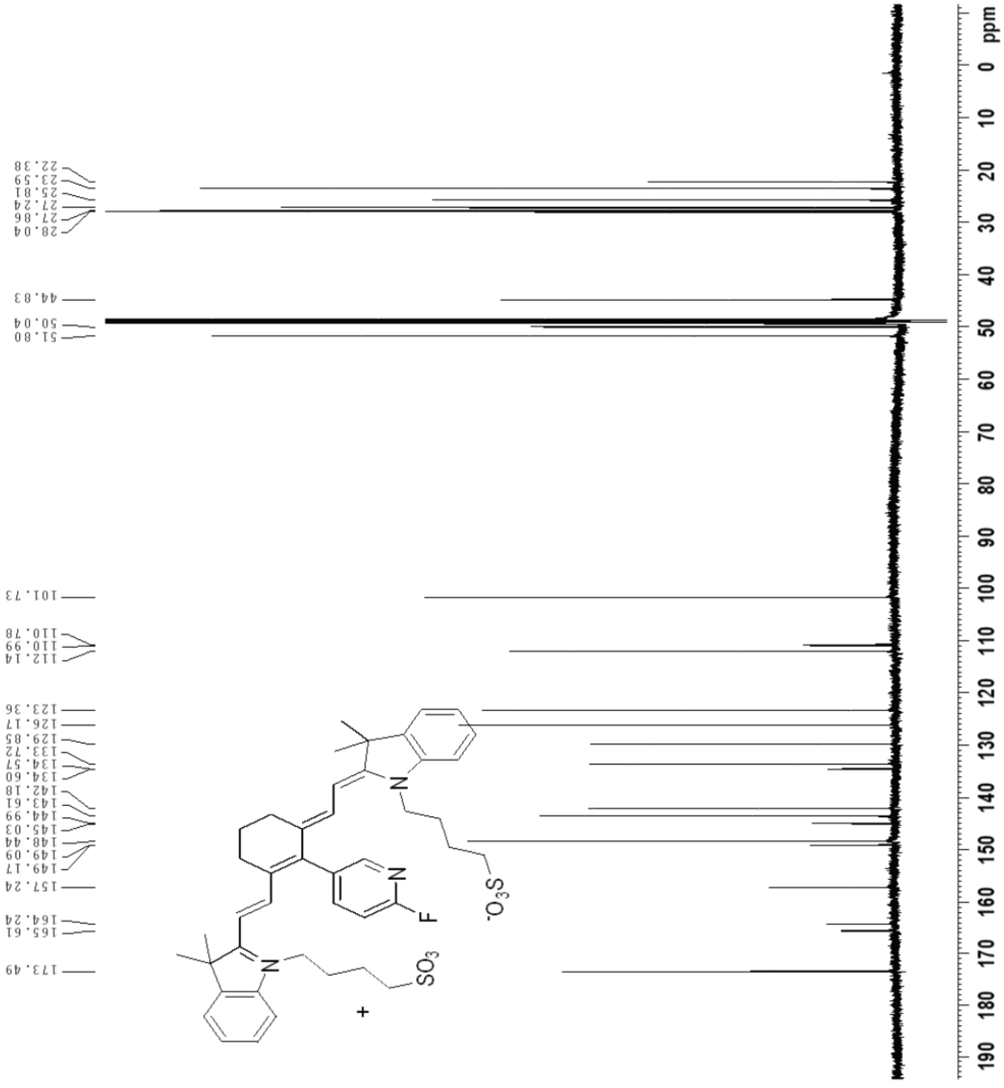

Figure S3. HRMS of **7** (ESI$^+$)

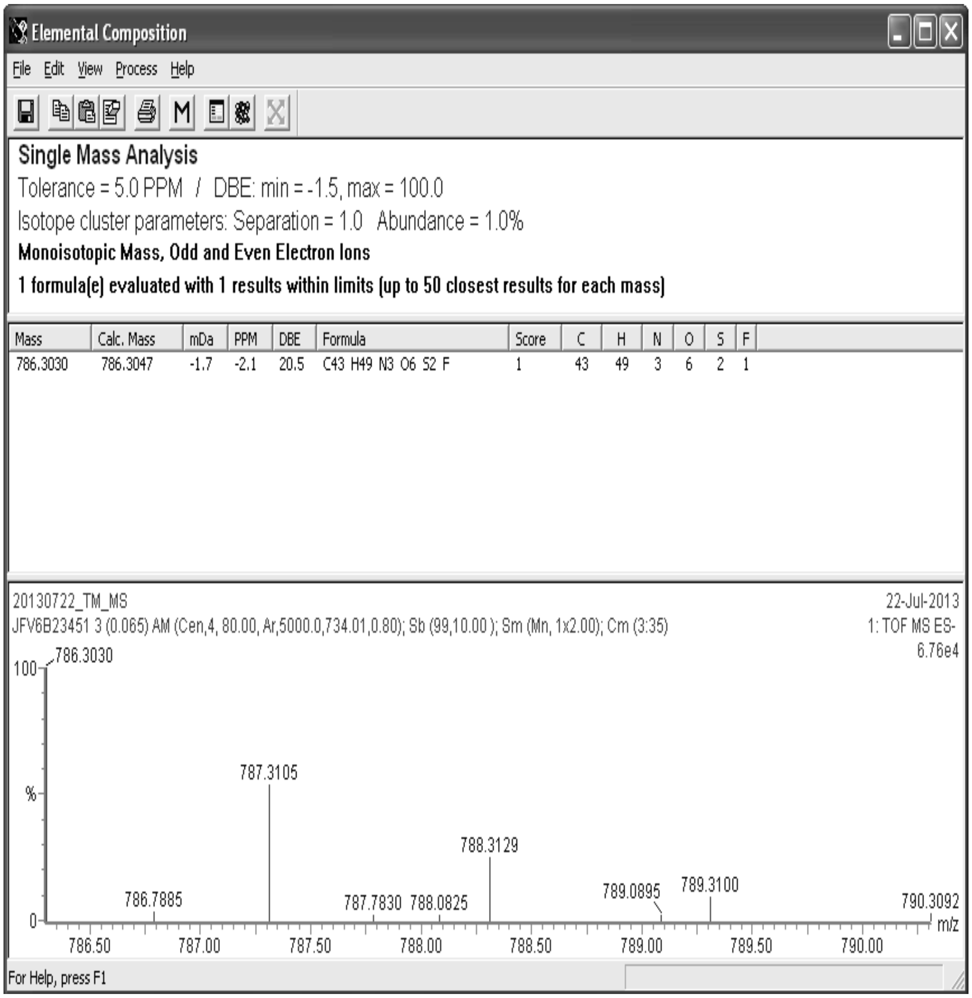

Single Mass Analysis

Tolerance = 5.0 PPM / DBE: min = -1.5, max = 100.0

Isotope cluster parameters: Separation = 1.0 Abundance = 1.0%

Monoisotopic Mass, Odd and Even Electron Ions

1 formula(e) evaluated with 1 results within limits (up to 50 closest results for each mass)

Mass	Calc. Mass	mDa	PPM	DBE	Formula	Score	C	H	N	O	S	F
786.3030	786.3047	-1.7	-2.1	20.5	C43 H49 N3 O6 S2 F	1	43	49	3	6	2	1

20130722_TM_MS 22-Jul-2013

JFV6B23451 3 (0.065) AM (Cen,4, 80.00, Ar,5000.0,734.01,0.80); Sb (99,10.00); Sm (Mn, 1x2.00); Cm (3:35) 1: TOF MS ES-

6.76e4

Figure S4. ^{1}H NMR spectrum of **9a** (600 MHz, MeOH-d4)

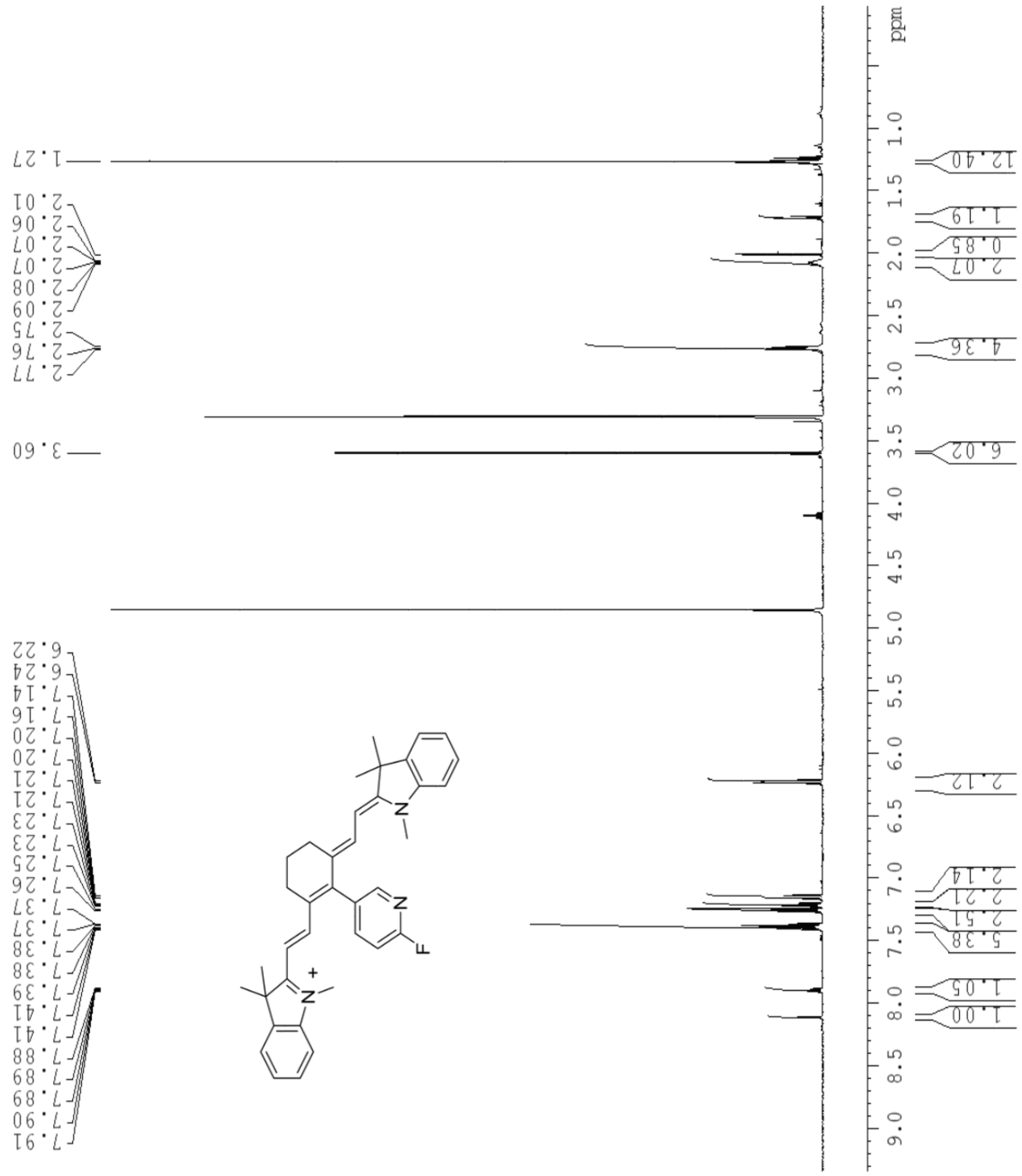

Figure S5. ^{13}C NMR spectrum of **9a** (150 MHz, MeOH-d4)

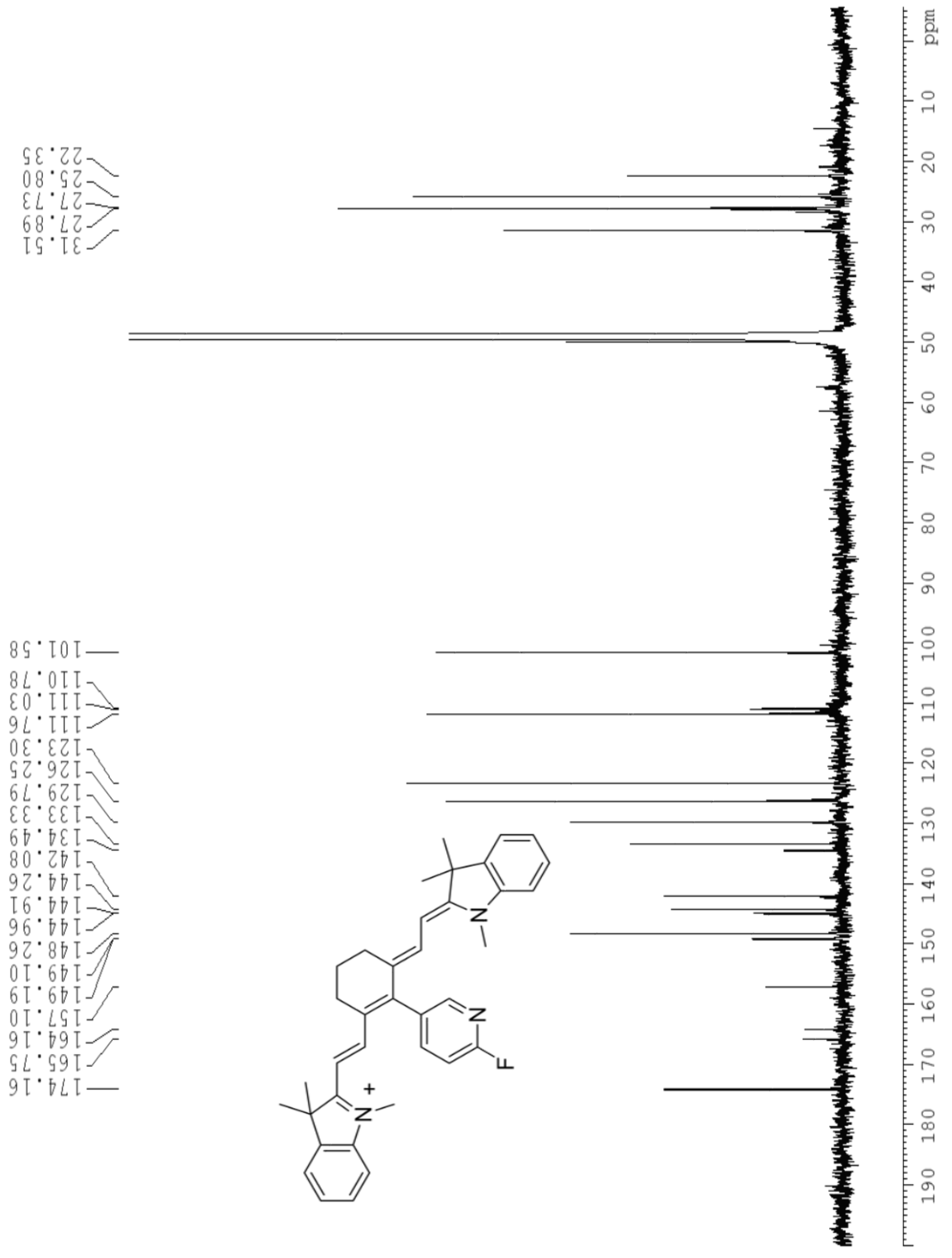

Figure S6. HRMS of **9a** (ESI$^+$).

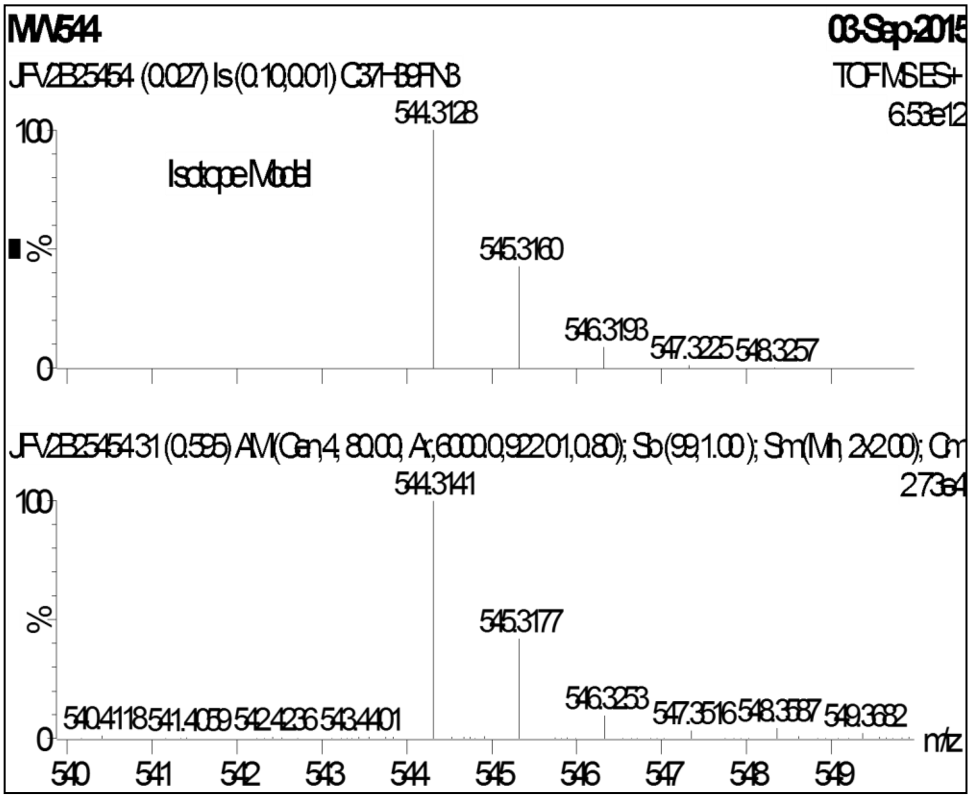

Figure S7. ^{1}H NMR spectrum of **11** (600 MHz, MeOH-d4)

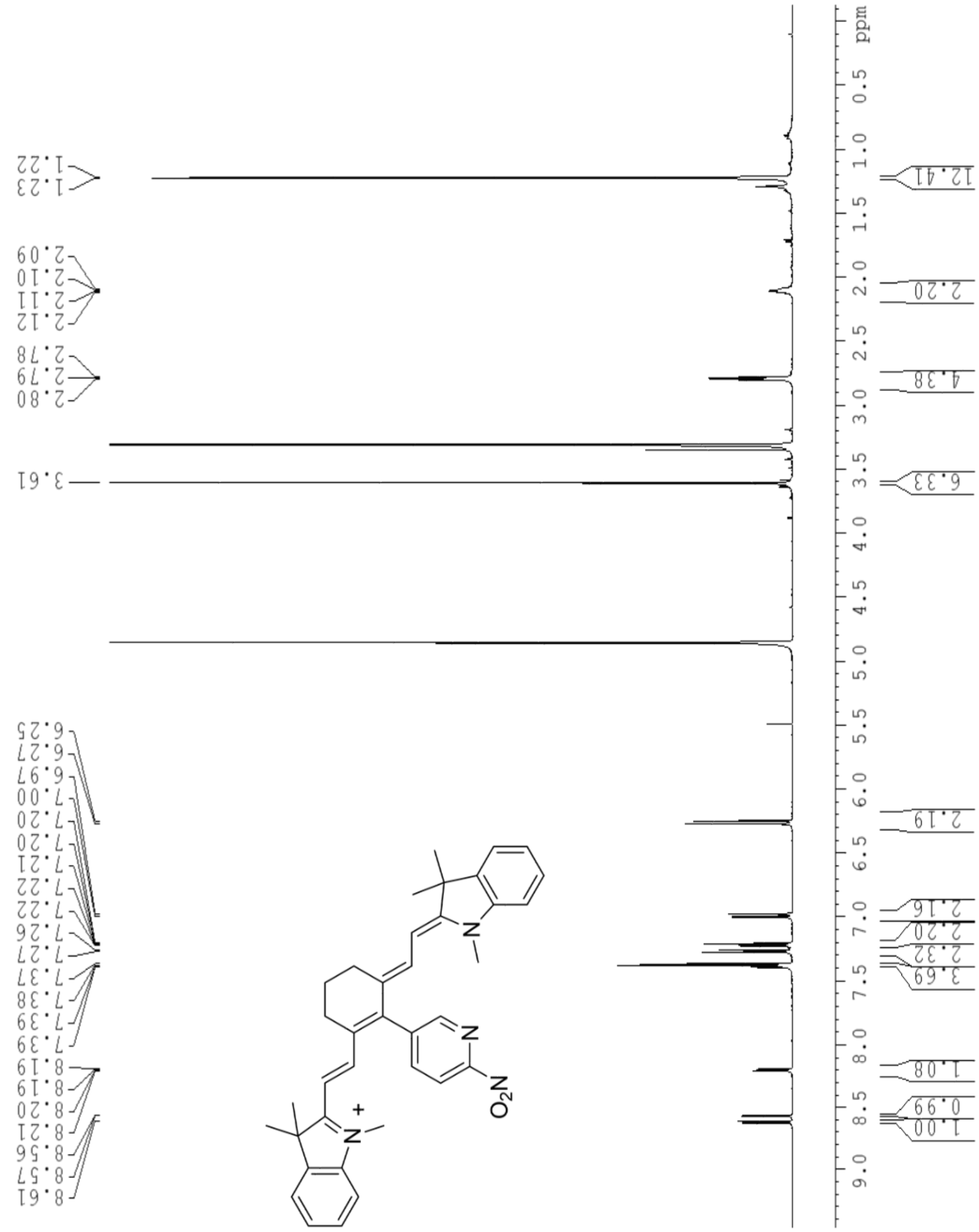

Figure S8. ^{13}C NMR spectrum of **11** (150 MHz, MeOH-d4)

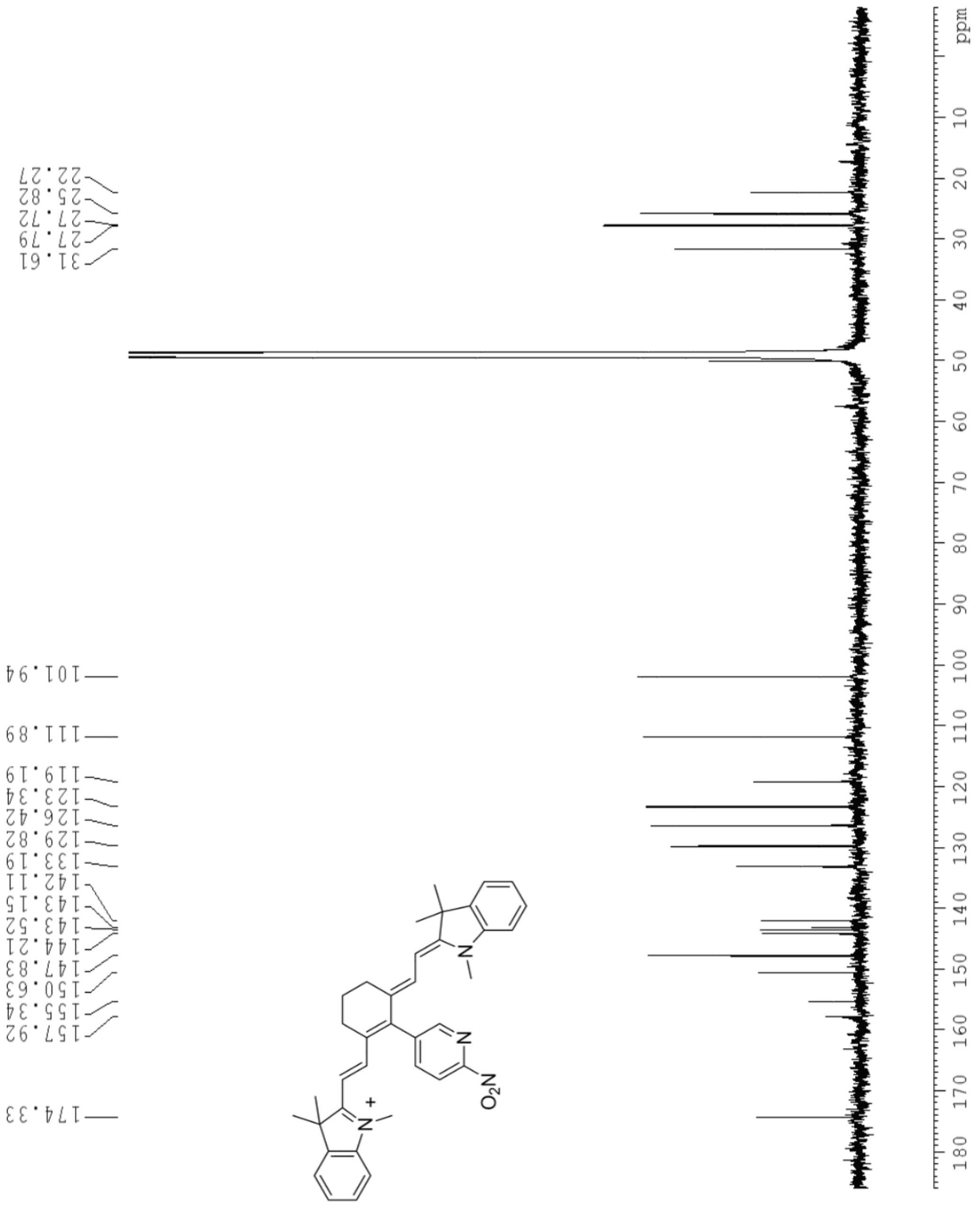

Figure S9. HRMS of **11** (ESI$^+$).

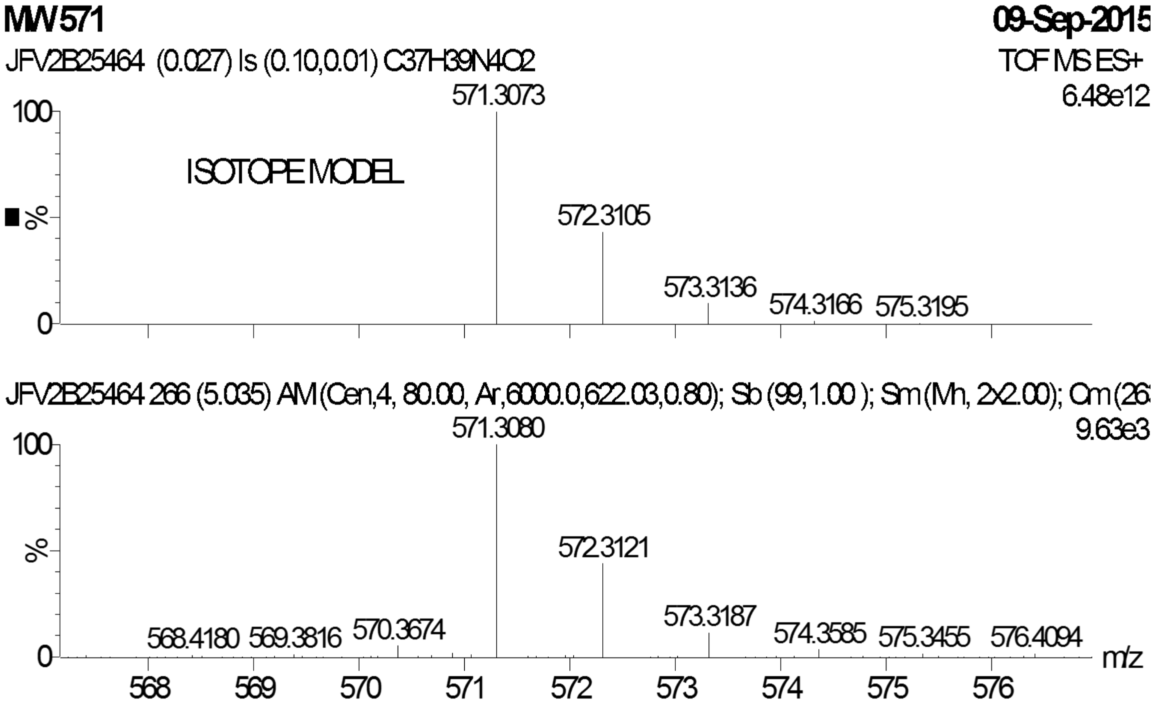

Figure S10. ^{1}H NMR spectrum of **13** (600 MHz, MeOH-d4)

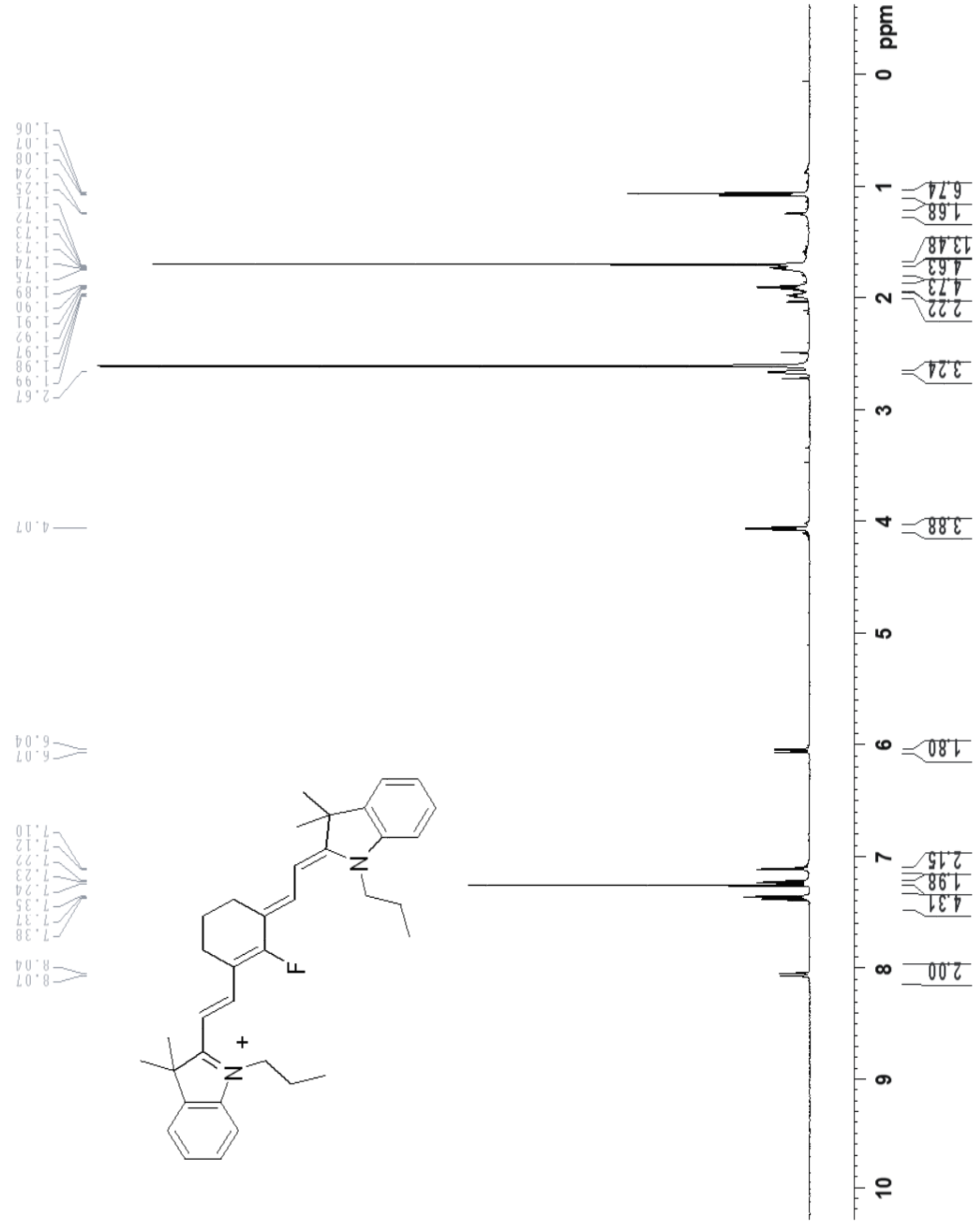

Figure S11. ^{13}C NMR spectrum of **13** (150 MHz, MeOH-d4)

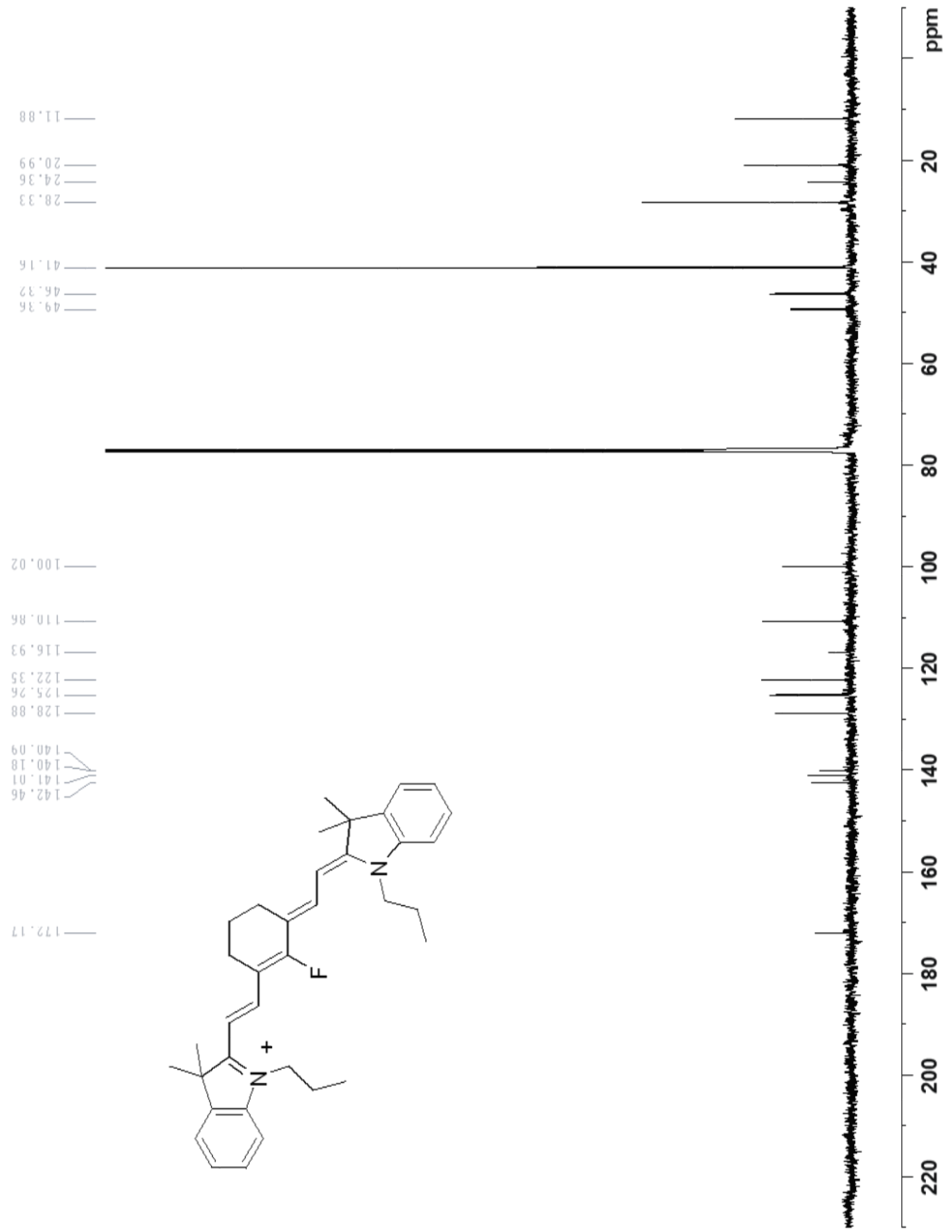

Figure S12. HRMS anlaysis for **13** (ESI$^+$).

Elemental Composition Report

Single Mass Analysis

Tolerance = 5.0 PPM / DBE: min = -1.5, max = 300.0

Selected filters: None

Monoisotopic Mass, Even Electron Ions

76 formula(e) evaluated with 1 results within limits (up to 50 closest results for each mass)

Elements Used:

C: 0-40 H: 0-50 N: 1-3 Na: 0-1 F: 0-2

Minimum:			-1.5		
Maximum:		5.0	5.0	300.0	
Mass	Calc. Mass	mDa	PPM	DBE	i-FIT
523.3503	523.3489	1.4	2.7	15.5	6.9

C36 H44 N2 F